THE UNIVERSITY
of EDINBURGH

NATURAL ANALOGUES FOR GEOLOGICAL CARBON STORAGE

By

Yutong SHU

A thesis submitted for the degree of Doctor of Philosophy

School of Geosciences, University of Edinburgh

October 2017

Declaration

This thesis is entirely the original work of the author, except where otherwise stated. All references are duly acknowledged. This thesis has not been submitted for a degree at this or any other universities. Permission is granted to the University of Edinburgh to lend the copy upon request, provided the source is acknowledged.

Yutong SHU

Summary

In CO_2 storage sites, seal has a vital role in inhibiting migration of the supercritical CO_2 to other geological strata. The major difficulties in studying seals include two aspects: lack of available samples (especially for saline aquifers), and the difficulty to study over geological time and spatial scales. The analysis of natural analogue has been chosen to overcome these difficulties. Hydrocarbon fields are used to investigate the pore throat radii, which is the major factor for capillary sealing of caprocks, using newly established statistics model. Natural CO_2 springs at Green River, Utah are used to study how the long-term CO_2 charge triggers chemical reactions and migration in shales.

One of the major sealing mechanism of caprocks is capillary sealing. Pore throat radius, as the main factor to decide the capillary sealing, has been investigated in this study. As an alternative to the traditional method of mercury injection porosimetry, a statistical model for effective pore throat radii determination has been established. The cumulative percentage and the probability distribution of the effective pore throat radii of the shale caprocks in the UK North Sea oil fields are obtained, which would be used as a reference for the saline aquifers in CO_2 storage siting in the future work. Monte Carlo simulation is utilised to get the distribution of the effective pore throat radii. The cumulative distribution from this study has been compared with the distribution by Yang and Aplin (1998). The distribution by the statistical model enables to narrow down the range of effective pore throat radii to 37nm~1700nm, and help to make a better prediction on the pore throat radii. The correlation between the controlling factors of faulting, burial depth, caprock thickness and the pore throat radii have been examined. Good correlation between the depth less than 3000m and the effective pore throat radii indicates clay diagenesis should be the major factor for shallowly buried caprocks. Faulting and caprock thickness present no significant correlation with the effective pore throat radii.

Crystal Geyser is used as an ideal natural analogue to study the Mancos Shale alteration. The interacted fluid that deposited travertine is important for the study. Hence, carbonate veins and reduction zones that associated with the activity of the main fault are used as records of the geochemistry of the paleo-fluid, the features of

which are compared to the present spring water. The result shows the paleo-fluid was much more saline than the present fluid, with greater flow-rate. The decreased flow-rate might be owing to the self-healing of the fault during the time.

Mancos shales outcropped in the hanging wall of the Little Grand Wash fault were sampled to investigate on the alterations triggered by the CO_2-charged fluid from the fault and fractures. The result shows the alteration radius of the Mancos has limited within the distance of 20m away from the fault. CO_2-rich fluid could interact with deformed shale (both dissolution and precipitation might happen), but no evidence shows the intact Mancos has been altered. The calcite cements in Mancos derived from CO_2 sequestration could reach up to 27% (%weight of the whole rock) at 15m away from the fault. The conclusion facilitates the carbon storage siting criteria by Chadwick et al., (2009), who proposed the cautionary thickness of the caprock to be 20m.

Acknowledgement

There are numerous people I would like to thank for helping me with this PhD. Firstly, I would like to thank my supervisors:

- Dr. Mark Wilkinson at the University of Edinburgh providing me the opportunity and resources to do this PhD. I am thankful for his enthusiasm, patience and precious support to assist my work.
- Dr. Mark Naylor at the University of Edinburgh for his assistance in the work of CO_2 column height conversion method.

I would like to thank China Scholarship Council and the University of Edinburgh for funding my research in the past four years.

For experiments work, I would like to thank Dr Nicholas Odling, Dr. Nicola Cayzer and Dr. Christopher Hayward and Mr. Colin Chilcott from the University of Edinburgh to help me with the geochemistry facilitates (XRD, SEM, Electron Microprobe). Mrs Anne Kelly from Scottish Universities Environmental Research Centre (SUERC) help me with Sr isotope experiments.

I would like to thank Dr. Niklas Heinemann from the University of Edinburgh for helping me with well logging data processing and shared his experience on geopressure research, and Dr. Kit Carruthers for providing me with the spring composition data of the Crystal Geyser. Also, I am thankful for other academics of the school of Geoscience to help me with little questions.

At last but not the least, I would like to thank my parents for all the support and encouragement, and all my friends for the cares and understandings.

Nomenclature

P_c	capillary pressure
P_{nw}	pressure in the non-wetting phase
P_w	pressure in the wetting phase
σ	interfacial tension
r_1, r_2	radii of curvature of the interface
θ	contact angle
r_t	radius of the tube
P_b	buoyancy force
J	starting pressure gradient
H_c	the thickness of the caprocks
K	Permeability
m, a, b	constants for flow velocity vs. pressure gradient equation
P_d	displacement pressure
P_p	pressure where the Hg-filament
$\gamma_{Hg,air}$	interfacial pressure between Hg and air
$\theta_{Hg,air}$	contact angle between Hg and air
$P_{c(Hg,air)}$	10% saturated mercury pressure
r_{35}	pore throat radius under mercury saturation of 35% in the MIP experiment
P_{c35}	capillary pressure under mercury saturation of 35%
$\emptyset$	core porosity
k	air permeability
$\Delta\sigma_{water-oil}$	interfacial tension between water and oil
$\Delta\sigma_{water-air}$	surface tension of water
$\Delta\sigma_{air-oil}$	surface tension of oil
T	Temperature
Rs	gas-oil ratio
$\Delta\sigma_{air-oil(T)}$	live oil-air surface tension after temperature correction
$\Delta\sigma_{air-oil(T,Rs)}$	live oil-air surface tension after temperature and Rs correction
ρ_{wr}	density of brine water at reservoir condition

$\rho_{w(standard)}$	density of brine water at reservoir condition
w_s	weight percent of dissolved salt
B_w	formation water volume factor at standard conditions
ΔV_{wp}, ΔV_{wt}	pressure and temperature correction factors
$\rho_{oil(reservoir)}$	density of oil at reservoir condition
$\rho_{oil(surface)}$	density of oil at surface
GOR	gas-oil ratio
FVF	formation volume factor
V_{total}	total volume of oil at reservoir condition
$V_{oil(surface)}$	volume if oil at surface condition
$V_{methane(surface)}$	methane volume at surface condition
API	API gravity, oil density compare to water density
$\Delta\sigma_{water-gas}$	interfacial tension between water and gas
T_c	critical temperature in K
ρ_{gas}	gas density
S_g	specific gravity of gas
B_{gas}	gas formation factor
P	Pressure at reservoir

Contents

Chapter 1: Introduction and background

1.1 Introduction to global warming and geological CO_2 storage

Modern industry brings us booming economics, yet it also brings about serious problems including climate change induced by Green House Gases (GHGs). The atmospheric concentration of GHG has increased to 430ppm and is likely to rise in the future (Gillett et al., 2013). The concentration of GHGs is demonstrated to be related to the surface temperature. The rise of the surface temperature is estimated to be continue over the 21st century if no effective GHGs mitigation measurements have been undertaken (Zickfeld et al., 2009, Collins et al., 2013). Carbon dioxide (CO_2) as the most important component in the GHGs that contribute to the climate change, should be the first target to tackle. The aim given by the IPCC (Intergovernmental Panel on Climate Change) is to reduce global CO_2 emissions by at least 50% by 2050 compared to 2000 level, and the corresponding temperature rise should be limited to between 2.0 to 2.4 °C (IEA, 2008). The increase of the CO_2 is largely derived from fossil fuel combustion and other industrial processes(Collins et al., 2013). Various methods have been applied to combat with the global warming. Carbon capture and storage (CCS) provides an effective way to reduce the large-scale CO_2 emission from power plants and other industrial processes.

Geological carbon storage is to inject captured CO_2 into underground storage sites. The predicted worldwide carbon storage potential at a technical level is around 2,000 Gt by IPCC (IPCC, 2005). IEA (International Energy Agency) published the potential to be between 8,000 Gt to 15,500 Gt. The BLUE MAP scenario aimed to capture 9.4 Gt of CO_2 from power plants and other industrial processes by the year 2050 (IEA, 2008). The estimated worldwide capacity is far more than enough to accomplish this objective.

Potential storage sites include depleted hydrocarbon reservoirs, saline aquifers, and unmineable coal beds. Three requirements should be considered in the evaluation of the suitability of a site for carbon storage (Bachu and Bennion, 2008):

- The efficacy of the confining zone to inhibit CO_2 leakage, which means the storage sites should be confined by low-permeability rock which act as barriers.
- The injectivity of the storage site, which means the reservoir rocks should be porous and permeable.
- A large enough capacity, which concerns a reservoir's geological framework, reservoir quality and the seal rock's properties.

Depleted hydrocarbon reservoirs have been proved to be capable of trapping hydrocarbons for millions of years. Therefore, depleted hydrocarbon reservoirs are often regarded as among the best choice for CO_2 storage. Saline aquifers, with substantially greater storage potential, are very attractive for CO_2 storage, but the disadvantage is obvious: the lack of knowledge of the geological framework of the site, especially for the existence, extent and effectiveness of the seal rock.

In CO_2 storage sites, seals play an important role in preventing the supercritical CO_2 from migrating to other geologic strata. Seal failure may happen by leakage from the fractures and faults, or by diffuse flow within the pore network where the pore pressure as determined by the column height of the fluids exceeds the capillary entry-pressure of the seal rock (Barnard and Cooper, 1981). CO_2 is colourless, odorless and non-flammable gas, but at high concentration, from a health and safety point of view, it could be rather harmful. In the case of a well blowout, high concentrations of CO_2 could lead to hearing loss, impaired vision and mental confusion to human beings, or death by asphyxiation. Long term leakage would potentially impact on local ecosystem, as well as defeating the purpose of CCS.

Extensive work has been done on the security of the sealing rocks. In general, major research methods to investigate seal rocks include laboratory experiments, establishing mathematical models and using natural analogues.

Laboratory experiments can provide measured physical parameters of seal rocks and fluids. For example, the interfacial tension between hydrocarbons and brine (Ren et al., 2000, Yan et al., 2001), brine and air (Speight, 2005), CO_2 and brines (Da Rocha et al., 1999, Yang and Aplin, 2004, Yang et al., 2004, Bachu and Bennion, 2008, Georgiadis et al., 2010, Chiquet et al., 2007). For some small scale, short term processes, lab experiments could give relatively reliable results. For

example, many studies investigated the mechanisms of residual trapping and solubility trapping using lab experiments. However, the laboratory results are difficult to apply over geological time and reservoir spatial scales. Therefore, capillary leakage and mineral reactions cannot be effectively measured in the lab.

Numerical modelling is also an effective method to describe and predict the long-term fate of CO_2 and the sealing capacity of the caprocks. However, the modelling predictions still cannot cover a wide range of spatial and temporal scales by using empirically derived equations. For basic mechanistic models, the problem is whether the mathematical descriptions are appropriate for the natural geological storage sites, and whether an individual model has universal applicability. Thus, the models should be verified by real cases, i.e. parameters of real geological sites should be used to confirm the models.

Natural analogues provide a way to obtain real-world data, providing evidence of long-term geological storage safety and feasibility, and they are analogues for CO_2 behavior on appropriate temporal and spatial scales. For example, Wilkinson et al. (2009b) used gas accumulation with a high natural CO_2 content in the Fizzy and Orwell fields to study CO_2-mineral reactions, and calculated the percentage of CO_2 trapped by minerals and solutions(Wilkinson et al., 2009b). The results of the natural analogues can be very different from those of computer models. To avoid the limitations of computer models and laboratory experiments, using natural geological reservoirs as analogues to study the behaviour of the naturally stored CO_2 or hydrocarbons, provides an effective way to predict the long-term fate of engineering CO_2 storage.

The study of analogues is aided by the availability of relevant data. From the UK Oil and Gas Data database (https://www.ukoilandgasdata.com/; Schlumberger) and published papers on hydrocarbon fields, detailed descriptions of the exploration history, depositional environment, stratigraphy, trap and seal types, reservoir qualities, etc. are available. In the development of an actual storage site, developers could get more data and information from company files and some purchased sources. Unfortunately, much less information could be obtained if the target storage site is saline aquifer, with few explorations have been taken place.

1.2 Issues with CO_2 leakage from different pathways

Commercial carbon storage projects need to handle large quantity of CO_2 for storage. The identification and evaluation of potential leakage pathways are especially important for a robust project. The possible leakage pathways can be generalized as 4 major categories: a) from injection facilities; b) from injection wells or other wells; c) from caprocks and d) from faults and fractures. The impurities in the CO_2 stream and the injection temperature/pressure are also important factors when we identify potential leakage pathways.

a. CO_2 streams

- Impurities in CO_2 streams cause leakage: the injected CO_2 into storage sites is supercritical CO_2 with small amount of impurities, such as water, hydrogen, nitrogen and sulphur oxides. The liquid phase CO_2 could break down lubricants, cause damage to elastomers and cause internal corrosion of carbon steel and cements (DNV, 2010).
- Temperature and pressure of injected CO_2: the properties of CO_2 is sensitive to temperature and pressure when close to the critical point (31° C, 74 bars, Figure 1-1). Very low temperatures could form solid CO_2 and cause blockage to wells or pipes (Bachu, 2002, DNV, 2010).

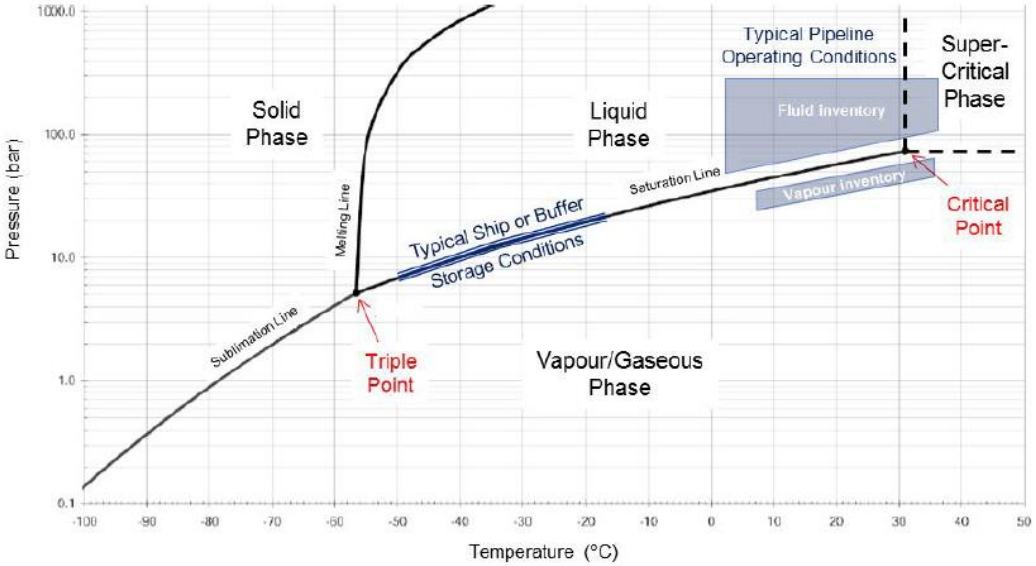

Figure 1- 1: CO_2 phase diagram with typical transport and storage conditions (DNV, 2010).

b. Injection facilities:

- The injection facilities include pig receivers, flow meters, manifolds, pressure boosting/reducing facilities, pipelines, etc. (DNV, 2010). The transported CO_2 is liquefied conditions with low pressure and temperature (7 bars at -50°C to 20 bars at -20°C, blue lines in Figure 1-1), so that compression and heating systems are needed before injection. The integrity of these facilities should be carefully checked for cracks or potential for corrosion.
- Injection wells and other wells: the configurations for injection wells associated with the nature of storage site (capacity and injectivity), the rate and pressure of injection, the pressure/temperature conditions of the storage sites, etc. The choice for material should consider corrosion conditions and the desired injection rate. The integrity of wells should be monitored and tested during and post- injection to ensure the CO_2 is sealed with cement and plugs (DNV, 2010).

c. Carbon storage site

Depleted oil fields could be used as natural analogues, but the physical and chemical properties of injected CO_2 is different to oil, so that capillary sealing and possible thermal fracturing should be investigated carefully. The factors to be considered include:

- Integrity of seal: the existence of a laterally extensive and continuous seal above the injection zone stops CO_2 migration. A secondary seal is required if the primary seal cannot be guaranteed to effectively seal. The preferred thickness of the seal is greater than 100m (Chadwick et al., 2008). The capillary entry pressure of the seal should be larger than the injection induced pressure increase to avoid capillary leakage.
- Faults and fractures: faults that penetrate the storage site could provide flow-paths or barriers to the stored CO_2. Fault seal analysis (FSA) is required to identify the nature of faults. The thermal effects on field stress and fracturing need to be analysed because the injected CO_2 is normally much cooler than reservoir temperature. The temperature drop gives rise to changes of field stress around well boles and could result in thermal fracturing.

The sealing efficacy of the caprocks is especially important for the security of geological carbon storage, which is the focus of this project. Typical sealing rocks are evaporates (halite, gypsum-anhydrite), argillaceous carbonate mudstone (clay-rich micrite), mudrock (shale, mudstone, siltstone, claystone), chert and other siliceous mudstone lithofacies, and some volcanic deposits such as basalt (Burruss, 2009, Michael et al., 2010, Griffith et al., 2011). Mudstones are the most common caprocks due to their thickness, geographic extent and low permeability. Evaporites have exceptional low permeability and good ductility. But the spatial extent and thickness can be limited (Burruss, 2009).

There are three major ways that might cause the leakage from caprock: diffusive loss; leakage controlled by capillary entry pressure of the rock matrix; and leakage through faults or fracture controlled by capillary pressure and permeability of faults and fractures. Among the three leaking pathways, diffusive loss is rather slow and insignificant (Song and Zhang, 2012). The key failure modes that need to be considered are capillary leakage and fracture / fault induced leakage.

1.3 Aims of this study

The study presented in this thesis aims to utilise natural analogues to study the key factors controlling the capillary entry pressure of seal rocks, and how CO_2-enriched pore fluid could chemically alter shales. Natural oil and gas fields of UK North Sea are used to study capillary entry pressure. For the preferred depth of trapping depth of 800m to 2500m (Chadwick et al., 2008), the density and buoyancy of CO_2 and hydrocarbons are comparable (Burruss, 2009). The trapping mechanisms that hold the buoyant oil and gas can be hence applied to CO_2 storage. This is also important for carbon storage in saline aquifers which offers huge potential storage but has untested caprocks.

Crystal Geyser which is located near Green River (Utah, USA) is utilised as an analogue to investigate the chemical alteration of shales in the presence of a CO_2-rich pore water. CO_2-riched waters leak to the surface from the Jurassic-age Navajo Sandstones, forming travertines which are well exposed due to erosion (Wilkinson et al., 2009a, Kampman et al., 2012). Two big faults (Little Grand Wash fault and Salt Wash Graben Fault) have actively leaked CO_2 for over 400,000 years (Burnside, 2010, Burnside et al., 2013, Kampman et al., 2012). Previous studies on Crystal Geyser mainly focused on the hydrologic regime that associated with the migrating CO_2 (Heath et al., 2004, Wilkinson et al., 2009a, Kampman et al., 2012), the origin and degassing of the CO_2 while migration upwards (Assayag et al., 2009, Wilkinson et al., 2009a) how the leakage was associated with the structure of the faults (Dockrill and Shipton, 2010), and how the sandstone rocks have been altered by the CO_2-rich fluid (Dockrill and Shipton, 2010, Kampman et al., 2014). However, few studies mentioned the fluid-rock interaction in the Mancos shales on the hanging wall of the Little Grand Wash fault, which is the focus of this research.

1.4 Structure of thesis

This thesis includes six chapters that covers topics related to capillary sealing and fault related leakage. Since these are two separate topics that both related to geological caprock sealing and leakage, each chapter contains an abstract, introduction, literature review, methodology and discussion of the results.

Chapter 2 uses oil and gas fields of the UK North Sea as analogues for carbon storage. Data sets from the UK North Sea are used to establish mathematic model for pore throat radii. The controlling factors for caprock capacity (depth of burial, thickness) are determined.

Chapter 3 reviews the geological framework of the Green River region and previous studies on how CO_2 could alter shale caprocks.

Chapter 4 investigates the composition and saturation state of the paleo-fluid that deposited the vein samples at Crystal Geyser, and compares this with present Crystal Geyser spring water. The circulation pattern of the fluid in the fault has been modelled.

Chapter 5 quantifies how the fluid could alter caprock shales using petrographic and stable isotope methods. The fluid flow-path in the shales has been modelled.

Chapter 6 is the general conclusion of the research, and put forward suggestions on future work.

Chapter 2: Capillary pressure, pore throat radii and caprock retention capacity

Statement of Work

Parts of this chapter have been published as: Wilkinson, M., Chen, Z., and Shu, Y., 2014, Retention capacity of seals from hydrocarbon field analogues for appraisal of saline aquifers. International Journal of Greenhouse Gas Control, 28, 126 – 133 (Wilkinson et al., 2014).

The breakdown of work for this chapter is:

Wilkinson: designed the work scope; supervised both Zhengao Chen and Yutong Shu; selected fields plausibly limited by capillary leakage; assessed the degree of faulting of the fields; wrote the final text for the published paper.

Chen: compiled the original table of oilfield data; performed initial calculation of pore throat radius (mostly superseded by new calibration data).

Shu: updated and error corrected table of oilfield data; completely revised the models used to calculate input parameters for calculation of pore throat radius, resulting in new results and conclusions. Performed a new literature review. The Monte-Carlo approach to error assessment, cumulative and probability distribution, prediction model and controlling factor correlation were not in the published paper.

2.1 Introduction

The aim of this chapter is to present a probability distribution of the pore throat radii of typical North Sea seals, for the use in the assessment of the potential sites for geological carbon storage, especially for saline aquifers, which normally has little direct data regarding the potential seal. For carbon storage in a depleted oil or gas field, seal has been tested to be capable of retaining buoyant fluids (oil or gas) over a geological period of time, and hence may be presumed to be able to hold CO_2.

Capillary sealing is believed to be the major mechanism in sealing hydrocarbon and CO_2 reservoirs, and the capillary force acts to stop a buoyant fluid migrating upward.

2.1.1 Capillarity and wettability

The pore spaces of a reservoir rock are filled with hydrocarbon and brine, and in the case of carbon storage CO_2 will be present as well. As the contact between either two fluids or between a fluid and a mineral surface, the molecules exert *van der Waals force*, which causes force of attraction (Nelleon, 1952). The interfacial tension at a liquid surface in contact with air and its vapour is defined as surface tension, which makes the liquid acquire the least surface area possible. Liquid surface could be regarded as being covered with an elastic skin. Abrupt changes in molecular forces occur between different fluids. Surface tension is an inherent characteristic of medium interfaces (Brackbill et al., 1992).

In terms of the interaction of oil and water, when these liquids meet a solid surface, one of the three conditions must exist: water-wet, oil-wet, or intermediately wet (Truong and Wayner Jr, 1987). The three conditions are defined based on the contact angle, which is the angle measured from the solid through to the liquid interface, conventionally measured through the water phase in a reservoir. In general, when the contact angle is between 0 and 60 to 75 degree, the liquid is defined as water-wet, while if the contact angle is between 180 and 105 to 120 degree, it is defined as oil-wet. An intermediate contact angle is intermediately wet (Anderson, 1987). In a reservoir with two or more liquids, the liquid with higher adhesion to mineral surfaces is defined as the water-wet (or wetting phase) liquid while that with lower adhesion is the non-wetting phase. The liquids in the pores of a reservoir rock compete for a place on the surface of minerals.

The difference in the degree of *van der Waals* bonding between two liquids in contact with each other results in a curve on the interface of the two liquids, and interfacial tension. To balance this tension, there is a pressure difference between the two liquids, defined as the capillary pressure, given by Young Laplace's equation (Adamson and Gast, 1967, Dullien, 2012):

$$P_c = P_{nw} - P_w = \sigma\left(\frac{1}{r_1} + \frac{1}{r_2}\right) \qquad \text{Equation 2-1}$$

Where: P_c = capillary pressure; P_{nw}= pressure in the non-wetting phase; P_w= pressure in the wetting phase; σ = interfacial tension; r_1, r_2 = radii of curvature of the interface, measured perpendicular to each other. One possible geometry that could be applied to Young Laplace's equation is capillary tube (schematic diagram is as Figure 2-1):

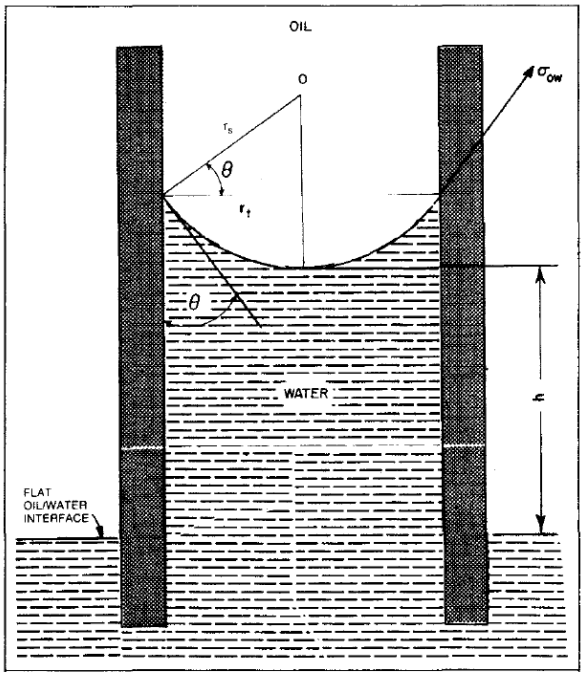

Figure 2- 1: Oil/Water interface in a capillary tube (Anderson, 1987)

When the tube is small enough, the interface can be approximated as a portion of a sphere with radius r_s ($r_1 = r_2 = r_s$). In this way, the equation changed to::

$$P_c = \frac{2\sigma cos\theta}{r_t} \qquad \text{Equation 2-2}$$

Where θ=contact angle; r_t= radius of the tube. If the pressure in the water is greater than the pressure in the oil, liquid rises. Otherwise, the liquid will move downward.

The capillary pressure is determined by several parameters: local pore geometry, wettability, saturation and saturation history (Anderson, 1987). For most porous media, the capillary pressure is much more complicated than the calculated result from the equation above.

2.1.2 Drainage and imbibition processes

There are two basic types of capillary pressure processes: drainage and imbibition (Anderson, 1987). In the drainage process, the nonwetting phase displaces the wetting phase, while in the imbibition process explains the other way around. Amann-Hildenbrand et al. tried to explain the process relating to mudrocks with in-situ experiments on core plugs (Amann-Hildenbrand et al., 2013). In a completely brine saturated core plug, the pressure of non-wetting fluid was made to increase firstly and decrease again. The full capillary path is described in the Figure 2-2 below.

After the pressure has overcome the pore entry pressure (Pc-entry), the non-wetting phase began to displace the wetting phase and the brine saturation decreases. When the pressure reaches the breakthrough pressure (Pc-brthr), non-wetting phase fluid has passed through the pore and was detected at the outflow side of the core plug. Subsequently the pressure keeps increasing leading to progressive drainage and an increase of the effective non-wetting phase fluid permeability until the pressure reaches the maximum. The drainage process stops and imbibition process starts, which associates with an increase in wetting phase saturation and a reduction of the effective permeability of non-wetting phase. The imbibition process stops when the last interconnecting capillary is sealed. At this point the irreducible water saturation (IRWS) has reached and the associated pressure is termed as “snap-off” pressure (Pc-snap-off). Thereafter, only diffusion can be detected (Busch and Amann-Hildenbrand, 2013, Hildenbrand et al., 2002, Hildenbrand et al., 2004). The processes of drainage and imbibition are shown in the Figure 2-2 as below.

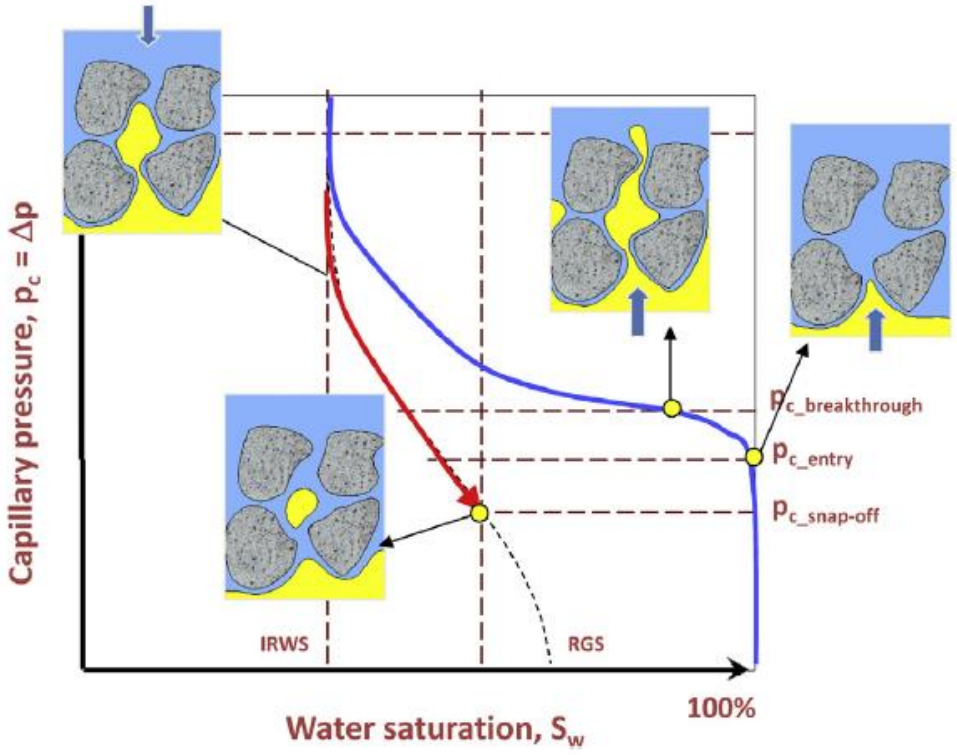

Figure 2- 2: Schematic diagram of capillary process by Busch and Amann-Hildenbrand (2013). Blue line shows drainage process; red line shows imbibition process. From 100% of water saturation the non-wetting phase starts to displace wetting phase.

2.1.3 Capillary sealing

Capillary sealing is a result of the balance between the buoyancy of a defined column exerted on caprock and capillary pressure. The calculation equations for buoyancy force and capillary pressure are shown in Equation 2-3 and Equation 2-4. For a seal to be effective, the buoyancy force must not exceed the capillary pressure at the crest of the reservoir (Equation 2-5):

$$P_b = \Delta \rho g h \qquad \text{Equation 2-3}$$

$$P_c = 2\sigma \cos\theta / r \qquad \text{Equation 2-4}$$

$$P_b \leq P_c \qquad \text{Equation 2-5}$$

Where, P_b= buoyancy force of the target column; $\Delta\rho$= the density difference between brine and the target phase (for hydrocarbon or CO_2); g= acceleration due to gravity; h =column height; P_c= capillary pressure; σ=interfacial tension (IFT); θ= contact angle; r= pore throat radius. When $P_b = P_c$, the column height can be expressed as:

$$h = \frac{2\sigma cos\theta}{\Delta\rho g\gamma} \qquad \text{Equation 2-6}$$

With the Equation 2-6, Naylor et al. (2011) established a practical methodology to calculate the potential CO_2/natural gas conversion factor and CO_2 column height of North Sea natural gas reservoirs (CO_2 column height equals to conversion factor multiplied by natural gas column height) (Naylor et al., 2011). The calculated conversion factor values ranges from 0.696 to 1.326.

2.2 Literature review

2.2.1 Pore throat radii in sealing rocks

Pore throat acts to block the migration of non-wetting phase fluids (petroleum or CO_2) and balance the buoyancy pressure in sealing rocks. High quality reservoir rocks usually have pore sizes greater than 30 μm and pore throat radii of greater than 1μm, which is defined as “macroporosity”. This study focuses on sealing rocks which have pore throat of less than 1 μm, which is normally defined as “microporosity” (Nelson, 2009). Between the macroporosity and microporosity is mesoporosity. Hence, 1 μm of pore throat size is usually the border to distinguish low quality and high quality reservoir sandstones (Nelson, 2009).

Before the advent of geological carbon storage, pore throat in seal rocks is not a common studied parameter in oil industry. Instead, petroleum geologists are more accustomed to use porosity, permeability and grain size to characterize the reservoir quality. Nelson (2009) stated that pore size is greater than pore throat size, but the two are still in the same order of magnitude (Nelson, 2009). Pore throat size usually indicates the smallest pore size among interconnected pores, which gives the largest resistance to displacement. In the realms of geological carbon storage, pore throat radius could be defined as the narrowest passages that non-wetting phase

fluid (petroleum or CO_2) must passes through in order to travel through a volume of pores.

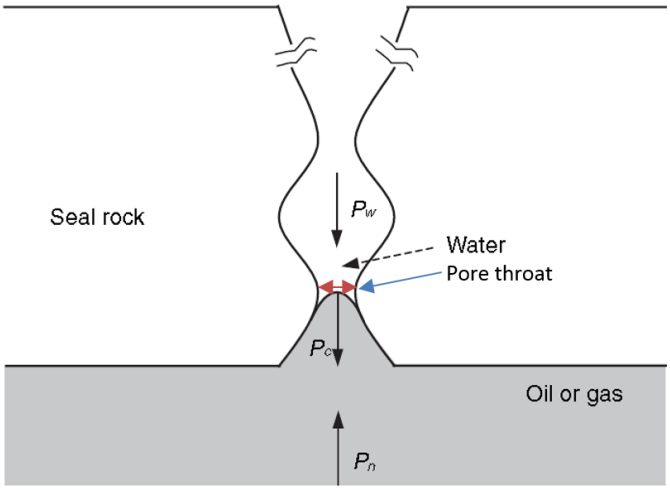

Figure 2- 3: Schematic of capillary sealing of a seal rock (Li et al., 2005). The pore throat size is marked with red arrow.

The general range for the pore throat radii of argillaceous samples is quite widespread. Katsube et al. studied the pore throat of ten samples of Jurassic and Cretaceous Shales from Scotian Shelf, Canada. The geometric mean of pore throats range from 8-16nm (Katsube et al., 1991). Katsube and Issler examined the pore throat of 20 Pliocene shales from Beaufort-Mackenzie Basin in Canada, and the derived mean pore throats of the samples range from 9-44 nm (Katsube and Issler, 1993). Cranganu and Villa (2005) studied the pore throat size of the Pennsylvanian shales in Anadarko basin with 21 samples. The minimum, arithmetic and maximum pore throat pore throat are respectively 20nm, 50nm and 116 nm (Cranganu and Villa, 2005). Lash investigated the samples from Appalachian Basin and found out the pore diameters of the samples range from 7nm to 24nm (Lash, 2006). Clayton and Hay measured mudstones, siltstones and limestones samples from UKCS, offshore Holland, Haltenbanken Norway, Western Canada Basin and Dorset UK and got the pore throat ranges from 8 to 2100 nm (Clayton and Hay, 1994). Benson and Cole measured samples from deltaic mudstones and also got a large pore throat range, which is from 140 to 3000 nm (Benson and Cole, 2008). Loucks et al. used SEM to obtained an approximately range of pore throat of Mississippian Barnett shale, ranging between 5 to 750nm (averaged at about 100nm) (Loucks et al., 2009). Borst studied the effects of compaction and geological

time on pore throat distribution. The mean pore size of argillaceous rocks from different active exploration areas ranges from 15 to 980nm, and the time ranges from Pleistocene to Silurian (Borst, 1982).

Winland R35 pore size classes (Kolodzie Jr, 1980) is normally used for geometry classification of pore size. Megapores is defined as pore size that larger than 10μm; macropores is from 2-10 μm; mesopores are from 0.5-2 μm; micropores are from 0.1-0.5 μm; nanopores are from 0.01-0.1 μm. The target pore size in this study locate within mesopores, micropores and nanopores. In this research, effective pore throat radius is used to represent the radius that controls the sealing capacity of the caprocks on reservoir scale.

2.2.2 Associated factors for pore throat radii and sealing capacity

Several previous studies have investigated on the factors that might associated with the sealing capacity of mudstones.

- Burial depth

Borst used graphic statistics to analyse the relationship between mean pore throat size and factors including depth of burial, geological age and porosity for mudstones (Borst, 1982). The samples are from various explorational wells of different basins. The pore throat size is measured by mercury porosimetery and nitrogen sorption methods. The results show that the burial depth and porosity are in good linear relationship with mean pore size, with correlation coefficient of 0.8, 0.72, respectively (Table 2-1), while geological age does not show strong correlation.The pore size distribution shows great variations for different depth as well. Figure 2-4 show the pore size distributions in various depth interval. It is clear to see highly compacted rocks has smaller pore size than shallow burial rocks, which demonstrates compaction level (burial depth) is one of the controlling factor for pore size.

Table 2- 1: Correlation coefficients between mean pore size and burial depth, geological age, porosity, pore surface area, sorting and skewness for mudstones (Borst, 1982). N is the number of samples.

Mean pore size	Depth of burial	Geological age	Pore parameters			
			Porosity	Surface area	Sorting	Skewness
(*r*)	0·80	0·41	0·72	0·17	0·71	0·41
(*N*)	(110)	(145)	(146)	(140)	(147)	(147)

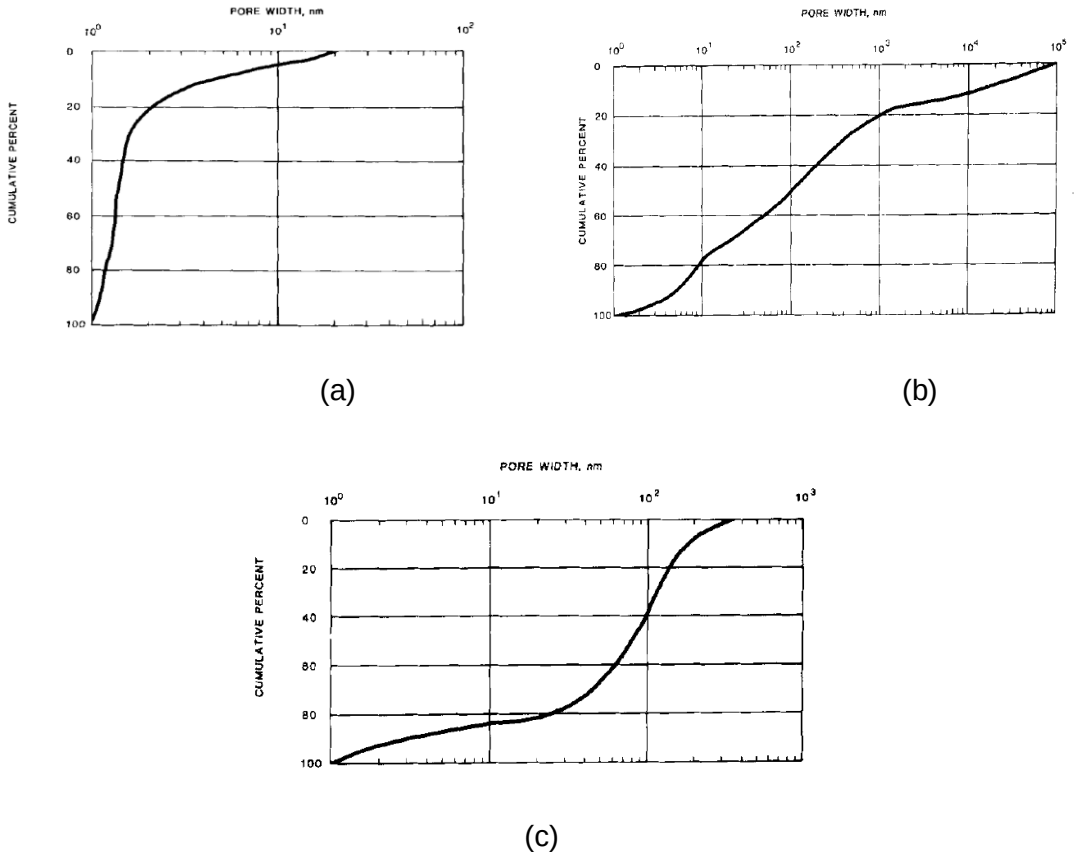

Figure 2- 4: typical accumulative curve of the pore size distribution of (a) highly compacted shales with depth of 3527m, (b) very shallow burial with depth of 88m, (c) moderate burial with depth of 453m.

- Clay content

Yang and Aplin investigated the relationship between porosity, clay content and pore size by studying the petrographic properties of 30 mudstones from different regions (14 from North Sea, 8 from Gulf of Mexico, 1 from Caspian Sea well) (Yang and Aplin, 2007). The burial depth ranges from 2 to 5 km. Clay mineral content of solids is around 13-66%, and the porosity ranges from 5.5-26.5%. Mercury porosimetry was used for pore size calculation. The measured mean pore throat radius ranges from 15nm to 1400nm. Figure 2-5 below shows the relationship between porosity, mean pore throat size and clay content in this study. Both lithology (clay content) and porosity have an influence on mean pore throat size distribution, but porosity has more significant influence.

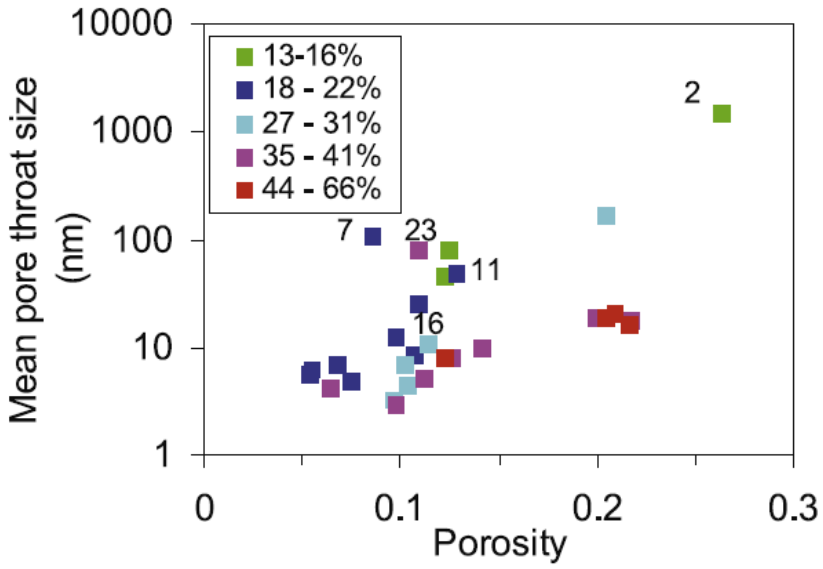

Figure 2- 5: Effect of clay content on porosity and mean pore throat size from mercury injection porosimetry (Yang and Aplin, 2007). The label shows sample number.

- Thickness of the caprock

It seems the thickness of the caprock is irrelevant with the capillary sealing capacity based on the Washburn equation (Equation 2-2). However, Thickness of the

caprock has always been used as one important parameter for caprock quality assessment for CO_2 storage. Chadwick et al. introduced the thickness of the caprock as one criteria for the efficacy of caprocks for geological CO_2 storage (Chadwick et al., 2008). In the table of criteria for assessing the effectiveness of a seal, 20m is set to be the minimum thickness of the caprock and 100m as the positive indicator (Table 2-2). Chadwick et al. (2008) proposed these criterions without reasoning the basis.

Table 2- 2: Key indicators for geological carbon storage after Chadwick et al., 2008.

	Positive indicators	**Cautionary indicators**
RESERVOIR EFFICACY		
Static storage capacity	Estimated effective storage capacity much larger than total amount of CO_2 to be injected	Estimated effective storage capacity similar to total amount of CO_2 to be injected
Dynamic storage capacity	Predicted injection-induced pressures well below levels likely to induce geomechanical damage to reservoir or caprock	Injection-induced pressures approach geomechanical instability limits
Reservoir properties		
Depth	>1000 m < 2500m	< 800 m > 2500 m
Reservoir thickness (net)	> 50 m	< 20 m
Porosity	> 20%	< 10%
Permability	> 500 mD	< 200 mD
Salinity	> 100 gl^{-1}	< 30 gl^{-1}
Stratigraphy	Uniform	Complex lateral variation and complex connectivity of reservoir facies
CAPROCK EFFICACY		
Lateral continuity	Stratigraphically uniform, small or no faults	Lateral variations, medium to large faults
Thickness	> 100 m	< 20 m
Capillary entry pressure	Much greater than maximum predicted injection-induced pressure increase	Similar to maximum predicted injection-induced pressure increase

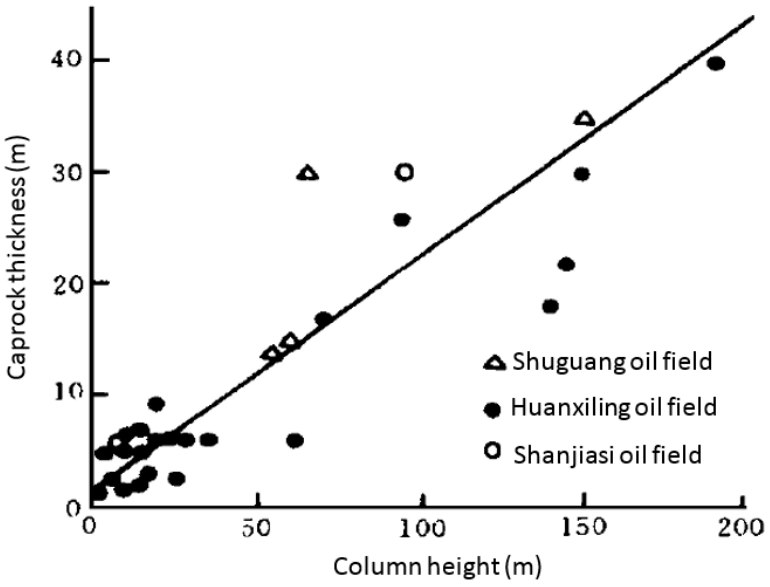

Figure 2- 6: Column height vs. caprock thickness (Tong and Niu, 1989).

Some previous studies proposed the correlations between the thickness of the caprock and the height of the hydrocarbon columns for some studies. Pang et al. (1998) demonstrated there exists strong linear relationship between the caprock thickness and the gas column height for Wanglong field and Taihe field in South Sichuan oil and gas clusters of China (庞雄奇 et al., 1998) (equivalent to (Pang et al., 1998)). Tong and Niu (1989) has also found correlation between caprock thickness and column height for caprocks of Shuguang oil field, Huanxiling oil field and Shanjiasi oil field (童晓光，牛嘉玉, 1989) (equivalent to (Tong and Niu, 1989)). Jiang (1998) studied core samples from the caprocks of gas fields in Jiyang Sag, and found correlation between the caprock thickness and the “effective caprock thickness” (蒋有录, 1998) (equivalent to (Jiang, 1998)). He stated that, most caprocks are good enough to hold gas column of hundreds of meters, but the real column height is much lower. Hence, he introduced the conception of “threshold effective caprock thickness”, which means the minimum thickness required for an associated hydrocarbon column height. For a certain column height, the real

caprock thickness should be equal or greater than “threshold effective caprock thickness” (Figure 2-7).

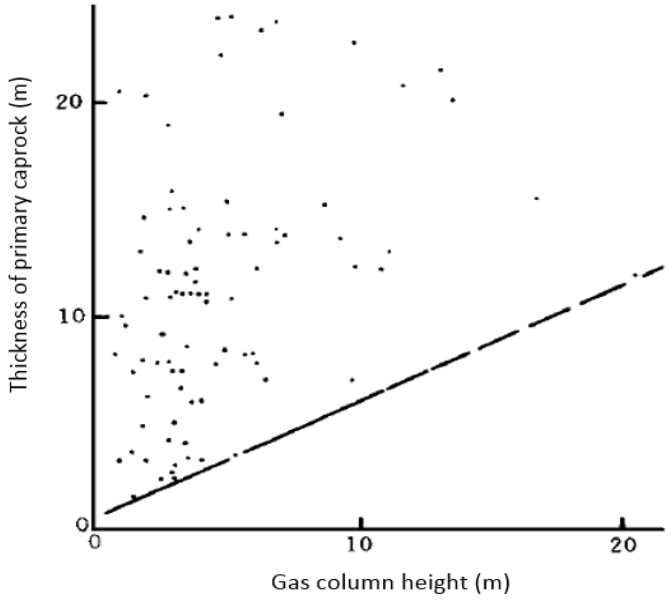

Figure 2- 7: Caprock thickness against gas column height for Jiyang Sag (蒋有录, 1998) (equivalent to Jiang, 1998).

The horizontal axis is gas column height in metre and the vertical axis is the thickness of the primary caprock in metre. The dashed line marks the threshold effective caprock thickness.

Fu (2006) also put forward a possible interpretation for the positive proportional relationship between gas column height and caprock thickness (付广, 2006) (equivalent to (Fu, 2006)). Statistically, big pore throat in thick caprocks is more likely to be connected with small pore throat thus blocking the pathways for thick units, thus resulting in better sealing capacity. In addition, experiments result has proved there exists a positive correlation between measured capillary sealing pressure and the lengths of core samples (付广, 2006) (equivalent to (Fu, 2006)). The longer the core samples, the greater the capillary sealing, hence the smaller the calculated pore throat radii.

Zhang et al. (2010) proposed a new model to explain the hydrocarbon breakthrough motion in low permeable caprocks (Zhang et al., 2010). According to his theory, when the buoyancy force is greater than capillary force, the fluid has the motion

potential and a force named the 'boundary force' begins to act. The fluid could enter the caprock only when the buoyancy force is greater than the combined capillary force and boundary force. Figure 2-8 shows the relationship between flow velocity and pressure gradient in low permeable medium. When the pressure gradient is greater than dot d, the flow velocity increases linearly as the pressure gradient. When the fluid pressure gradient is lower than dot d, there is a nonlinear relationship. When the pressure gradient is less than dot a, the fluid does not has a potential to flow. Hence, pressure gradient a is called starting pressure (or starting resistance, or boundary force) (Zhang et al., 2010, 吕延防，张绍臣，王亚明, 2000) (equivalent to Lv, Zhang, Wang, 2000).

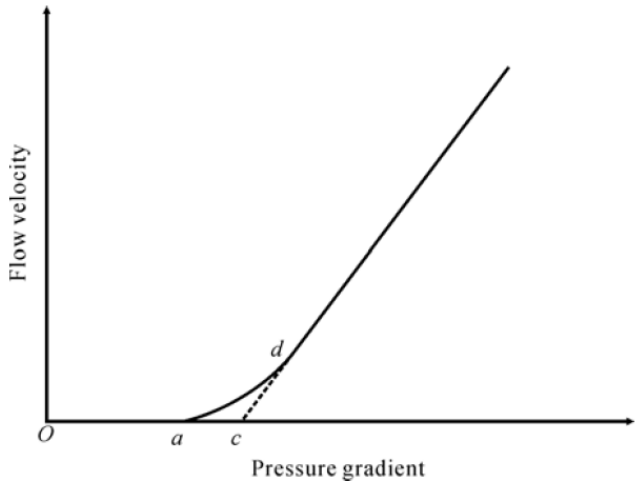

Figure 2- 8: Pressure gradient vs. flow velocity (Zhang et al., 2010). Pressure gradient is the pressure difference divided by the thickness of caprocks

Hence, the equation changes to:

$$P_b = P_c + J \cdot H_c \qquad \text{Equation 2-7}$$

$$J = m \cdot \frac{\mu^a}{K^b} \qquad \text{Equation 2-8}$$

Where P_b is buoyancy force in MPa; P_c is the capillary pressure in MPa; J is the starting pressure gradient in MPa/cm; H_c is the thickness of the caprocks in metre; K is permeability in $10^{-3}\mu m^2$; m, a and b are constants. The Equation 2-7 demonstrated the sealing capability of caprock is not only a function of capillary

force, but also associated with the thickness and the starting pressure gradient of fluid.

2.2.3 Measurements of pore throat radii and capillary pressure

Pore throat radius is a very important parameter in the determination of capillary pressure. The smaller the radius of the connected throat, the larger the displacement pressure required. Several methods have been applied for the pore throat radius determination in history. The first is using visual ways for measurement, such as thin section, or scanning electron microscope photos which could be used to investigate the geometry and pore size distribution in a direct way (Aschenbrenner and Achauer, 1960). Pittman and Duschatko used rocks impregnated with plastic to make pore casts, and then use SEM for graphic illustrations. But this method has obvious limitations: samples could not give a reservoir scale picture of the pore throat radius. In addition, for sealing rocks, pores are usually too small to see even on an SEM (Pittman and Duschatko, 1970). Berg established crude empirical models for radius estimation for sandstones for packings of uniform spheres. His model illustrates the pore throat radius is a function of porosity and permeability (Berg, 1975).

The major methods for measuring the pore throat sizes of shales and tight sandstones at present days include mercury injection porosimetry experiments (MIP) and permeability correlation modelling. Both drainage capillary breakthrough pressure and imbibition capillary snap-off pressure are used for in-situ measurements on core plugs.

a. Mercury Injection Porosimetry

In 1921, Washburn was the first to suggest to use mercury injection method to determine the distribution of pore sizes in a porous medium. He suggested using the equation $P = \frac{-2\gamma cos\theta}{r}$ to determine the effective pore radius r (Washburn, 1921). High pressure mercury injection porosimetry (MIP) then became a conventional way to measure the capillary pressure. Many studies have been conducted since the study of Purcell, the theory and procedure of mercury injection porosimetry were

outlined (Purcell, 1949). Before the widely use of mercury injection porosimetry, mostly used methods for capillary pressure measurement including experimental methods include a) removing liquid from the core through high displacement pressure (Thornton and Marshall, 1947, McCullough et al., 1944, Bruce and Welge, 1947, Hassler and Brunner, 1945) and b) removing liquid from the core at high centrifugal forces in a centrifuge (McCullough et al., 1944, Hassler and Brunner, 1945). However, both of the methods contain significant shortcomings. The former method could not be applied to small, irregular samples and it is time-consuming. The latter method requires elaborate equipment (Purcell, 1949).

Schowalter used mercury injection porosimetry to investigate the capillary pressure as the main resistant force to secondary hydrocarbon migration (Schowalter, 1979). Mercury is introduced into the core sample by increasing the pressure. The injected volume and mercury saturation were measured at the same time until the injection pressure reaches 1,500 psi. A plot of pressure versus injected mercury volume was recorded (Schowalter, 1979) (pressure record example in Figure 2-9). This method could measure the displacement pressure, which is defined as the pressure required to form a continuous filament of non-wetting fluid through the largest connected pore throats. This method derives the pressure that mercury displaces air in pore throats with successively decreasing equivalent radii. Often the pressure at 10% mercury volume is equivalent to the displacement pressure (Schowalter, 1979). The shape of the curve suggests the pore throat size distribution (Rezaee et al., 2006). But this 10%-saturation approach strongly depends on surface texture which could result in significant variations on different surfaces. The surface roughness could influence the spatial distribution of fluids (Lenormand and Zarcone, 1984). Alternatively, Kolodzie suggested using 35% mercury saturation in the prediction (Kolodzie Jr, 1980). Pittman used 25% percentile of saturation on a cumulative mercury injection curve for the prediction (Pittman, 1992).

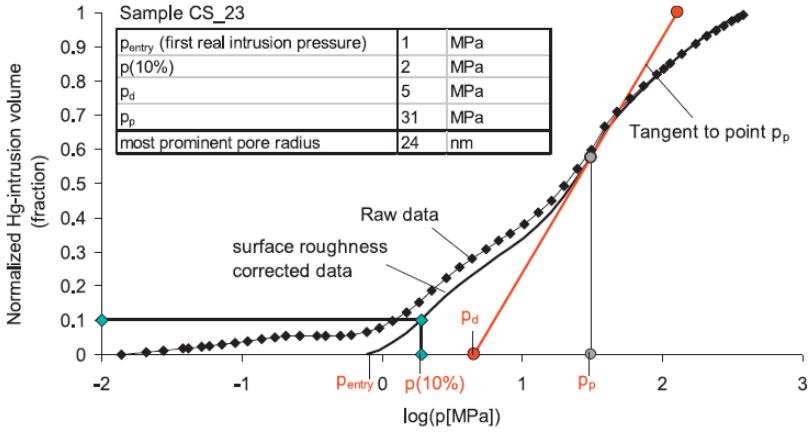

Figure 2- 9: Example of mercury injection porosimetry plot. Normalized Hg saturation vs. capillary pressure (Busch and Amann-Hildenbrand, 2013). P (10%) is capillary pressure; P_d is the displacement pressure which has to overcome to create complete Hg-filled filament. P_p is the pressure where the Hg-filament exists.

The capillary entry pressure (threshold pressure) can be converted from Hg-air to gas-brine system using the Equation 2-9 below. The wetting angle of mercury is usually assumed to be 140° and the interfacial tension to be 470-485 mN/m (Hildenbrand et al., 2002, Dewhurst et al., 2002).

$$P_c = P_{c(Hg,air)} \frac{\gamma cos\theta}{\gamma_{Hg,air} \cdot \cos(\theta_{Hg,air})} \qquad \text{Equation 2-9}$$

Where $\gamma_{Hg,air}$= interfacial pressure between Hg and air; $\theta_{Hg,air}$= contact angle between Hg and air; $P_{c(Hg,air)}$= 10% saturated mercury pressure. For CO_2 storage, the aiming predicted system should be CO_2/brine. If the contact angle of mercury and air is assumed to be 140° and the interfacial tension is 480mN/m, the equation changes to:

$$P_{c(CO2,brine)} = P_{c(Hg,air)} \frac{\gamma_{(CO2,brine)} \cos\theta_{(CO2,brine)}}{-94.95} \qquad \text{Equation 2-10}$$

The contact angle and interfacial pressure between CO_2-brine systems will be discussed later in this chapter.

Shortcomings of mercury injection porosimetry:

The conversion from mercury/air system to liquid/brine system is based on the general assumption that mercury interfacial tension and contact angle is constant. However, Hills and Høiland reported the interfacial tension could range from 420mN/m at 75MPa to 480mN/m at 0.1MPa (Hills and Høiland, 1984).

In addition, the size of samples has effects on the result. Busch and Amann-Hildenbrand reported MIP data from conventional core plugs are greater than those from cuttings (standard methods) (Amann-Hildenbrand et al., 2013, 付广 and 许凤鸣, 2003) (equivalent to Fu and Xu, 2003). Unfortunately, not every literature clearly stated the size of samples used for measurement. In addition, the ways of cutting and preparation processes on samples could have effects on the measurements.

b. Gas Breakthrough Experiments

Another major method is using in-situ gas breakthrough experiments to measure the breakthrough pressure directly. Many researchers have done experiments to test the leakage pressure and the properties of caprocks with gases (He, Ar, CH_4, or N_2). The pressure on one side of the core plug is increased gradually until fluid was detected to be leaking from the other side of sample plug. Both breakthrough pressure and snap-off pressure were recorded. Snap-off pressure is defined as the "endpoint of the spontaneous imbibition process, i.e. the point where the wetting fluid has shut off the last connecting pore throat of the flow paths" (Amann-Hildenbrand et al., 2013). Usually, snap-off pressure is usually lower than the breakthrough pressure in the drainage path (Hildenbrand et al., 2002, Amann-Hildenbrand et al., 2013, Boulin et al., 2010) (Figure 2-2).

Li et al. studied on the gas breakthrough pressure test results and the performance of Weyburn field sealing rock (evaporates). He tested the breakthrough pressure by increasing the pressure gradually, and obtained the pressure increase pathway in Figure 2-10. Wollenweber et al. did permeability test and gas breakthrough test to limestone samples and marl samples (Wollenweber et al., 2010). Amann et al. investigated on the sorption, transport sealing capacity features of the caprocks (Amann et al., 2011). His samples include different types of sealing rocks, ranging from poorly consolidated clays to highly compacted shales and limestones.

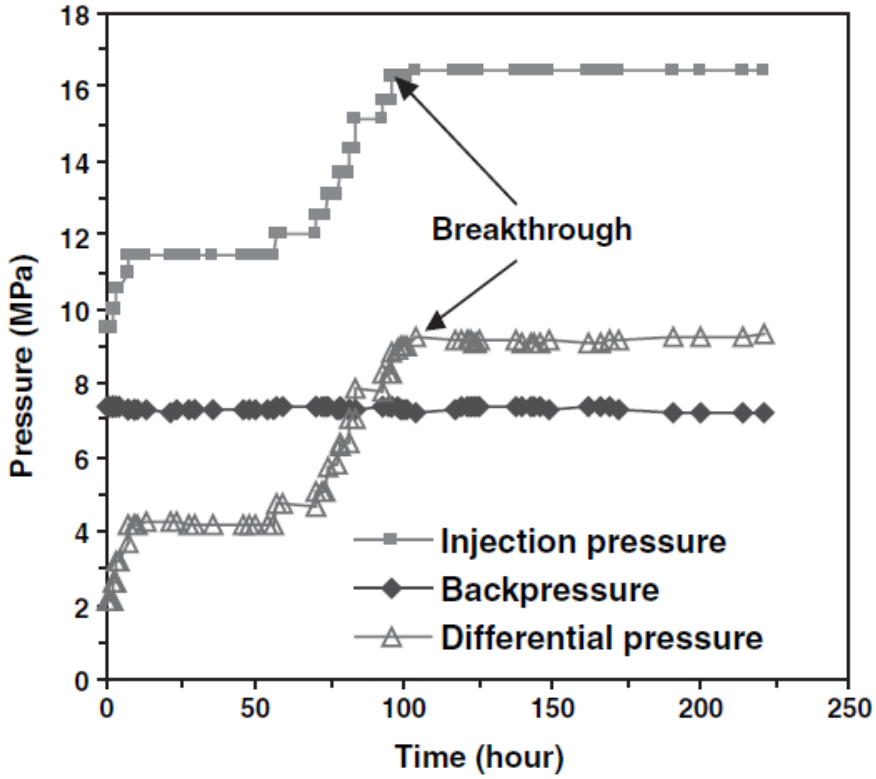

Figure 2- 10: CO_2 breakthrough pressure test history for seal-rock (backpressure: constant at 7.3Mpa; differential pressure: breakthrough pressure minus backpressure) (Li et al., 2005).

Shortcomings:

The core samples of caprocks are not always available. In addition, as caprocks are usually not permeable comparing to reservoir rocks, gas breakthrough experiments might take days or weeks. Especially for shales containing swelling clays such as montmorillonite, samples swell after saturation, it is usually very hard to re-establish water-saturation system.

c. Accumulated pore throat radii distribution

Yang and Aplin (1989) established accumulated pore throat size distribution model for mudstones from Norwegian North Sea based on measured pore throat radius by high pressure mercury injection (Yang and Aplin, 1998):

$$F(x) = \frac{1}{1+\exp(a-bx-cx^3)}$$ Equation 2-11

$$x = \ln(r - 0.5)$$ Equation 2-12

Where $F(x)$ = cumulative distribution of pore size, r = pore throat radius (>0.5nm); a, b, c are positive coefficients derived from regression. 0.5nm was set to be the smallest pore throat radius because it is to the half of the interlayer spacing of glycolated smectite. The density distribution is also derived by differentiation:

$$f(x) = \frac{F(x)}{d(x)} = \frac{(b+3cx^2)\exp(a-bx-cx^3)}{[1+\exp(a-bx-cx^3)]^2}$$ Equation 2-13

The calculation of mean pore throat radius $r(\mu)$ is established

$$r(\mu) = \int_{-x}^{x_{max}} f(x)[\exp(x) + 0.5]dx$$ Equation 2-14

Where x_{max} = the largest pore radius, $exp(x) + 0.5$ is the pore throat radius (by solving the equation 2-14: $x = \ln(r - 0.5)$)

The results show a very good fitting between the modelled pore throat radius and measured ones.

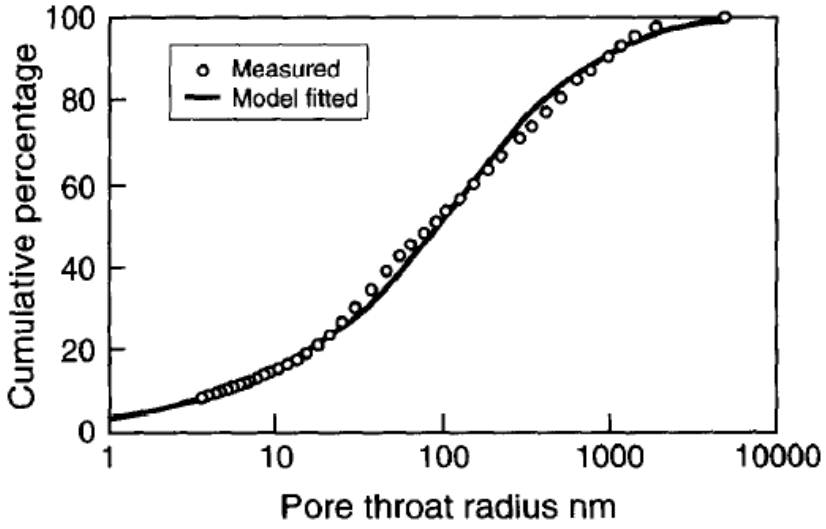

Figure 2- 11: Measured and modelled pore throat radius (Yang and Aplin, 1998)

Winland (1972) developed a method for average pore throat radii calculation based on Weyburn, Spindle and Hidalgo fields (Winland, 1972). The input parameters

include permeability (air) and porosity from core plugs. The equation below is the prediction model:

$$Logr_{35} = 0.732 + 0.588logk - 0.864log\emptyset \quad \text{Equation 2-15}$$

Where r_{35} = pore throat radius under mercury saturation of 35% in the MIP experiment; $\emptyset$ = core porosity; k = air permeability.

If capillary pressure is incorporated into the equation, and $\sigma = 480mN/m, \theta = 140°$, the equation is changed into:

$$\frac{108.1}{P_{c35}} = 5.395[k^{0.588}/(100\emptyset)^{0.864}] \quad \text{Equation 2-16}$$

Where P_{c35} = capillary pressure under mercury saturation of 35%; k = air permeability; $\emptyset$ = core porosity.

Kolodzie (1980) modified the equation based on Spindle data to establish the equation as below (Kolodzie Jr, 1980):

$$Logr_{35} = 0.9058 + 0.5547logk - 0.9033log\emptyset \quad \text{Equation 2-17}$$

Where r_{35} = pore throat radius under mercury saturation of 35%; k = air permeability; $\emptyset$ = core porosity. Kolodzie (1980) also compared the modelled result with the experimental measured result, and the result shows the model could give good estimation (Figure 2-9). In the study, he managed to relate core porosity and permeability to log data (Kolodzie Jr, 1980). Density logs were used to calculate porosity. Permeability could be correlated with Self Potential (SP) log with the equation below:

$$K = 0.0567 \cdot SP(normalized) - 0.2694 \quad \text{Equation 2-18}$$

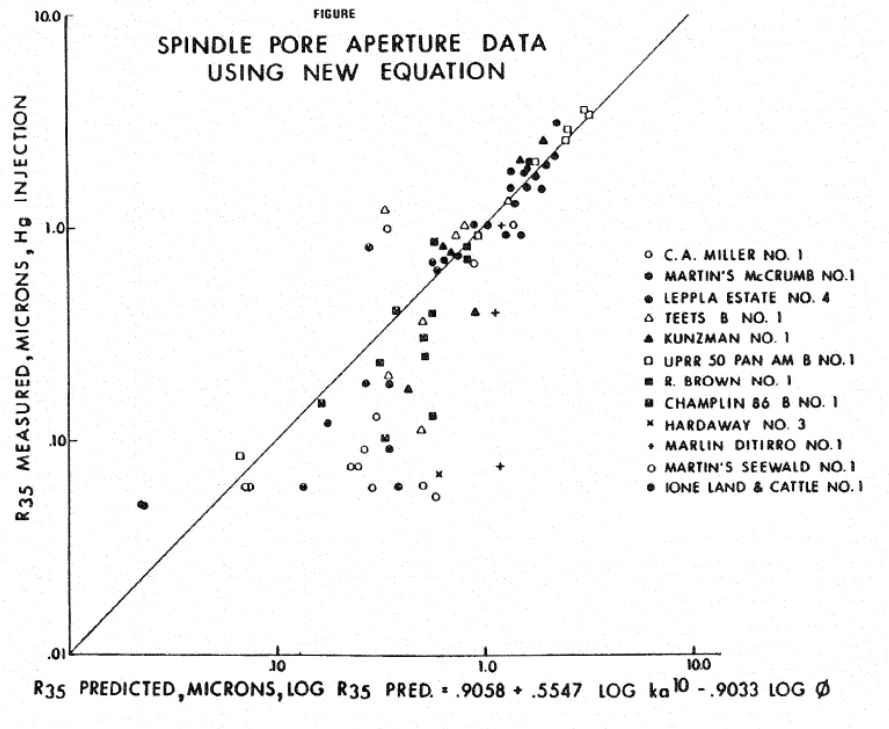

Figure 2- 12: Measured pore throat radii from MIP (vertical axis) vs. modelled pore throat radii using Equation 2-17 (horizontal axis) (Kolodzie Jr, 1980).

2.2.4 Interfacial tension, wettability and contact angle

Pore throat radius is a crucial parameter for the assessment of the capillary sealing capacity of caprocks. Based on equation 2-4, to calculate the pore throat, hydrocarbon-brine interfacial tension, the rock wettability and contact angle need to be investigated.

- Oil-brine interfacial tension:

Duchateau and Broseta (2012) proposed a simplified way to calculate the interfacial tension for the brines containing strong electrolytes and slightly soluble gas. The interfacial tension equals to the brine surface tension (brine-air) minus the hydrocarbon surface tension (hydrocarbon-air). (Duchateau and Broseta, 2012).

Baker and Swerdloff (1956) proposed empirical equation of oil surface tension corrected by temperature (Baker and Swerdloff, 1956). Abdul –Majeed (2000) made

corrections for live oil (gas-oil ratio) in his research (Abdul-Majeed and Abu Al-Soof, 2000). Statistics shows after his modification, the prediction is more accurate comparing to Baker and Swerdloff's method (1956).

- Gas-brine interfacial tension:

Zuo and Stenby (1998) and Yan et al. (2001) proposed the linear gradient theory model to calculate the gas-brine interfacial tension that combined with Peng-Robinson equation of state (LGT-PG) and the Soave-Redlich-Kwong equation of state (SRC-EoS) (Zuo and Stenby, 1998, Yan et al., 2001). Many previous studies have provided interfacial tension of the methane-water system covering wide range of pressure and temperature. Wiegand and Frank (1994) tested the interfacial tension of methane and water under temperature of between 298K to 473K and pressure of between 0.1MPa to 240MPa (Wiegand and Franck, 1994). Tian et al. (1997) investigated the interfacial tension between 0.1 MPa to 100MPa (田宜灵 et al., 1997) (equivalent to (Tian et al., 1997)). Ren et al. (2000) documented more results in a smaller pressure range of 1MPa to 30MPa (Ren et al., 2000). With great experimental data compilation, Schmidt et al. (2007) reviewed these open literature data, and he concluded that the model could successfully be applied to pure component and binary components (Schmidt et al., 2007).

- Wettability and contact angle:

Wettability is also one important factor that could influence capillary pressure, which could be expressed by the contact angle between the solid surface and the fluid. Contact angle is the function of wetting phase type and mineral substance (hydrophilic & hydrophobic) of the rocks (Shah et al., 2008). In hydrocarbon/brine system, sealing rocks could be regarded as wetting phase with contact angle of 0º and $\cos\theta\left(\frac{hydrocarbon}{brine}\right) = 1$ (Naylor et al., 2011). For CO_2/hydrocarbon/brine system, the presence of CO_2 could alter the wettability of minerals. According to experimental results (Chiquet et al., 2007, Shah et al., 2008, Daniel and Kaldi, 2008) contact angle of CO_2/hydrocarbon/brine system increases as the pressure and salinity rises. The contact angle of major minerals in shales under typical reservoir conditions has been reported by previous studies: for mica and quartz, $\cos\theta$ = 0.66 and 0.85, respectively (Li et al., 2005, Chiquet et al., 2007); for calcite: $\cos\theta$ = 0.77 (Espinoza and Santamarina, 2010).

2.2.5 Knowledge gaps and study objectives

Yang and Aplin (1998) have established pore size distribution (Figure 2-11, Equation 2-11, 2-12, 2-13, 2-14), and derived good fittings comparing with measured pore throat radii data from MIP. But the model is based on only eleven mudstones from Norwegian Margin with burial depth from 855m to 3605m. This study will increase the dataset to all the UK North Sea hydrocarbon fields for which data is available. The aim of this chapter is to obtain the pore throat radii distribution of UK North Sea fields, and to correlate the pore throat radii with oil fields parameters to make a predictive model that could be used for the assessment of a seal in a candidate CO_2-storage aquifer.

In this study, a new model for pore throat radii calculation has been created using available data from open publications and CDA database (reservoir temperature, pressure, API gravity (American Petroleum Institute gravity), GOR (gas oil ratio), Formation Volume Factor (FVF), salinity, column height, gas expansion factor, gas gravity). The advantage of this method is to reduce the dependence on experimental measurements for the seal retention capacity analysis. Usually, for hydrocarbon exploration, the caprock core samples are scarce. Even if a few core plugs could be obtained, it is difficult to know if they can represent reservoir-scale conditions, especially when the caprocks are highly heterogeneous. For example, the measured pore throat radius of Haltenbanken (Norway) range from 100nm to 21,000nm using mercury injection method (Clayton and Hay, 1994). It is difficult to estimate the real effective pore throat radius that limit the height of the existing hydrocarbon column. The new method which is based on the capillary sealing mechanism, calculated the real effective pore throat radius that works as the limiting parameter for the retention capacity.

Monte Carlo simulation method is used for fitting the calculated pore throat radius, allowing the uncertainties of each parameter to be taken into account.

2.3 Statement of new work

The new work in this study is summarized as:

- A statistic model using data from the UK North Sea for effective pore throat radii have been established in section 2.5.1 and section 2.5.2. Two different models were used to calculate the interfacial tension between gas and brine for gas fields. A revised frequency distribution of the effective pore throat radii of the oil and gas fields of the UK North Sea fields have been obtained.
- A predictive model for effective pore throat radius has been proposed and the coefficients, application, and scope are discussed.
- Monte Carlo simulation is utilised in this study to get a reliable cumulative distribution and a probability distribution of the pore throat radius. The results are compared with the distribution by Yang and Aplin (1998).
- The possible controlling factors for the effective pore throat radius have been discussed, including faulting, burial depth and caprock thickness.

2.4 Data source

The major data sources for the North Sea include: Common Data Access (CDA: https://www.ukoilandgasdata.com), and the compilation of the hydrocarbon fields of the UK North Sea (Gluyas and Hichens, 2003, Abbotts, 1991).

The required data has been organized into the following categories:

- Composite logs (CDA database)
- Trap: Trap type, depth to crest, lowest closing contour, oil/gas column height
- Field characteristics: area, initial pressure, pressure gradient, lithostatic pressure, temperature
- Petroleum property data: API, formation volume factor, gas oil ratio, gas gravity, gas expansion factor
- Reservoir characteristic data: formation name, gross thickness, net:gross ratio, average porosity (range), average permeability (range)
- Fluid data: salinity
- Field reports and documents (CDA database)

In total, 100 reservoirs of UK North Sea have been reviewed, 66 of which have both sufficient data to allow calculation and capillary pressure is plausibly the controlling factor for hydrocarbon sealing (for analysis of this see below). Fields with column

height controlled by spill point (lowest closing contour is the same as oil-water contact) are exclude from analysis, because the fields that are filled to spill point are not limited by capillary sealing, structural trap might be the limiting factor. Fields used for calculation are listed in Appendix 1.

2.5 Methodology for pore throat radii calculation

The methodology has been established in the published paper: *Retention capacity of seals from hydrocarbon field analogues for appraisal of saline aquifers* (Wilkinson et al., 2014). According to Equations 2-3, 2-4 and 2-5, pore throat radii could be derived from the following equation:

$$R_e = \frac{2cos\theta\Delta\sigma}{(\rho_w - \rho_h)gh} \qquad \text{Equation 2-19}$$

Where R_e: effective porethroat in caprock; ρ_w: density of saline water; ρ_h: density of hydrocarbon; $\Delta\sigma$: water-hydrocarbon interfacial tension; g: standard gravity; h: hydrocarbon column height; $cos\theta$: contact angle from minerals to hydrocarbons. Different models shall be used for oil fields and gas fields. The calculated pore throat radii are derived from the assumption that the buoyancy force is exactly equals to capillary pressure, which only be the case if the caprock is in a critical leaking point, that any increase of the column height would result in a breakthrough of the retained hydrocarbon In real cases, the buoyancy force must be lower than capillary pressure, which means the real pore throat must be smaller than the calculated “effective pore throat radii”.

2.5.1 Parameters used for effective pore throat radii calculation for oil fields

The parameters used to calculate the effective pore throat radii include:

- Wettability

In the presence of hydrocarbon phase, many minerals will be generally water wet giving an assumption that the contact angle between oil and brine is 0°, therefore $\cos(\theta_{oil/brine}) = 1$ (Naylor et al., 2011), which gives the calculated pore throat radii the maximum value.

- Interfacial tension (IFT) between oil and brine

The IFT between the oil and brine is calculated using IFT of water/air and air/oil after (Duchateau and Broseta, 2012) :

$$\Delta\sigma_{water-oil} = \Delta\sigma_{water-air} - \Delta\sigma_{air-oil} \quad \text{Equation 2-20}$$

In this methodology, the water-oil interfacial tension corrected by temperature and oil-gas ratio (Rs), shall be written as a function of API, temperature, and oil-gas ratio.

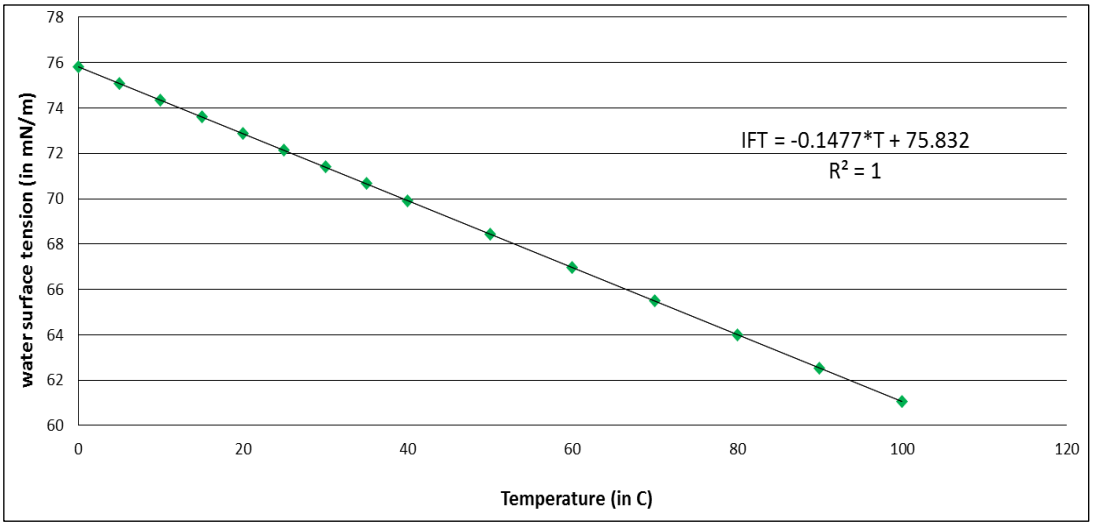

Figure 2- 13: Surface tension of water vs. temperature. Data is derived from Lange's Handbook of Chemistry (Speight, 2005).

Figure 2-13 shows the water surface tension is in significant linear correlation with temperature, hence the surface tension of the water could be calculated using equation of:

$$\Delta\sigma_{water-air} = -0.1477\mathrm{T} + 75.832 \ (\mathrm{T\ in\ °C}) \quad \text{Equation 2-21}$$

$\Delta\delta_{air-oil(T)}$: live oil-air surface tension after temperature correction (Baker and Swerdloff, 1956) is:f

$$\Delta\sigma_{air-oil(T)} = (38.085 - 0.259API) \times 1.11591 - 0.00305T \ (T\ in\ °C) \quad \text{Equation 2-22}$$

$\Delta\sigma_{air-oil(T,Rs)}$: live oil-air surface tension after temperature and Rs correction is: (Rs is gas-oil ratio (m^3/m^3)) (Abdul-Majeed and Abu Al-Soof, 2000). GOR to Rs

conversion: Rs=GOR*0.1761 (GOR is in scf/bbl).

For Rs<50m^3/m^3

$$\frac{\Delta\sigma_{air-oil(T,Rs)}}{\Delta\sigma_{air-oil(T)}} = \frac{1}{1+0.02549Rs^{1.0157}} \quad \text{Equation 2-23}$$

For Rs≥50m^3/m^3

$$\frac{\Delta\sigma_{air-oil(T,Rs)}}{\Delta\sigma_{air-oil(T)}} = 32.0436Rs^{-1.1367} \quad \text{Equation 2-24}$$

- ρ_{wr}: density of brine water at reservoir condition

The density calculation model is derived from Danesh in Equation 2-25~2-29 (Danesh, 1998):

$$\rho_{w(standard)} = 62.368 + 0.438603w_s + 1.60074 \times 10^{-3}w_s \quad \text{Equation 2-25}$$

$$\rho_{wr} = \frac{\rho_{w(standard)}}{B_w} \quad \text{Equation 2-26}$$

$$B_w = (1 + \Delta V_{wp})(1 + \Delta V_{wt}) \quad \text{Equation 2-27}$$

Pressure and temperature correction factor:

$$\Delta V_{wp} = -P(3.58922E-7 + 1.953E-9T) - P^2(2.25341E-10 + 1.72834E-13T)$$

Equation 2-28

$$\Delta V_{wt} = -1.001E-2 + 1.33391E-4T + 5.50654E-7T^2 \quad \text{Equation 2-29}$$

Where w_s is weight percent of dissolved salt; B_w is formation water volume factor at standard conditions; ΔV_{wp} and ΔV_{wt} are pressure and temperature correction factors; $\rho_{w(standard)}$ is the density of brine water at reservoir condition. All the density analysis in this section is in bm/ft^3, T in K, P in MPa.

- $\rho_{oil(reservoir)}$: density of oil at reservoir condition.

Suppose when oil migrates from reservoir to surface, methane will exsolve from the oil. The calculation equations for the reservoir density of oil are:

$$\rho_{oil(surface)} = \frac{141.5 \times 999.016}{API + 131.5} \quad \text{Equation 2-30}$$

$$\rho_{oil(reservioir)} \times V_{reservoir} = \rho_{oil(surface)} \times V_{oil(surface)} + \rho_{methane(surface)} \times V_{methane(surface)} \quad \text{Equation 2-31}$$

$$\rho_{oil(reservoir)} = \frac{\rho_{oil(surface)} \times V_{oil(surface)} + \rho_{methane(surface)} \times V_{oil(surface)} \times GOR}{V_{oilsurface} \times FVF} \quad \text{Equation 2-32}$$

$$\rho_{oil(reservoir)} = \frac{\rho_{oil(surface)} + \rho_{methane(surface)} \times GOR}{FVF} \quad \text{Equation 2-33}$$

Calculation of methane density=0.678kg/m^3.

Where $\rho_{oil(surface)}$ is the density ofoil at surface condition; $\rho_{methane(surface)}$ is density of methane at surface condition; $\rho_{oil(reservoir)}$ is density of oil at reservoir condition; GOR is gas-oil ratio; FVF is formation volume factor; V_{total} is the total volume of oil at reservoir condition; $V_{oil(surface)}$ is volume if oil at surface condition; $V_{methane(surface)}$ is methane volume at surface condition.

The parameters used for the calculation of the effective pore throat radii of the oil fields have been listed in Appendix 2.

2.5.2 Parameters used for effective pore throat radii calculation for gas fields

- Gas-brine contact angle: $cos\theta = 1$

In the presence of the hydrocarbon phase, many minerals will generally be water wet giving a contact angle of zero giving a contribution to the denominator of the ratio of cos(0)=1. (Naylor et al., 2011).

- $\Delta\sigma_{water-gas}$

There are two solutions to calculate the interfacial tension between the water and gas:

Solution 1: Use the empirical model established with the data from the previous lab studies. The following graph gives the interfacial tension under the temperatures of 298K, 373K and 473K. For intermediate temperatures, linear interpolation shall be used.

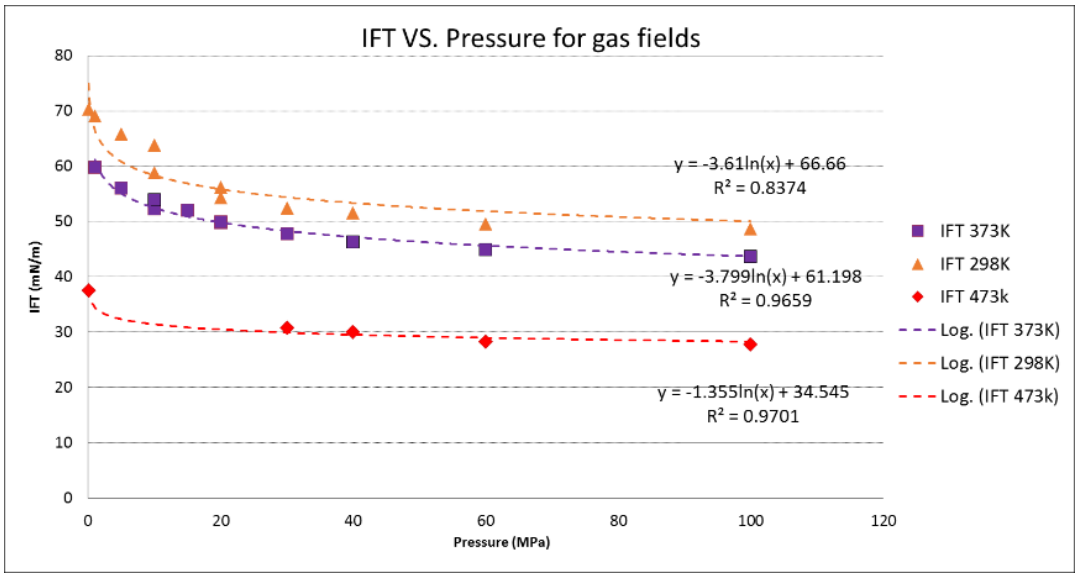

Figure 2- 14: Interfacial tension vs. pressure and temperature. Data is derived from compiled literatures (Ren et al., 2000, 田宜灵 et al., 1997) (equivalent to (Tian et al., 1997)).

Solution 2: Use Firoozabadi and Ramey equation to calculate brine-gas IFT (Firoozabadi and Ramey Jr, 1988):

$$\Delta\sigma_{water-gas} = 111(\Delta\rho)^{1.024}({}^{T}/_{T_c})^{-1.25} \qquad \text{Equation 2-34}$$

Where $\Delta\sigma_{water-gas}$= brine-gas interfacial tension, mN/m; $\Delta\rho$= difference in density between brine and gas, g/cc; T_c is critical temperature in K. Assuming the gas is 100% of methane, the T_c=190.6.

- ρ_{gas}: gas density at reservoir condition.

The gas density is calculated with gas specific gravity and gas formation factor. The following equation is derived from Danesh (2007) and Naylor (2010).

$$\rho_{gas} = 1.2086 \times S_g \times \left(\frac{1}{B_{gas}}\right) \qquad \text{Equation 2-35}$$

Where S_g=specific gravity; B_{gas}=gas formation factor $= \frac{1}{gas\ expansion\ factor}$.

2.5.3 Monte Carlo simulation

2.5.3.1 Brief of Monte Carlo

Monte Carlo simulation method is widely used for probabilistic estimation of hydrocarbons resources a nd CO_2 capacity of saline aquifers. This method allows various of distribution types for input to make the final distribution. The author predicts the distribution of input parameters of different hydrocarbon fields and calculate pore throat radius based on the equations listed in section 2.5.1 and 2.5.2. Pore throat radii distribution of 31 fields is obtained (only for fields with mudstone caprocks). The iteration for every field is 1000 times. Then a compiled distribution of the 31 fields is derived to show an overall situation for North Sea hydrocarbon fields. R script for Monte Carlo simulation is in Appendix 3.

2.5.3.2 Uncertainties of input parameters

The input parameters used for pore throat radii calculation include: column height (H), API, Temperature (T), Pressure (P), Gas Oil ratio (Rs), Formation Volume Factor (FVF), weight percent of dissolved salt (w_s), wettability ($cos\theta$).

In borehole depth measurements, many factors are reported to affect the accuracy of wireline depth measurement: elastic stretch, inelastic stretch, temperature, mud radial pressure, etc. In the report of Sollie and Rodgers (1994), up to 6m of inaccuracy is reported for the depth measurement by well logs (Sollie and Rodgers, 1994). Therefore in this study, the distribution of column height is defined as uniform distribution with uncertainties of $\pm 6m$, as the The wettability ($cos\theta$) is defined as uniform distribution ranging from 0.9-1.0 after Naylor et al., (2011). As it is very difficult to define the types of distribution for most of the paramters, this study use normal distribution with standard deviation of 5% for the rest parameters. The uncertain assumptions of different input parameters are listed in the table below:

Table 2- 3: uncertainties assumptions of the input parameters for the Monte Carlo simulation.

Parameters	Column height/m	API	Temperature/K	Pressure/psi
Type of distribution	Uniform	Normal distribution	Normal distribution	Normal distribution
Uncertianties	±6 (Uniform distribution)	5% (standard deviation)	5% (standard deviation)	5% (standard deviation)
Parameters	Gas oil ratio	Formation volume factor	Dissolved salt	Wettability
Type of distribution	Normal distribution	Normal distribution	Normal distribution	Uniform
Uncertianties	5% (standard deviation)	5% (standard deviation)	5% (standard deviation)	0.9-1.0 (Uniform distribution)

2.6 Results and analysis

2.6.1 Pore throat radii distribution

100 fields of the UK North Sea have been reviewed, and 66 of which are included in this study (see the field list in Appendix 1), excluded the fields where the column height is controlled by a spill point and those that lack sufficient data. Evaporite caprocks usually show very small effective pore throat radii compared to shale caprocks, because of the evaporates lack conventional porosity, and any fractures can reseal due to the high solubility of evaporate minerals (Wilkinson et al., 2014). Limestone has also been excluded for the complicated porous feature. Hence, the major study objects narrowed down to oil fields with shale caprocks, so the number of fields decreases to 54 for this study.

The result of the pore throat distribution is shown in Figure 2-15. The total range of the calculated pore throat radii is from 22-601 nm with the shape of the distribution appears to be like a log-normal (Wilkinson et al., 2014). This result is in accordance with the results of published studies (Benson and Cole, 2008, Chalmers and Bustin, 2012, Clayton and Hay, 1994, Kaldi and Atkinson, 1997). Benson and Cole (2008) reported a wide range of measured pore throat radii of between 140-3000nm (Ben

and Cole, 2008); Chalmers and Bustin (2012) reported a much smaller pore throat radius for less than 300nm for shale from gas shale and tight gas reservoirs (Chalmers and Bustin, 2012); Clayton and Hay (1994) measured mudstones from offshore Holland and Haltenbanken Norway displays a range of 80nm to 21,000nm (Clayton and Hay, 1994); the fractured caprocks from deltaic settings have pore throat radii of 76-1350nm (Kaldi and Atkinson, 1997).

The possible controls of pore throat radii are thought to be the degree of faulting, the extent to which the hydrocarbon is sealed by faults, the depth of burial and thickness of the caprocks. The correlations between these factors and pore throat radii are investigated respectively.

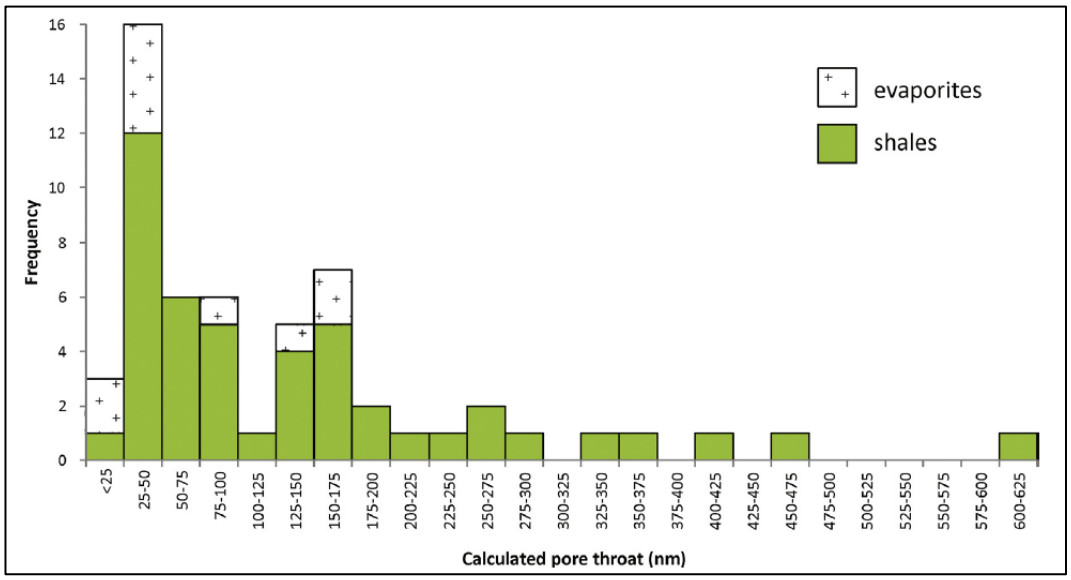

Figure 2- 15: Pore throat radii distribution of data of North Sea caprock

The results of this part of the study has been included in published paper titled "*Retention capacity of seals from hydrocarbon field analogues for appraisal of saline aquifers"* co-authored with Mark Wilkinson and Zhengao Chen (*International Journal of Greenhouse Gas Control,* enclosed in Appendix). My major contribution is to improve the calculation model for parameters used for effective pore throat radii determination, as described in section 2.5.1 and 2.5.2, and made the calculation model more reliable for reservoir conditions.

2.6.2 Discussion of controlling factors for pore throat radii

The influence of the probable factors that controlling the pore throat radii have been investigated in this section.

- Faulting and fault sealing

No previous papers have been found to investigate the relationship between pore throat radii and faulting. But it is acknowledged that faults can act as conducts or seals for the fluids, which is assumed to be able to affect the effective pore throat of the caprocks. The damaged zone, which refers to the volume of deformed wall rocks around a fault surface that results from the initiation, propagation, interaction and build-up of slip along faults, could especially associated with large pore throat radii and leakage.

The degree of faulting of a caprock is the first controlling factor to be investigated. Figure 2-16 shows the frequency of pore throat radii based on the degree of faulting (some fields are excluded with no information). The faulting has been defined as three categories based on the fault throw: a) “Large faults” is defined as faults penetrate beyond the immediate caprocksand sometimes extend to the surface; b) medium fault is defines as the faults penetrate the immediate seal but not the overburden; and c) small faults is defined as there is no big faults or the faults are restricted to the reservoir that not influence the caprocks. The demonstration seismic cross-section used for classification is shown in Figure 2-16 (b), (c). The applicant of these criteria might bring about uncertainties, because all the judgements are from seismic cross section-image or schematic seismic cross-section figure plus the descriptions from publications (Gluyas and Hichens, 2003, Abbotts, 1991). Figure 2-16 shows no discernible correlation between faulting degree and pore throat radii frequency. The reasons could be:

a. The definition of “faulting degrees” is quite vague. More detailed resource is needed for more accurate classification, such as 3D seismic data.
b. The dataset (54 fields) is not big enough to reach a solid conclusion.
c. It does not necessary mean “faulting level” is not a factor for effective pore throat radii. The distribution shows most fields with “small faults” still locate in the area less than 100nm.

d. This chart shows a compiled frequency distribution of the fields from the whole UK North Sea. The faulting mechanism for different area could be very different from one region to another. To study the relationship between pore throat radii, more details are required rather than just the presence or absence of faults. Other parameters should also be taken into account, such as faults density, conductivity, formation, age, displacement and compartmentation in the future study.

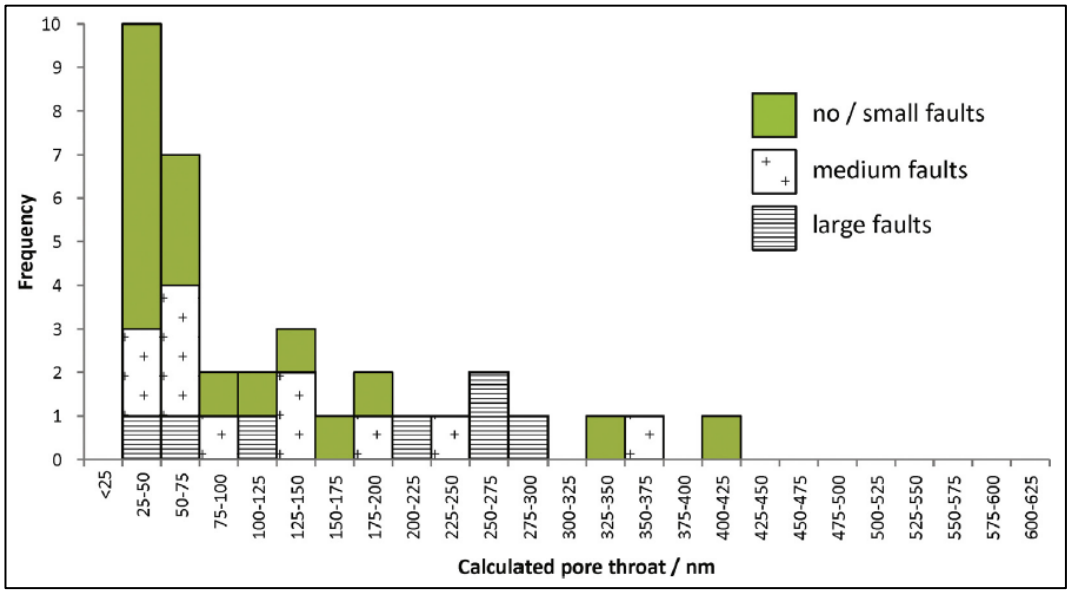

(a)

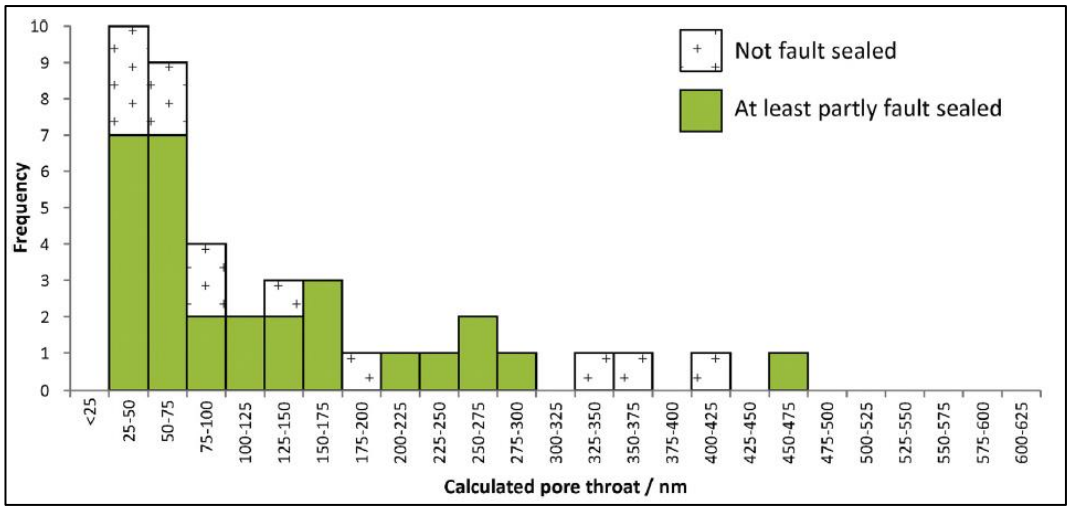

(b)

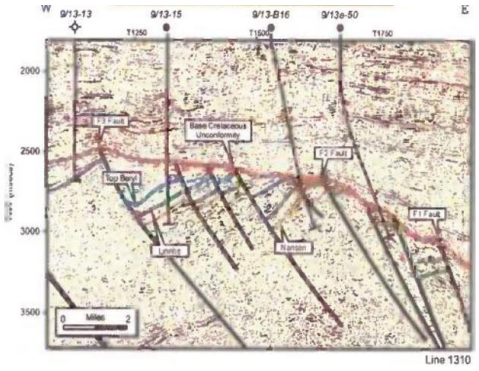

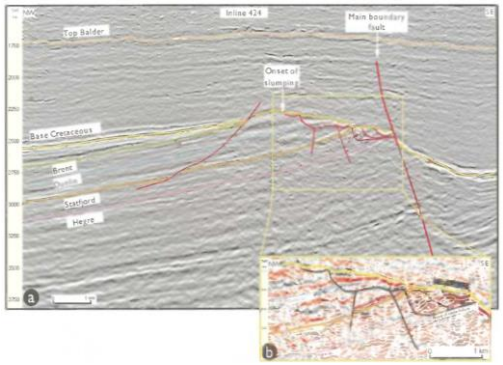

(c) (d)

Figure 2- 16: (a) Distribution of calculated pore throat radii according to the degree of faulting (shales caprock only; some fields have been excluded for no clear cross-section images could be found); (b) Calculated limiting pore throat radius for fields with and without at least a component of fault sealing, for shale seals only; (c) schematic cross-section for Beryl field with small/no faults (Karasek et al., 2003); (d) interpreted seismic image for Statfjord Field with moderate faults (Gibbons et al., 2003).

Figure 2-16 (b) shows the distribution of pore throat radii for shale seals separated into fields that are fault sealed versus those that are not. The presence of a known fault seal doesnot have an obvious impact upon the effectiveness of the seal. Note that some fields are excluded as no data are available to assess the degree of fault sealing.

- Burial depth

Theoretically speaking, burial depth should have correspondence with pore throat radii (see earlier discussion in section 2.2.2). With deeper burial, more compaction occurs, reducing the porosity. Since porosity is related to pore throat radii (Equation 2-15 and 2-17), it is likely that the burial depth is inversely correlated with the pore throat radius

Figure 2-17 shows how the present-day burial depths (current depth of burial data in table 2-4) relate to the calculated pore throat radii. There is weak correlation ($R^2 = 0.216, n = 34$) for the fields in Northern and Central North Sea. The result is not

consistent with previous research. Borst (1982)'s study shows relatively strong correlation between burial depth with pore throat radii ($R^2 = 0.8, n = 34$). The reasons could be:

a. Borst used mean pore size obtained from mercury injection porosimetry, which cannot represent the limiting or effective pore throat radii that control the capillary pressure. Besides, the result of MIP is influenced by sample preparation, sample size, and the way of cutting, which are not clearly illustrated in his paper.
b. The burial depth of his samples range from 3m to 4572m, while the range of burial depth in this study is much narrower.
c. Borst did not illustrate clearly the source of samples. He only mentioned "the type of samples include sidewall and conventional cores, drill hole cuttings and outcrop samples" and the age span of the samples ranging from Pleistocene to Silurian. It is hard to make a comparison from the fields of North Sea (Borst, 1982).
d. Present day burial depth might not be the decisive factor for fields of North Sea, because the fields in the Southern North Sea have been structurally inverted, i.e. are currently more shallowly buried than the previous maximum burial. As the deepest burial depth of the fields of Southern North Sea should be much deeper, it is possible that the limiting pore throat radii are smaller than those of the fields of similar depth.
e. The infill of hydrocarbons might be the reason that weaken the correlation between burial depth and pore throat radii. Infilling of hydrocarbon could result in porosity preservation (Wilkinson et al., 2006), which could also lead to pore throat radii preservation.

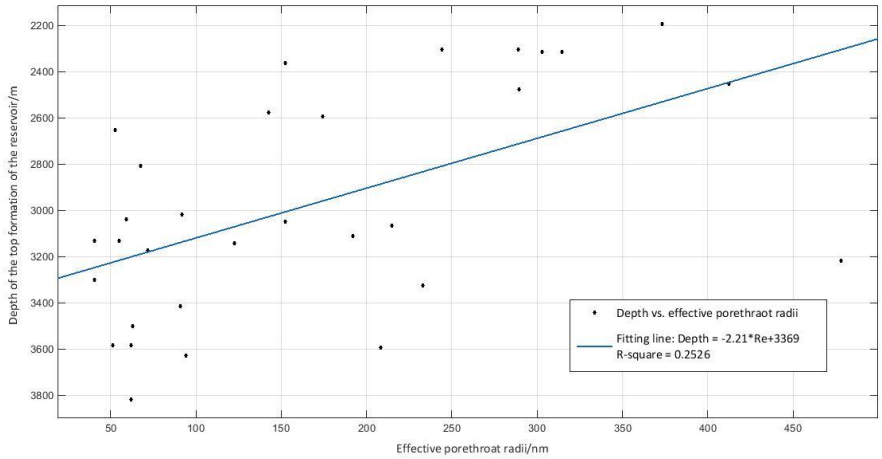

Figure 2- 17: The correlation between calculated effective pore throat radii and the burial depth of the top formation

Interestingly, stronger linear correlation has been discovered for the fields with burial depth less than 3000m (Figure 2-18). The trend line equation is:

$$Depth = -1.119Re + 2699; \quad (\text{Depth } < 2699, \text{n} = 13, \text{R} - \text{square} = 0.49)$$

Equation 2-36

Where $Depth$ indicates the vertical depth from the sea level to the top formation of the reservoirs in meter; Re is effective pore throat radii in nano meter. The decrease of pore throat radii with the increasing depth probably due to the mechanical compaction, or the diagenesis induced by increase of the temperature. The correlation between temperature and the burial depth less than 3000m shows in Figure 2-18. The reservoir temperature increases as the burial depth goes deeper for the burial depth less than 3000m. The temperature for the fields shallower than 3000m range from approximately 70°C to 140°C (temperature information see Appendix 2).

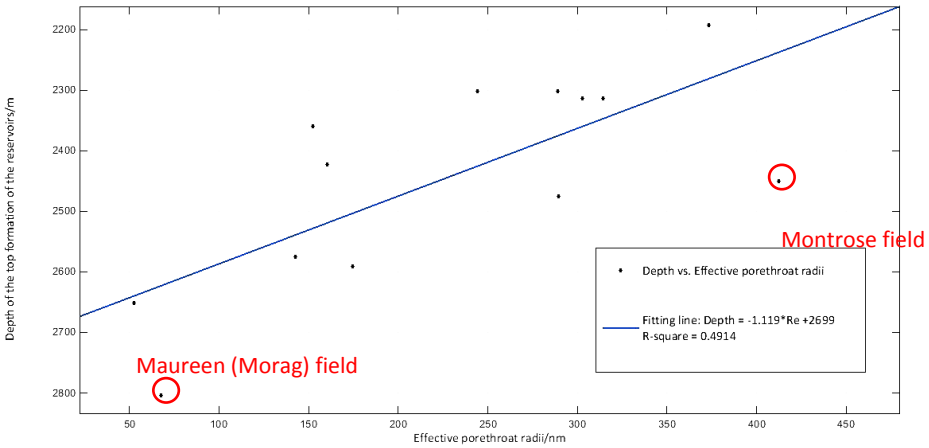

Figure 2- 18: the correlation between calculated effective pore throat radii and present burial depth shallower than 3000m.

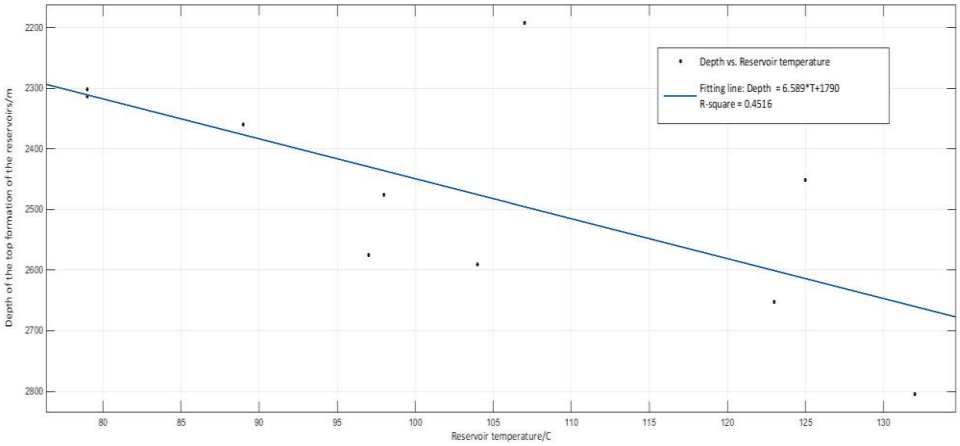

Figure 2- 19: The correlation between reservoir temperature and present burial depth shallower than 3000m.

Wilkinson and Haszeldine studied the illitisation of smectitie during the detrital burial (Wilkinson and Haszeldine, 2002), and suggested the transformation from smectite to illite could lead to smaller pore size, and result in more effective at capturing and storing fluids. The model of Wilkinson and Haszeldine concluded that the diagenesis change starts from 1500. Within the depth from 1500m to 4000m, there displays a dramatic increase from smectite to illite against the depth (Figure 2-20). The precipitation of illites is believed to start at approximately 60°C (around 1500m to

2000m in depth) (Nadeau, 2011). The presence of carbonates might increase the stability of the clay reactant to approximately 80°C (Nadeau, 2011).

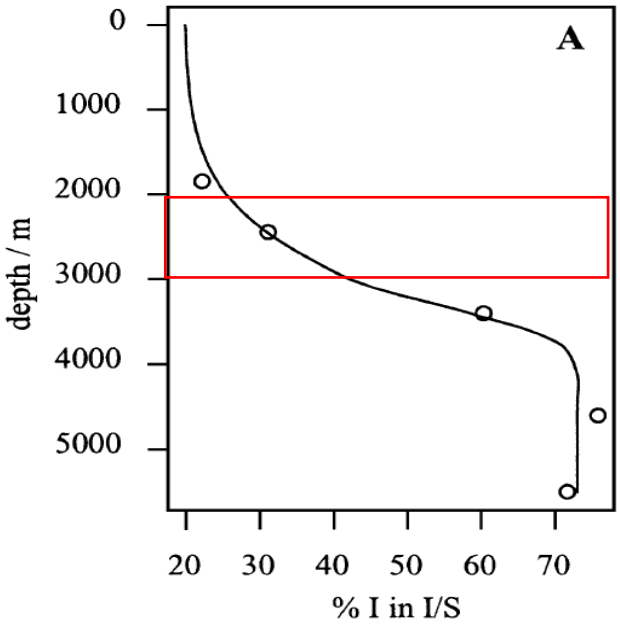

Figure 2- 20: Proportion of illite in illite/smectite system (Wilkinson and Haszeldine, 2002).

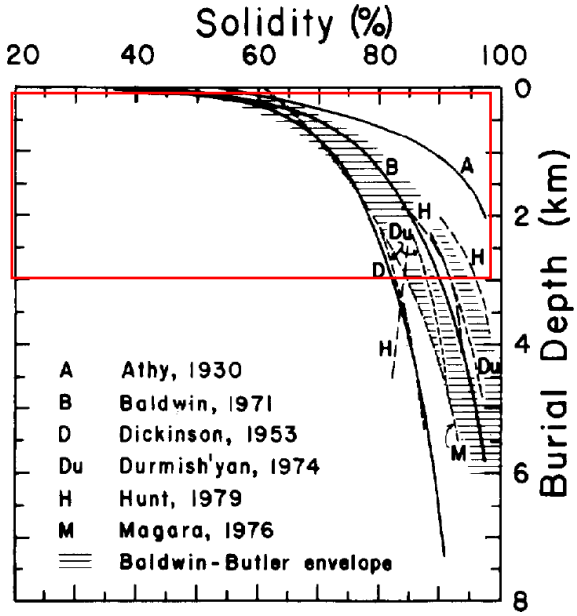

Figure 2- 21: Selected compaction curve for argillaceous sediments (Baldwin and O. Bulter, 1985)

Figure 2-21 shows the solidity-depth curves from argillaceous sediments from six sources (Baldwin and O. Bulter, 1985). The data is a compilation from 15 articles. The solidility equals to 100 minus porosity. It is clear to see from the Figure 2-21 that compaction causes rapid porosity decrease during shallow burial depth (0-3000m), while deeper than 3000, the porosity reduction rate decreases dramatically.

The result in Figure 2-18 and Figure 2-19 is in accordance with the result from Wilkinson and Haszeldine (2002) and Nadeau (2010). From 2000m to 3000m, the pore throat radii decreases drastically with the current burial depth increases. Therefore, here we assume the clay diagenesis should be one of the dominant factor for the pore throat reduction, which might effects on pore throat radii coupled with physical compaction at shallow depth of less than 3000m.

The Maureen (Morag) field and the Montrose field show deviations in the model. The present burial depth the reservoir Maureen (Morag) is 2804m, which is beyond the application scope of the Equation 2-36. The real effective pore throat radii is 68nm and the associated burial depth would be predicted to be 2623m. The burial depth of Montrose fields is 2450m and the estimated pore throat radii based on Equation 2-36 would be predicted to be 220nm, while the real effective pore throat radii is 412nm. The estimation of the Equation 2-36 for these two fields seems to be underestimated the pore throat size. The possible reason for the deviation has been investigated. The caprocks of the Maureen field and the field Montrose are mudstones from Palaeocene, while the caprocks of other fields are mudstones from Upper Jurassic Kimmeridge Clay Formation (age of caprocks see Appendix 2). The underestimation is probably owing to two reasons: firstly, the young aged mudstones from Palaeocene are less affected by diagenesis modification; secondly, the mudstones from Palaeocene are less overpressured comparing to the Upper Jurassic mudstones.

For the fields with present burial depth greater than 3000m (n=19), no significant correlation between depth and effective pore throat radii could be found (Figure 2-22). But most of the pore throat radii of the fields are less than 250nm. The weak correlation with depth could be interpreted as that at depth greater than 3000m, both the diagenesis and compaction effect stop. The correlation between temperature and depth is very weak when the burial depth is deeper than 3000m (Figure 2-23), which means the temperature does not proportional increase as the burial depth.

The field Curlew B is the only outlier with exceptional large effective pore throat radius of 478nm. The possible explanation for this deviation could be the structure of Curlew B is highly overpressured and dissected centrally by a normal fault and intra-reservoir faults divides the field into compartments (Eneyok et al., 2003). Alternatively, the overpressure might act as a way to prevent compaction and diagenesis thus remains the pore throat radii.

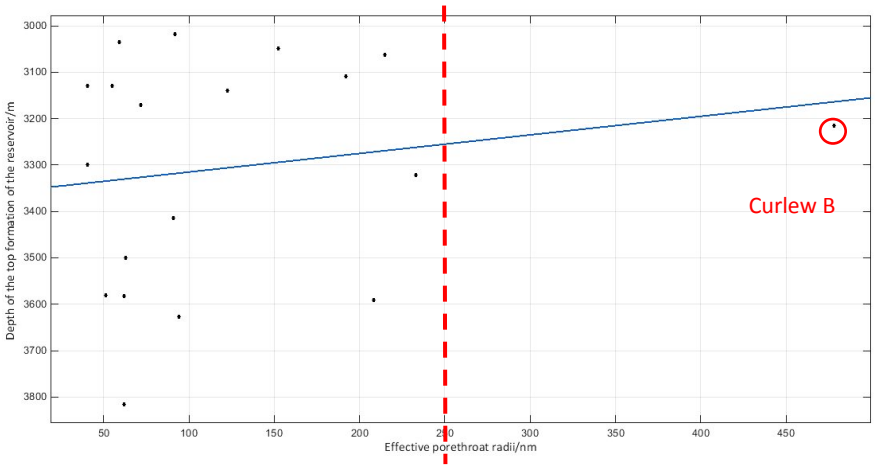

Figure 2- 22: The correlation between calculated effective pore throat radii and present burial depth deeper than 3000m (R-square<0.2)

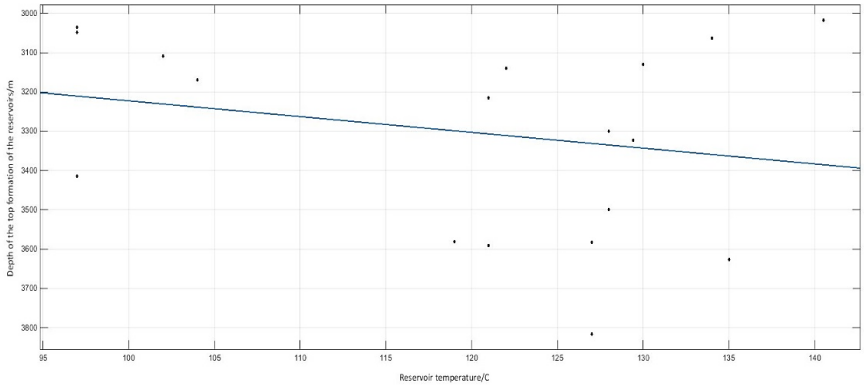

Figure 2- 23: The correlation between reservoir temperature and present burial depth deeper than 3000m (R-square<0.2).

In summary, if the depth is from 2000m to 3000m, clay diagenesis might be one of the important factor in pore throat radii determination. However, for the depth

greater than 3000m, no clear correspondence has been discovered, and the effective pore throat radii remain to be less than 250nm for the majority of the fields.

Equation 2-36 could be applied to seals of unknown sealing capacity that are formed of the Kimmeridge Clay Formation (KCF) at depths of less than 3000 m, as this is the formation from which the majority of the calibration data were derived. The application of the equation to caprocks of other formation could be misleading. For example, caprocks of the Maureen and Montrose fields are of Paleocene age, which are younger and less affected by diagenesis, and are less overpressured compared to the Kimmeridge Clay Formation. As an exception, field Curlew B shows a much larger pore throat radius than the other fields deeper than 3000m. It is probably because the formation is highly overpressured, which will inhibit compaction resulting in higher porosities, larger pore throats and hence lower seal efficiency at any given depthHence, the geological age and the overpressure condition are candidate factors for the effective pore throat radius.

- **Caprock thickness**

Some previous studies show positive correlation with sealing capacity (column height) and the thickness of the caprock (蒋有录, 1998, 付广 and 许凤鸣, 2003, 付广, 2006) (equivalent to Jiang, 1998, Fu and Xu, 2003, Fu, 2006). Caprock thickness is also used as an important indicator for caprock quality assessment for geological CO_2 storage (Chadwick et al., 2008). The interpretation for the possible correspondence between pore throat radii and the sealing capacity could be generalized as the following points:

a. Experiments demonstrated there is positive correlation between capillary sealing pressure and the lengths of core samples (付广 and 许凤鸣, 2003, 付广, 2006, Amann-Hildenbrand et al., 2013) (equivalent to Fu and Xu, 2003, Fu, 2006). The longer the core samples, the greater the capillary sealing, hence the smaller the effective pore throat radii, as the large pores thicker formations are has bigger chances to be connected with smaller pores, thus resulting in the increase in the entry capillary pressure.

b. Many studies have shown the correlations between the column heights of hydrocarbon fields and the capillary sealing pressure (蒋有录, 1998, 付广, 2006, 童晓光，牛嘉玉, 1989) (equivalent to Jiang, 1998, Fu, 2006, Tong and Niu, 1989).

However, the caprocks of the UK North Sea show weak correlation between the column height (hydrocarbon) vs. caprock thickness (Figure 2-24) and effective pore throat radii vs. caprock thickness (Figure 2-25). For oil fields with the pore throat radii less than 100nm, the thickness of caprock could range from 21m (Dunbar West) to 313m (Scott field) (Figure 2-24). Caprocks in one producing area with very similar caprocks and pore throat radii might have very different thickness. For example, Dunbar west flank and Dunbar frontal have similar effective pore throat radii (63nm and 41nm), but the thickness of the caprocks for these two reservoirs are 21m and 178m, respectively. This is because the thick mudstones of the Upper Jurassic Kimmeridge Clay Formation on top of the West Flank has been seriously eroded by an intra-Heather unconformity (Ritchie, 2003).

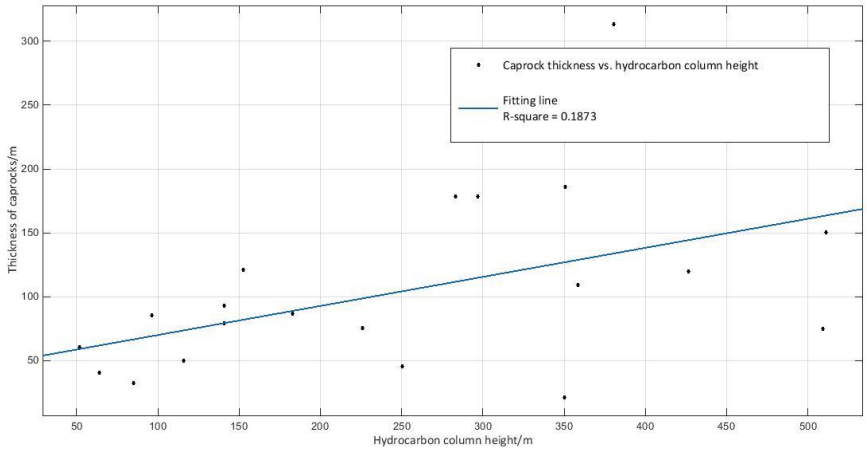

Figure 2- 24: The correlation between hydrocarbon column height and the thickness of caprocks.

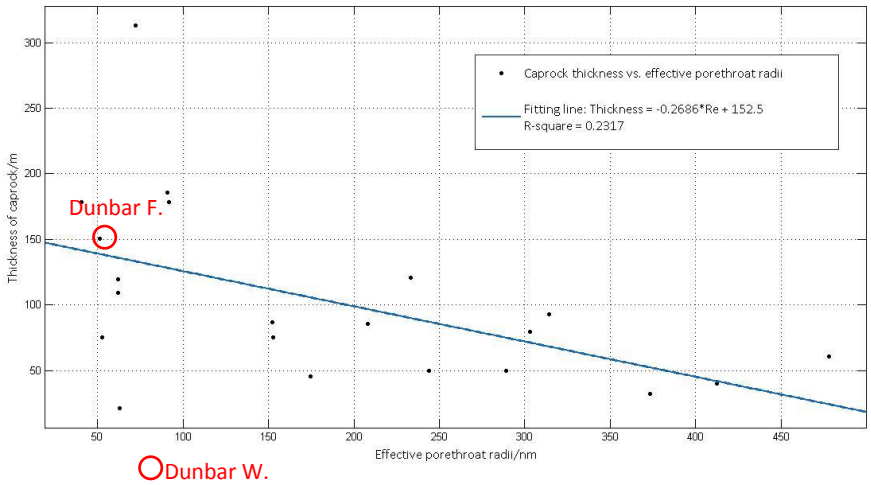

Figure 2- 25: The correlation between calculated effective pore throat radii and the thickness of caprocks.

Current thickness of the caprock is obviously not a controlling factor for the effective pore throat radius determination, for the current thickness could be a result of erosion, and it is not an input parameter according to Washburn equation (Equation 2-2). Most of the caprocks of the UK North Sea are provided by the mudstones from Heather Formation and Kimmeridge Clay Formation from Upper Jurassic, which experienced differential block tilting, elevation and erosion (Badley et al., 1988), and thus leading to various caprock thickness of the same regional caprocks.

In summary, there is no significant correlation between effective pore throat radii and current caprock thickness for the UK North Sea hydrocarbon fields. However, it does not necessarily mean there is no correlation between the original caprock thickness and capillary sealing capacity since the lab experiments and statistical analysis have demonstrated the correlation. Thin caprocks due to erosion could also have good sealing capacity. The thinnest caprock of the studied fields is still greater than 20m (Dunbar West Flank), which supports the siting criteria put forward by Chadwick et al. for geological carbon storage, that the caprock thickness should not be less than 20m (Chadwick et al., 2008).

2.6.3 Multi-parameters for effective pore throat radii prediction model

A 3D correlation between pore throat radii and caprock thickness, burial depth is also investigated. However, there is weak correlation with R-square of 0.327 (Figure 2-26). Comparing to the 2D correlation of pore throat radii vs. caprock thickness (Figure 2-25) and pore throat radii vs. burial depth (Figure 2-17), 3D correlation a comparatively better correlation (Figure 2-17). The prediction equation for the fitting surface is:

$$Re = 537.1 - 0.6891 \times Thickness - 0.09467 \times Depth \ \ (n = 21,\ R - square = 0.327)$$

Equation 2-37

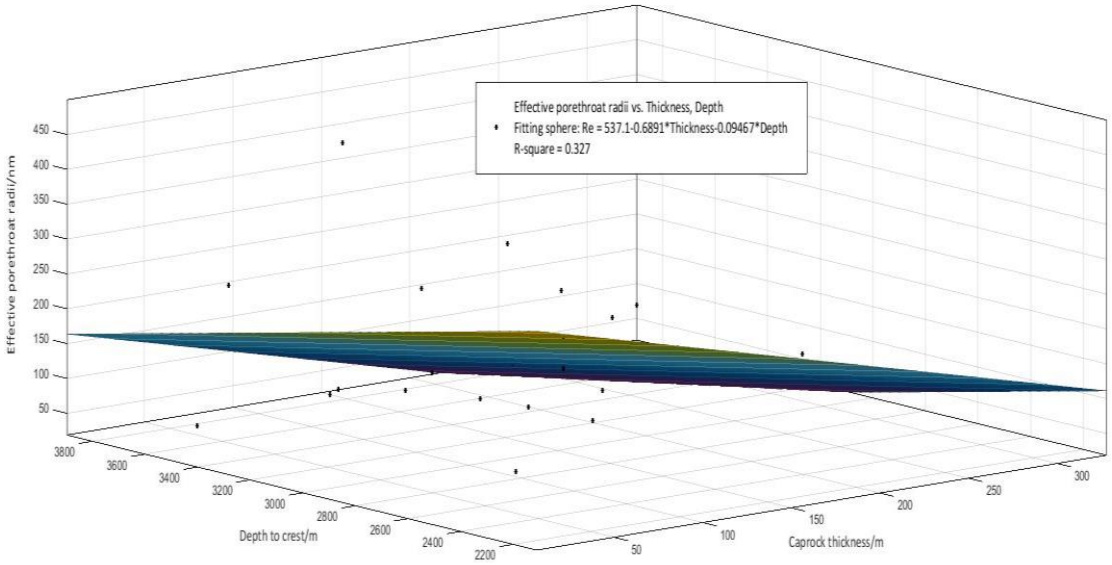

Figure 2- 26: 3D correlation model of effective pore throat radii vs. caprock thickness, depth.

Table 2- 4: the predicted pore throat radii from the 3-D estimation model and the real effective pore throat radii. The third column is the predicted effective pore throat radii comparing to the effective pore throat radii calculated from the model. The fifth column is the error (error = (predicted Re – Re)/predicted Re).

FIELD name	Effective pore throat (radii /nm) /error bar	Caprock thickness (I, m)	Depth of burial (Z, m)	Predicted Re (I, Z)	Error

Beryl (Nansen)	91	±10	186	3414	85.8	-0.06
Beryl A	152	±6	87	3048	188.9	0.19
Central Brae	51	±2	151	3581	94.2	0.46
Curlew B	478	±15	61	3216	190.9	-1.50
Don	233	±15	121	3322	139.1	-0.68
Dunbar.W	63	±1	21	3500	191.3	0.67
Dunbar.F	41	±1	178	3300	101.8	0.60
Fulmar	92	±5	178	3018	128.7	0.29
Ivanhoe (Main)	314	±40	93	2313	254.0	-0.24
Ivanhoe (Supra)	303	±30	79	2313	263.5	-0.15
Montrose	412	±15	40	2451	277.4	-0.49
Nelson	373	±25	32	2192	307.4	-0.21
Rob Roy (supra)	289	±15	50	2301	285.1	-0.01
Rob Roy (main)	244	±10	50	2301	285.1	0.14
Scott	72	±3	313	3170	21.0	-2.42
South Brae	53	±2	75	2652	234.4	0.78
Statfjord (Brent)	153	±10	75	2360	261.9	0.42
T-Block (Thelma)	208	±3	85	3816	116.9	-0.78
T-Block (Tiffany)	62	±3	120	3627	111.2	0.44
T-Block (Toni)	62	±2	109	3591	121.9	0.49
Thistle	175	±20	46	2591	260.4	0.33

In real cases, the burial depth of the reservoir top formation might be easier to get. Especially for caprocks with very large column height or burial depth, this prediction model may result in large error. Therefore, this 3D model is not plausible prediction model in effective pore throat radii determination.

2.6.4 Results of Monte Carlo simulation

Based on the new mathematical models in section 2.5 incorporation with Monte Carlo simulation, distribution of pore throat radii for 31 fields could be obtained here (only for fields with shale caprocks). Figure 2-27 shows the frequency distribution of effective pore throat radii of the Dunbar field (see R script in Appendix 3, distribution of the rest of the fields in Appendix 4). Figure 2-28 shows the frequency plots compiled results of the total 31 fields.

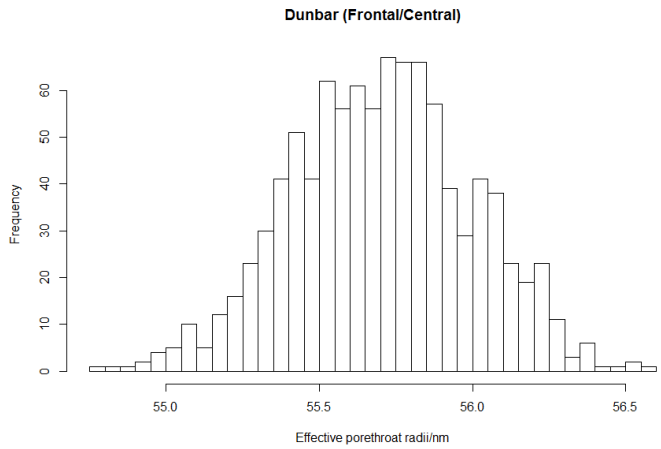

Figure 2- 27: The frequency distribution of effective pore throat radii for Dunbar field (see the rest of the fields in Appendix 4) after Monte Carlo simulation.

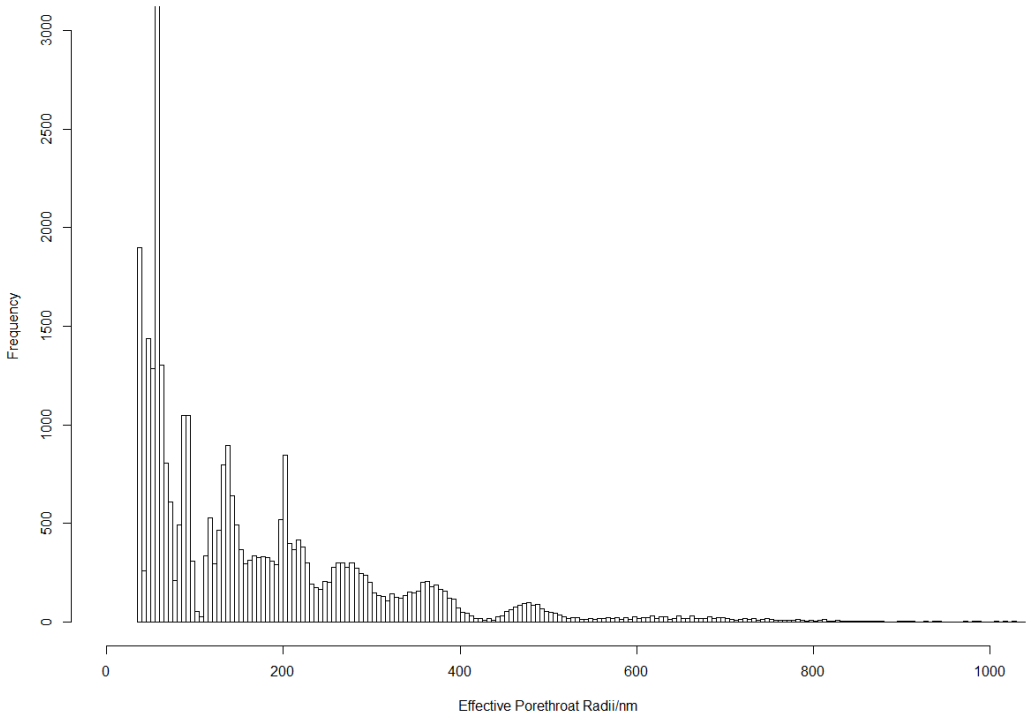

Figure 2- 28: Compiled pore throat radii distribution of the 31 fields.

- **Cumulative distribution**

The cumulative distribution describes the probability that the probability of less or equal to a certain effective pore throat radius. The cumulative distribution model of the effective pore throat radii of the shale caprocks of the oil fields of the UK North Sea fields is also established. The Equation 2-38 shows an accurate estimation with R-square of 0.9862:

$$F(x) = \frac{1}{1+\exp(a-bx-\frac{c}{x})} \qquad R^2 = 0.9862 \qquad \text{Equation 2-38}$$

Where F(x) is cumulative distribution of pore throat radii. For the UK North Sea, a=0.3152; b=0.006998; c=-92.28.

Thus, the cumulative distribution of effective pore throat radii is derived as:

$$F(x) = \frac{100}{1+\exp(0.3152-0.006998x+\frac{92.28}{x})} \qquad R^2 = 0.9862 \qquad \text{Equation 2-39}$$

The cumulative distribution of effective pore throat radii is displayed in Figure 2-29 and Figure 2-30.

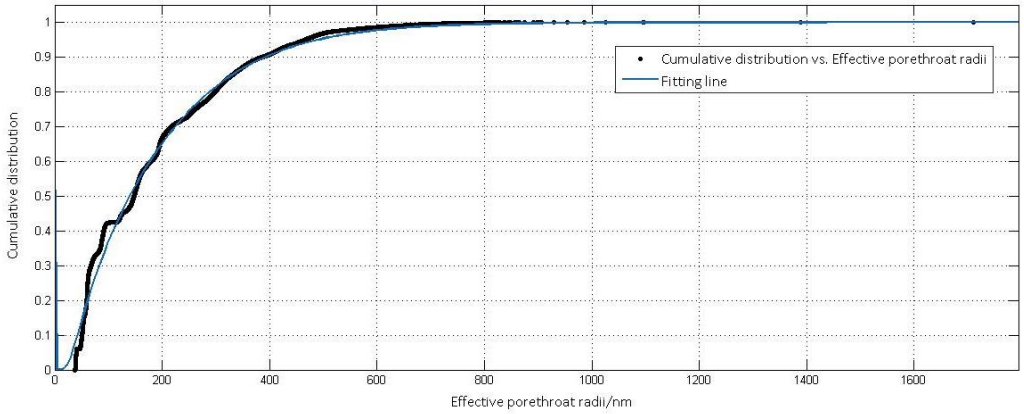

Figure 2- 29: Cumulative distribution of effective pore throat radii of the shale caprocks of the oil fields the UK North Sea.

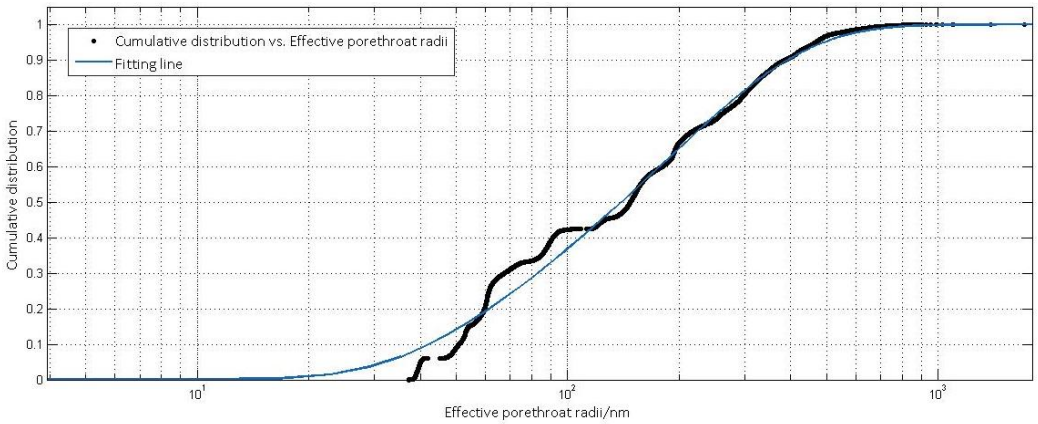

Figure 2- 30: Cumulative distribution of effective pore throat radii of the shale caprocks of the oil fields the UK North Sea (x-axis in log).

Table 2- 5: cumulative distribution probabilities and the associated

Re (nm)	<10	<20	<50	<80	<100	<200	<300	<400
Probability	7.6878e-05	0.083	0.1405	0.2872	0.3686	0.6509	0.8141	0.9049

Re (nm)	<500	<600	<700	<800	<900	<1000	<1100	<1200
Probability	0.9525	0.9766	0.9885	0.9943	0.9972	0.9986	0.9993	0.9997

Where Re=effective pore throat radii.

From the cumulative distribution curve, there is 90% of probability that the effective pore throat radii are smaller or equal to 400nm for the shale caprocks of the caprocks of the UK North Sea oil fields. More than 60% of probability that the effective pore throat radii are smaller than 200nm.

- **Probability distribution:**

The cumulative distribution function of pore throat radii is derived by differentiating Equation 2-39 to get the probability distribution of the effective pore throat radii:

$$f(x)=\frac{dF(x)}{dx}=\frac{(b-cx^{-2})\exp(a-bx-cx^{-1})}{[1+\exp(a-bx-cx^{-1})]^2} \qquad \text{Equation 2-40}$$

For the shale caprocks of the UK North Sea oil fields, the probability distribution is derived as:

$$f(x)=\frac{dF(x)}{dx}=\frac{(0.6998+9228x^{-2})\exp(0.3152-0.006998x+92.28x^{-1})}{[1+\exp(0.3152-0.006998x+92.28x^{-1})]^2} \qquad \text{Equation 2-41}$$

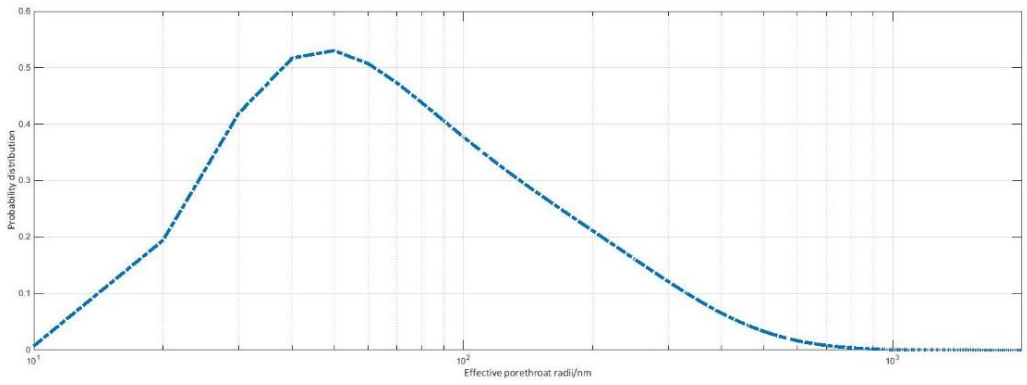

Figure 2- 31: Probability distribution of effective pore throat radii of the shale caprocks of the UK North Sea oil fields using Equation 2-40 (after Monte Carlo method).

Table 2- 6: Probability estimation of effective pore throat radii using Equation 2-41.

Re (nm)	10	20	50	80	100	200	300	400
Probability	0.0071	0.1945	0.5303	0.4385	0.3776	0.2114	0.1214	0.0652
Re (nm)	500	600	700	800	900	1000	1100	1200
Probability	0.0333	0.0166	0.0082	0.0040	0.0020	0.00097	0.00048	0.00023

From the probability distribution figure (Figure 2-31) and calculation Table 2-6, it is clear to see that the effective pore throat radii of the shale caprocks of the UK North Sea concentrated between 50-100nm. There is 19.4% of possibility that the effective pore throat radii of a fields is 20nm in the UK North Sea field. The possibility increased dramatically to 53.0% for the pore throat radii of 50nm and peaked between 50nm and 60nm, and then the probability decreases drastically from 60nm onwards. There is very small possibility for the effective pore throat radii to be larger than 400nm.

- **Comparing with Yang and Aplin's distribution:**

Yang and Aplin reported the pore size distribution based on the mudstones from the Norwegian North Sea using mercury injection porosimetry experiments. The result has been illustrated in section 2.2.3. The established equation is Equation 2-14, and the cumulative distribution is in Figure 2-11.

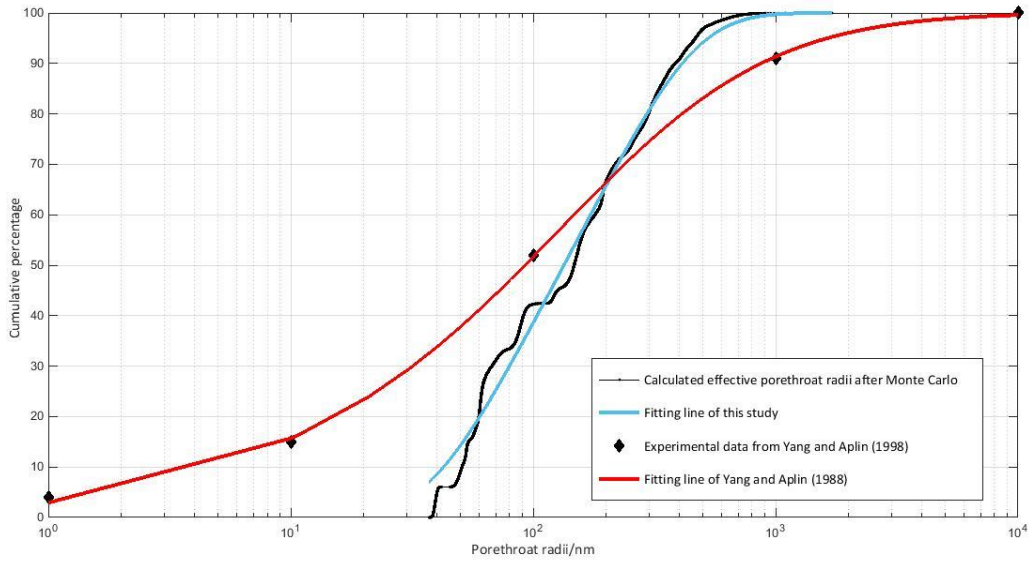

Figure 2- 32: Comparisons of cumulative percentage of pore throat radii of this study and that of Yang and Aplin (1988). The black line is the calculated effective pore throat radii after Monte Carlo simulation (Figure 2-28); the blue line is the fitting model of the cumulative percentage (Equation 2-48); the solid diamonds stand for data from mercury injection porosimetry experiments of Yang and Aplin (1998); the red line is the fitting model of the cumulative percentage of Yang and Aplin from the Norwegian Margin using Equation 2-14.

Yang and Aplin (1998)'s probability model:

$$f(x) = \frac{F(x)}{d(x)} = \frac{(b+3cx^2)\exp(a-bx-cx^3)}{[1+\exp(a-bx-cx^3)]^2} \qquad \text{Equation 2-42}$$

Using mudstones from the Norwegian Margin, then Equation 2-42 changes to Equation 2-43:

$$f(x) = \frac{(0.6031+0.0116x^2)\exp(3.084-0.6031x-0.003859x^3)}{[1+\exp(3.084-0.6031x-0.003859x^3)]^2} \qquad \text{Equation 2-43}$$

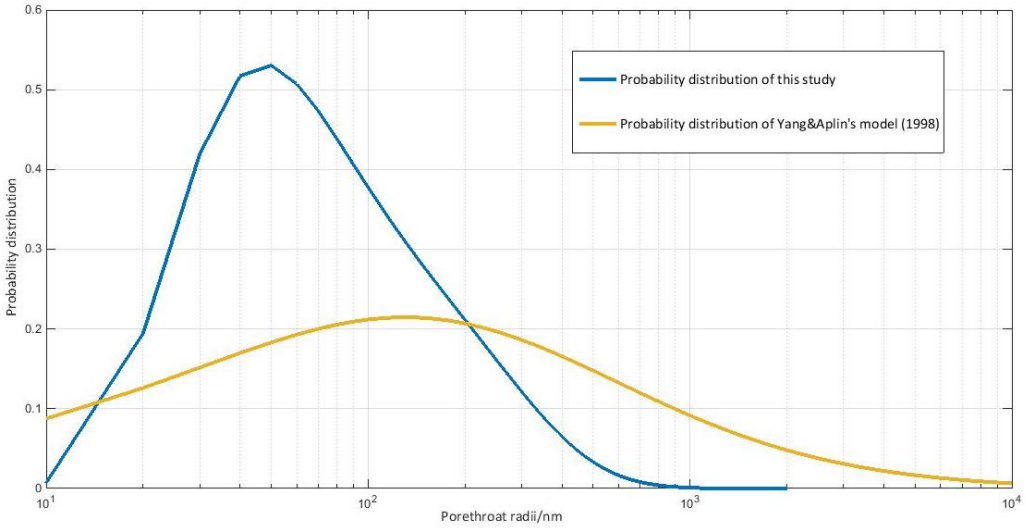

Figure 2- 33: Comparisons of probability distribution of pore throat radii of this study and the distribution by Yang and Aplin (1988). The blue line is the probability distribution of effective pore throat radii using Equation 2-41 of this study; the yellow line is the probability distribution of Yang and Aplin's model using Equation 2-43.

These two cumulative models show similar exponential trends, but there are several obvious differences between these two distributions:

- Yang and Aplin's model covers a much larger range of pore throat radius, from 1nm to 10,000 nm. In this study, the distribution of the pore throat radii is narrower, from 37nm to 1700nm.
- The probability distribution of Yang and Aplin's model is approximately a normal distribution. The probability peaks at the pore throat radii about 100nm.
- The two distributions have different degrees of skewness. The distribution of this study is more positively skewed (the tail on the right side is fatter than the left side), with predominantly small pores around 30nm to 100nm than larger pores. However, Yang and Aplin's distribution is closer to a normal distribution, with most abundant pore throats between 40-400nm.

The difference in pore throat distributions may be owing to a number of factors:

- Yang and Aplin used mercury injection porosimetry experiments to measure the pore throat radius, while in this study, the pore throat radii are derived from hydrocarbon column heights.

- The measured pore throat radii from Yang and Aplin's study are measured data from core samples, but the effective pore throat radii from this study is calculated at the reservoir-scale.
- In this study, there are no calculated pore throat radii smaller than 37nm, which could be owing to: a) the effective pore throat radii derived from this study will include fractures, if fractures are of greater dimensions than the matrix pore throats; b) the calculated pore throat radii from this study are based on the assumption that the buoyancy force equals to the capillary entry pressure. But the capillary entry pressure may be greater than the buoyancy pressure, so that the real, or measured pore throat radii will be smaller than the calculated value.

2.7 Conclusion

In this chapter, a new calculation model for effective pore throat radius has been established. The cumulative and probability distribution of the effective pore throat radii for caprocks of the UK North Sea have been obtained and compared with the distributions from Yang and Aplin (1998). The correlation between the controlling factors and the pore throat radii have been studied, and a prediction model has been established. The important conclusions for the chapter are as follows:

- A new model for the effective pore throat radius in caprocks of the UK North Sea has been established as a cumulative probability distribution that could be used for assessment of a CO_2 storage site if no sample of caprock is available.
- 31 oil fields with mudstone caprocks are included in pore throat radii calculation. Calculated effective pore throat radii range from 28nm to 601nm using conventional calculation, but 37nm to 1700nm using the Monte Carlo method which allows for uncertainty in input parameters. The most probability pore throat radii for the oil fields from the UK North Sea is 50nm (53% of possibility).
- For burial depths less than 3000m there is a linear correlation between the depth and the effective pore throat radii, while the burial depths greater than 3000m there is no correlation. It is interpreted that during shallow burial pore throat radii is influenced by clay diagenesis.

Compared to previous model for pore throat distribution by Yang and Aplin (1988), the range of the effective pore throat radius has been refined down, that the effective pore throat radii of the shale caprocks of the UK North Sea concentrated between 50-100nm. Hence, there is less uncertainty if the distribution is used to represent a seal for which no samples are available

Chapter 3: Introduction and background of the Crystal Geyser

This chapter is to provide an overview of the geologic framework on Green River region (especially the Crystal Geyser), and to review some previous studies related to CO_2-induced alterations. The geological structure of the region, the characteristics of the Little Grand Wash Fault -the major fault of the area, and the fault related mineralization have been reviewed in detail. Crystal Geyser as a natural CO_2 spring that used for the study of geological carbon storage, has been carefully introduced on the origin, the migration pattern, and the mechanisms to form carbonate travertines. The later part of the chapter reviewed the CO_2 induced reactions in different systems (section 3.8).

3.1 Geological structure of the Crystal Geyser region

Crystal Geyser locates on the cross section of the Green River and the Little Grand Wash fault, which is in the northern end of Paradox Basin (location map see Figure 3-1), contains a number of hydrocarbon fields and CO_2 fields. The Little Grand Wash fault is to the south of the travertines. The Paradox basin is an intracratonic basin infilled with thick evaporate, limestones, dolomite, organic shales, and clastic sequences from late Palaeozoic to Mesozoic. The shape of the basin is defined by the extent of evaporates in Pennsylvanian time (Dockrill and Shipton, 2010, Nuccio and Condon, 1996). The organic-rich shale is of great importance because of the petroleum-generation potential (Nuccio and Condon, 1996). During later tectonic events, the shape of the basin was modified by the uplift of Colorado Plateau and downcutting of the Colorado River and its tributaries. The basin is bordered by uncompahgre, San Juan dome, Monument uplift and San Rafael Swell. The north-east part of the basin is defined as Paradox fold and faults are consisted of northwest-trending faults, anticlines and synclines (Kelley, 1958, Nuccio and Condon, 1996). The age of the outcrops are quite diverse ranging from Pennsylvanian to early Cretaceous.

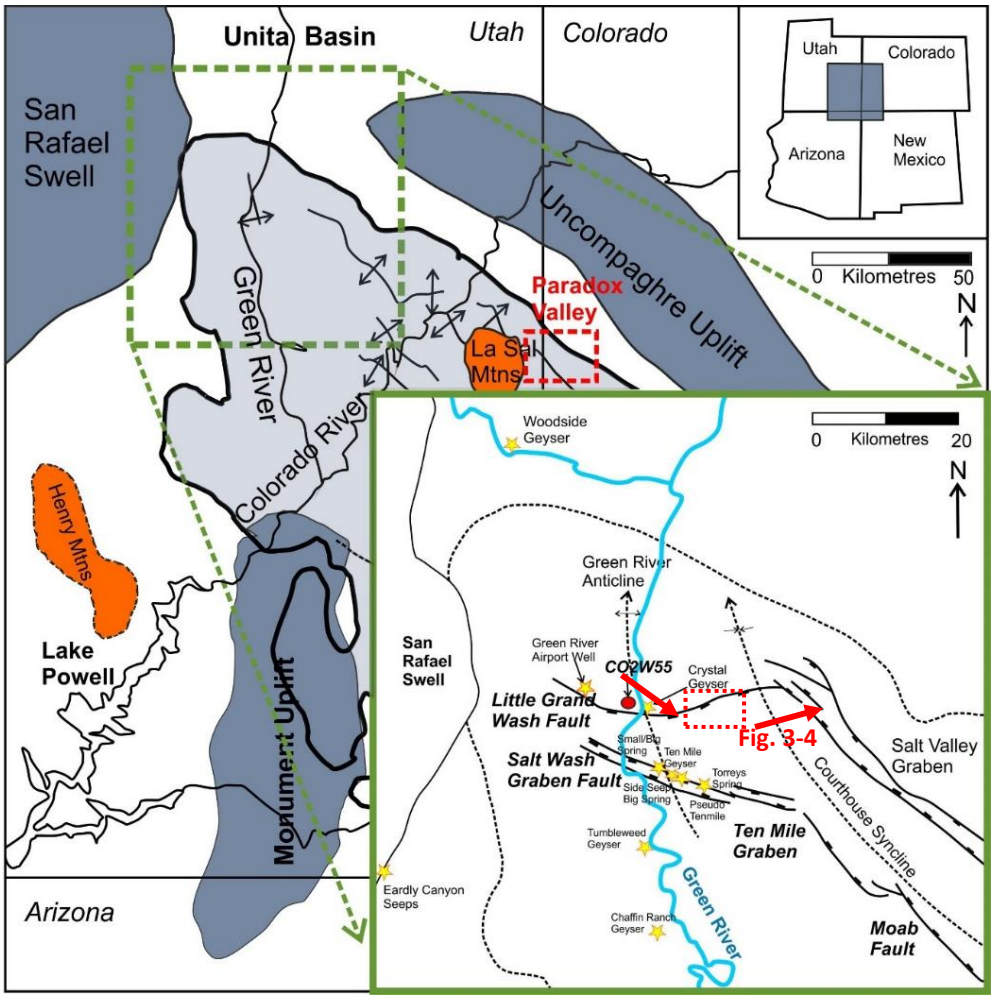

Figure 3- 1: Geological map of Paradox basin and the studied area (Nuccio and Condon, 1996, Kelley, 1958), showing the relationship between the CO2 springs and the Little Grand Wash fault and Salt Wash Graben fault (Dockrill, 2006). The green box shows the zoom out of the studied area. The bold red arrow marks the ground water flow trajectory (Kampman et al., 2009)

The main structural features of the studied area include the north-south trend of Green River anticline and Courthouse syncline plus east-west trend Little Grand Wash fault and Salt Wash Graben fault (Figure 3- 1). Green River anticline is an open north trend fold cut by the Little Grand Wash fault and Salt Wash Graben fault. The Little Grand Wash fault is south dipping and west-east trending, the outcrop of which encounters Upper Jurassic and Cretaceous deposit. The abandoned wells (Amerada Hess 1 and 2) intersect the fault in depth at Pennsylvanian age, indicating the downdip extent of the fault is at least as deep as Pennsylvanian age (Shipton et al., 2004).

The studied area is included in the maximum throw of the Little Grand Wash fault area. (T1, T2, T3 travertines are within 500m east of the Green River; T4, T5 and T6 travertines are about 1500m to the east of the Green River) (travertine locations see Figure 3-4).

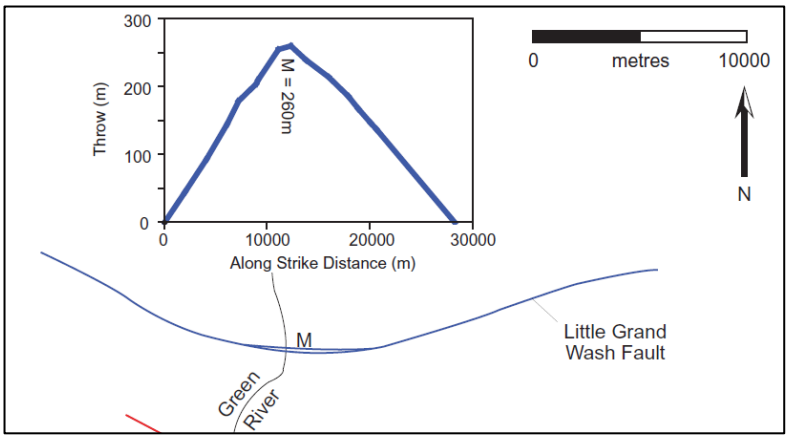

Figure 3- 2: Throw profile for the Little Grand Wash fault in relationship with the Green River (Dockrill, 2006).

3.2 Tectonic history

Paradox Basin is described as intraforeland flexural basin that developed along the southwestern flank of the basement-involved Uncompahgre uplift in Utah and Colorado during Pennsylvanian-Permian Ancestral Rocky Mountain (Barbeau, 2003). The deposition of thick evaporates is of great importance on the regional structure. Faults below the Paradox basin were reactivated from the mid-Pennsylvanian to late Triassic, that initiated the salt anticline movement to form a series of north-west trending salt anticlines and pillows (Doelling et al., 1988). During the end of Permian age, compression happened to initiate north-west trend salt anticline (Kelley, 1958). The subsequent younger formations deposited bilaterally to produce thin and tilting formations until the upper Jurassic, until which the salt flowage appears to have ceased (Kelley, 1958).

From Cretaceous to the early Tertiary, the Paradox basin had been influenced by Laramide orogeny. Faulting and folding had been reactivated that forming some principal tectonic elements of the region such as Uncompahgre plateau, San Rafeal Swell, Mounument upwarp that boardering the Paradox basin (Figure 3-1) (Kelley,

1958). The Colorado Plateau has experienced an uplift from the late Cenozoic until present (Hunt, 1956, Nuccio and Condon, 1996), accompanied by erosion that making salt anticlines close to the surface. The flow of ground waters through the fractures and joints caused the collapse of salt anticlines and infilled with Quaternary deposits (Doelling et al., 1988, Dockrill, 2006). Some faults also related to activities in Quaternary.

3.3 Stratigraphy of the Paradox basin

The Paradox Basin is basically Pennsylvanian aged evaporites covered by Triassic and Jurassic aged sediments (Nuccio and Condon, 1996). The youngest sequence is Lower Cretaceous Dakota Sandstone and dark, organic-rich Mancos shale formation (Nuccio and Condon, 1996, Shipton et al., 2004) (the stratigraphic column see Figure 3-3).

The organic black shale in the Paradox Formation is the important source rock for most of the hydrocarbons extracted from the region (Doelling et al., 1988, Chan et al., 2000). Permian is mostly composed of deposition of Cutler Group (Elephant Canyon Formation, Organ Rock Formation and White Rim Sandstone, Kaibab Limestone). Only small parts outcropped on San Rafeal Swell, but it is hydrocarbon bearing formation around the flanks of San Rafeal Swell (Irwin, 1971). Triassic age deposited Moenkopi and Chinle Formations in the Green River area. The sediments thickens along the Courthouse syncline and thins along the Green River anticline indicating the folding relates to salt movement was active at that time (Doelling et al., 1988). The lower Jurassic age is represented by Glen Canyon Group including Wingate Sandstone, Kayenta Formation and Navajo Formation. The deposition environment changed to aeolian dune and interdune well-sorted, fine-grained sandstones with cementation. The mid Jurassic contains by San Rafael Group, which is divided into Carmel Formation and Entrada Sandstone Formation. In the studied area, the Entrada is transferring from thin to massive cross-bedded and horizontal layers in wet-aeolian system (Dockrill, 2006). It is the major aquifer in the studied area with medium grained, moderately sorted quartzarenites and deformations. The late Jurassic age is composed of Curtis, Summerville and Morrison Formations. There is no significant variations in sediment thickness suggesting no salt migration. The outcrops is largely eroded, so that it is hard to

detect whether the fault is active during the period (Dockrill, 2006). Isolated sandstone channels and volcanic ash from nearby volcanism is found in the upper units of Brushy Basin Member(Turner and Fishman, 1991). Morrison Formation is also acted as aquifer. Formations of deposited at Cretaceous age outcropped at south part of the Little Grand Wash fault. Most of them have been heavily eroded away. The remaining could be divided into Cedar Mountain Formation, Dakoda Sandstone Formation and Mancos shale. Cedar Mountain Formation consists of the lower Buckhorn Conglomerate and upper shale member. Buckhorn Conglomerate is conglomeratic sandstones deposited in a fluvial environment (Dockrill, 2006). The upper shale member deposited in similar environment as Brushy Basin Member of the Morrison Formation, with mudstone, siltstone and thin bedded limestone(Trimble and Doelling, 1978). Dakota Formation is very thin conglomerates with thin sandstone lenses, deposited as coastal plain unit deposited in front of the advancing Mancos Sea (Molenaar, 1981). The Mancos shale is thick marine deposit composed of mudstones and siltstones with subordinate sandstone. Mancos shale in the studied region is divided into three members: the Tununk Shale Member, Ferroan Sandstone Member and Upper Mancos Shale Member. The Ferroan Sandstone is a thin, fine-grained, thin bedded marine sandstone interbedded with grey shale, and the upper Mancos Shale, which is the subject of this study, is thick black grey shale with some fine-grained sandstone and lenses of limestone (Dockrill, 2006). The Mancos shale was deposited as part of the extensive Western Interior Cretaceous seaway (Nuccio and Condon, 1996). The detailed introduction on Mancos shale will be presented in chapter 5.

The series of travertine mounds deposited by CO_2-charge cut Mancos shale and a north plunging anticline, associating with salt movement in the Paradox Formation at depth (Shipton et al., 2004). Salt anticline loading was initiated by the Pennsylvanian or Permain clastic shed off. The reactivation of the salt anticline and faults occurred during Laramide contraction in Tertiary (Chan et al., 2000).

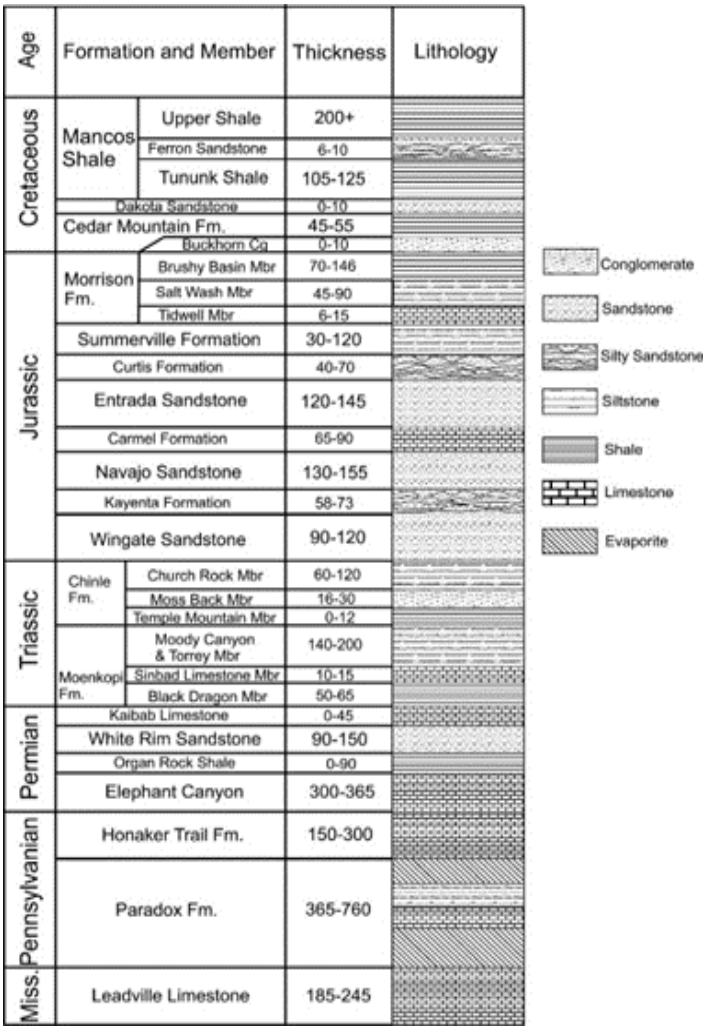

Figure 3- 3: Stratigraphic column of the studied area. Redrawn from (Kampman et al., 2014).

3.4 Little Grand Wash fault

Little Grand Wash fault is about 30km long with two main strands in the central part, and between which exist many minor faults of varing dipping. The dip of the main strands are averaged at around 70° to the south direction. The fault throw decreases systematically from the centre to the side tails. It has two strands encountering at abandoned wells (Amerada Hess 1, Amerada Hess 2) located at the south of the fault (Shipton et al., 2004). The fault zone contains 70cm to 3m of foliated clay gouge (Shipton et al., 2004), and complicated minor faults and relays are common in the studied area (Shipton et al., 2004, Dockrill and Shipton, 2010).

Smaller faults contains foliated purple-black, clay-rich fault gouge and occasional thin calcite veins with sub-horizontal fibres (Shipton et al., 2005). A number of travertines deposits (active and fossil) are located at the footwall of the Little Grand Wash fault, that immediate north of the fault zone (Figure 3- 4).

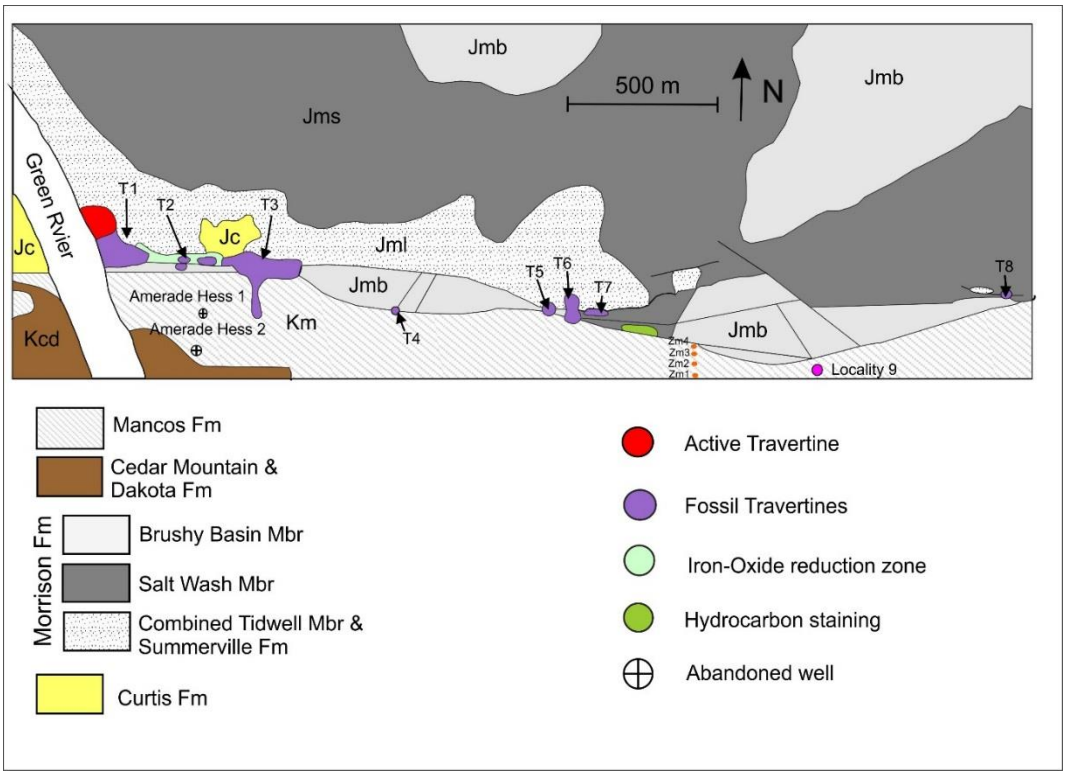

Figure 3- 4: Redrawn map of the Little Grand Wash fault showing the locations of travertines, gas and oil seeps, and abandoned wells (figure compiled from Shipton et al., 2004 and PhD thesis of Dockrill, 2006). The labelled travertine number is used in this study for chapter 4 and chapter 5.

Fault zones can either play a role of channel or seal for fluid flow. They are normally composed of fault core and damaged zone (Caine et al., 1996). Fault core, which is typically around 1-3m wide, normally contains principal elements of clay-rich gouge, slip zones, and entrained sections of host rock (see Figure 3-5) (Caine et al., 1996, Dockrill and Shipton, 2010). The gouge is composed of the mixture of quartz and clay minerals, with some halite, calcite, feldspar and hematite. The clay content increases from wall rocks to fault gouge because of fault-induced diagenesis. In the Little Grand Wash fault, the clay content increases from 65%-75% in wall rocks to 90%-99% in gouge (Dockrill and Shipton, 2010, Dockrill, 2006). The slip zones are

highly polished striated surfaces, separating gouges and entrained sections from the host rock. The universal existence of argillaceous-rich gouge in the Little Grand Wash fault (LGWF) suggests the fault could be seal. In addition, the Mancos shale of the hanging wall is also supposed to prevent the migration of fluids, because the fossil travertines concentrate on one side of the fault, suggesting the fluid cannot migrate across the fault (Shipton et al., 2004, Heath et al., 2009, Burnside et al., 2013).

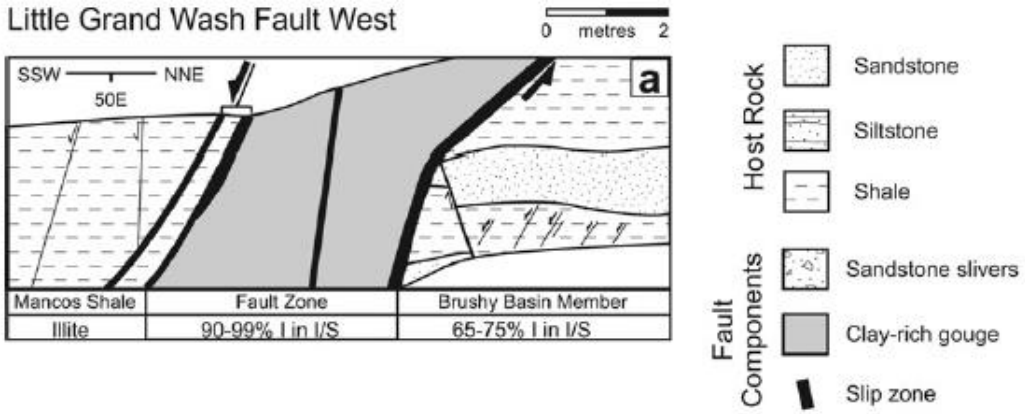

Figure 3- 5: Structural cross-section of the fault core (see location in Figure 3-1 (Dockrill and Shipton, 2010).

Damaged zone is a series of subsidiary structures that include small faults, fractures, cleavages, veins and folds, that bound the fault core that may enhance the relative permeability (Caine et al., 1996). In the studied area, fractures are normally filled with carbonates or sulphates (Dockrill, 2006). Fault associated fluid flow is recognized in the footwalls of the LGWF through the presence of travertines as well as diagenetic alteration of Jurassic sandstones (iron-oxide reduction, sporadic hydrocarbon staining and carbonate and sulphate veining). By studying the characteristics of the fault damage zones, previous studies assumed that the fractures in the damage zones of footwalls are responsible for the CO_2 leakage from subsurface (Dockrill, 2006).

Illite age investigation indicates the age of fault movement and graben development initiated at 40Ma ±10 corresponding to the early Tertiary tectonism (van der Pluijm et al., 2001, Shipton et al., 2004). Some small faults may associated with activities in Quaternary (Shipton et al., 2004, Dockrill and Shipton, 2010).

3.5 Natural CO_2 springs and hydrocarbon seeps

Multiple natural CO_2 springs and hydrocarbon seeps occur in Green River area. Oil exploration drills has encountered CO_2 gas and CO_2-charged brine in the Navajo Sandstones and Jurassic Wingate Sandstone; supercritical CO_2 and CO_2-charged brine in the Permian White Rim Sandstone and Pennsylvanian carbonate and evaporates (Airport Well Grand fault, Glen Ruby #1, Green Town Federal 36-11) (Kampman et al., 2014).

CO_2-rich fluid deposited travertines along the footwall of Little Grand Wash fault and Salt Wash fault. The travertines could be divided into active travertines which are still in growth under the influence of active spring, and ancient travertines which are elevated and not influenced by the springs any more.

Crystal Geyser is an active cool CO_2 spring, which locates at the intersection of Little Grand Wash fault and the apex of Green River anticline. The present-day Crystal Geyser began erupting when the Glen Ruby # well was drilled in 1935. The abandoned exploration well was drilled to the base of Triassic (TD = 801m) (Shipton et al., 2004). But the presence of fossil travertine suggested eruptions must start much longer time ago. The driller records documents reported that old travertines had been there before the drilling. U-Th dating demonstrated the leakage of CO_2 in Crystal Geyser started at least 400 ka ago (Burnside, 2010). Kampman et al. advocated that the CO_2 leakage is controlled by fracture opening which is potentially caused by the changes of hydraulic behaviour and overpressure condition. Each CO_2 pulse (CO_2 leakage) is followed by climate warming, and the interval between each pulse is around 20ka to 30ka (Kampman et al., 2012).

The eruption pattern of the Crystal Geyser has been recorded though time. Papers reported the eruption is up to 25m at 4-12 hours intervals (Shipton et al., 2004, Mayo et al., 1991, Wilkinson et al., 2009a). At present, the eruption height is much lower and the interval is longer than before. Bimodel pattern of eruptions was recorded in the eruption history. Four types of eruption have been observed (Figure 3-7, Figure 3-8): large eruptions (longer duration) were classified as type B and type D with larger pressure, temperature reduction and column height. Small eruptions were classified as type A and C eruptions in between of the large eruptions (Kampman et al., 2014, Baer and Rigby, 1978, Murray, 1989, Gouveia and Friedmann, 2006, Han et al., 2013). Both of the large and small eruptions cause the

drop in pressure and temperature at the mouth of the geyser and the extent of the drop is related to the magnitude of the eruption (Han et al., 2013). The maximum column height observed in 2010 is around 10m above the surface, which has been largely reduced comparing to the historic record in before 1990s (~20 to 40m from the surface) (Murray, 1989, Baer and Rigby, 1978). After the major eruption of type B and type D, the pressure (at the mouth) drops dramatically for about 0.045MPa and the temperature drops for 0.6 °C, while after the type A and C eruption, the pressure drops for 0.018MPa and the temperature drops for 0.4 °C (Han et al., 2013).

(a) (b)

Figure 3- 6: Pictures of Crystal Geyser eruptions from the abandoned well (a): type A and type C eruption. (b): type B and type D eruption (Han et al., 2013).

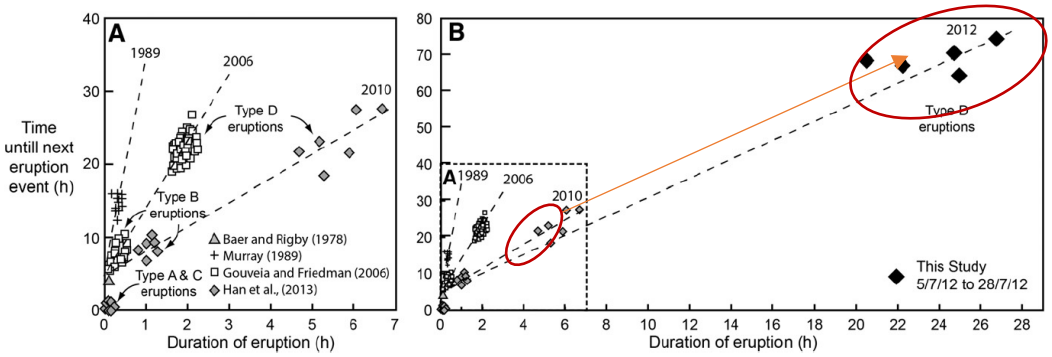

Figure 3- 7: (a) Compilation of eruption interval and duration data of Crystal Geyser after Baer and Rigby (1978), Murray (1989), Gouveia and Friedman (2006) and Han et al., (2013); b) eruption data from well CO2W55.

The eruption pattern changed significantly with time. Comparing the fluid eruption regulation of the year 1989, 2006, 2010 and 2012, it is discovered that the duration of eruption of the same eruption type is quite different, especially after the scientific well CO2W55 was drilled in 2012. Significant variations were observed in both eruption interval (~17-30h in 2006 and 2010; ~55-75h in 2012) and duration (~2h in 2006, ~5-7h in 2010 and ~20-27h in 2012) for type D eruption, which performed with

much longer duration and much lower frequency after the drilling of hoe CO2W55 in 2012, indicating that it took much more time for fluid charge for longer eruption duration. The magnitude of the fluid is reported to be reduced.

The conceptual model from Han et al. suggests there might be a “chamber” at shallow depth for fluid charge to enable periodic eruption (Han et al., 2013). It assumed that when the Glen Ruby #1 well drilled in 1936, the wellhead encountered pre-existing chamber that accidentally connected the chamber with the surface. During the following 80 years, the eruption characteristics at Crystal Geyser changed greatly. Type B eruption during drilling comprises short duration and large magnitude comparing with the historical record, and only type B eruptions were observed during drilling (Figure 3-8(b)).

Table 3- 1: Interval and duration of different types of eruption recorded from 1976 to 2013 (Martinez, 1976, Murray, 1989, Glennon and Pfaff, 2005, Han et al., 2013)

Interval/duration	Type A (overflow)	Type C (overflow)	Type B	Type D
Martinez (1976)	60min/5min	60min/5min	na	na
Murray (1989)	15min/10min	15min/10min	na	na
Glennon & Pfaff (2005);	30min/5-10min	30min/5-10min	8h/20min	20h/2h
Han et al., (2013)	10min-60min /10min	10min-60min /10min	10h/1h	20-30h/5-7h
note	Data in Han et al. is from the year 2010			

There is no conclusive explanation for the reason of the change. The possible reason for taking longer time for refill and eruption could be the seismic activities may have changed the tectonic stress and pressure system subsurface, thus changing the eruption pattern. Record shows the multiple seismic events of magnitude greater than 2.0 during between the year 1936 until now. It is possible that the seismic activities enhanced the volume of chamber, which requires longer interval to refill and longer time for eruption. The reason for the reduced magnitude could be the generation of cementation by the fluids. The mineral-rich fluids would react with the rocks, resulting in cementations that continuously blocking the flow

pathways. The eruption pattern is depended on the permeability contrast between the geyser chamber and surrounding rock. Significant change of the eruption characteristics happened after the drilling of well CO_2W55, which might indicate the change of the subsurface chamber and flow pathways.

3.6 Fault related mineralization and diagenesis

3.6.1 Gypsum and Celestine precipitation in LGWF

Extensive Gypsum fillings were found in the fractures of the host rocks of travertines that associated with the Little Grand Wash Fault. The precipitation of gypsum ($CaSO_4.2H_2O$) and celestine ($SrSO_4$) vein in the Mancos shale and Entrada Sandstones might due to the dissolution and migration of gypsum beds within the Carmel Formation (Dockrill, 2006, Dockrill and Shipton, 2010). The meteoric water dissolved the gypsum and transported it to the overlying formation. The source of Sr is probably from the dissolved evaporates of Pennsylvanian Paradox and Honaker Trial Formations (Dockrill, 2006). The Precipitation of Celestine might from Pennsylavian-derivd, Sr^{2+}-rich fluids, mixed with shallower SO_4^{2-}-rich meteoric waters or surface water. Based on the elemental analysis of current water samples, it is undersaturated in terms of sulphur (Heath et al., 2004), therefore the deposition of gypsum must be from paleo-water, which should be saturated in terms of sulphur. The timing of the precipitation of sulphate would be, if hydrocarbons were responsible for iron-oxide reduction, sulphate precipitation commenced during or after the early Tertiary and ceased before start of the present-day meteoric conditions (Dockrill, 2006, Dockrill and Shipton, 2010).

3.6.2 The formation of reduction zones in Crystal Geyser

The fault fluid could induce the bleach the formations (Chan et al., 2000). The potential reduction fluid capable of reducing Fe^{3+} to Fe^{2+} include: hydrocarbons, organic acids, methane and hydrogen sulphide (H_2S) (Chan et al., 2000, Garden et al., 2001). Previous studies believed the bleach of the footwall sandstones should

be related to hydrocarbons (Chan et al., 2000, Garden et al., 2001). The source of the hydrocarbons is the organic-rich black shales from the Pennsylvanian Paradox Formation (Carboniferous). The timing of hydrocarbon migration is around the early Tertiary along the Moab Fault to the east. The hydrocarbons migrated along the Moab Fault and linked to Paradox Formation source (Garden et al., 2001).

However, scarcely found hydrocarbon stains in northern footwall of Salt Wash Fault indicates there might be other reasons for reduction fluid. Some others suggested that CO_2 might be involved in the reduction (Haszeldine et al., 2005, Kampman et al., 2014). The Hematite content in sandstones have been reduced while in contact with CO_2-riched brines (Kampman et al., 2014). Comparing with the unbleached sandstones, the bleached part is enriched with dolomite and clay while depleted in hematite, calcite and feldspar. It is possible that the CO_2-rich brine interacted with hydrocarbons and reduced hematite to pyrite and gypsum. The involving reactions could be (Kampman et al., 2014):

$$4Fe_2O_3 + 15CO_2 + 6H_2O + CH_4 \rightarrow 8Fe^{2+} + 16HCO_3^- \quad \text{Equation 3-1}$$

$$Fe_2O_3 + 4CO_2 + H_2O + 2HS^- \rightarrow Fe^{2+} + 4HCO_3^- + FeS_2 \quad \text{Equation 3-2}$$

Dockrill (2006) compared the reduction zone and non-reduction zone of the host rocks isotopically. The reducing fluid did not introduce carbonates based on isotopic studies. The aragonite veins and travertines carbonates show isotopic similarities while a separate reducing fluid deposits the reduction zones in fractures.

3.7 The origin and the migration pathways of CO_2

The gases emitted from Green River springs are comprised of predominantly CO_2, nitrogen and trace noble gases (Heath et al., 2009). Several processes might contribute to the production of CO_2 (Selley, 1998):

- Mantle degassing
- Metamorphism or decarbonation of carbonates
- Oxidation or bacterial degradation of organic matters
- Maturation of hydrocarbons

Heath et al. suggested crustle originated by Helium analysis (Heath et al., 2004, Shipton et al., 2004). The most possible source for the CO_2 is high temperature

decomposition of Mississippian Leadville Limestone or the decomposition of kerogen within the Leadville Limestone or Paradox Formation under the temprature of 100 to 200 °C. (Cappa and Rice, 1995, Baumgartner and Valley, 2001). Mayo et al. also suggested that thermal decomposition of carbonate minerals might be one of the origin of CO_2 for Crystal Geyser based on the results of stable isotope analysis (Mayo et al., 1991).

However, Wilkinson et al. believed that an alternate source for CO_2 in the Green River region should be taken into account, the mantle degassed CO_2 from the nearby igneous intrusions mixed with crustal originated CO_2 (Wilkinson et al., 2009a). The mixing proportion between the crustal source and the mantle source is 1-20% to 16-99% based on noble gas analysis (Wilkinson et al., 2009a).

Assayag et al. and Wilkinson et al., collected CO_2 gas sample from Crystal Geyser spring. Assayag et al. (2008) measured the $\delta^{13}C$ of CO_2 is about -7.0‰ V-PDB, and Wilkinson et al. reported -7.00 ‰ V-PDB for main Crystal Geyser and -6.68 ‰ V-PDB for side Crystal Geyser springs. Kampam et al. sampled seven different CO_2 samples from the Green River regional springs, and the $\delta^{13}C$ of the CO_2 displays a similar range of -7.09~ -6.28‰ V-PDB (Kampman et al., 2014).

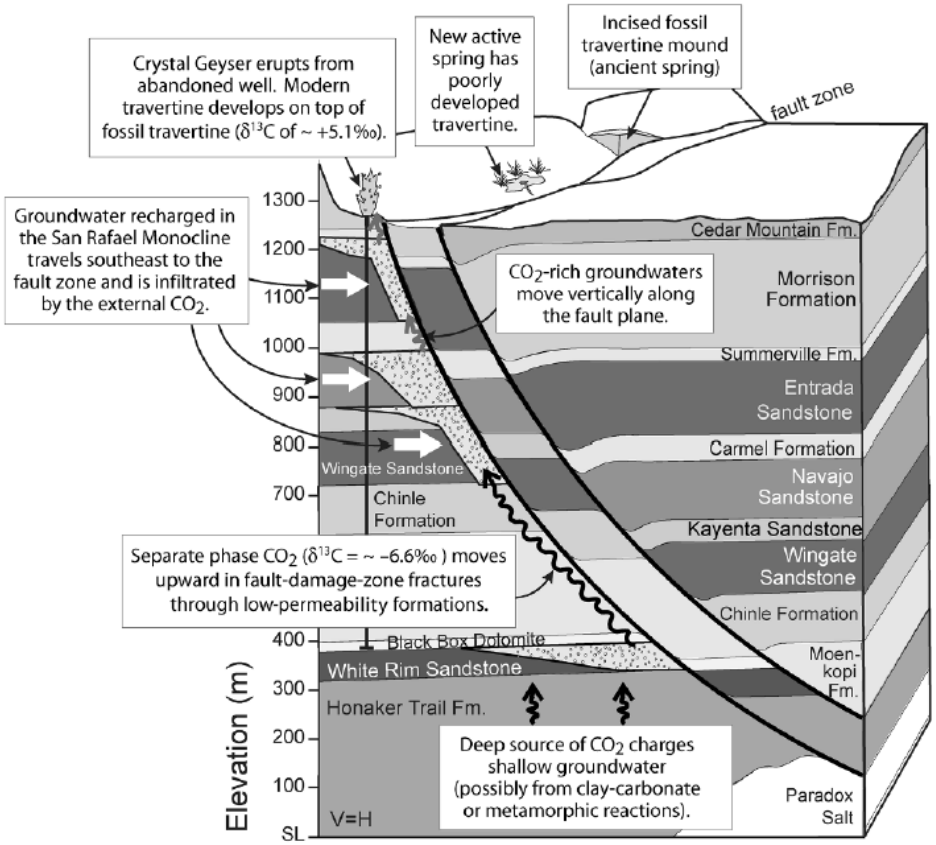

Figure 3- 8: Schematic cross-section across the Little Grand Wash and Salt Wash faults showing the fluid migration pattern (Heath et al., 2009)

Heath et al. and Shipton et al. assumed the anistrophy character of the fault make the free-phase CO_2 upwards instead (Heath et al., 2004, Shipton et al., 2004) (migration pattern see Figure 3-9). Even though the mineralization occurs during CO_2 migrating to the surface, self-sealling has not happened. Fractures that derived by faulting allow the infill of the CO_2 rather than self-sealing (Heath et al., 2004). By measuring the CO_2 diffusion, the volume of eruption, and CO_2 dissolution in the aquifers, the CO_2 flux is twice the amount of maximum solubility of CO_2 in the Navajo aquifer, therefore Heath et al. believed that there should be some free-phase CO_2 exist when ascending from the Navajo aquifer (Heath et al., 2004). However, Wilkinson et al. suggested the solution should be undersaturated with CO_2 where it is deeper than Navajo Fm (Wilkinson et al., 2009a), and this result is in consistent with the study from stable isotope (Assayag et al., 2009) and the fluid sampling from the scientific well CO2W55 (Kampman et al., 2014).

Dockrill (2006) calculated the volume of leaked CO_2 to the surface with the model from Shipton et al. (Shipton et al., 2005), who estimated that about 10% of the CO_2 leaked to the surface is precipitated as travertine and the rest of which is released to the atmosphere. Ignoring the erosion of surface travertine, there is about 1.9Mt travertine deposit (Dockrill, 2006). Burnside et al. suggested much lower deposition rate for the travertine mound of only 1% for the fossil travertines, and the calculated amount of CO_2 leakage is 13.6Mt from the fault-focused leakage point (Burnside, 2010).

3.8 The formation of travertine

The existence of springs and travertines, deposition of veins and diagenetic alteration of adjacent host rocks are the proof of the faults acting as conduits for fluid migration (Curewitz and Karson, 1997, Hancock et al., 1999, Micklethwaite and Cox, 2004, Chan et al., 2000, Garden et al., 2001, Klein et al., 1999). The stress concentration cause active fracturing and re-opening of fluid conduits but also clogging of fractures due to mineral precipitation (Curewitz and Karson, 1997).

In the studied area, the fossil travertines with age of over 5000 yrs are not related to the recent drilling of Ruby well #1 (Dockrill, 2006, Burnside, 2010, Dockrill and Shipton, 2010). The deposited travertines are very thick, well developed, elevated and widely distributed alongside the faults (marked with purple in Figure 3-5), suggesting the change of the migration pathways of the fluid that deposited the travertines. The active travertines are still growing, and probably formed by the drilling of Ruby well in 1935.

In General, travertine deposits are preferentially located along faults and structurally complex zones (Pentecost, 2005a, Hancock et al., 1999). Travertine is formed from the CO_2 degassing of the Calcium-rich ground water (Pentecost, 2005a, Clark and Fritz, 1997):

$$2HCO_3^-(aq) + Ca^{2+}(aq) \rightarrow CaCO_3(s) + CO_2(g) + H_2O(l) \qquad \text{Equation 3-3}$$

The fossil travertines are topographically higher than the active travertines. The footwall sequence is from the sand-rich Curtis Formation to clay-rich Morrison Formation. The outcrops of the travertines have been seriously eroded. The

mineralogy of samples from ancient travertine and transects of reduction zones are analysed by Dockrill (2006). The lithofacies of the outcrops have been classified as 4 different types, including: (1) conglomerate (2) layered mats (3) white-banded veins, and (4) brown banded veins. In the fossil travertine, the white-banded veins are composed of aragonite, and the brown-banded veins contain a mixture of aragonite and goethite (Dockrill, 2006).

Radiometric ages of fossil travertine deposits along with faults have been analysed. The fossil travertines which are elevated about 30m above the active travertines were found predated than the drilling. Baer and Rigby suggested an age of 200,000 years for the highest level inactive travertines using U-Th dating The erosion rate is 0.0005m/yr, and the maximum travertine age is around 780,000 years along the LGWF. The radiometric age of the youngest travertine is around 6072±209 ya (Dockrill, 2006). The oldest fossil travertines alongside the Little Grand Wash fault was measured as around 100,000 years in the study of Burnside et al., (2013). The study of the illite of Moab fault suggested the fault was active during 60-50Ma, which is in consistent with salt movement and dissolution (Pevear et al., 1997, Chan et al., 2000).

3.9 CO_2 storage related reactions in different systems

The CO_2-rich fluid related reactions have been reviewed in this section.

3.9.1 Reactions in sandstone-shale system

- Dissolution vs. precipitation

Three steps of geochemical reactions happen during the CO_2 trapping (Hitchon et al., 1999). The first reaction is the CO_2 dissolve in water to alter pH and held in water as bicarbonate. Carbonic acid or bicarbonate ion and the proton will be produced to make the brine acid:

$$H_2O + CO_2 \leftrightarrow H_2CO_3 \leftrightarrow HCO_3^- + H^+ \qquad \text{Equation 3-4}$$

Experimental studies show the acid condition drives the dissolution of carbonate minerals in a short timescale comparing to silicate minerals (Chou et al., 1989, Bacci et al., 2011). The reactions involving calcite dissolution could happen during the first a few days performed under experimental conditions, but the dissolution of other

minerals could be six to nine orders of magnitude slower than carbonates (Rochelle et al., 2002, Espinoza et al., 2011).

CO_2 dissolves into water involves a series of reactions, plus the formation of bicarbonates and the increase of pH. The reaction rate for calcite and CO_2 acified water is 1.6 ~ $3.2*10^{-5}$ mol.m^{-2}s^{-1}, for Anorthite is $1.2*10^{-5}$ mol.m^{-2}s^{-1}, for Oligioclase is $1.2*10^{-8}$ mol.m^{-2}s^{-1}, for Albite is $3.6*10^{-9}$ mol.m^{-2}s^{-1}, and for Kaolinite is 10^{-14} to 10^{-15} mol.m^{-2}s^{-1}. The reaction rate is Calcite ≈ Anorthite >> Oligeioclase > Albite >> Kaolinite (Espinoza et al., 2011). The reaction rate of carbonates is faster than alumninosilicates and the dissolution rate is fast, but the overall amount of reaction is small. The reaction rate of minerals in CO_2-riched water depends on temperature, pressure (CO_2 solubility), and the concentration of other species. The quick dissolution should result in increase of porosity and permeability, but some of the real cases show controversial results: a very few cases show increase in injectivity after CO_2 injection (Cailly et al., 2005). The reason for the decrease of the injectivity could be the re-precipitation of the carbonates induced by pressure drops and temperature change from the borehole to the reservoir condition owing to the Joule-Thomson cooling effect (Oldenburg, 2007).

- Reaction with feldspars and clays

CO_2 dissolves in water forms in acid condition and attack on the silicate minerals, thus resulting in free ions of elements such as Ca^{2+}, Mg^{2+}, Fe^{2+} and neutralizing the pH shift.

$$H_2O + anorthite + H^+ \rightarrow Ca^{2+} + kaolinite \qquad \text{Equation 3-5}$$

One of the fastest geochemical reactions is the precipitation of calcium carbonate occurs when free Ca^{2+} and bicarbonate ion.

$$Ca^{2+} + HCO_3^- = CaCO_3 + H^+ \qquad \text{Equation 3-6}$$

The overall result is just the sum of these three reactions:

$$Anorthite + 2H_2O + CO_2 = Kaolinite + Calcite \qquad \text{Equation 3-7}$$

In sandstone system, the major function of CO_2 for the silicate minerals in sandstone-shale system is to neutralize the acid produced by the CO_2 dissolution. The most likely produced clay minerals is kaolinite. Non-carboante minerals that

contain divalent cations include Fe, Ca and Mg-bearing clay minerals (such as chlorite, saponite and other smectite minerals), and some zeolite minerals could also provide cations for CO_2 sequester (Baines and Worden, 2004, Zhang and DePaolo, 2017).

More complicated reactions could happen when CO_2 trapped as carbonates and clay minerals permanently in dolomite dominated system Hitchon et al. (1999), such as:

$$Feldspars + Clays + CO_2 \rightarrow Kaolinite + Calcite + Dolomite + Siderite + Quartz$$ Equation 3-8

Another type of possible reactions to sequester CO_2 from aqueous phase is (Gunter et al., 1997):

$$Albite + H_2O + CO_2 \rightarrow HCO_3^- + Na^+ + Na - smectite + Quartz$$ Equation 3-9

$$Annite + CO_2 \rightarrow HCO_3^- + K^+ + Muscovite + Quartz + H_2O$$ Equation 3-10

- Formation of dawsonite and ankerite

Another major minerals caused by CO_2 storage are dawsonite and ankerite ($Ca(Fe,Mg,Mn)(CO_3)_2$ in sandstone-shale system (Xu et al., 2005) (Eq. 3-11 and 3-12). The composition is closely related to dolomite, but having Mg replaced with Mn and Fe). The Fe^{2+} supply for siderite ($FeCO_3$) and ankerite deposition could be sourced from chlorite and hematic dissolution and reduction. Dawsonite is carbonate minerals that distinctly forms in high level of CO_2 concentration, and could be regarded as the implications for CO_2 sequestration (Bénézeth et al., 2007, Wopfner and Höcker, 1987).

$$Chlorite\ (NaClO_2) + Hematite\ (Fe_2O_3) + CO_2 \xrightarrow{Fe2+} Ankerite(Ca(Fe,Mg,Mn)(CO_3)_2), Siderite\ (FeCO_3)$$

Equation 3-11

$$Oligoclase\ (Ca,Na)(Al,Si)_4O_8 + CO_2 \xrightarrow{Na+} Dawsonite\ (NaAlCO_3(OH)_2$$

Equation 3-12

The deep North Sea reservoir (Utsira sand from Sleipner) has been simulated for CO_2 interaction with reservoir rocks, and the predicted precipitation are Dawsonite and Magnesite ($MgCO_3$) (Johnson et al., 2001, Haszeldine et al., 2005). This prediction is based on modelling of engineering CO_2 storage, and the situation is in accordance with natural analogues for CO_2 storage.

The timescale for mineral trapping based on modelling is much shorter than the real cases. Hitchon et al. (1999) modelled the kinetic water-rock reaction for Glauconitic Sandstone aquifer of Alberta Basin. The results show that the timescale for the deposition of kaolinite is 80 yrs; for biotite is 100yrs; for albite is 540 yrs; for K-feldspar is 820 yrs. The model shows there will be complete equilibrium in 820 yrs. Gunter et al. (1996) predicted the substantial trapping of CO_2 could form siderite, calcite and bicarbonate within 6 to 40 years under the reservoir condition of 105 °C and 90 bars of pressure. However, the natural analogues show quite different results: only small amount of CO_2 has been sequestered during a much longer time-scale. Wilkinson et al. used the natural CO_2 field - Fizzy as natural analogue, and the study shows less than 25% of the CO_2 has been sequestered as mineralogy after 50 Myr, and 0.7± 2% volume of dolomite cement is associated with CO_2 charge.

3.9.2 Reactions in carbonate reservoir systems

Baines and Worden studied the CO_2 accumulation in Blue Whale and Dolphin. The paragenetic sequence has been generalized in the following figure (Figure 3-10) (Baines and Worden, 2004):

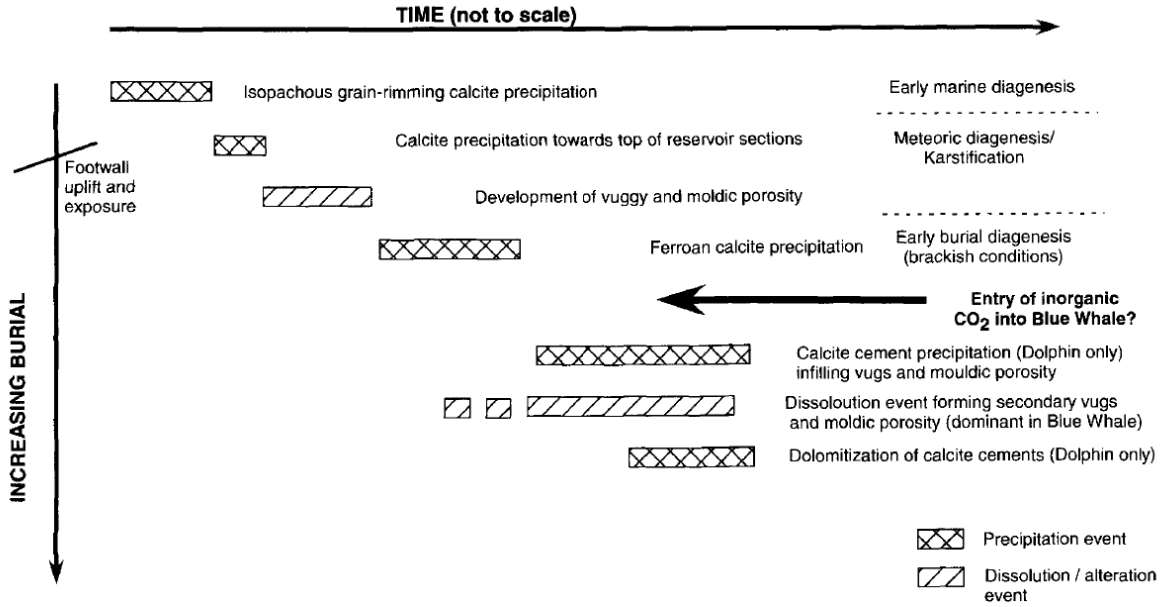

Figure 3- 9: The paragenetic sequence and diagenetic events in Blue Whale and Dolphin field (Baines and Worden, 2004).

Extensive late dissolution caused by CO_2 charge could be found in the carbonate reservoirs and the overall mudstone caprock. The large-scale CO_2 addition in limestones and dolostones results in mineral dissolution rather than precipitation, unless there is an independent supply of divalent cations from exotic sources (Baines and Worden, 2004).

However, Bacci et al. used TOUGH2 to simulate the injectivity of near wellbore and far field for a limestone field, the results show the injectivity reduced due to the decrease of the permeability occurring meters away from the wellbore. The flooding core experiments suggest the permeability and porosity increased at the inlet of the core. The carbonate deposition caused decrease in porosity for when it flows further away from the wellbore. Therefore, it is entirely possible that the injection of the CO_2 could induce the reduction the permeability in carbonate reservoir system (Bacci et al., 2011)

3.9.3 How CO_2 changes the mudstones

The CO_2-rock interaction in natural CO_2 seep Miller and Brae has been simulated, and the result shows mudrocks interacting with CO_2 shows more calcite, kaolin and

less feldspar comparing to the mudrocks distant from the CO_2 (Haszeldine et al., 2005). Lu et al. studied how the CO_2 alternated the mudrock seal of Miller field. He used isotopic ratios to demonstrate that free phase CO_2 could migrate upwards into the caprock formation and penetrate the seal thus inducing the dissolution and precipitation of the carbonates. In shales, much more framboidal pyrite in shales than in sandstones because of the high content of organic matters in mudrocks (Lu et al., 2009).

Organic matter in mudrocks has an important role in CO_2-rock reaction. Studies show that high organic content generates organic acids and increase acidity in the ambient is an important factor encouraging dissolution by affecting the dissolution rate, the saturation state, and the speciation of some elements (Carothers and Kharaka, 1978) . Taguchi et al. also suggested that solubility of quartz and other silicates might be enhanced through complexing with organic compounds which are released during the transformation of organic materials (Taguchi et al., 1988). The silica is likely to be transported to other strata rather than re-precipitate locally, therefore there could be much more quartz dissolution than quartz overgrowth in mudrock formations. Astin and Evans (1990) predicted of 10-20% of the solid volume loss during diagenesis, primarily through quartz dissolution and silica export. The large amount of precipitation of pyrite framboids should closely related to organic matters (Berner, 1984). The detailed information about the mudstones and the CO_2-related reactions will be introduced in chapter 5.

Chapter 4: Has the water erupted from the Crystal Geyser changed through time?

Erupted water from the Crystal Geyser has been studied and analysed. However, the present erupted spring may not be the same as the fluid that deposited the carbonates and travertines. If it could be demonstrated that the present water and paleo-water are of similar composition, then the present Crystal Geyser water could be applied to natural analogue instead for further fluid-rock reaction. In this chapter, veins from Crystal Geyser ambient travertines, have been studied as a record of the geochemistry and flow history of the paleo-water. Element distribution coefficients have been used to convert the geochemistry of veins to that of paleo-fluid. The result has been compared with those of present erupted water, which helps to unravelling the precipitation or dissolution events associated processes and circulation events related with the local tectonic events. The distribution patterns of veins and reduction zones have been analysed to illustrate the circulation model of the paleo-water.

4.1 Previous work on the subsurface waters in the Crystal Geyser area

4.1.1 Geochemistry and the mixing of the present water of Crystal Geyser

The pore water erupted from Crystal Geyser is mostly derived from the underlying Navajo aquifer (Wilkinson et al., 2009a, Kampman et al., 2012, Kampman et al., 2014). Spangler et al. investigated on the geochemistry of the reservoir fluid extracted from the Greater Aneth Oil Field in San Juan County, Utah, about 150km to the south-east of Green River (see the geological map in Figure 4-1). Brine samples from the Greater Aneth Oil Field collected from the reservoirs are used as end member in the study of the CO_2-charge springs in previous study (Wilkinson et al., 2009a). The Ismay brine contains the heaviest oxygen isotope ratio of all the Aneth brines and is likely to be the least contaminated by meteoric fluid in the area (Wilkinson et al., 2009a). The $\delta^{18}O$ of the brine water from the Paradox Valley (location see map Figure 4-1) range from 5.6 to -7.6 ‰ SMOW (Spangler, 1992).

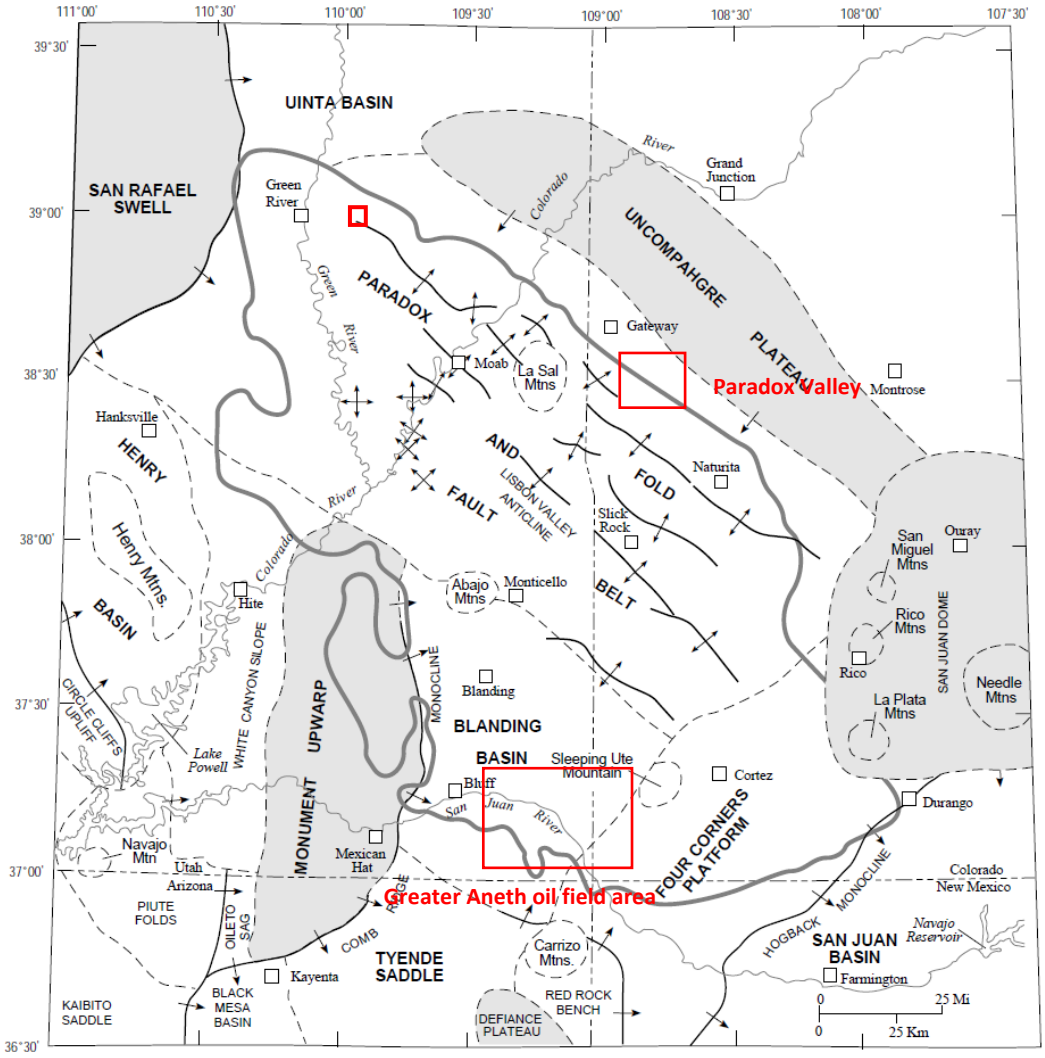

Figure 4- 1: Map of Greater Aneth oil field (red squared area) and the location of San Juan River and Paradox Valley brine Utah (Spangler, 1992).

The present spring water samples from Crystal Geyser have been collected for the analysis of pH, temperature, cations and anions (Table 4-1) (Shipton et al., 2004). The ratio of Cl^-/Na^+ is about 0.5-0.8, indicating that not all of the Na^+ is from the dissolution of halite. There must be other source of sodium, such as Na-bearing montmorillonite. The Crystal Geyser water is a mixture of re-dissolved marine evaporites and meteoric water. Shipton et al. assumed that paleo-fluid that deposited the veins observed in and below the eroded travertines might have had a similar composition to the present-day fluid, based on the analysis of the saturation state of the paleo-fluid.

Table 4- 1: Chemical data from field and laboratory on sample from Crystal Geyser (CG), Torrey's spring (T), and from the spring near Tenmile Geyser (SW).

				Cations (mmol/l)						
Sample number	Temp (°C)	pH	TDS (mg/l)	Ca	Mg	Na	K	Fe	Mn	Sr
CG92.1	16.0	6.96	13920	2.37	8.72	174.52	7.62	0.00	0.00	0.01
CG92.2	16.0	6.7	13685	9.71	8.80	171.74	7.67	0.00	0.02	0.05
CG92.3	16.0	6.46	13555	10.78	9.30	167.82	7.65	0.00	0.02	0.05
T1/T2	19.4	6.37	21188	20.83	7.86	218.63	10.44	0.14	0.02	0.14
SW1/SW2	23.0	6.26	20020	20.76	8.27	236.38	9.39	0.08	0.00	0.16

	Anions(mmol/l)				
Sample number	HCO_3	CO_3	Cl	SO_4	% Balance error
CG92.1	61.00	0.00	91.15	24.33	0.9
CG92.2	50.00	0.00	95.43	24.64	5.3
CG92.3	46.40	0.00	98.23	25.07	5.1
T1/T2	75.70	0.00	204.52	29.47	−8.3
SW1/SW2	58.90	0.00	186.38	30.81	−0.4

A scientific vertical well CO2W55 was drilled in 2012 to collect the fluid samples from the subsurface formations close to Crystal Geyser. The drilling penetrated a series of formations that containing CO_2-rich brine to a depth of about 322m (Kampman et al., 2014), that enables the study of the geochemical composition of the CO_2-charge formations of Entrada, Carmel (fault zone) and Navajo (surface and down-hole) formations. Fluid samples were collected from the spring eruption for every 30min from 12:00pm until 5:30pm on a single day. The composition of the fluid is listed in Table 4-2.

Table 4- 2: Geochemistry of the fluids from the samples of the well CO2W55 by formations of Entrada, Carmel and Navajo (Kampman et al., 2014)

Code	Formation	Depth	Temp	pH		DIC	Alkalinity	Al^{3+}	B^{+}	Ba^{2+}	Ca^{2+}	Fe^{2+}	K^{+}	Li^{+}	Mg^{2+}	Mn^{2+}	Na^{+}	Rb^{+}	SiO_2	Sr^{2+}	Zn^{2+}	Cl^{-}	SO_4^{2-}	F	Br
		m	°C	(surface)	(in situ)	mmol/l	mEq/L	µmol/l	µmol/l	µmol/l	mmol/l	µmol/l	mmol/l	µmol/l	mmol/l	µmol/l	mmol/l	µmol/l	µmol/l	µmol/l	µmol/l	mmol/l	mmol/l	µmol/l	µmol/l
ENTRADA	Entrada	98	13.6	6.3			45.00	0.3	67.8	0.4	27.6	348.9	3.3	44.8	10.7	42.3	47.6	4.8	105.8	186.3	0.4	26.8	17.9	#N/A	6.7
UDP001	Carmel	188	15.5	6.2			56.68	7.6	88.1	0.6	24.1	126.8	4.8	60.3	9.5	88.5	48.3	6.8	170.6	110.1	23.1	32.5	16.1	86.1	9.3
DSF001	Navajo	206	15.9		5.30	561	50.62	1.6	99.5	0.2	25.3	27.0	5.2	69.8	10.5	103.8	52.6	7.6	288.3	119.7	7.7	33.6	16.6	6.8	8.8
DFS002	Navajo	224	16.3		5.21	692	59.24	1.3	130.3	0.3	23.4	23.8	6.0	107.2	10.1	75.6	72.4	9.3	70.0	123.9	2.4	50.0	18.6	7.5	13.1
DFS003	Navajo	276	17.4		5.15	882	62.14	1.3	159.9	0.4	23.4	15.3	6.6	146.7	10.0	68.9	92.6	11.2	60.2	128.5	2.5	69.4	19.6	8.4	20.6
DFS004	Navajo	322	18.3		5.13	991	63.74	1.2	191.2	0.3	24.1	36.6	7.2	199.4	10.1	63.6	112.5	14.4	59.2	135.1	2.3	84.9	20.7	7.4	23.5
UDP002	Navajo	203	15.8	6.43			38.43	1.4	104.7	0.4	23.2	63.2	5.3	69.7	10.0	79.4	52.5	8.7	80.4	119.9	2.1	36.6	17.0	35.2	10.3
UDP003*	Navajo	206	15.9	6.42			80.24	1.2	130.0	0.6	22.6	1335.0	5.4	79.4	10.0	177.1	57.1	8.5	86.8	120.6	9.5	44.0	18.8	18.3	12.8
UDP004	Navajo	206	15.9	6.43			36.66	5.6	109.4	0.3	22.1	12.5	5.5	80.7	10.1	67.6	59.9	7.9	132.1	111.9	0.4	41.7	17.4	10.9	11.5
UDP005	Navajo	206	15.9	6.22			46.58	4.8	107.9	0.4	22.9	25.3	5.3	78.9	10.0	73.8	55.9	8.9	80.2	120.0	0.4	40.6	17.5	#N/A	12.1
UDP006	Navajo	206	15.9	6.43			51.50	0.9	99.0	0.5	20.4	117.5	5.4	71.9	9.1	70.8	52.5	9.0	62.3	114.8	2.2	39.0	16.4	5.5	11.3
UDP007	Navajo	224	16.3	6.52			59.82	0.9	120.9	0.3	23.3	33.9	5.7	94.9	10.1	81.8	67.1	9.2	78.7	117.1	0.6	48.2	18.2	5.6	13.7
UDP008	Navajo	224	16.3	6.58			58.92	1.7	139.3	0.3	24.0	26.9	6.2	116.7	10.4	74.9	76.9	10.2	64.4	128.3	0.5	59.4	19.0	5.5	15.7
UDP009	Navajo	286	17.6	6.23			52.17	1.0	151.4	0.4	23.4	19.9	6.5	135.2	10.1	73.0	88.9	9.2	83.5	116.7	0.2	66.3	19.8	#N/A	18.6
UDP010	Navajo	292	17.7	6.11			47.91	0.9	157.1	0.3	21.0	14.3	6.6	149.1	9.5	71.2	106.6	10.0	105.2	106.2	0.3	72.5	20.0	6.4	20.4
UDP011	Navajo	298	17.8	6.15			51.60	1.0	158.9	0.4	19.3	13.4	6.4	147.9	9.0	64.1	109.7	8.7	109.3	99.4	0.1	75.5	20.4	5.6	21.5
UDP012	Navajo	298	17.8	6.27			52.92	0.9	170.3	0.4	24.1	20.4	7.1	166.4	10.2	82.6	103.7	11.4	78.2	121.8	0.3	73.4	20.2	5.3	21.3
UDP013	Navajo	316	18.2	6.24			59.18	0.8	146.2	0.3	20.7	35.8	6.1	132.6	9.1	66.8	90.6	10.2	67.1	110.4	0.2	72.6	20.2	4.0	21.2
UDP014	Navajo	322	18.3	6.51			62.50	0.6	157.4	0.3	21.2	20.5	6.3	148.2	9.1	65.5	94.9	10.5	58.4	117.3	0.2	80.1	20.1	5.5	22.5

The spring fluid is demonstrated to be a physical mixture of CO_2-saturated Carboniferous water (called the Paradox brine after the deeply-buried Paradox Formation), CO_2-undersaturated meteoric water recharge (Kampman et al., 2014). Wilkinson et al. used hydrogen and oxygen stable isotope to study the mixture of present pore water in Crystal Geyser and the nearby Green River springs (Figure 4-2) (Wilkinson et al., 2009a), and came to the conclusion that the present spring water is composed of 10-20% of Ismay brine and 80-90% of local meteoric water from the Navajo aquifer (Wilkinson et al., 2009a).

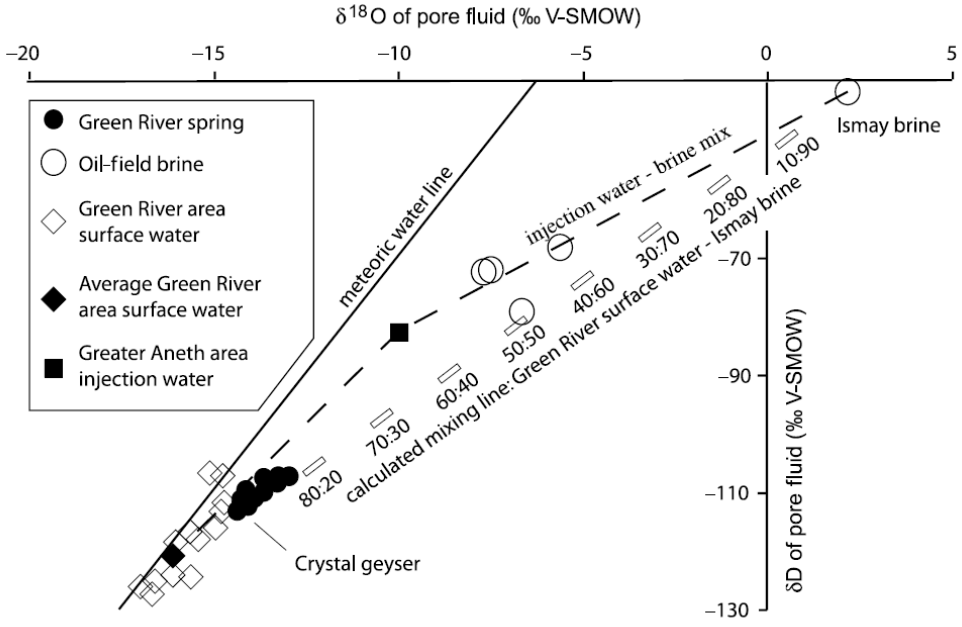

Figure 4- 2: Stable oxygen and hydrogen isotope ratio crossplot for pore water mixture model for the Paradix basin (Wilkinson et al., 2009a).

Kampman used conservative tracers (Cl and Br) to trace the brine mixing for different CO_2 springs in the Green River area. Paradox brine and the Airport well (no significant input of paradox brine) are used as end members (Rosenbauer et al., 1992, Kampman et al., 2014). The result shows that the Torreys Spring is the most saline spring in the region, containing 5.14% of Paradox brine. The rest of the springs are composed of brine water ranging from 3.0 to 5.1 %. Crystal Geyser is only contians around 3.0 % of Paraodox brine (Kampman et al., 2014).

4.1.2 Fluid circulation and carbonate veins growth

In the studied area, faults (Little Grand Wash fault and Salt Wash fault) and the associated geysers, springs, seeps and travertines record the fault-related leakage and fluid circulation both temporally and spatially, and provide evidence for the history of the behaviour of faults. Faults can be either conduits and impermeable barriers to fluid circulation. The sealing nature of faults is related to mechanical and chemical processes, and the nature is variable in time and space (Eichhubl et al., 2000, Hancock et al., 1999, Solum et al., 2010, Renard et al., 2009).

Kampman et al. demonstrated there has been fluid leakage in the Green River region for more than 400kpa by U-Th dating on veins inside the footwall of the fault beneath the ancient travertines (Kampman et al., 2012). They compared the travertine growth rate and the change of the stable isotopic values ($\delta^{18}O$ and $\delta^{13}C$) of aragonite veins (Fig. 4-3). The results suggest four major decreases in the isotopic ratios over the past 140kyr. The decrease of the fluid $\delta^{13}C$ suggests the addition of fresh unfractionated CO_2 into the groundwater system. Each pulse of CO_2 release happens around 100-2,000 yrs after local climatic warming, thus resulting in the opening of fractures, changes of underground hydrology and the unloading of the CO_2 free-gas cap (Kampman et al., 2012).

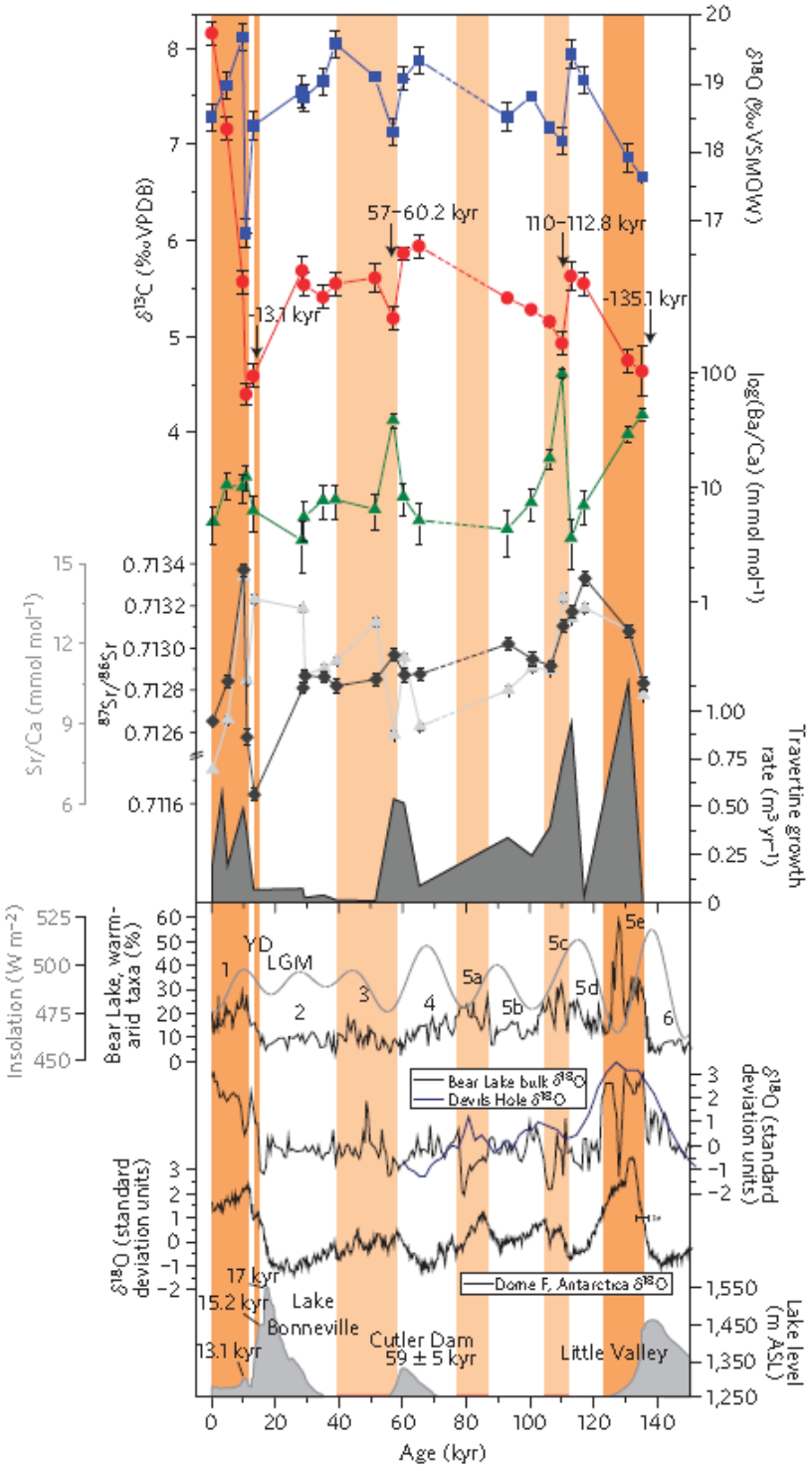

Figure 4- 3: Isotope and trace-element ratios of U-Th dated aragonite veins and travertine growth rate (Kampman et al., 2012).

Gratier et at. investigated on the mode of carbonate growth within the travertine mounds (Gratier et al., 2012). U-Th dating showed that a horizontal vein at shallow depth grew from the top downwards. Therefore, Gratier et al. (2012) advocated that the growth of the horizontal vein is driven by the force of crystallization, which has been demonstrated experimentally that enables to uplift significant weight and induce fracturing (Taber, 1916, Noiriel et al., 2010).

Dockrill established a schematic model for the regional flow migration and the formation of travertines and veins (Figure 4-4) (Dockrill, 2006). The lithology of the geyser related rocks is summarized as: conglomerates, layered carbonate mats, white-banded veins and brown-banded veins. The CO_2-rich fluid migrates upward vertically through the fault damage zone and erupts as a spring. The conglomerates are normally located between the host rock and layered mats. They were formed by cementation of colluvium and are effectively impermeable. Then the layered mat of carbonate precipitates deposited on top of the conglomerate layer to form the travertine. Vertical and horizontal white banded veins forms on the migration paths (damage zone and within the travertines). Brown banded veins were formed in the latest stage and crosscut the white banded veins (Dockrill, 2006).

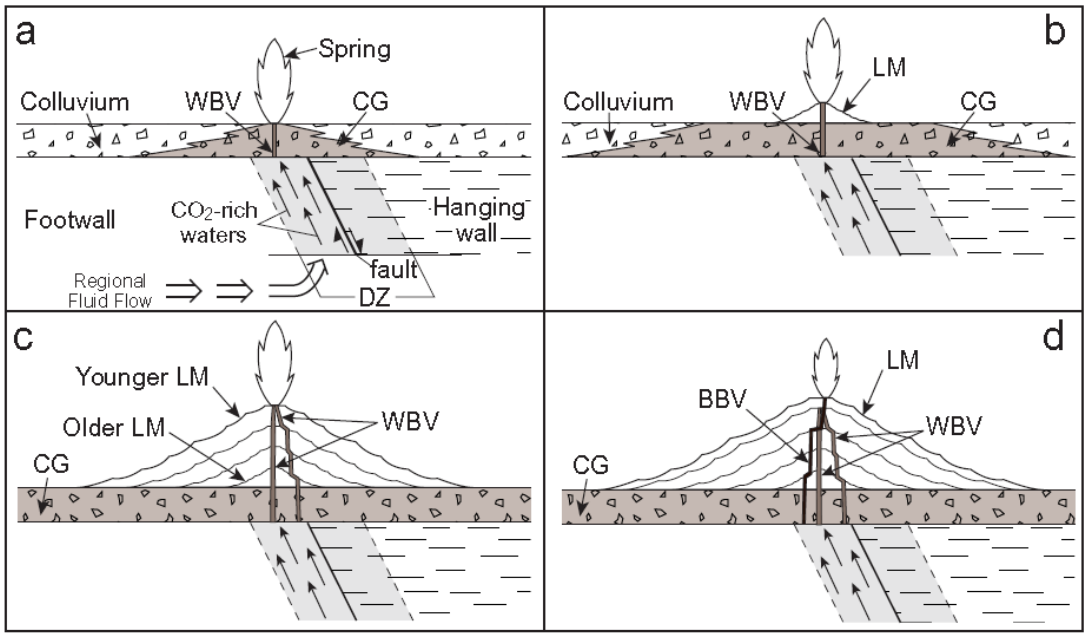

Figure 4- 4: Schematic diagram for travertine formation and fluid transportation (Dockrill, 2006). CG: Crystal Geyser; BBV: brown banded veins; LM: layered mats; WBV: white banded veins.

4.1.3 The formation of calcite and aragonite: determination factors for mineralogy and morphology

Veins precipitated by the reaction between CO_2-rich fluid and rocks are mostly calcite or aragonite, which have the same chemical formula, but different crystal structure. Aragonite has an othorhombic structure while calcite has a rhombohedral structure (Tucker and Wright, 1990). The large cell of orthorhombic aragonite preferentially incorporates cations larger than calcium ion (that is Sr, Na, Ba, and U), but calcite favours substitution of smaller ions such as Mg, Fe, Mn, Zn, Cu, Cd (Veizer, 1983). The crystal structure of aragonite and calcite are shown in Figure 4-5 (Pentecost, 2005b).

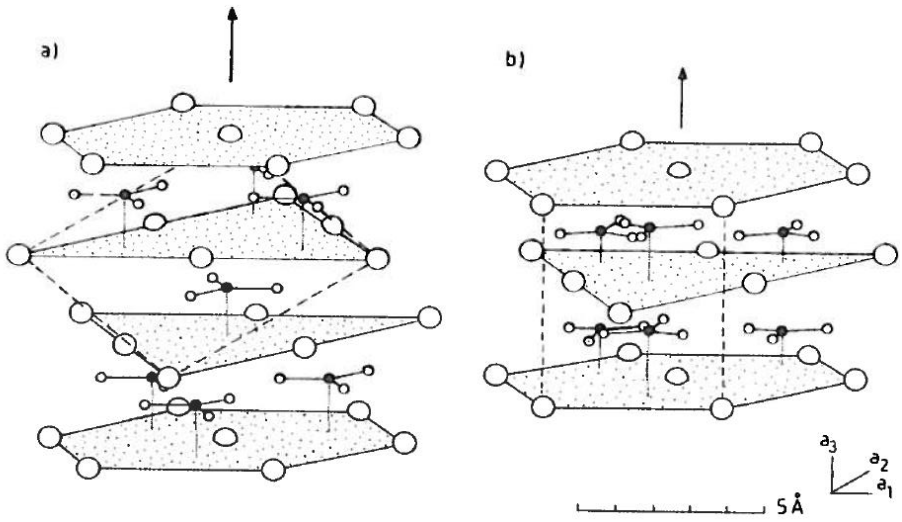

Figure 4- 5: The structure of calcite and aragonite. (a) Calcite; (b) Aragonite (Pentecost, 2005b)

Aragonite is less stable than calcite at room temperature, but it is more frequently be found in hot springs or porewater with high Mg: Ca ratio and high bicarbonate ions (Pentecost, 2005b). Figure 4-6 presents the how the travertine mineralogy associated with deposition temperature and Mg concentration level. When the concentration of Mg of porewater is over 10 mmol/L or the ratio of Mg/Ca is higher than 0.8, aragonite deposition occurs more often. At low Mg concentration, when the temperature is over 40 ºC, it is more likely to precipitate aragonite than calcite.

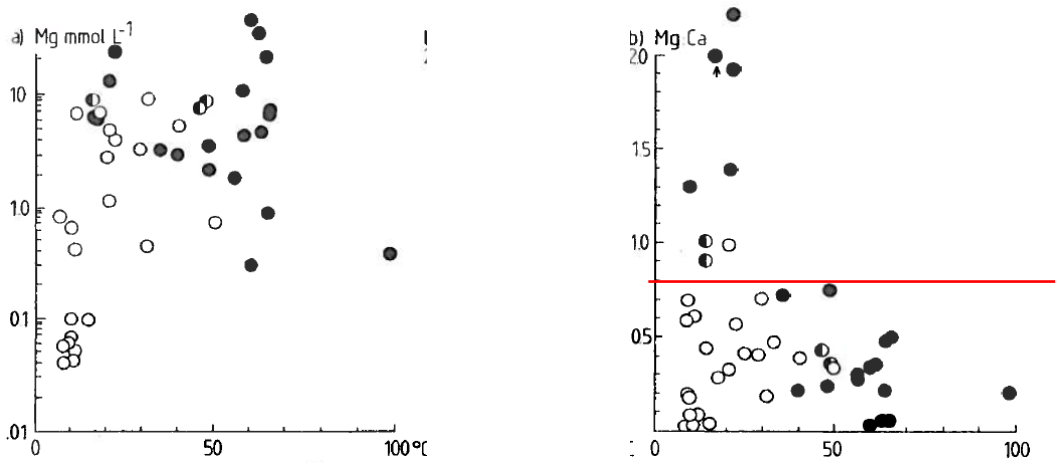

(a) (b)

Figure 4- 6: Abundance of (a) calcite and aragonite in travertine in relation to the deposition temperature and the concentration of Mg in solution, and (b) calcite and aragonite in relation to the deposition temperature and the ratio of the concentration of Mg: Ca (molality ratio). The solid dots indicate aragonite deposit; the hollow dots indicate calcite deposit (Amundson and Kelly, 1987, Duchi et al., 1978, Folk, 1994, Kitano, 1963, Malesani and Vannucci, 1975, Rastall, 1926, Risacher and Eugster, 1979, Scholl and Taft, 1964) (compiled by Pentecost, 2006).

Another important factor that might influence would be the supply of reactants. The growth of carbonate crystals should be controlled by the availability of Ca^{2+} ions and CO_3^{2-}. In natural fluid where the pH of fluid is usually between 6 to 8, most of carbonate ions exist as state of bicarbonate, which is much less than the Ca^{2+} ions. As would suggest the growth rate of the crystals is controlled by the availability of CO_3^{2-} ions (Doremus, 1958, Lahann, 1978). The growth rate of the crystals determines the morphology and minerology of the carbonates: the higher growth rate is predominantly related to aragonite and acicular shaped crystals; while the lower growth rate relate to calcite and equant shaped crystals. In CO_2 degassing condition (for example, in vadose pores), it is likely to deposit aragonite where bicarbonate ions are ionized to affluent carbonate ions (Eq. 4-1) for carbonates deposition (Given and Wilkinson, 1985).

$$2HCO_3^- \rightarrow CO_2 + CO_3^{2-} + H_2O \qquad \text{Equation 4-1}$$

In summary, aragonite tends to occur when the supply rates are high, while calcite tends to deposit when the rates are low (Given and Wilkinson, 1984).

In general, three physical factors are important for determining whether calcium carbonate forms as calcite or aragonite:

- Temperature; aragonite is more common at higher temperatures (>40 ºC; Fig. 4-6) (Pentecost, 2005b).
- The Mg: Ca ratio of the porewaters; aragonite favours to deposit from the fluid with high Mg: Ca ratio (Fig. 4-6).
- The rate of supply of CO_3^{2-} ions; aragonite tends to deposit from fluid with high supply of CO_3^{2-} (Given and Wilkinson, 1985).

4.1.4 Aragonite and calcite in the Crystal Geyser travertines

Precipitated veins in Crystal Geyser were classified as several different types in previous studies (Frery et al., 2015, Dockrill, 2006):

a. Thin veins: isolated millimetre-thick carbonate veins and 3D denser network of veins have been found. This type of veins is normally deposited at the base of the travertine on both sides of the faults and the 3D network veins increase the density at the centre of hanging wall of fault zones (Figure 4-7). Thin veins can be either calcite or aragonite (Dockrill, 2006), though calcite is much more commonly found at the base of the travertines and close to the fault plane of the hanging wall.

b. Thick veins: normally vertical carbonate veins within the fault planes and some horizontal veins in the upper part of the foot wall which outcrop at the surface. The higher the position, the thicker the veins. This type of carbonate veins is mostly aragonite (Dockrill, 2006) (Figure 4-8 (a) and (b)).

c. Veins filling fractures with reduction halos: gypsum, aragonite, quartz and minor calcite infill the fractures (Figure 4-9) (Dockrill, 2006).

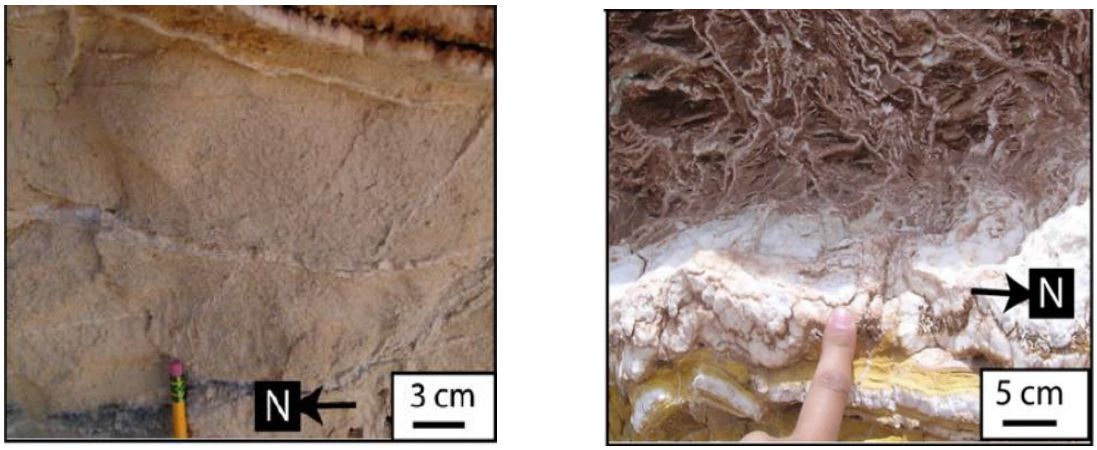

(a) (b)

Figure 4- 7: Example of thin veins in the fossil travertines of Crystal Geyser: a) millimetre-thick carbonate veins in Entrada Sandstones in Salt Wash-Ten Mile Graben; b) 3D denser boxwork structure of carbonate veins in Crystal Geyer travertine (Frery et al., 2015).

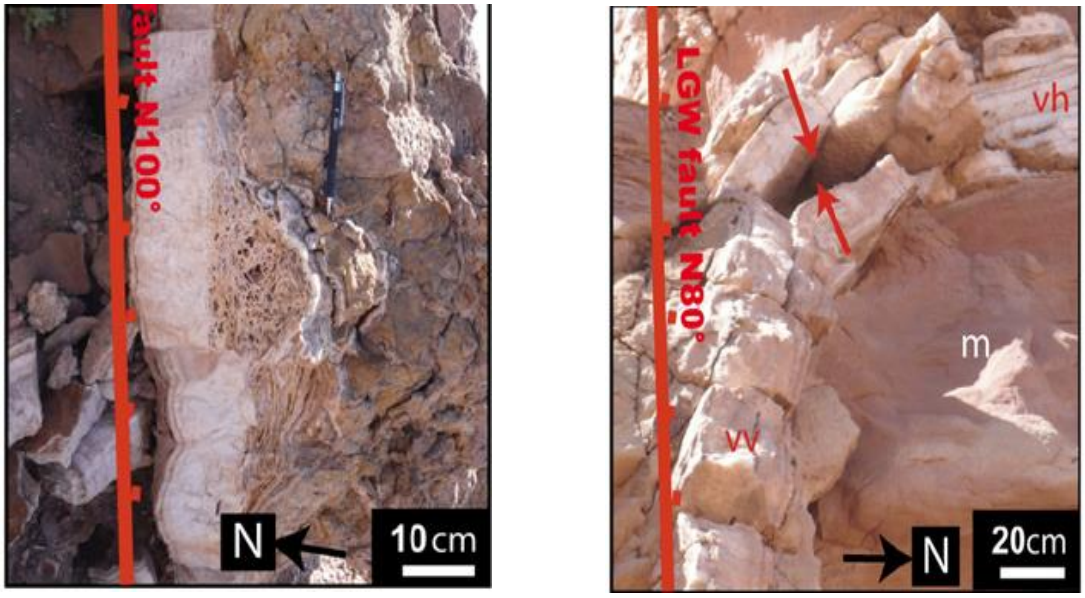

(a) (b)

Figure 4- 8: Thick carbonate veins in the travertines of the Crystal Geyser: a) thick horizontal veins located in the fault zones, next to a boxwork structure cross-cut thin

veins; b) thick calcite veins growing gradually vertically to horizontally. The red arrow marks the growth direction of the vein.

(c)

Figure 4- 9: Detrital veins filling the fractures of the reduction haloes (Dockrill, 2006).

4.1.5 Trace elements partition in solution and solids

During crystal growth, element substitution within the crystal and partition between the crystal and the solution occurs. From a thermodynamic viewpoint, if the crystal is in equilibrium with the solution, each element will partition between solid and liquid to make its chemical potential equal in each phase (McIntire, 1963). In an open system (where the concentration of a trace element is small compared to the host constituent), then:

$$(\frac{Tr}{Ca})_s = k(\frac{Tr}{Ca})_l \qquad \text{Equation 4-2}$$

Where the all the elements in molar concentration; Tr is the concentration of the trace element; Ca is concentration of the host constituent; s and l are solid and liquid, respectively and k is the partition coefficient (Tucker and Wright, 1990). If the

coefficient is greater than unity, it means the solid will be enriched in the trace element; if k is less than unity, it means the solid will be impoverished with trace element.

Partition coefficients of trace elements in calcium carbonate are influenced primarily by two factors: temperature and the precipitation rate of crystals. Comparatively, precipitation rate is the more important factor (Veizer, 1983). The relationship of precipitation rate and distribution coefficient has been well studied for calcite. However, there is limited published research about this relationship in aragonite.

There are three major mechanisms of substitution in carbonate crystals: a. substitute for Ca^{2+}; b. ions in interstitial positions at lattice defect sites; c. adsorption due to remnant ionic charges or as non-carbonate inclusions (Veizer, 1983). The third way is an unpredictable mechanism of incorporation. Here we focus on the first two ways of incorporation.

- Sr incorporation

Alkaline earth metals, including strotium, barium and radium, with similar properties as calcium, are likely to be incorporated in aragonite crystals by substitution for Ca^{2+}. The distribution coefficient of Sr in aragonite is normally in small range of 0.9-1.2, and the highest value from the literature is 1.6 (Kitano et al., 1968, Kitano et al., 1973, Holland et al., 1964). Generally, there is not much Sr substitution in calcite, so that when aragonite alters to calcite, the ratio of Sr/Ca decreases. Small amount of manganese substitution will increase the concentration of Sr (Ichikuni, 1973). Strontium is always divalent and has no redox potential. Any incorporated strontium inherits its isotopic composition from the parent solution without any fractionation (Veizer, 1983).

- Magnesium

Aragonite precipitates in moderately Mg-rich environment. In a general sense, the Mg/Ca ratio of ambient fluid influences the minerology and morphology of carbonate crystals. The concentration of Mg in solution is usually very low in cold springs. The relationship of Mg concentration, temperature and crystal polymorph is shown in the figure 4-6 (Pentecost, 2005). The Mg substitute for Ca in aragonite crystals is temperature dependant.

- Alkali Metals

For calcite, alkali metals can substitute for Ca, but are more likely to occupy interstitial positions in the crystal lattice, with a frequence of occurrence: Li > Na> K > Rb (Pentecost, 2005b). Hence the concentration of alkali metals indicates the crystal growth rate. In aragonite, alkali metals are more likely to substitute for calcium. Two alkali metal ions substitute for one Ca ion to maintain charge balance (Busenberg and Niel Plummer, 1985). The presence of Na decreases Li, K, and Rb incorporation into aragonites.

- Transition metals (Iron, Mangnese, Cobalt, Zinc, Copper)

The incorporation of Fe and Mn as altervalent elements is complicated. In open waters and meteoric waters, Fe^{2+} and Mn^{2+} could substitute Ca^{2+}, but they are very likely to be oxidized into higher valence (Fe^{3+}, Mn^{3+}, Mn^{4+}), which have greater radii making them difficult to substitute into calcite (maybe easier to go into aragonite) (Veizer, 1983). For aragonite, the distribution coefficient is dependent of temperature (30-60 °C), Mn concentration and ionic strength (Busenberg and Niel Plummer, 1985)

- Anions (sulphate ion)

Substitution of the larger SO_4^{2+} ion for the smaller CO_3^{2+} ion in the calcite structure increases proportionately with the crystal growth rate (Busenberg and Niel Plummer, 1985). The relationship of SO_4^{2+} with the crystal growth rate of aragonite is unknown.

In general, during the precipitation of aragonite, some elements will incorporate into the crystal lattice to substitute Ca ion during co-precipitation, for example: alkaline earth elements (Sr, Ba, Ra), alkali metal elements (Li, Na, K, Rb), transition metals (Mn, Fe, Co, Zn, Cu). Some elements are adsorbed onto the carbonate crystal and go into the defect sites, for example: Mg.

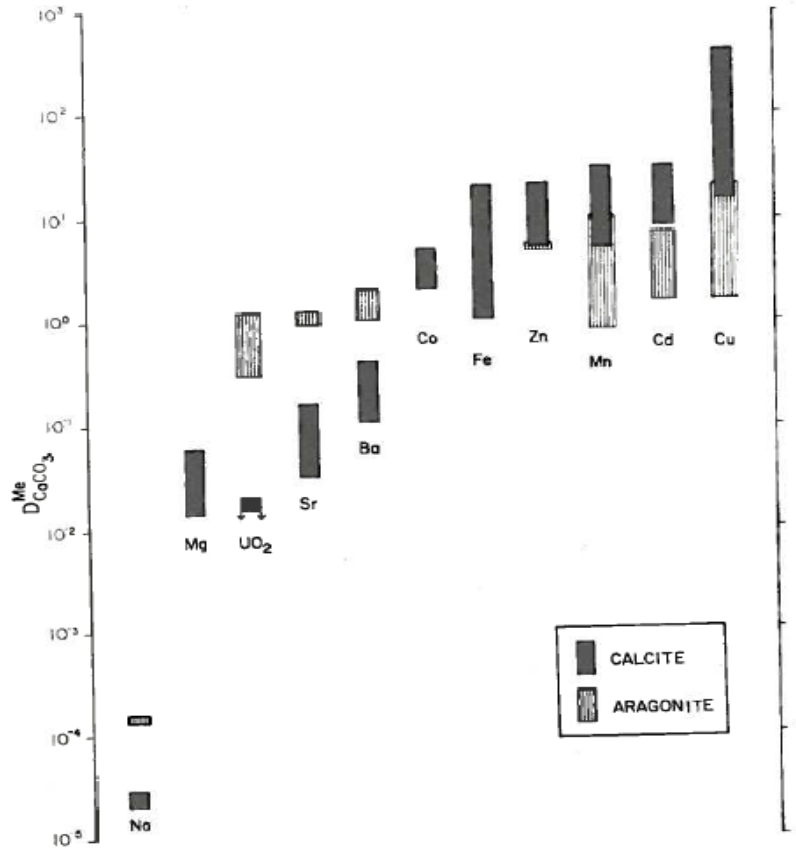

Figure 4- 10: Approximate trace element distribution coefficients for calcite and aragonite (Veizer, 1983).

In general, the exact values of distribution coefficient are very hard to estimate. However, the approximate range of the coefficient can be taken from Figure 4-10, so that an approximate estimate of fluid composition could be deduced from a crystal analysis. That might give enough information to estimate if the present-day composition of fluids is the same as paleo-fluid.

4.2 Sampling and methods

Samples have been collected from the fossil travertines and veins located in the hanging wall of the Little Grand Wash fault (Figure 4-11 to 4-19). The numbering of the travertines is based on the travertine numbers in Figure 3-5.

4.2.1 Vein sampling

Various vein samples from the sandstone formations of T2 and shale formation of T3, T4 and L9 have been collected for analysis. The sample numbers used in this chapter are outlined in Table 4-3.

Table 4- 3: Samples and the associated location description and analytical methods in this chapter.

Sample name	Figure number	Location description	Analytical methods
T2-vein	Figure 4- 11	Thick banded vein from T2	ICP-MS, XRD, SEM, light microscope, electron microprobe, isotope (Sr, C and O),
YS014-09	Figure 4-13 (b)	Thick banded vein from T2	Isotope (Sr, C and O)
YS014-27	Figure 4-13 (h)	Thin vertical vein from T5	
YS014-42	Figure 4-20 (a)	Calcite veins sticking out from the Mancos shale in L9	
YS014-65	Figure 4-19 (c)	Veins in the contact of two coloured Mancos shales (from T4)	

a. Veins in sandstone formations

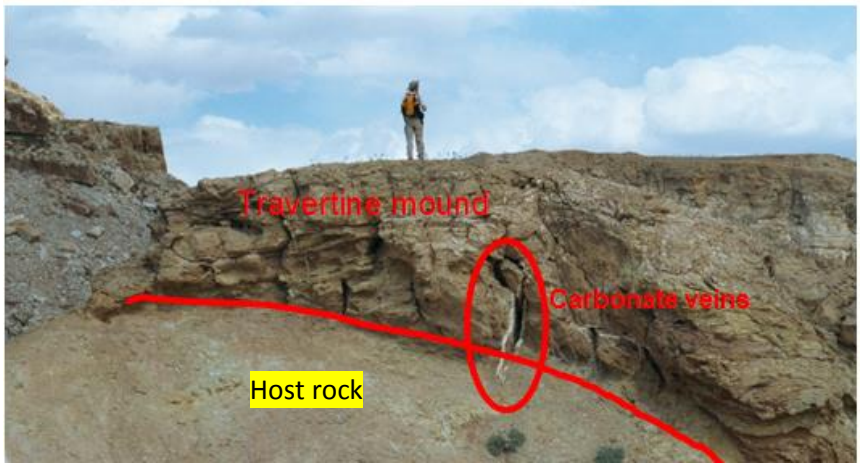

Figure 4- 11: Vertical thick carbonate veins, travertine mound (T2) and bed rocks at the footwall the Little Grand Wash fault (photo by Mark Wilkinson). The thick vein has been sampled for analysis (sample T2-vein was collected from here).


Fig4-12(c)

(a)

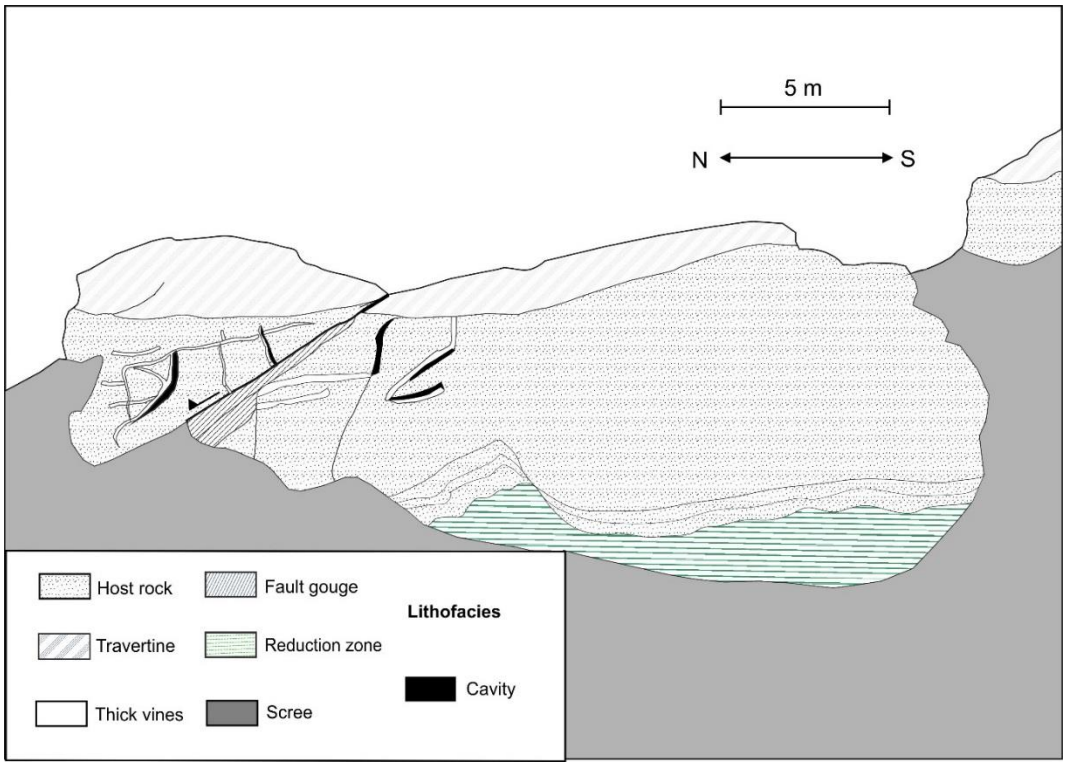
5 m
N
S
Host rock
Fault gouge
Lithofacies
Travertine
Reduction zone
Cavity
Thick vines
Scree

(b)

(c)

Figure 4- 12: (a) T2 outcropped at the footwall of the main fault: travertine on top of Morrison Formation; (b) annotated schematic sketch of the T2; (c) the close-up of the fracture. Thick veins seal the fracture (the location of the T2 travertine refers to Figure 3-4)

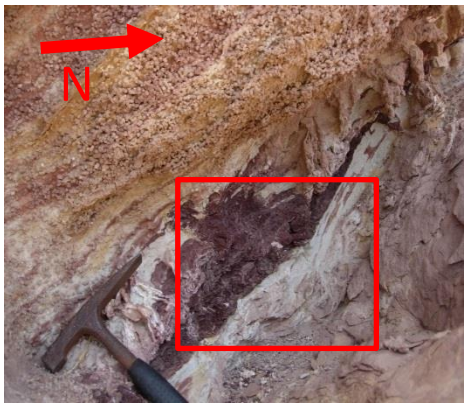

(a)

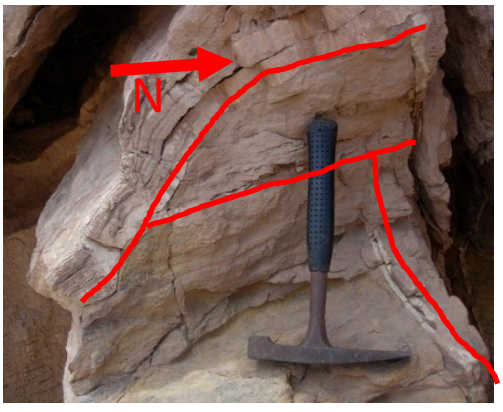

(b)

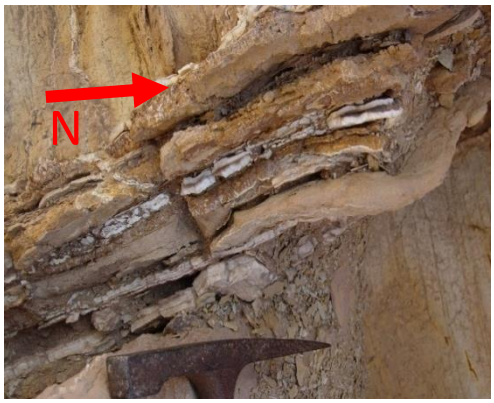

(c)

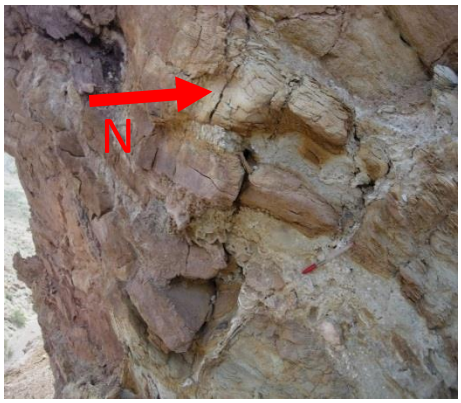

(d)

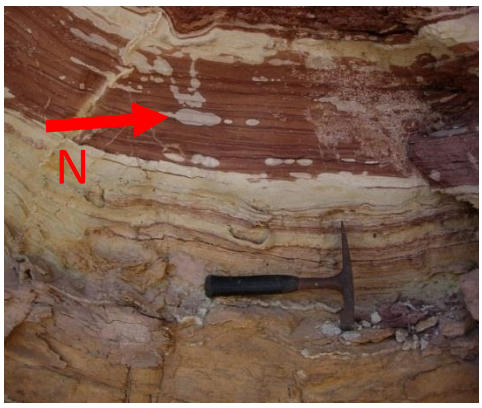

(e)

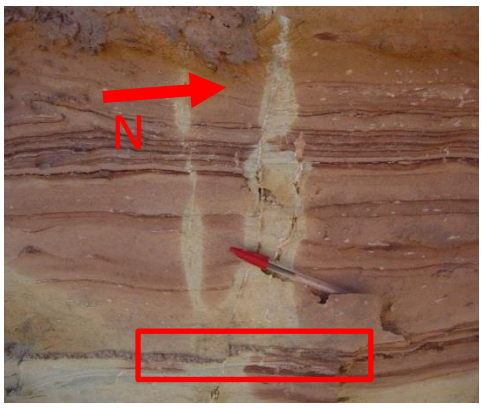

(f)

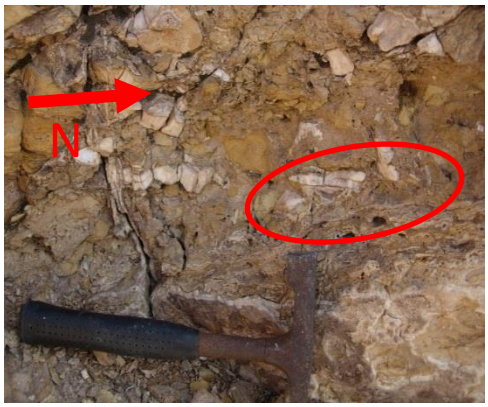

(g)

(h)

(r)

Figure 4- 13: (a) Boxwork structure cross-cut by thick sub-horizontal carbonate veins. (b) Centimetre thick symmetrical carbonate veins. The vertical veins become progressively more horizontal towards the surface. In the left side there is one horizontal vein extending from the bottom and crosscut by horizontal vein. This site is just next to the fault. (c) Network of white layered veins of 2-3 centimetres. (d) Trace of carbonate-rich fluid migration. (e) Network of millimetre veins and reduced zone of Brushy Basin Member of Morrison formation (on top of Salt Wash Member). (f) Bleached zone of Morrison sandstones with little local deformation and displacement (in the red box). The vertical vein (gypsum) and the bleach formed after the deformation and displacement. (g) White veins in the cracks and dissolution feature (vuggy porosity). (h) Vertical millimetre carbonate veins inside the fractured sandstones in T5. (r) Network of cracks and thin veins in T5

b. Veins and reduction zones in shale formations (samples number in Table 4-3)

In the hanging wall of Little Grand Wash fault, the Mancos Shale Formation is exposed to the south of the Little Grand Wash fault (Fig. 4-14 and Fig. 4-15) (travertine location see Fig. 3-5).


Little Grand Wash fault
(N80˚ direction)
15m
Fig. 4-16 (a)
Fig. 4-16 (c)

(a)

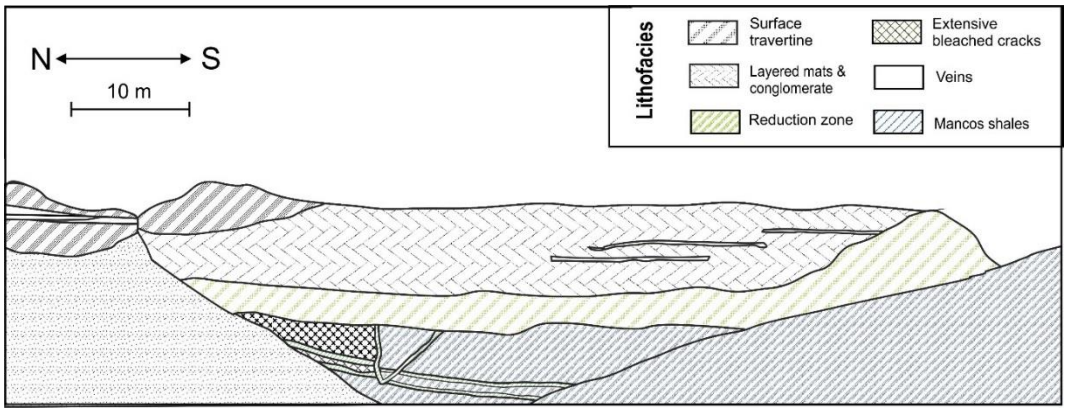
N
S
10 m
Lithofacies
Surface travertine
Extensive bleached cracks
Layered mats & conglomerate
Veins
Reduction zone
Mancos shales

(b)

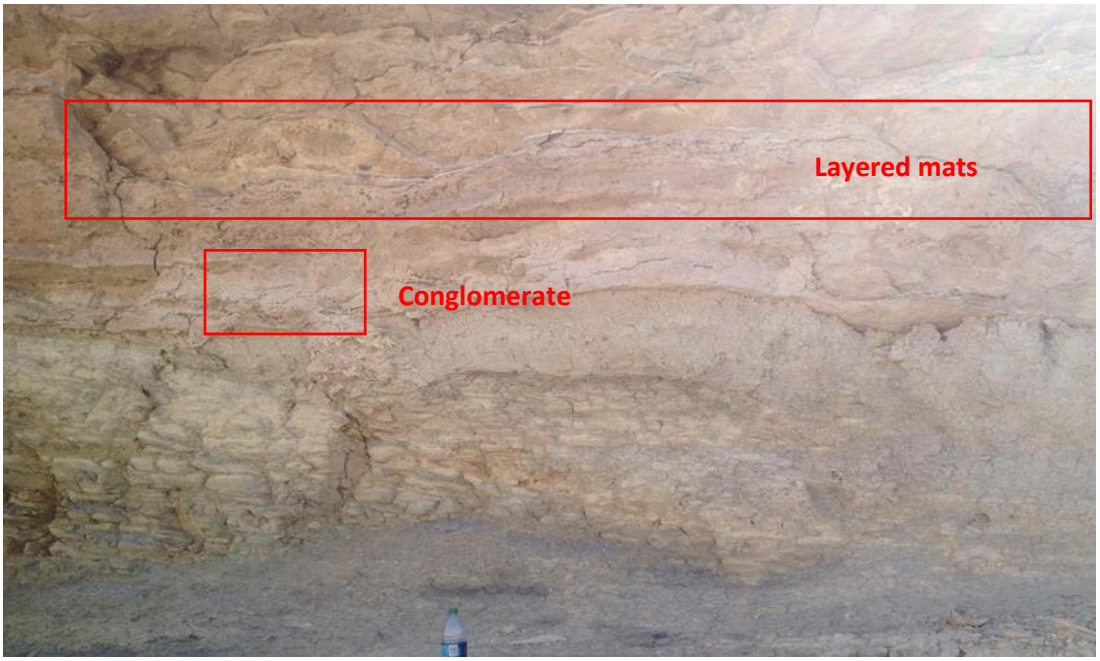
Layered mats
Conglomerate

(c)

(d)

Figure 4- 14: West side of T3, at the hanging wall of the Little Grand Wash fault. (a) Picture of T3. The Little Grand Wash fault is about 15m away from the shale unit of Figure 4-14(a); (b) schematic picture of T3; (c) horizontal carbonate veins in the transition zone between travertine and shale unit; (d) close-up of the conglomerate between layered mats and shale unit. (location of the T3 travertine refers to Figure 3-4.

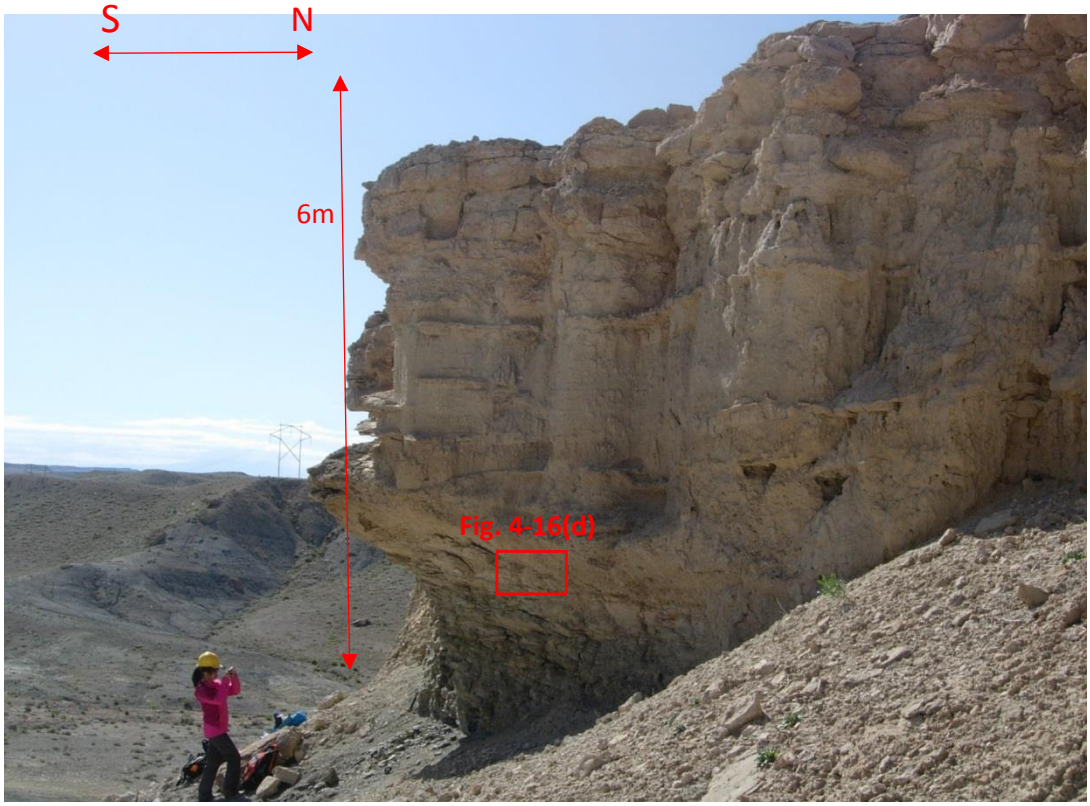

Figure 4- 15: East side of Travertine 3 (for travertine number see Fig.3-5).

T3 deposit overlies the Mancos Shale Formation (Fig. 4-14 and 4-15). There is bleached reduction zone in between the travertine surface and the Mancos shale unit (Fig. 4-14(b)). The main fault is about 15-20 m away, to the north of T3. Horizontal thick carbonate veins have been found in the surface travertine. Bleached fractures are parallel and subparallel to the main fault 15m away (Fig. 4-14(a)). Bleached fractures are more common in the north part of the Mancos shale unit, i.e. closer to the main fault. However, millimetre-thick gypsum veins are more extensive in the south part of the outcrop (Figure 4-16(e)).

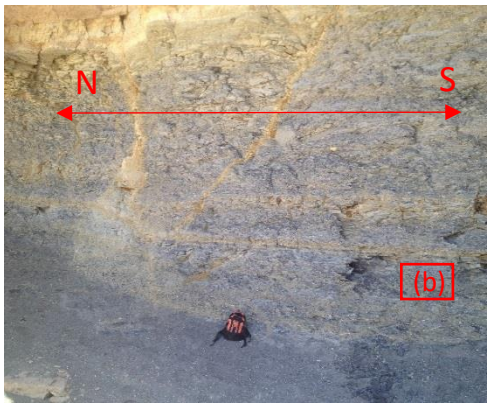

(a)

(b)

(c)

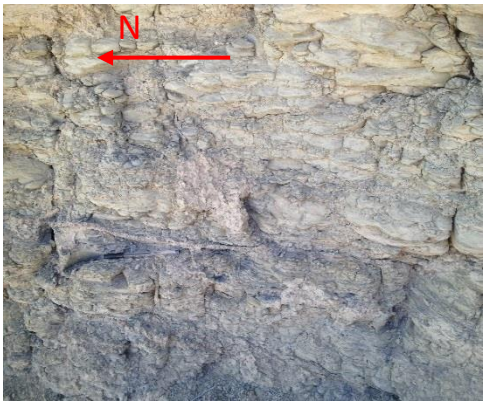

(d)

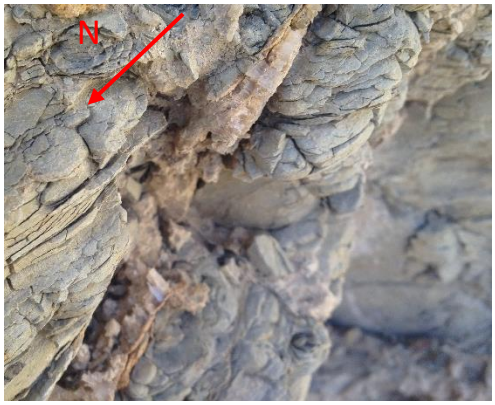

(e)

(f)

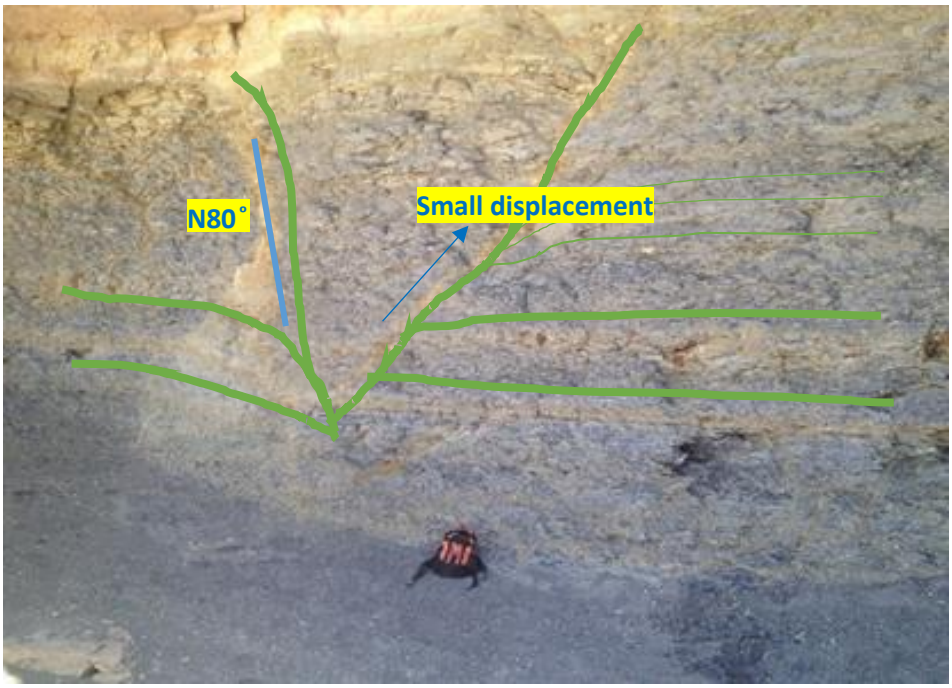

(g)

Figure 4- 16: (a) Bleached fractures and reduction zone on the west side of T3. (b) Laminated Mancos shale unit and millimetre thick gypsum veins in west side of T3. (c) Gypsum veins in the east side of T3. (d) Transition layer from upper conglomerate travertine to lower fractured, laminated Mancos shale in the east side of T3. Gypsum veins infilled the fractures. (e) Close-up of infilled gypsum veins inside the laminated shales. (f) Oxidized ferroan deposit in the lower part of the Mancos shale of the east side of T3. (g) The local fault displacement in T3.

Figure 4- 17: Location of T4 (red circle; close-up in Fig. 4-18(a)). The travertine is on a junction of the Little Grand Wash fault and a small cross fault. The bedded unit on the horizon is sandstone unit in the footwall of the main fault. Vein sample of YS014-65 was collected from this site.

Sample YS014-65 is a carbonate vein associated with a very small fossil travertine (T4, 50 cm in diameter) found round 500 m east of T3 (Figure 4-18(a)). T4 is on the intersection of the main fault and a small cross fault.

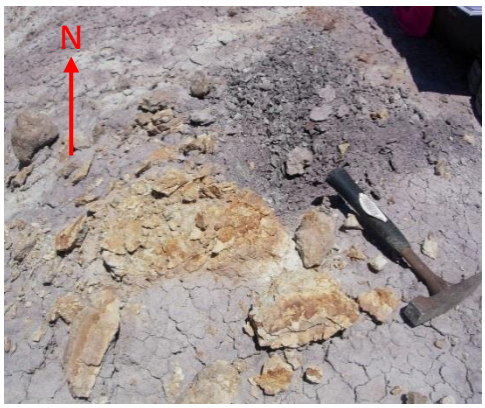

(a)

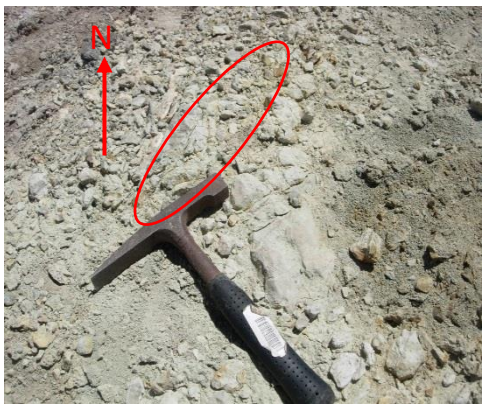

(b)

(c)

Figure 4- 18: (a) The small travertine 4 on top of Mancos Shale. YS014-65 was sampled from the contact of the purple coloured fault part and grey coloured Mancos shale unit; (b) carbonate vein (sample YS014-62) with 2 phases of growth in the Mancos shale; (c) the close up of the two-phase vein sample YS014-62 (approximately 5 cm across). The location of T4 travertine refers to Figure 3-3.

(a)

(b)

(c)

Figure 4- 19: (a) Locality 9, in relationship with the main fault; (b) pieces of carbonate veins in locality 9; (c) broken veins and elongated vein plane.

Locality 9 is around 2,000m east of T4 (Fig. 5-19(a), see location map in Fig. 3-5). It is on the damage zone of the fault that covered by Mancos shales. Extensive broken pieces of carbonate veins that sticking out from the surface. The size of the veins varies from 10cm long to just a few millimetre big. Some elongated vein plane could be observed (Figure 4-19 (b)), suggesting the small vein pieces could be the broken of the intact elongated vein plane by the fault movement activity.

Among all the samples veins, thick, banded T2-vein is selected as the focus of the analysis, for the universal display and the association with travertine formation (right below the travertine). XRD was used to analyse the mineralogy; reflected/transmited microscope (polarization contrast) was used to take pictures of the thin section samples; SEM was used to image the crystal structure; electron microprobe analysis was used to determine the element composition of very small zonation (10-20μm). ICP-MS was used to analyse element concentrations for lower detection limit analysis.

4.2.2 XRD for mineralogy study

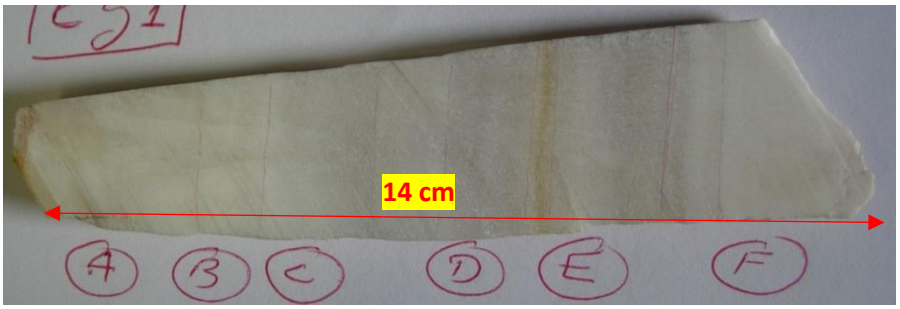

Figure 4- 20: White banded vein sample from T2 (T2-vein) for XRD analysis. The vein growing direction is from A to F. The length of the sample is about 10cm.

Color alterations are evident in T2-vein (light brown bands, Fig. 4-20). Sample T2-vein has been studied petrographically (for sample location see Fig. 4-11). The sample was divided into six sub-samples along the direction of vein growth from the wall of the vein to the centre (sub-samples CG-A, B, C, D, E, F). XRD analysis is used to analyse the mineralogy of the vein samples. The experiment was performed at the Grant institute of the School of Geosicence at the University of Edinburgh using a Bruker D8 Advance with a Sol-X Energy Dispersive detector. The software

used for analysis is EVA coupled with the International Centre for Diffraction Data (ICDD) database. Each sub-sample was cut and ground into a fine powder.

4.2.3 Reflected/transmited microscope for crystal analysis

Another white banded vein sample (from the same location with T2-vein) was cut into 4 sections (Figure 4-21; the vein growth direction is marked by arrows).

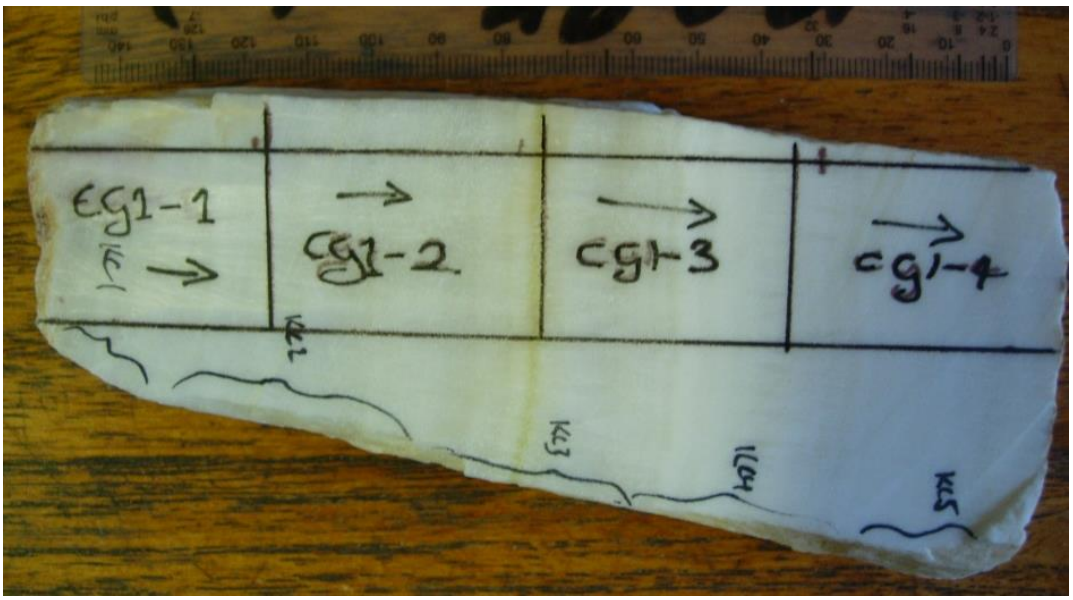

Figure 4- 21: Sample for reflected/transmitted microscope was divided into 4 sections (cg1-1, cg1-2, cg1-3, cg1-4). The arrow marks the vein growing direction from the wall of the crack to the centre.

Reflected/transmitted light polarizing microscope was used for crystal structure analysis under Leica DMLP (DFC 420C camera and Leica Application Suite v4.00).

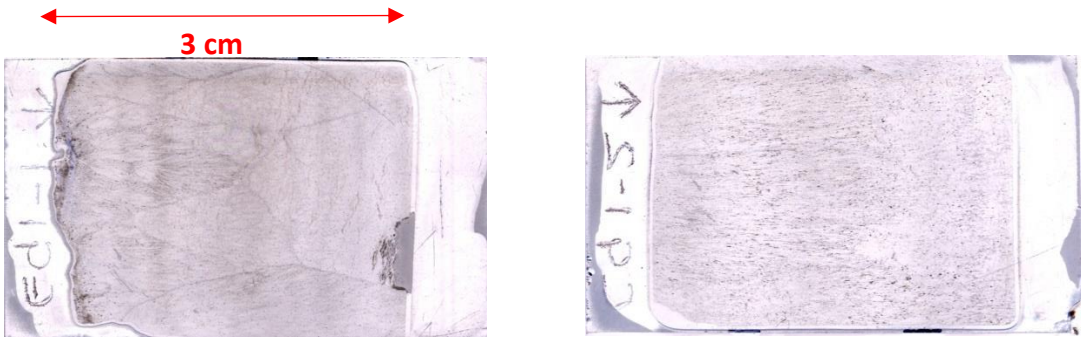

cg1-1

cg1-2

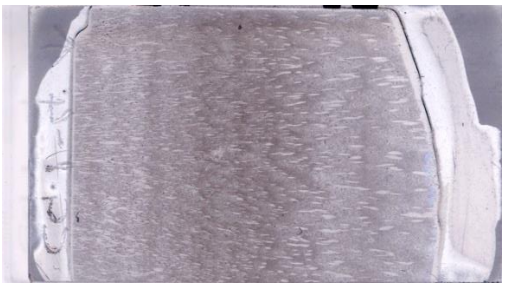

cg1-3

cg1-4

Figure 4- 22: Scanned photos of the thin sections for refelcted/transmitted microscopre (from the sample in Figure 5-21). Clear bands were observed in sample cg1-1, cg1-3, and cg1-4. The arrows marks the growing direction of the vein from the vein wall.

In the scanned photos of the thin sections (Figure 4-22), growth bands are clear in samples cg1-3 and cg1-4. In sample cg1-3, there is a band in the centre deviding the left half and right half. In sample cg1-4, there are several lighter-colored bands in the left edge and right edge of the sample.

4.2.3 Electron probe for elemental analysis of crystal

The electron probe is a microanalyser that can make quantitative analyses of most elements in the Periodic Table between boron and uranium. The analyses were performed with a Camerca SX100 combined with data processing software in the Grant Insitutue, School of Geosicences at the University of Edinburgh. The spatial resolution of the analysis could be as high as 1 micron with good precision. (http://www.ed.ac.uk/geosciences/research/facilities/electron)

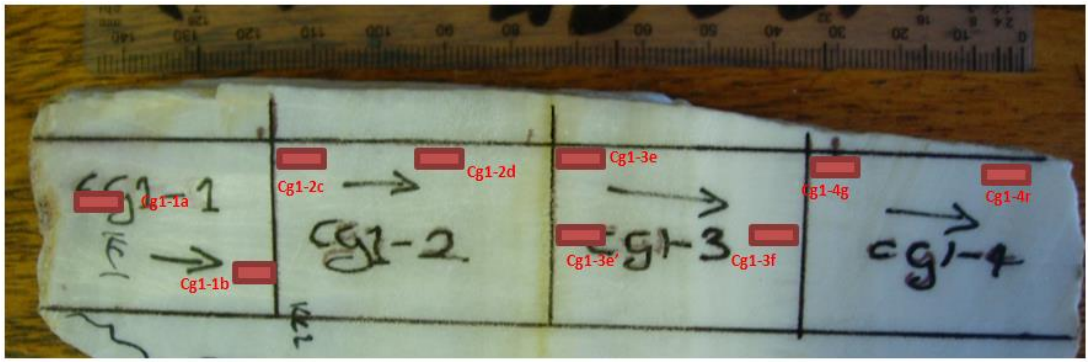

Figure 4- 23:Vein sample (Sample T2-vein) before cutting. The red small boxes indicate the selected zones for reflected/transmitted picture and Electron Microschope. Sample names: cg1-1a, cg1-1b, cg1-2c, cg1-2d, cg1-3e, cg1-3e', cg1-3f, cg1-4g, cg1-4r

Figure 4-23 shows the sample for electron probe before cutting and the chosen zones for analysis. Areas for analysis were chosen using optical petrography to include the observed range of crystal morphologies. Seven elements were selected to be analyzed: Ca, Na, S, Fe, Al, Sr, Si (carbon cannot be measured because the samples were coated with carbon). From a preliminary set of analysis, three elements (Al, Si, Fe) have been ruled out for analysis because of very low concentrations compared to the instrument error or high detection limits. Routine detection limit ranges from 0.009 wt% to 0.05 wt%. Calcium is also ruled out for analysis because the samples are predominantly calcium carbonate with no significant variation in calcium content. The examples of the transmited-light pictures of zone cg1-3e and cg1-3e' are shown in Figure 4-24. Analtyical traverses have been selected along the fibers of the crystal to investigate any elemental differences along crystals and between different shapes of crystals.

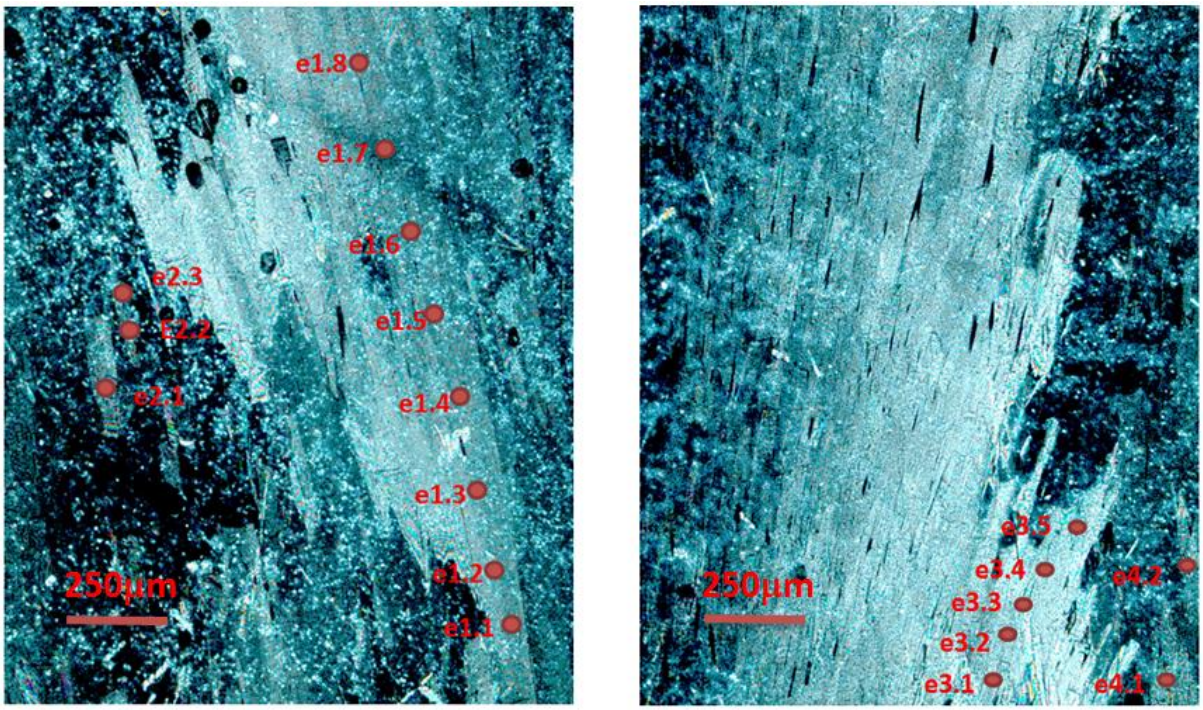

Figure 4- 24: Transmitted pictures of samples cg1-3e and cg1-3e'. The red dots show how the traverse is located along crystals. See Figure 4-23 for location of these areas.

4.2.4 ICP-MS for trace element analysis

ICP-MS is used for the determination of trace elements concentrations. In the electron microprobe study, only Ca, Na, S and Sr were analysed. For more comprehensive understandings of the elemental concentration, the ICP-MS was adapted for its superior detection capabilities. Around 0.001g sample were totally dissolved in 10g of 2% HNO_3. The analysis was performed with ICP-MS equipment (Agilent 7500ce with a collision cell and an integrated LC system) at the School of Chemistry of the University of Edinburgh. Fifteen samples have been selected in a traverse to make a continuous study of the changes during the growth of vein. One darker yellow band is apparent in the middle of the vein samples (Fig. 4-25). It was hoped that the analysis would detect the cause of the colouration.

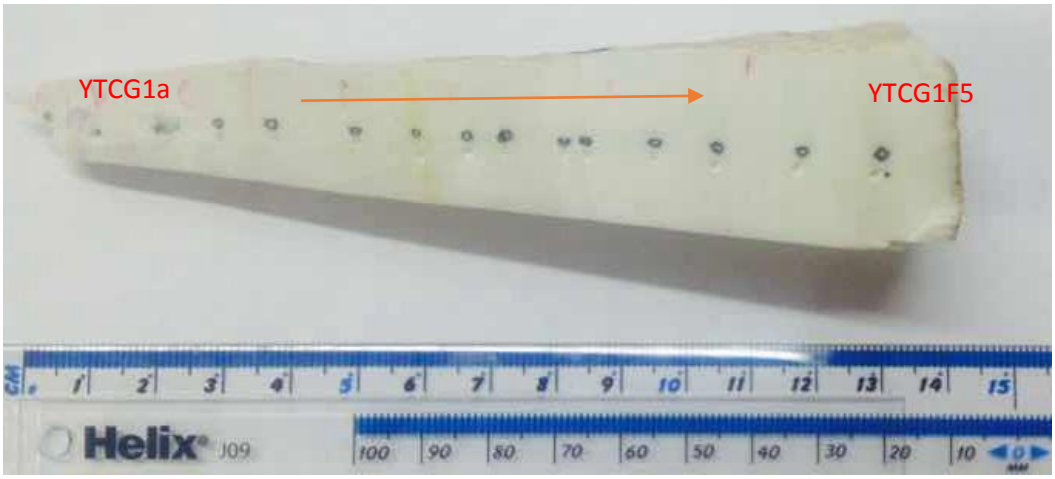

Figure 4- 25: Sample T2-vein for ICP-MS analysis before cutting. The sample is from the same vein with the samples for XRD and electron probe. The arrow shows the vein growing direction. The black zonation marked the location of the subsample zones: YTCG1a, YTCG1b, YTCG1C1, YTCG1C2, YTCG1C3, YTCG1D1, YTCG1D2, YTCG1E1, YTCG1E2, YTCG1E3, YTCG1F1, YTCG1F2, YTCG1F3, YTCG1F4, YTCG1F5 from left to right.

4.2.5 Isotopic study

a. Stable isotope analysis ($\delta^{13}C$ and $\delta^{18}O$)

Six powdered samples (in traverse) from vein sample (Fig. 4-20) were analysed for carbon and oxygen isotope at the stable isotope laboratory of the University of Edinburgh (sub-sample CG A-F of sample T2-vein). The analyses were performed on 0.02 - 0.1 mg sub-samples. The carbonate vein samples were reacted with 100% orthophosphoric acid at 75 °C in a Kiel carbonate III preparation device, and the resulting CO_2 was then analysed on a Thermo Electron Delta$^+$ Advantage stable isotope ratio mass spectrometer.

The standard deviation (n=31) of a powdered coral laboratory standard (COR1D, $\delta^{13}C$ = -0.648, $\delta^{18}O$ = -4.920) run as a sample on the same days as the study samples, was $\pm$ 0.06‰ for $\delta^{13}C$ and $\pm$ 0.08‰ for $\delta^{18}O$. All carbonate isotopic values are quoted relative to V-PDB.

b. Strontium isotope ($^{87}Sr/^{86}Sr$)

Five vein samples from different locations were analysed for $^{87}Sr/^{86}Sr$ (sample descriptions in Table 4-3). The analyses were carried out in Scottish Universities Environmental Research Centre (SUERC). Powdered vein samples were digested in dilute HCl in PFA Teflon (savillex) beakers. After the total dissolution of the powder, Sr in the samples were separated using method adopted from Christian Pin (1994) using Triskem Sr spec resin with the Sr ratio determined by VG sector 54-30 thermal ionisation Mass Spectrometer.

Strontium ratios in ground water can be used as an effective indicator for the source of the fluid and the degree of fluid-rock interaction. CO_2-enrich water tends to be acidic, which causes the dissolution of high-^{87}Sr silicate and carbonate minerals. Aragonite inherit the $^{87}Sr/^{86}Sr$ from the parent fluid directly without fractionation. Therefore, the ratio of $^{87}Sr/^{86}Sr$ could be used as an indicator for silicate and carbonate mineral dissolution and (indirectly) the influence of CO_2-enriched water.

4.3 Results and discussion

4.3.1 Vein morphologies in sandstones and shales

Carbonate veins sampled from T2 and T5 (for travertine numbers see Figure 3-5 and sample numbers see Table 4-3) give some evidence for the pattern of fluid cycling. In T2 the outcrop is an approximately 2m thick travertine mound on top of the sandstone unit (Figure 4-12(a)). The outcrop is tilted and deformed by normal fault movement. The bigger normal fault on the north part made the footwall part deformed.

Three types of carbonate veins were found in sandstone units of T2 (footwall of the main fault):

a. Thick (5-50cm) white, banded, horizontal or vertical veins sealing fractures (Figure 4-13(b) and Figure 4-12(c)). This kind of vein is widespread in the host rock of T2 and the travertine mound. The vertical and horizontal veins crosscut the host rock and seal the fractures. They are more concentrated in the footwall which is more sandy than the shaly hanging wall. The aragonite

vein analysed in the following section 4.3.2 to section 4.3.5 is a vertical vein from T2.

b. Millimetre thin, vertical or horizontal calcite veins with reduction zones in sandy host rock in T2. The reduction zone can be tabular or haloes (Fig. 4-13(e) & (f)) with large tabular reduction zone at the base of the outcrop of more than 2m thickness. This type of vein is not associated with obvious larger fractures. Above the tabular reduction zones are the reduction haloes vary from millimetre to tens of centimetres in diameter. Small displacements of the reduction areas were found in the laminated reduction zone, indicating the reduction happened before the minor displacement (Fig. 4-13(f)).

c. Isolated millimetre-thick sub-vertical veins infilling the fractures of sandstone formation. The direction of the veins is parallel or sub-parallel to the Little Grand Wash fault (Fig 4-13(h)), suggesting the veins formed during the movement of the Little Grand Wash fault.

Veins and reduction features are different in the Mancos shale units. In general, three types of veins have been observed in the shale unit and the travertine covering the shale unit from T3 and T4:

a. Very thin gypsum veins (1-5 mm) filling the fractures and cracks of the shale unit in T3 (Figure 4-16 (b)~(e)). The shale unit below T3 is very likely to be influenced by the fault movement and small local fault displacement, as the Little Grand Wash fault is only around 15m to the north. The horizontal bleached zones (Fig. 4-16(a)) are displaced by these veins, showing movement happened post-dated to the bleaching. The cross network of the bleached lines proved reduction fluid migrated through the shale unit. The source of the gypsum could be either from the weathering of pyrite, or from the dissolution of the thick gypsum layer in Carmel Formation, which is situated below the Mancos shale. Further investigations are required to investigate the real derivation of the gypsum.

b. T4 is the fault transition zone with colour variations in shales. Carbonate veins have been found in ridge of the unit (Figure 4-18(b)). One of the vein sample contain two movement traces that perpendicular with each other, indicating more multiple local displacement that affected the T4 unit (Figure 4-18(c)). From field evidence, it cannot be proved whether the carbonate vein is related to the CO_2-rich fluid from the fault, so that further geochemistry studies are required.

c. Extensive pieces of carbonates that weathering out from the shale surface could be found in Mancos shale outcrop that not associated spatially with any travertine. Geochemical analysis is required to demonstrate the source of the carbonate veins.

When we compare the carbonate veins in sandstones and Mancos, it is evident that thick veins are much more commonly found in sandstone unit than in shales. It seems centimetre-thick carbonate veins are not likely to deposited in less permeable shale unit, even for the shales with micro-fault in place (Figure 4-16). It is assumed that large flow-rate fluid cannot penetrate the shale unit and deposit thick veins. Further geochemistry analyses are required to investigate the source of the carbonate veins i.e. whether they are related to the CO_2-rich fluids that form the travertines.

4.3.2 XRD analysis

XRD result shows that over 99% of the vein sample is aragonite (Appendix 5). Aragonite precipitates preferentiallty from hot water higher than 40 ºC (Pentecost, 2005b). Crystal Geyser is a cold spring, with the water escaping from the well is roughly 18°C from Navajo aquifer (Barth, 2012, Kampman et al., 2012, Kampman et al., 2014). The molality Mg/Ca ratio of present fluid is around 0.3-0.5 (calculated from data of Kampman et al., 2014), which is lower than the ratio that aragonite favours to deposit (the favourable ratio for aragonite deposition is presented in Fig. 4-6, when Mg/Ca=0.8). The possible reason for aragonite deposition in cold spring would be either the Mg/Ca of paleo-fluid is higher or the supply rate of CO_3^{2-} ions is high due to high concentrations of bicarbonate (Given and Wilkinson, 1985).

Dockrill also suggested that the variations in mineralogy were controlled by the concentration of the carbonate ion: white-banded veins (aragonite and calcite) precipitated first from the CO_3^{2-}-rich waters. After discharging to the surface, the concentration of CO_3^{2-} ions in the water decreased downstream, resulting in pure calcite veins at the distal margin of the mound (Dockrill, 2006).

4.3.3 Optical petrography

Figure 4- 26 is the transmitted microscope pictures of the aragonite crystals of variable morphology. Samples cg1-1a and cg1-1b (Fig. 4-26 (a) and (b)) show elongated, radiating aggregates of crystals with length of about 11,000μm, with lateral growth limited by adjacent aggregates. Similar shaped-crystal has been observed in samples of cg1-2 (cg1-2c, cg1-2d in Fig. 4-26 (c) and (d)). However, in the right part (later growth period) of sample T2-vein (cg1-3e), more randomly-oriented, smaller crystals set (mostly smaller than 100μm) could be observed in the large aggregates. In zonation cg1-3f, denser irregular random small crystals can be seen. In addition, long, needle-like morphology is also found (the longest crystal is up to 10,000μm in length). In zonation cg1-4 last growth period of the vein, crystals about 1,000 to 2,000μm in length that lack well-defined crystal faces are observed.

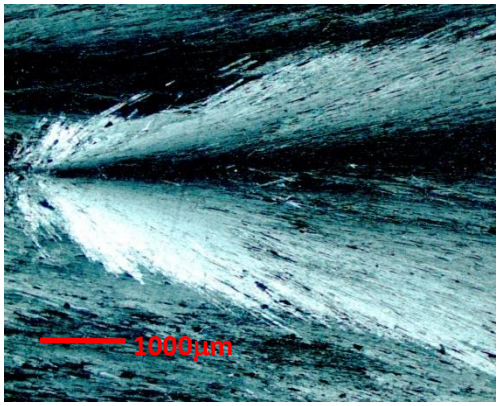

a

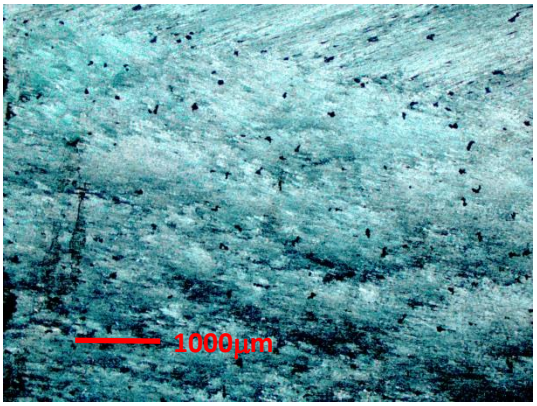

b

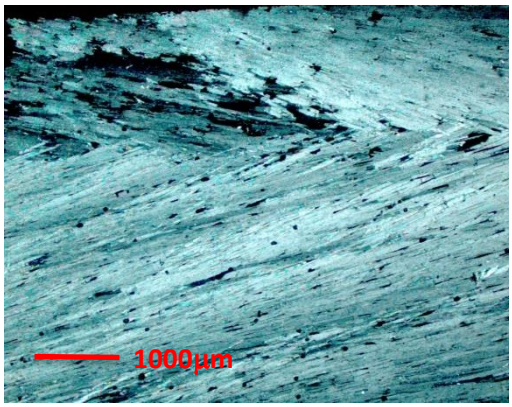

c

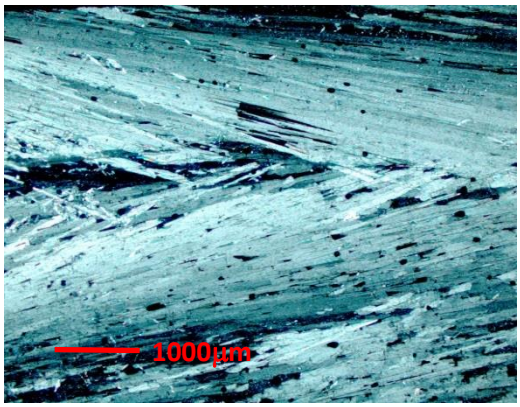

d

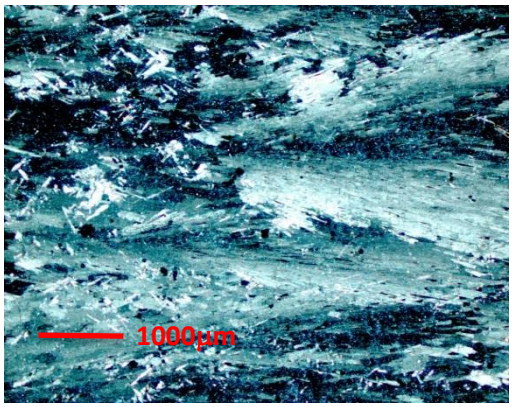

e

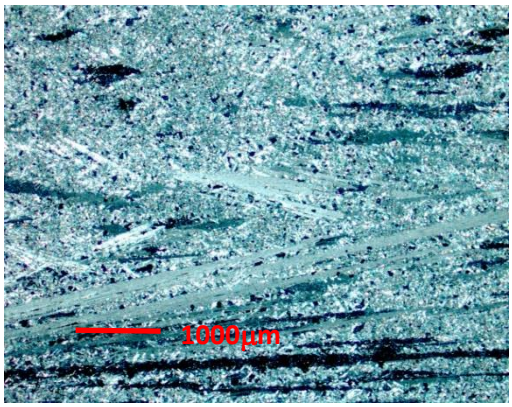

f

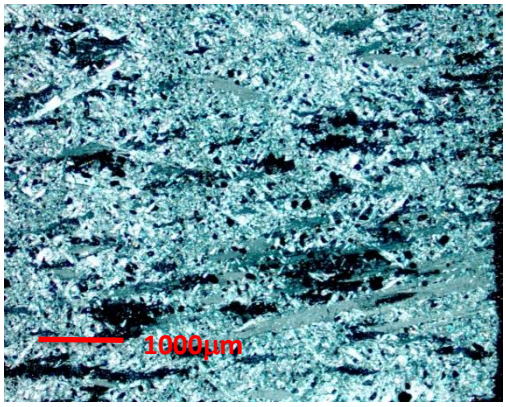

g

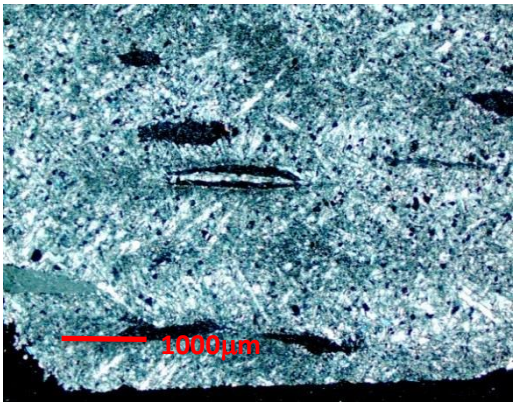

h

Figure 4- 26: Photomicrographs a - h show transmitted microscope pictures of cg1-1a, cg1-1b, cg1-2c, cg1-2d, cg1-3e, cg1-3f, cg1-4g, cg1-4r respectively. The sample name is the same as the red labels in Figure 4-23.

In general, calcite crystals of T2-vein could be classified as four types :

a. The elongate radiating acicular crystal aggrgates at the early growth period in zonation cg1-1a, cg1-1b, cg1-1c and cg1-1d.

b. The randomly oriented, smaller bladed crystals growing in the middle of sample in zonation cg1-3e, cg1-3f, cg1-3g, cg1-3r.

c. The less common, elongated, fibrous crystals in zonation cg1-3f.

d. Crystals that lack well-defined crystal faces at the late vein growth period in zonation cg1-4r.

4.3.4 Electron Microprobe analysis

Crystals in different morphologies are compared in terms of elemental abundance for Na, S, Sr and Ca. Figure 4-27 shows an example for zonation cg1-3e in sub-sample CG1-3, no obvious trend or difference can be seen in any of these 4 elements. No significant elemental differences were observed between the different crystal morphologies. The conclusion is the same for selected traverse on other 3 samples CG1-1, CG1-2 and CG1-4 (for results see Appendix 6).

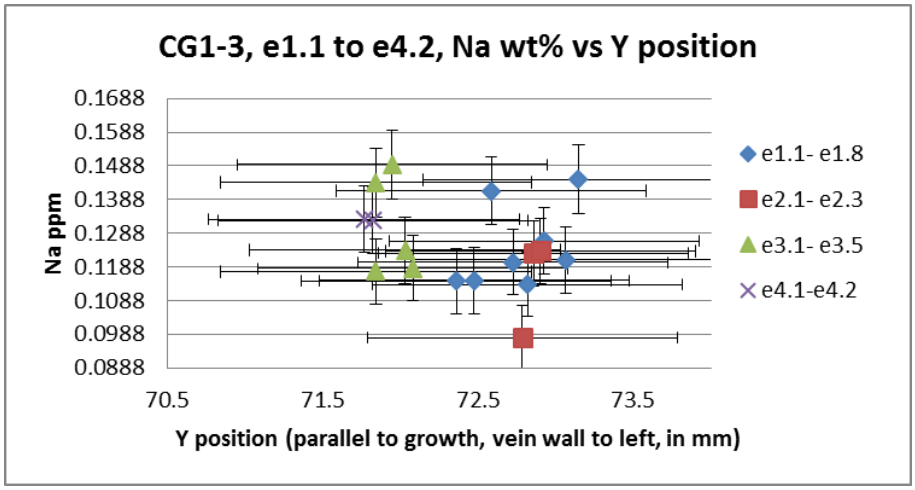

(a)

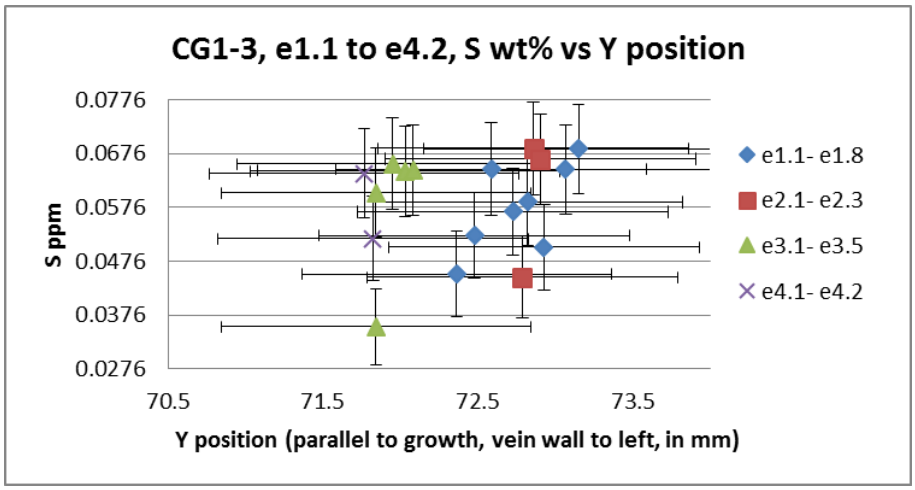
CG1-3, e1.1 to e4.2, S wt% vs Y position
S ppm
0.0776
0.0676
0.0576
0.0476
0.0376
0.0276
70.5
71.5
72.5
73.5
Y position (parallel to growth, vein wall to left, in mm)
e1.1- e1.8
e2.1- e2.3
e3.1- e3.5
e4.1- e4.2

(b)

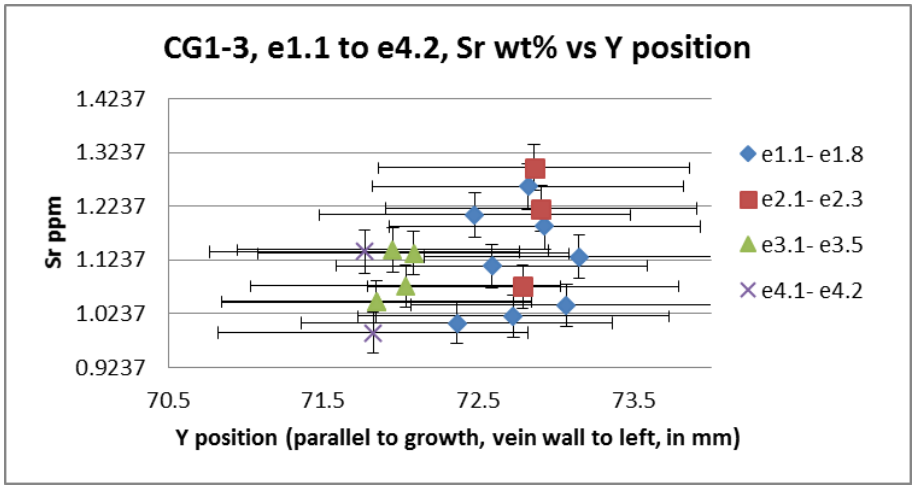
CG1-3, e1.1 to e4.2, Sr wt% vs Y position
Sr ppm
1.4237
1.3237
1.2237
1.1237
1.0237
0.9237
70.5
71.5
72.5
73.5
Y position (parallel to growth, vein wall to left, in mm)
e1.1- e1.8
e2.1- e2.3
e3.1- e3.5
e4.1- e4.2

(c)

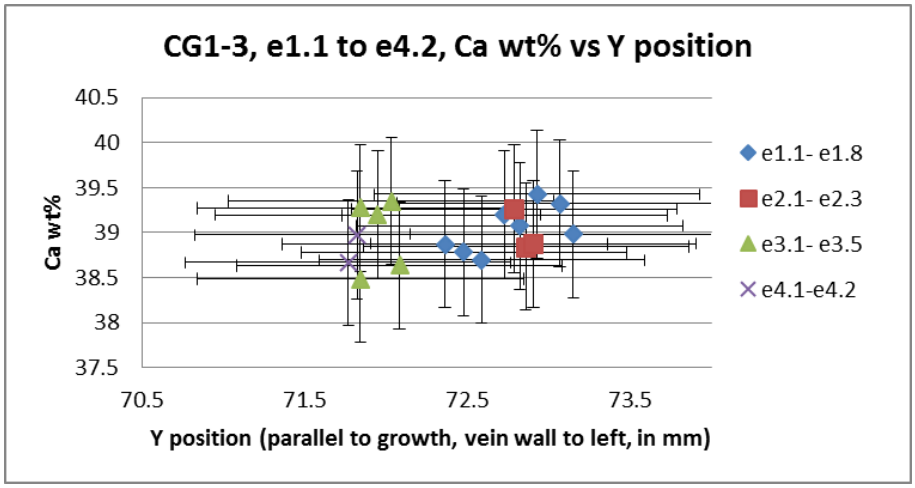
CG1-3, e1.1 to e4.2, Ca wt% vs Y position
Ca wt%
40.5
40
39.5
39
38.5
38
37.5
70.5
71.5
72.5
73.5
Y position (parallel to growth, vein wall to left, in mm)
e1.1- e1.8
e2.1- e2.3
e3.1- e3.5
e4.1-e4.2

(d)

Figure 4- 27: Elemental analysis by electron microprobe on zonation cg 1-3 of Sample T2-vein. The y-axis is weight% for Calcium but ppm for other elements. The x-axis is the distance from the wall where the vein is growing from (in mm). The vertical error bar is standard deviation of the data and the horizontal error bar is fixed value of 1mm. The blue diamond symbol stands for the elongate radiating crystals; the green triangle symbol, the red rectangle symbol and the purple cross symbol represent random, small crystals growing in the middle of big crystals, needle-like crystals and crystals that lack well-defined crystal faces, respectively.

Figure 4-28 shows the combined element concentration changes along the vein sample. It is evident that the concentration of Na and S decreases during vein growth (Fig. 4-28 (a) and (b)), while the concentration of Sr (Fig. 4-28 (c)) remains relatively constant from the beginning to the end of the vein.

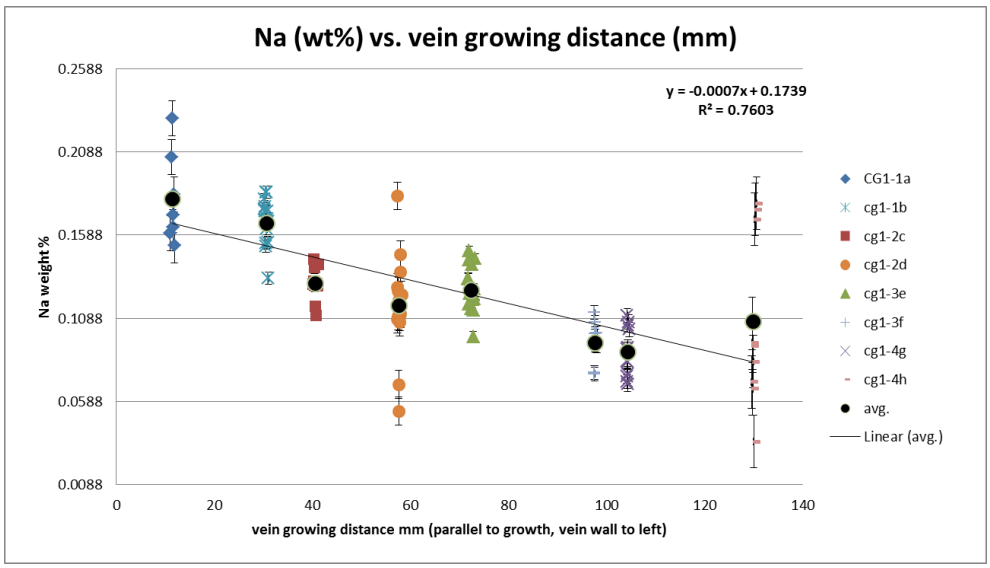

(a)

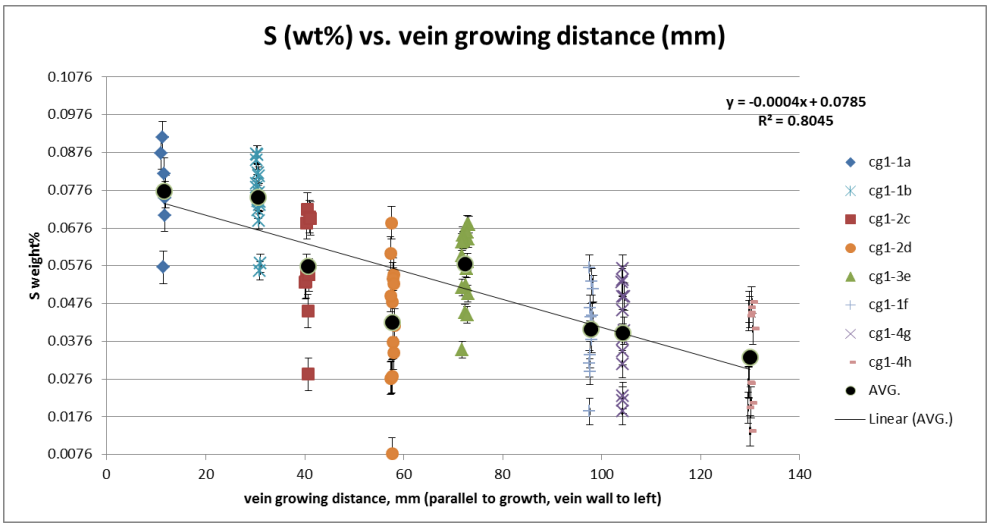

(b)

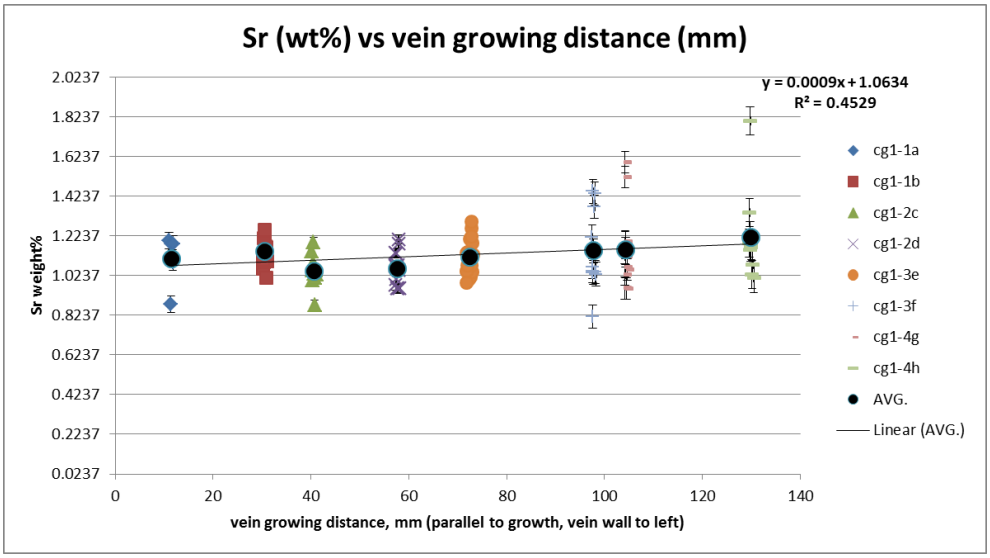

(c)

Figure 4- 28: The element concentration changes along the vein growth direction (vein wall to left). The black circles are arithmetic averages.

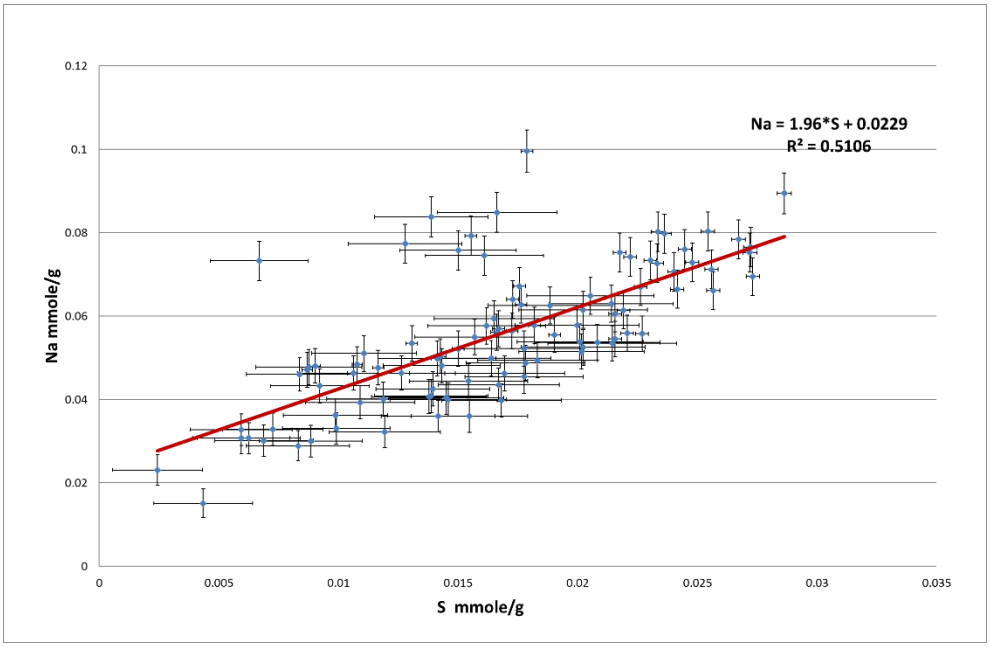

Figure 4- 29: Molar concentration of Na vs. S.

Interestingly, the concentration of elements Na and S correlate strongly (Fig. 4-29; R^2=0.51) in a ratio close to 2:1. The reason for this fixed ratio for Na and S could be the existence of sodium sulphate (Na_2SO_4) or sodium sulphide (Na_2S) inclusions for calcite crystals.

4.3.5 ICP-MS analysis

Figure 4-30 shows the results of ICP-MS analysis. The yellow band within the vein sample (illustrated in Figs 4-23 and 4-25) is shown in Fig. 4-30 for reference. The data from the experiments are shown in Appendix 6.

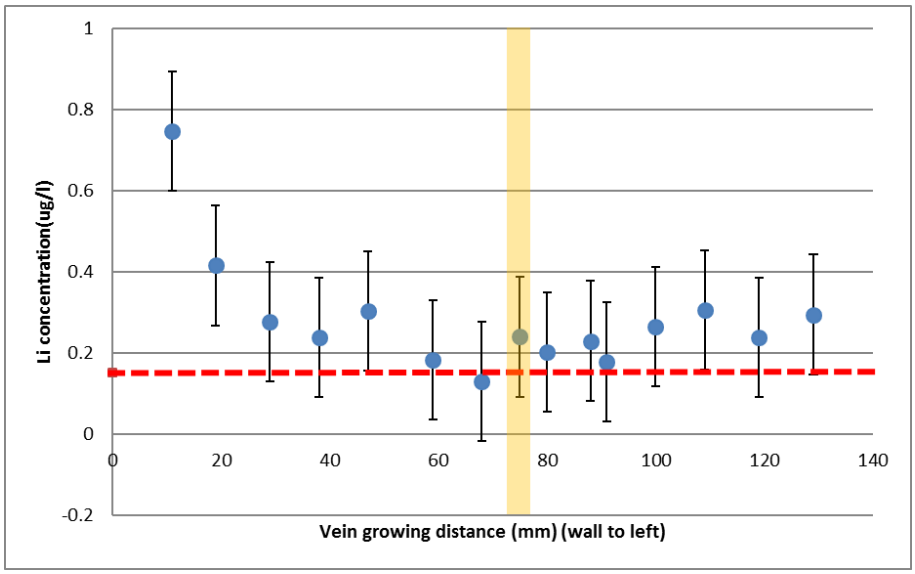
1
0.8
0.6
0.4
0.2
0
-0.2
Li concentration(ug/l)
0
20
40
60
80
100
120
140
Vein growing distance (mm) (wall to left)

(a)

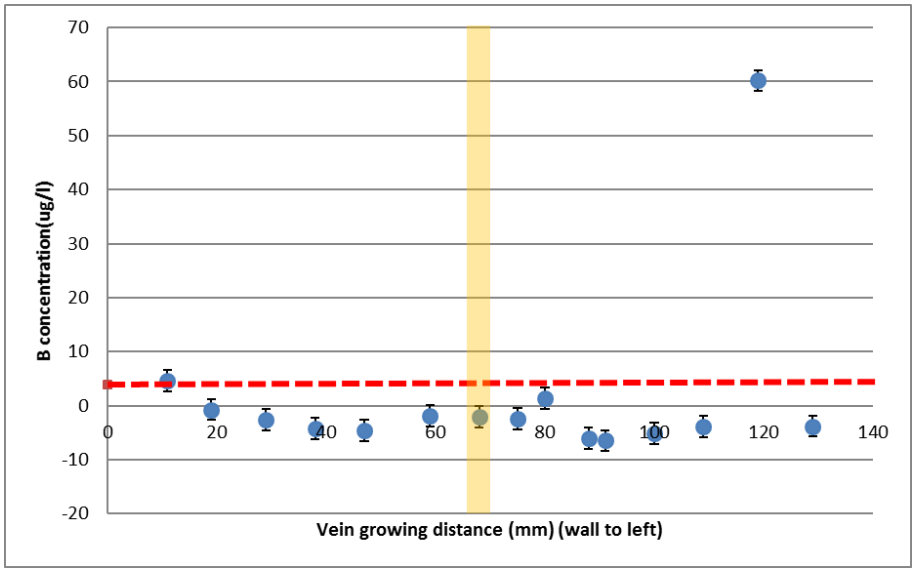
70
60
50
40
30
20
10
0
-10
-20
B concentration(ug/l)
0
20
40
60
80
100
120
140
Vein growing distance (mm) (wall to left)

(b)

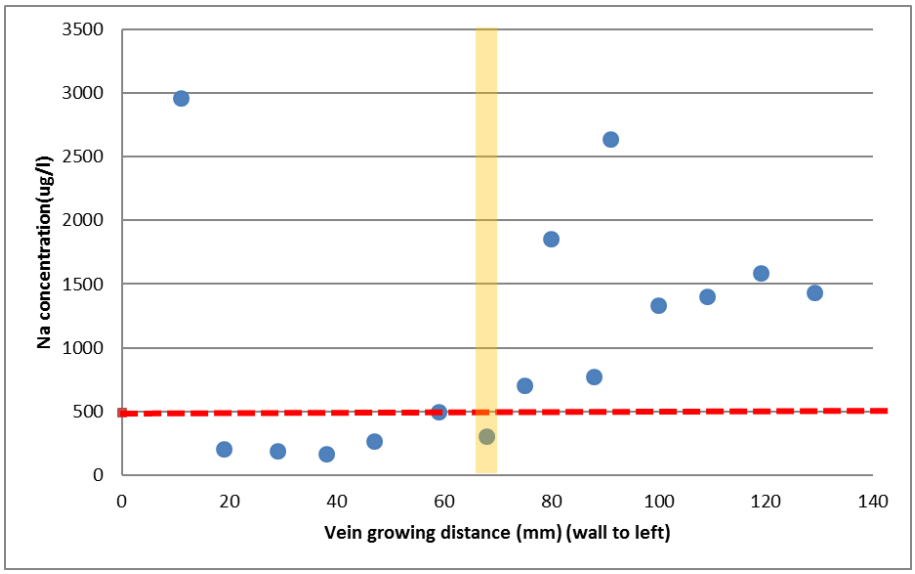
3500
3000
2500
2000
1500
1000
500
0
Na concentration(ug/l)
0
20
40
60
80
100
120
140
Vein growing distance (mm) (wall to left)

(c)

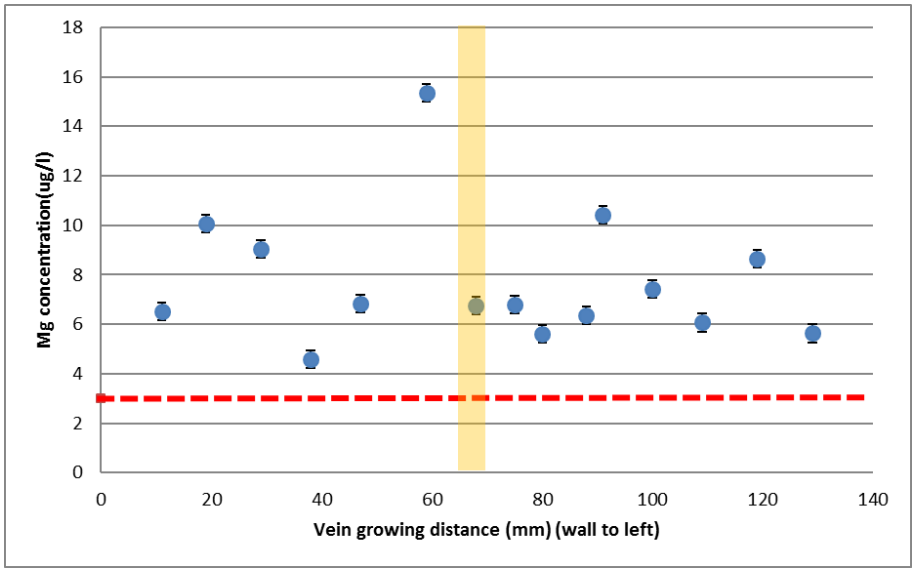
18
16
14
12
10
8
6
4
2
0
Mg concentration(ug/l)
0
20
40
60
80
100
120
140
Vein growing distance (mm) (wall to left)

(d)

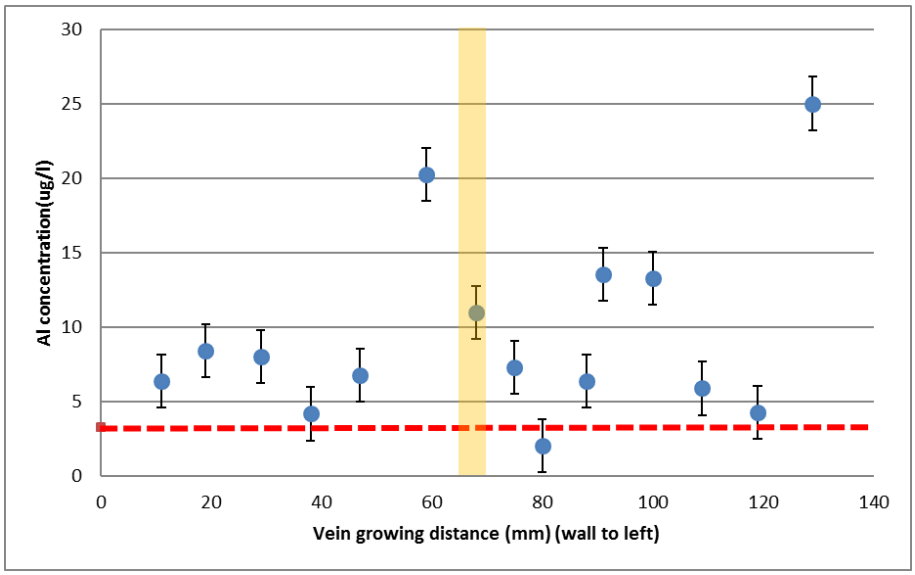
Al concentration(ug/l)
30
25
20
15
10
5
0
0
20
40
60
80
100
120
140
Vein growing distance (mm) (wall to left)

(e)

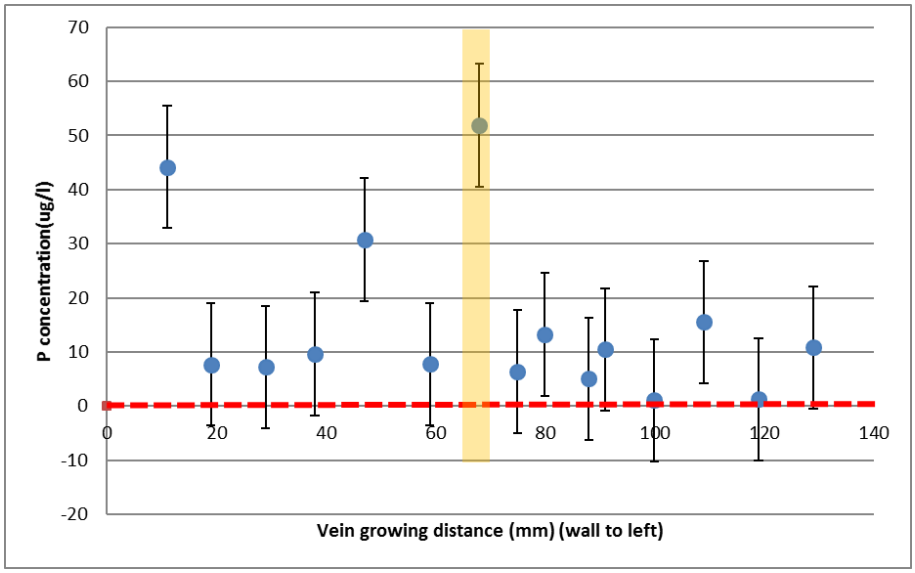
P concentration(ug/l)
70
60
50
40
30
20
10
0
-10
-20
0
20
40
60
80
100
120
140
Vein growing distance (mm) (wall to left)

(f)

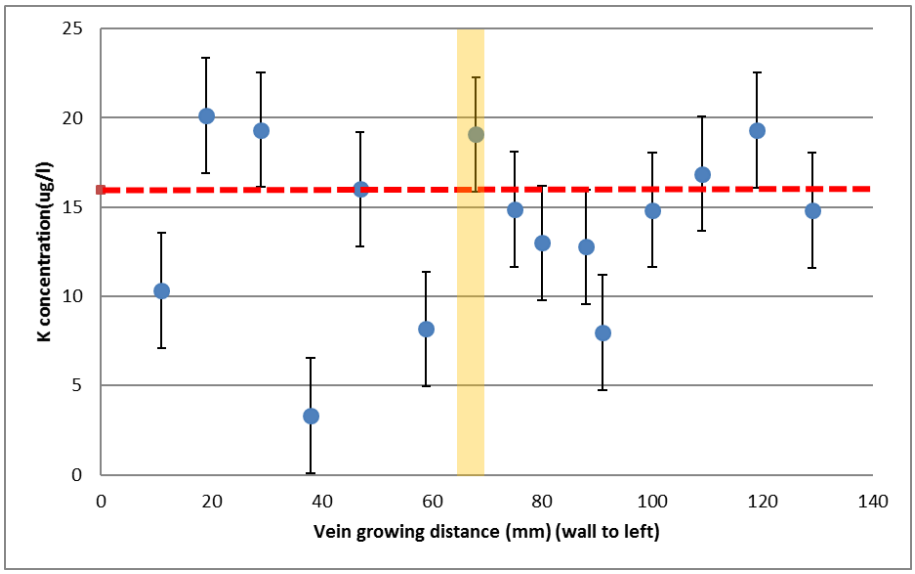
25
20
15
10
5
0
K concentration(ug/l)
0
20
40
60
80
100
120
140
Vein growing distance (mm) (wall to left)

(g)

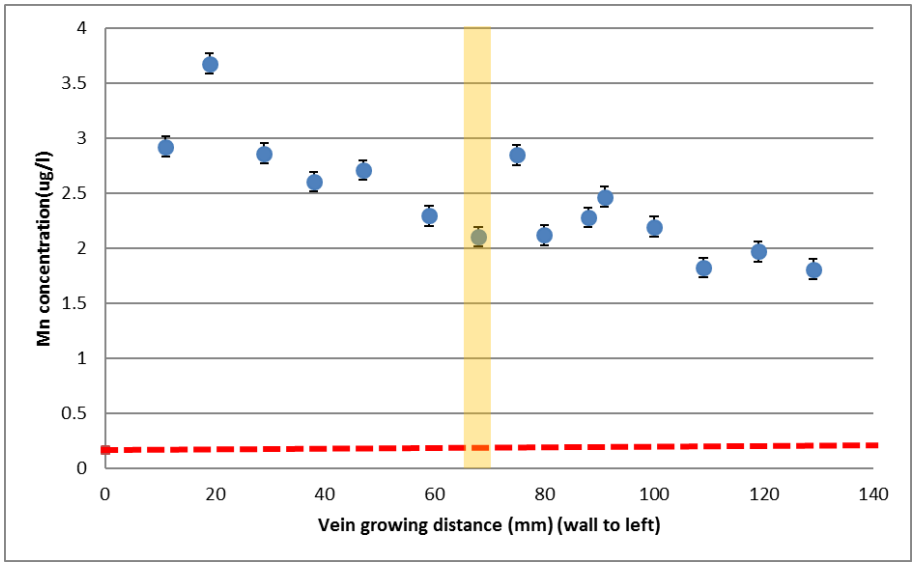
4
3.5
3
2.5
2
1.5
1
0.5
0
Mn concentration(ug/l)
0
20
40
60
80
100
120
140
Vein growing distance (mm) (wall to left)

(h)

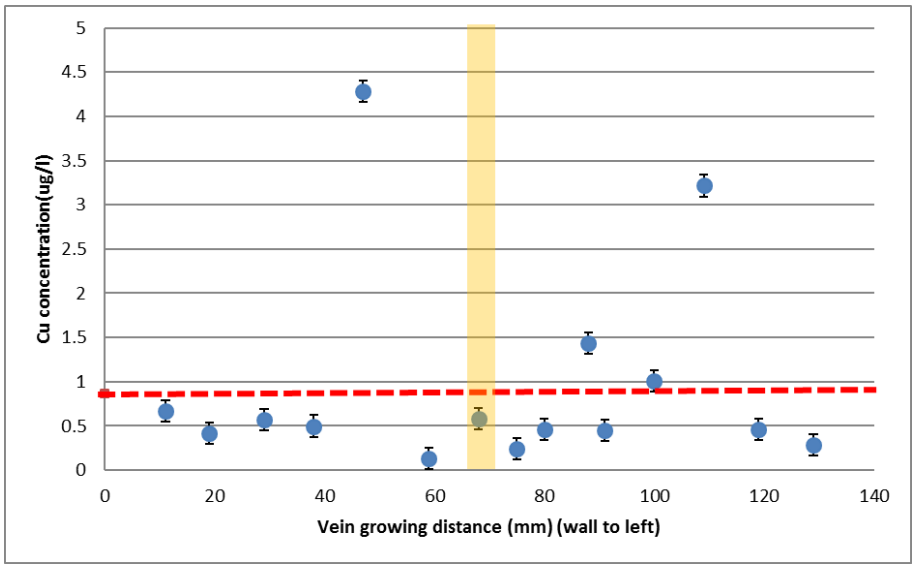
Cu concentration(ug/l)
5
4.5
4
3.5
3
2.5
2
1.5
1
0.5
0
0
20
40
60
80
100
120
140
Vein growing distance (mm) (wall to left)

(i)

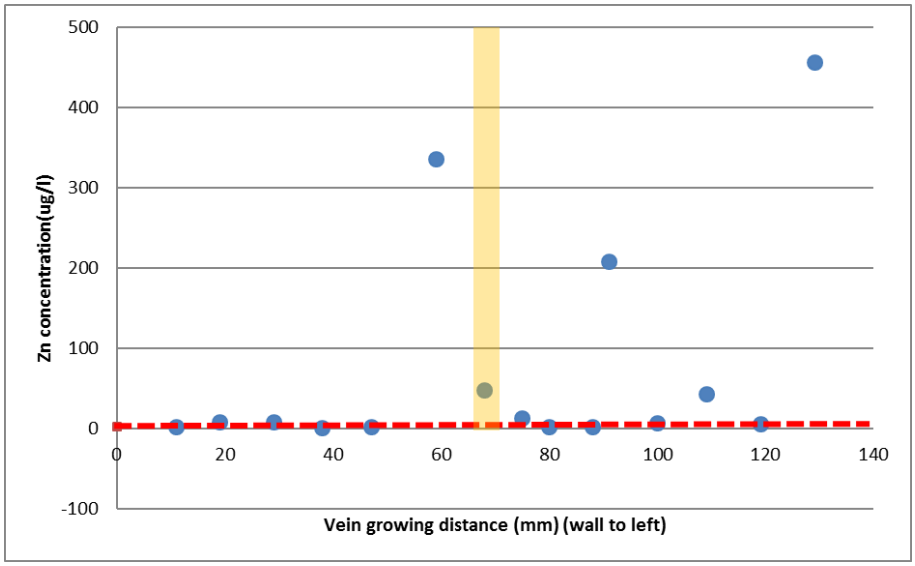
Zn concentration(ug/l)
500
400
300
200
100
0
-100
0
20
40
60
80
100
120
140
Vein growing distance (mm) (wall to left)

(j)

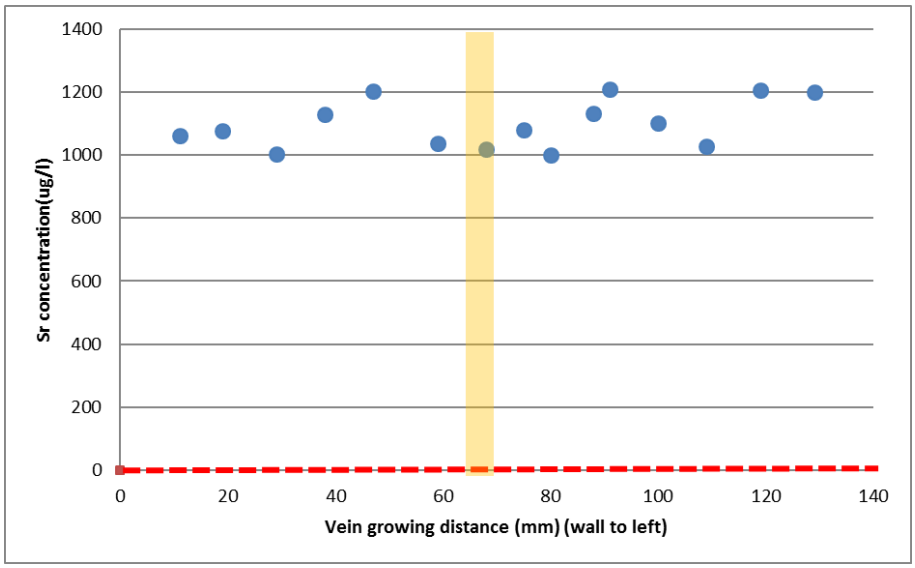
1400
1200
1000
800
600
400
200
0
Sr concentration(ug/l)
0
20
40
60
80
100
120
140
Vein growing distance (mm) (wall to left)

(k)

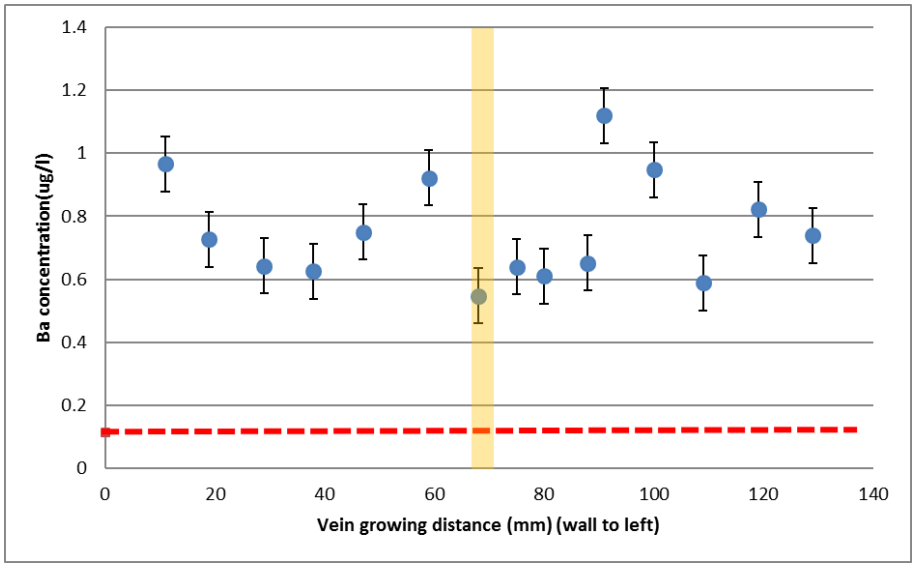
1.4
1.2
1
0.8
0.6
0.4
0.2
0
Ba concentration(ug/l)
0
20
40
60
80
100
120
140
Vein growing distance (mm) (wall to left)

(l)

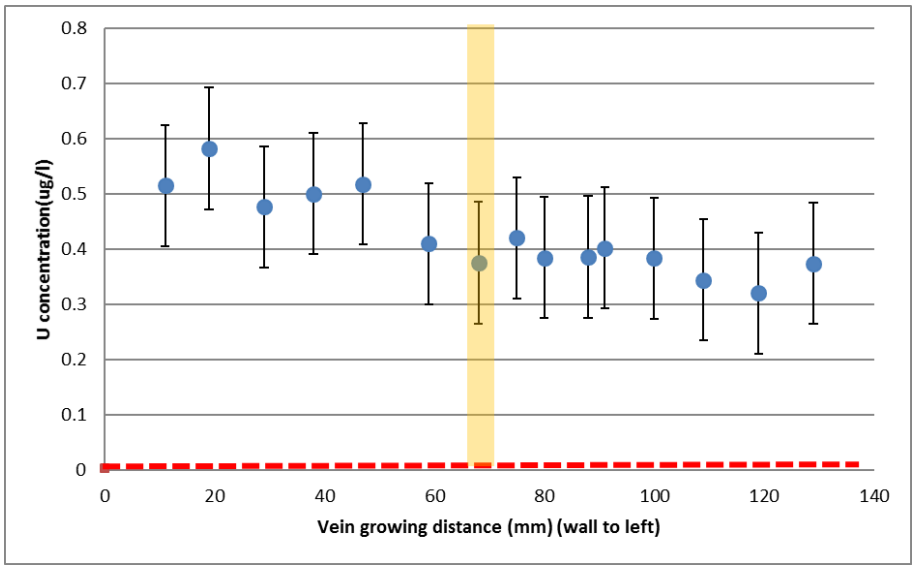
0.8
0.7
0.6
0.5
0.4
0.3
0.2
0.1
0
U concentration(ug/l)
0
20
40
60
80
100
120
140
Vein growing distance (mm) (wall to left)

(m)

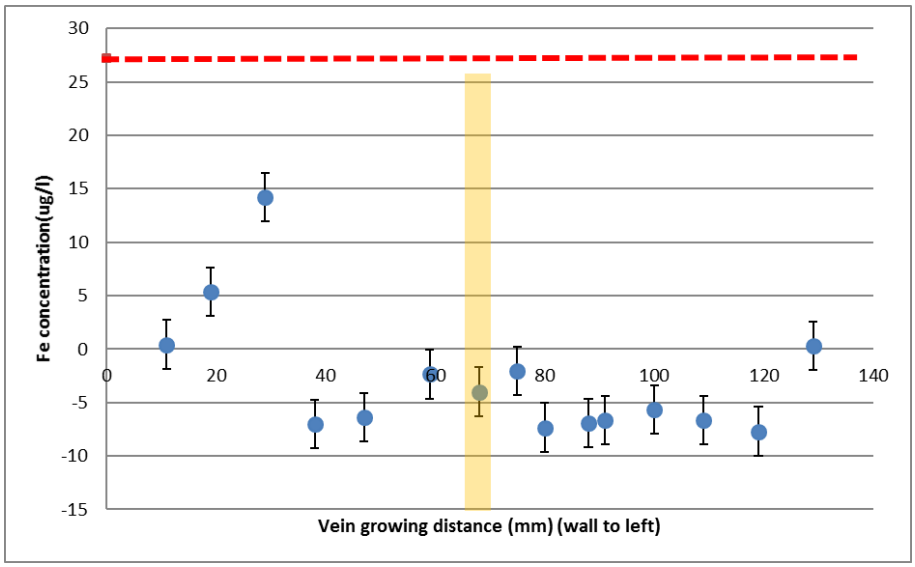
30
25
20
15
10
5
0
-5
-10
-15
Fe concentration(ug/l)
0
20
40
60
80
100
120
140
Vein growing distance (mm) (wall to left)

(n)

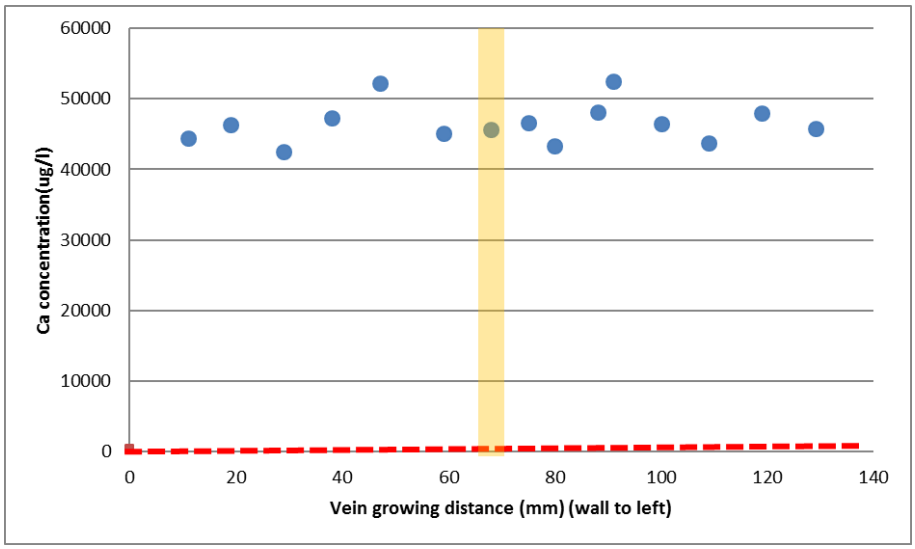

(o)

Figure 4- 30: Elemental concentration vs. vein growing distance based on the results of ICP-MS. The yellow-banded zone marks the colour variation of the thick, white aragonite vein. The vein wall is to the left of x-axis. Fifteen measured elements include: Li, Na, Mg, Al, P, Ca, Mn, Sr, Zn, Ba, K, U, Fe, B, Cu. The red dashed horizontal line is the level of the limit of detection and the error bar is the standard deviation calculated from blank samples.

The results for Fe, B, Cu are not useable for the study, because the element concentrations are lower than the limit of detection. The results for Li, Na, Mg, Al, P, Ca, Mn, Sr, Zn, Ba, K, U that exceed the detection limit are used for further analysis. No significant trend for any element concentration, or an obvious relationship between the visible banding and elemental concentrations could be observed. The reason for the observed colour variation cannot be resolved from element analysis.

4.3.6 Estimation of the composition of the paleo-fluid

Alkali metal elements and alkaline earth metals are known to substitute for Ca in aragonite crystals. The substitution is influenced by temperature and precipitation rate, so that the distribution factors could be various under different deposition environment. Comparatively, precipitation rate is a more important factor, the concentration in the precipitates rises with the increasing growth rate. The

distribution factors for aragonite are compiled by Veizer as the Table 4-4 below (Veizer, 1983):

Table 4- 4: Distribution coefficient for trace elements in aragonite

Element	Distribution factor	Reference
Sr	1	(Kitano et al., 1968, Kitano et al., 1973, Holland et al., 1964)
Na	0.00014	(White, 1977, Kitano et al., 1975)
Mg	0.0006-0.005	(Brand and Veizer, 1983)
Mn	0.86	(Raiswell and Brimblecombe, 1977, Brand and Veizer, 1983)
Ba	1-2	(Kitano et al., 1971, Kitano et al., 1973)

Using the element distribution equation of Eq. 4-2, the composition of paleo-fluid could be re-constructed using the composition of vein samples, which is obtained by electron microprobe and ICP-MS.

For paleo-fluid composition, the result of electron microprobe is used for Na analysis as for some samples, the concentration of Na is below the limit of detection for ICP-MS. 90 samples were selected for evaluation (Table 4-6). For other elements (Sr, Mn, Mg, Ba), ICP-MS results are used for better resolution for trace elements than the electron microprobe (Table 4-5).

Table 4- 5: The calculated geochemical composition of paleo-fluid using the distribution coefficienct given by Table 4-4. The distribution factors are in a range, here we use the maximum and minimum value of the distribution coefficient (Dc).

Samples ID ICP-MS	Ba/Ca max (Dc=2)	Ba/Ca min (Dc=1)	Mg/Ca max (Dc=0.005)	Mg/Ca min (Dc=0.0006)	Mn/Ca (Dc=0.86)	Sr/Ca (Dc=1)
YTCG1a	6.7E-06	3.3E-06	4.3E-01	5.1E-02	3.0E-04	1.1E-02
YTCG1b	4.8E-06	2.4E-06	6.3E-01	7.6E-02	4.4E-04	1.1E-02
YTCG1C1	4.6E-06	2.3E-06	6.2E-01	7.5E-02	4.3E-04	1.1E-02
YTCG1C2	4.1E-06	2.0E-06	2.8E-01	3.4E-02	2.0E-04	1.1E-02
YTCG1C3	4.4E-06	2.2E-06	3.8E-01	4.6E-02	2.7E-04	1.1E-02
YTCG1D1	6.3E-06	3.1E-06	9.9E-01	1.2E-01	6.9E-04	1.1E-02
YTCG1D2	3.7E-06	1.8E-06	4.3E-01	5.2E-02	3.0E-04	1.1E-02

YTCG1E1	4.2E-06	2.1E-06	4.3E-01	5.1E-02	3.0E-04	1.1E-02
YTCG1E2	4.3E-06	2.2E-06	3.8E-01	4.5E-02	2.6E-04	1.1E-02
YTCG1E3	4.2E-06	2.1E-06	3.9E-01	4.6E-02	2.7E-04	1.1E-02
YTCG1F1	6.5E-06	3.3E-06	5.8E-01	7.0E-02	4.0E-04	1.1E-02
YTCG1F2	6.2E-06	3.1E-06	4.6E-01	5.6E-02	3.2E-04	1.1E-02
YTCG1F3	4.1E-06	2.1E-06	4.0E-01	4.9E-02	2.8E-04	1.1E-02
YTCG1F4	5.3E-06	2.6E-06	5.3E-01	6.3E-02	3.7E-04	1.2E-02
YTCG1F5	4.9E-06	2.5E-06	3.6E-01	4.3E-02	2.5E-04	1.2E-02

Table 4- 6: The calculated Na/Ca of paleo-fluid using the distribution factor given by Table 4-5. The measured concentration of Na and Ca are from the electron microscope analysis ($Dc_{(Na/Ca)}$ =0.00014).

Sample ID	Na/Ca	Sample ID	Na/Ca	Sample ID	Na/Ca	Sample ID	Na/Ca
a-1	50.97	c1-5	41.04	e1-7	38.26	g1-4	24.18
a-3	65.80	c1-6	36.85	e1-8	46.22	g2-1	35.25
a-4	72.27	c1-7	35.04	e2-1	31.02	g2-2	28.70
a-5	52.36	c1-8	41.47	e2-2	39.40	g2-3	23.69
a-6	54.47	c1-9	41.08	e2-3	39.56	g2-4	22.75
a-7	58.11	c1-10	45.24	e3-1	45.63	g3-1	61.69
a-8	49.34	d1-1	40.86	e3-2	37.99	g3-2	26.09
b1-1	57.90	d1-2	34.01	e3-3	47.40	g3-3	22.44
b1-2	56.45	d1-3	39.99	e3-4	39.18	g4-1	34.12
b1-3	55.24	d1-4	38.32	e3-5	38.13	g4-2	32.42
b1-4	58.96	d1-5	34.63	e4-1	42.80	r1-1	29.60
b1-5	59.34	d1-6	47.01	e4-2	42.37	r1-2	29.22
b1-6	55.08	d1-7	34.42	f1-1	35.76	r1-3	26.47
b1-7	53.84	d1-8	39.56	f1-2	23.79	r1-4	10.99
b1-8	42.47	d2-1	57.71	f1-3	34.19	r1-5	53.04
b2-1	56.23	d2-2	34.93	f1-4	30.08	r1-6	54.89
b2-2	54.29	d2-3	21.78	f1-5	29.65	r1-7	56.49
b2-3	49.05	d2-4	17.29	f1-6	31.73	r2-1	22.21
b2-4	49.43	d2-5	33.69	f1-7	61.05	r2-2	33.58
b2-5	52.46	d2-6	43.58	f1-8	54.39	r2-3	23.25
b2-6	54.03	e1-1	36.71	f2-1	24.31		
b2-7	49.30	e1-2	36.83	f2-2	31.65		
c1-1	41.28	e1-3	45.50	f2-3	29.68		
c1-2	42.04	e1-4	38.16	g1-1	26.89		
c1-3	46.30	e1-5	36.20	g1-2	33.42		
c1-4	44.57	e1-6	39.96	g1-3	28.88		

The elemental composition data of present fluid are calculated using the data from the study of Kampman et al. (2007). Major elements of Na, Ca, Mg and minor elements of Sr, Mn and Ba are used for elemental study(Table 4-7). The ratio of Ba, Mg, Mn, Sr and Na againest Ca have been calculated (Table 4-5) and compared with the composition with the paleo-fluid.

Table 4- 7: Calculated ratio of chemical elements against Ca of the present Crystal Geyser using data from Kampman et al., (2007). The original data see Appendix 8.

Sample ID	Ba/Ca	Mg/Ca	Mn/Ca	Sr/Ca	Na/Ca
CG1	4.9E-07	3.7E-01	1.1E-03	5.6E-03	6.3E+00
CG2	4.9E-07	3.7E-01	1.1E-03	5.7E-03	6.3E+00
CG3	4.2E-07	3.7E-01	1.1E-03	5.7E-03	6.4E+00
CG4	5.3E-07	3.7E-01	1.1E-03	5.7E-03	6.4E+00
CG5	4.1E-07	3.7E-01	1.1E-03	5.7E-03	6.6E+00
CG6	4.2E-07	3.7E-01	1.0E-03	5.7E-03	6.5E+00
CG7	4.7E-07	3.7E-01	1.0E-03	5.7E-03	6.5E+00
CG8	4.7E-07	3.7E-01	1.0E-03	5.7E-03	6.6E+00
CG9	4.1E-07	3.6E-01	1.0E-03	5.7E-03	6.5E+00
CG10	4.9E-07	3.7E-01	1.1E-03	5.6E-03	6.1E+00
CG11	5.0E-07	3.7E-01	1.1E-03	5.6E-03	6.1E+00
CG12	5.1E-07	3.7E-01	1.1E-03	5.7E-03	6.0E+00
CG13	4.4E-07	3.7E-01	1.1E-03	5.7E-03	6.0E+00
CG14	5.1E-07	3.7E-01	1.1E-03	5.7E-03	5.9E+00
CG15	5.4E-07	3.7E-01	1.2E-03	5.8E-03	5.6E+00
CG16	6.0E-07	3.8E-01	1.2E-03	5.9E-03	5.0E+00
CG17	6.3E-07	3.8E-01	1.2E-03	6.0E-03	4.8E+00

Figure 4-31 is the box and whisker plot of the comparisons of paleo-fluid (n=15) and present fluid of the Crystal Geyser (n=17). Box and whisker plot display the degree of dispersion, skewness and outliers. The upper whisker shows largest value and lower whisker shows smallest value; the lower upper and lower parts of the box show upper and lower quartile; the line in the middle shows median.

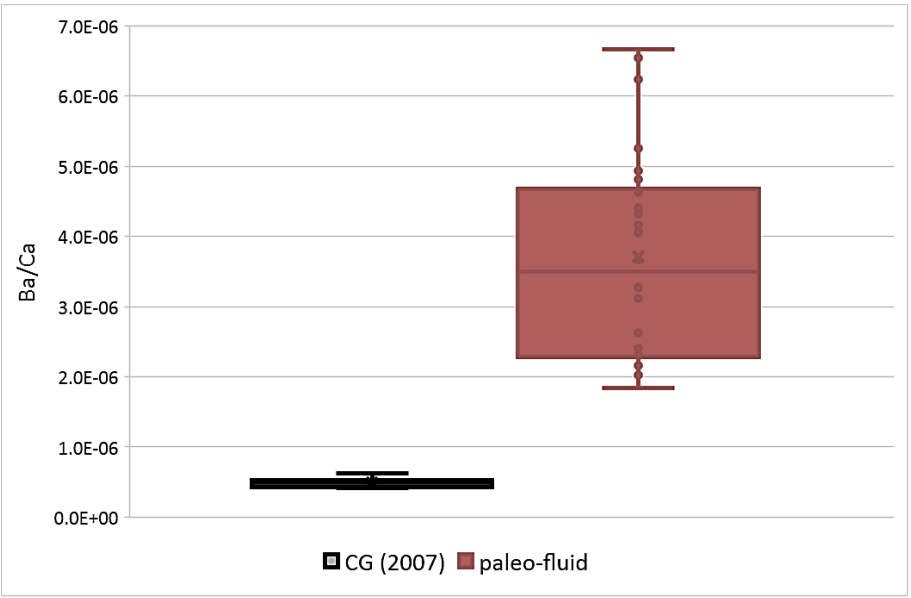
7.0E-06
6.0E-06
5.0E-06
4.0E-06
3.0E-06
2.0E-06
1.0E-06
0.0E+00
Ba/Ca
CG (2007)
paleo-fluid

(a)

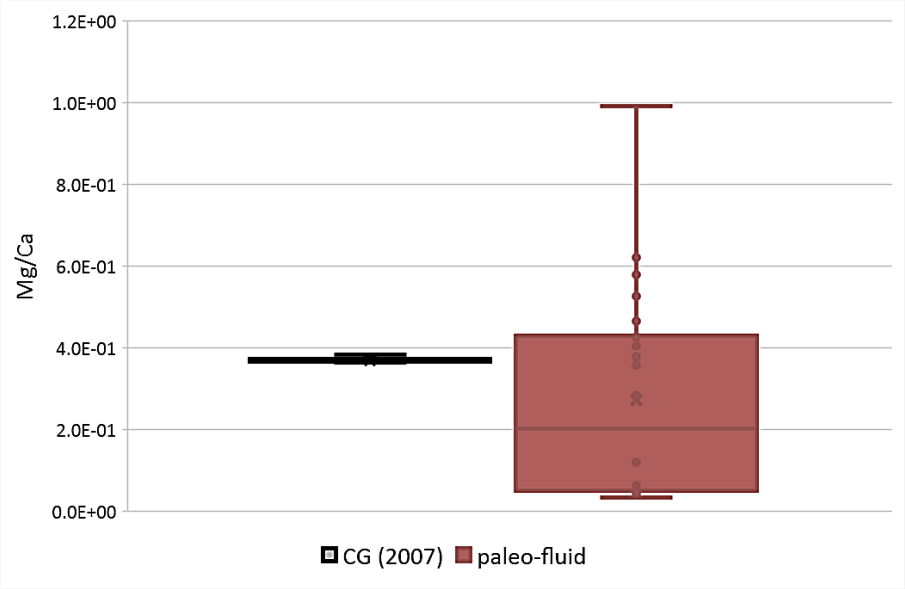
1.2E+00
1.0E+00
8.0E-01
6.0E-01
4.0E-01
2.0E-01
0.0E+00
Mg/Ca
CG (2007)
paleo-fluid

(b)

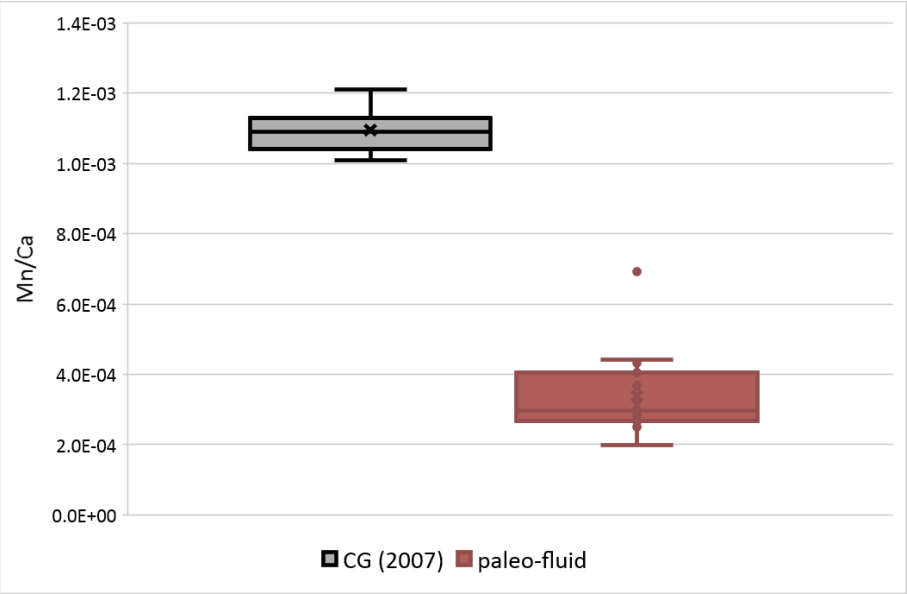
1.4E-03
1.2E-03
1.0E-03
8.0E-04
6.0E-04
4.0E-04
2.0E-04
0.0E+00
Mn/Ca
CG (2007)
paleo-fluid

(c)

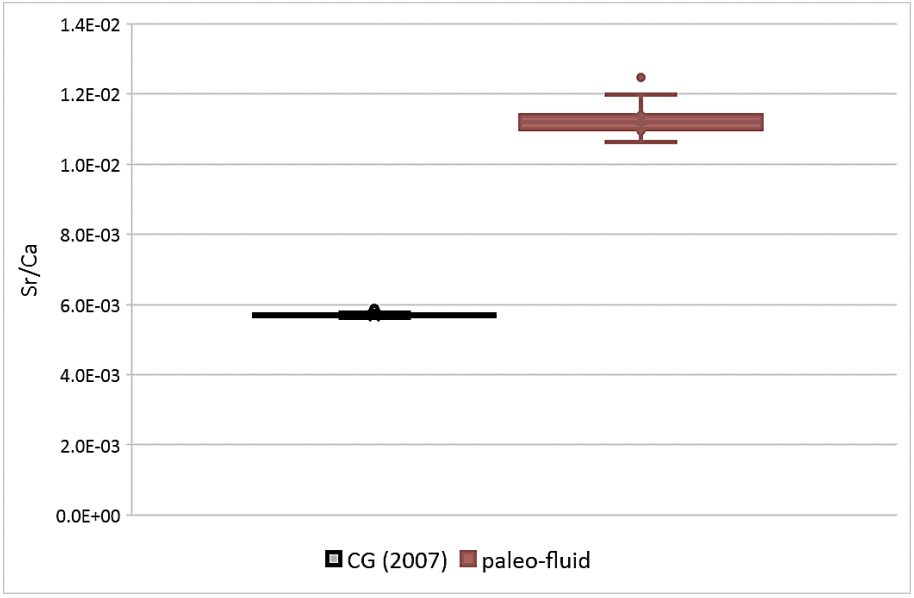
1.4E-02
1.2E-02
1.0E-02
8.0E-03
6.0E-03
4.0E-03
2.0E-03
0.0E+00
Sr/Ca
CG (2007)
paleo-fluid

(d)

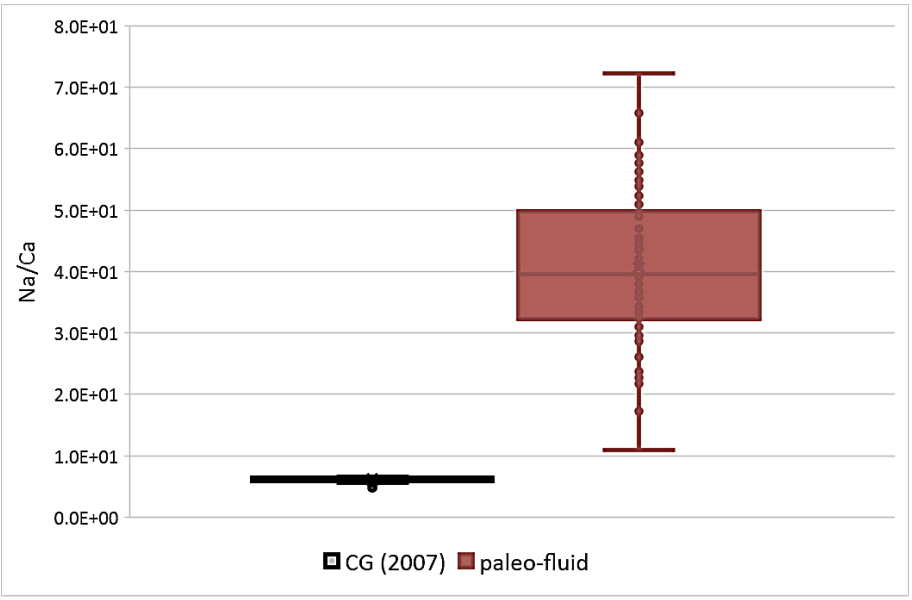

(e)

Figure 4- 31: Box plot for elemental comparisons of paleo-fluid calculated from veins and present fluid of Crystal Geyser. (a) Na/Ca; (b) Sr/Ca; (c) Mn/Ca; (d) Mg/Ca; (e) Ba/Ca. The present fluid data is compiled from data from Kampman et al. (2007). The red box is calculated molar ratio of elements for paleo-fluid and the grey box is that of present Crystal Geyser spring.

The composition of present Crystal Geyser is quite consistent during the eruptions, while that of paleo-fluid displays much larger range (especially for Ba/Ca, Mg/Ca and Na/Ca). The reason for the bigger change for the paleo-fluid composition could be a) the fluid composition actually varied during the deposition of the aragonite veins; and b) the distribution coefficients varied because of changes in temperature and /or growth rate. The distribution coefficient used for Ba/Ca ranges from 1-2, and for Mg/Ca is from 0.0006 to 0.005 (Table 4-3).

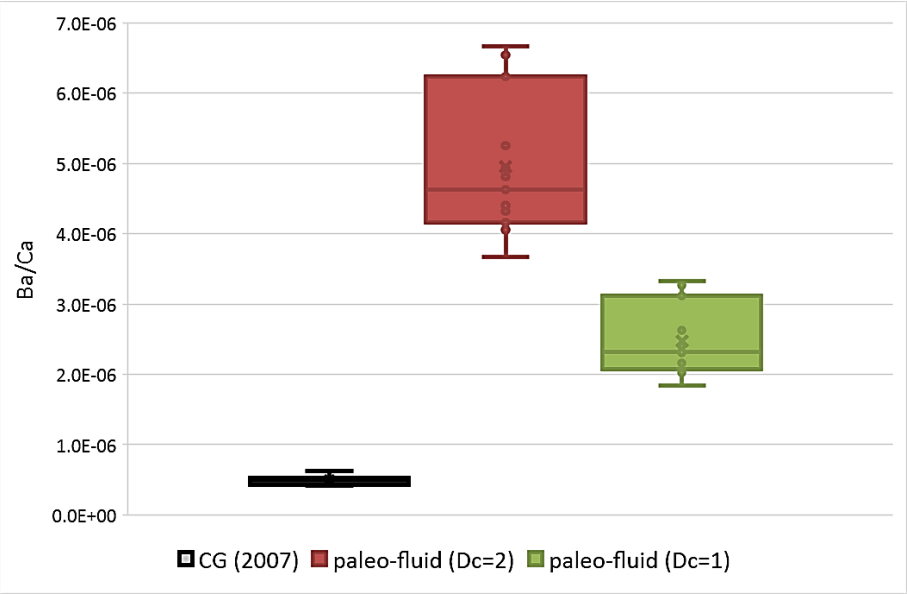

(a)

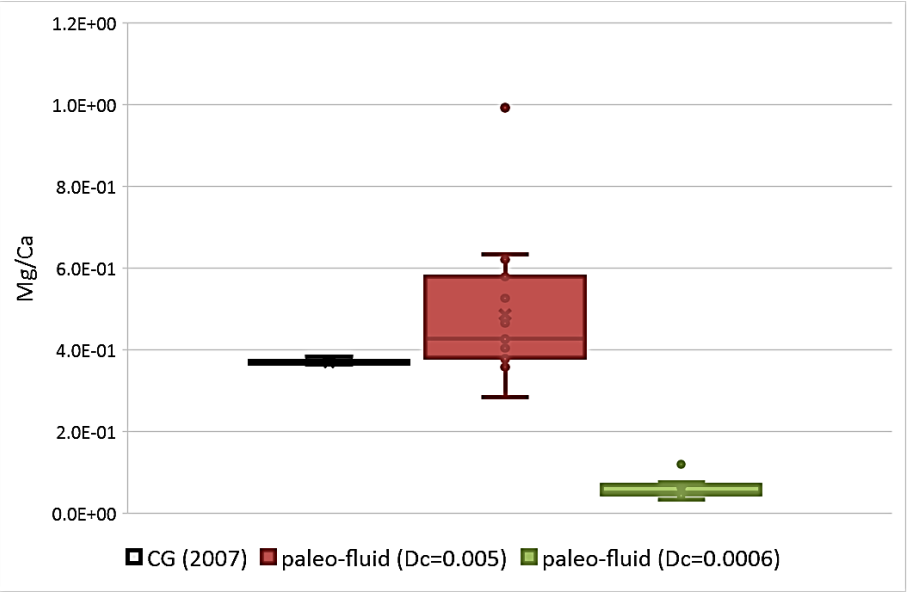

(b)

Figure 4- 32: Comparisons of the elements with big range of distribution coefficient (Dc(Ba/Ca) =1~2; Dc(Mg/Ca) =0.0006~0.005).

The maximum and minimum distribution coefficient have been utilized to compare where the big variations are derived from (Fig. 4-32). It is evident to see that even we use the single number of coefficient, the distribution of Ba/Ca and Mg/Ca for the paleo-fluid (n=15) is still wider than the present samples fluid (n=17). Therefore, we

could confidently conclude that the composition of paleo-fluid had been changed during the precipitation of the aragonite vein (T2-vein).

By comparing the paleo-fluid and present composition data, we can conclude that CO_2-rich fluid has changed since the vein was deposited. The reason behind this change is unknown, however it is possibly owing to ongoing seismic activity, or the self-healing and sealing by mineral precipitation of fractures (Faulkner et al., 2010), which modified the fault system, fluid pathways and circulation pattern. Whatever the reason is, the present fluid erupted from the Crystal Geyser appears to be different from the paleo-fluid that deposit the sampled aragonite vein.

- Comparing paleo-fluid to multiple CO_2 springs in Green River

In order to have a more comprehensive comparison, the calculated paleo-fluid composition is compared with other CO_2 springs in Green River region by the Little Grand Wash fault and Salt Wash Graben fault system: Torrey's Spring, Tenmile Geyser, Pseudo-Tenmile Geyser, Chaffin Ranch Geyser, Green River Airport Well, Big Bubbling Spring, Small Bubbling Spring, Side Seep Big Bubbling and Tumble Weed Geyser. The geochemical composition of fluids are compiled from Spangler et al. (1996), Kampman et al. (2007) and Carruthers (2012, doctorate thesis) (data see Appendix 9). Crystal Geyser and Green River Airport Well locate on the footwall of the Little Grand Wash Fault; Tumber Well Geyser locates to the south of the Salt Wash Graben Fault system, by the side of the Green River; the other springs cluster at the north strand of the Salt Wash Graben Fault. The location of studied geysers is shown in Figure 3-1.

The calculted ratio of elemets vs. Ca are listed in Appendix 9. The change of the elemental composition of the geysers are compared using the fluid samples from the year 1996, 2007 and 2012 (Figure 4-33). The elemental ratio (elements against Ca) is used instead of pure elemental concentration to reduce the errors derived from the experimental processes.

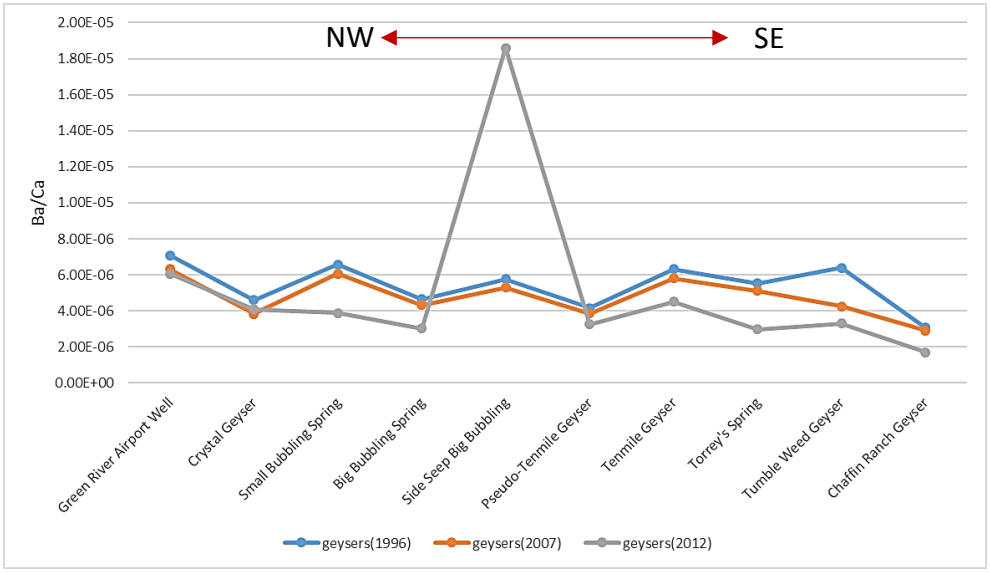
NW
SE
Ba/Ca
2.00E-05
1.80E-05
1.60E-05
1.40E-05
1.20E-05
1.00E-05
8.00E-06
6.00E-06
4.00E-06
2.00E-06
0.00E+00
Green River Airport Well
Crystal Geyser
Small Bubbling Spring
Big Bubbling Spring
Side Seep Big Bubbling
Pseudo-Tenmile Geyser
Tenmile Geyser
Torrey's Spring
Tumble Weed Geyser
Chaffin Ranch Geyser
geysers(1996)
geysers(2007)
geysers(2012)

(a)

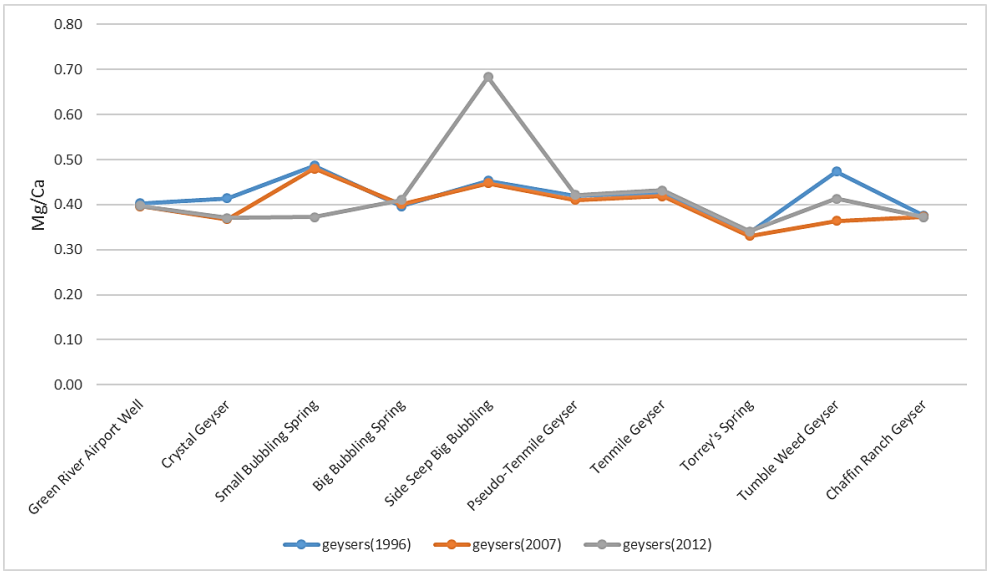
Mg/Ca
0.80
0.70
0.60
0.50
0.40
0.30
0.20
0.10
0.00
Green River Airport Well
Crystal Geyser
Small Bubbling Spring
Big Bubbling Spring
Side Seep Big Bubbling
Pseudo-Tenmile Geyser
Tenmile Geyser
Torrey's Spring
Tumble Weed Geyser
Chaffin Ranch Geyser
geysers(1996)
geysers(2007)
geysers(2012)

(b)

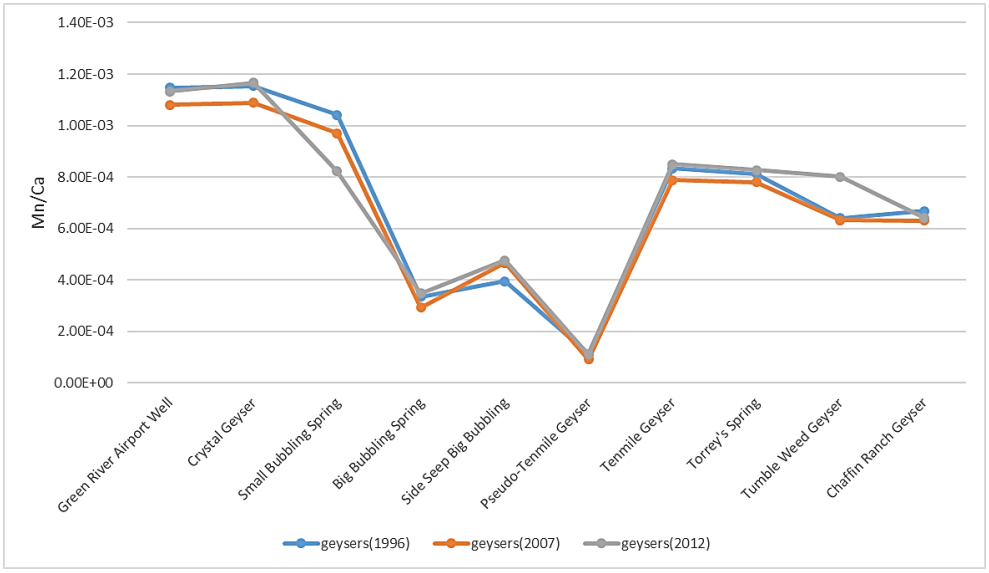
1.40E-03
1.20E-03
1.00E-03
8.00E-04
6.00E-04
4.00E-04
2.00E-04
0.00E+00
Mn/Ca
Green River Airport Well
Crystal Geyser
Small Bubbling Spring
Big Bubbling Spring
Side Seep Big Bubbling
Pseudo-Tenmile Geyser
Tenmile Geyser
Torrey's Spring
Tumble Weed Geyser
Chaffin Ranch Geyser
geysers(1996)
geysers(2007)
geysers(2012)

(c)

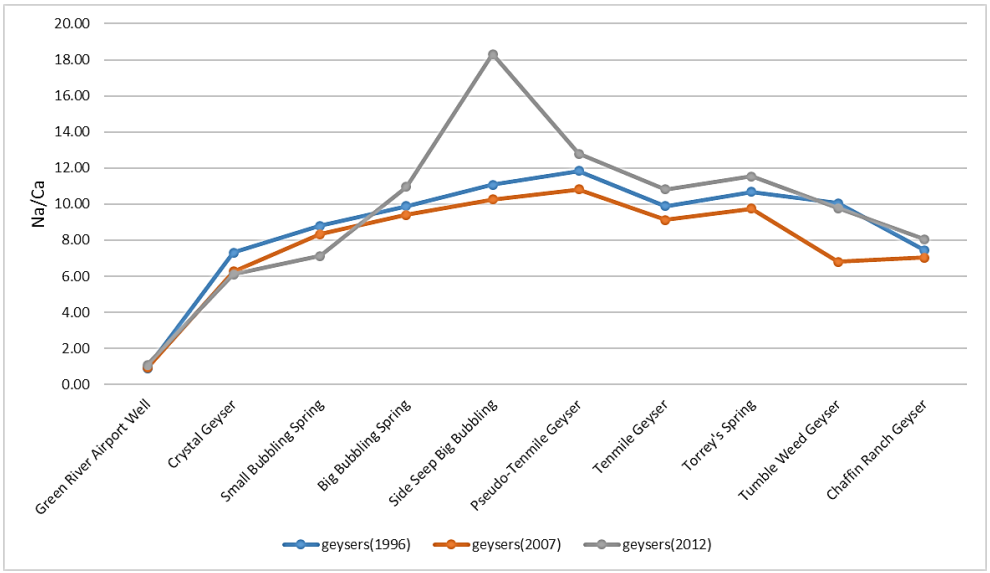
20.00
18.00
16.00
14.00
12.00
10.00
8.00
6.00
4.00
2.00
0.00
Na/Ca
Green River Airport Well
Crystal Geyser
Small Bubbling Spring
Big Bubbling Spring
Side Seep Big Bubbling
Pseudo-Tenmile Geyser
Tenmile Geyser
Torrey's Spring
Tumble Weed Geyser
Chaffin Ranch Geyser
geysers(1996)
geysers(2007)
geysers(2012)

(d)

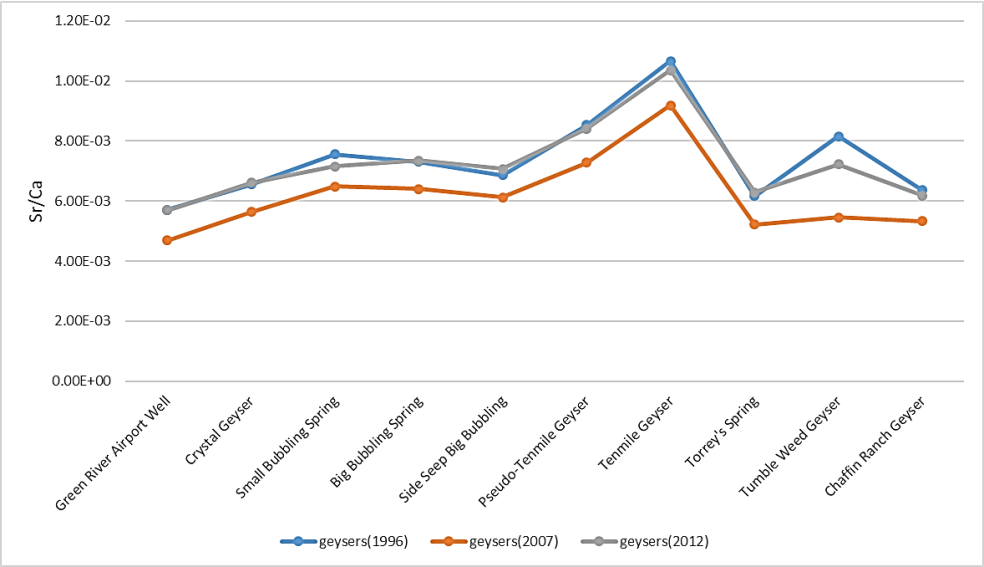

(e)

Figure 4- 33: elemental composition of the total ten CO_2 geysers near the Little Grand Wash fault and Salt Wash fault system based on the fluid sampled in the year 1996 (blue), 2007 (orange) and 2012 (grey) by Spangler et al., Kampman et al. and Carruthers. The x-axis from the left to right are listed the geysers from the north to the south according to the latitude. The locations of the springs refer to Figure 3-3.

The change in geochemistry composition is not significant from the year 1996 to 2012 according to the comparison. Except for one exceptional high Ba/Ca, Mg/Ca and Na/Ca values occurs to Side Seep Bubbling, no significant variations happened during this period. In general, the concentration of the studied elements decreased slightly from 1996 to 2012. The cause for the dramatically high element ratios of Ba/Ca, Mg/Ca and Na/Ca for Side Seep Bubbling in 2012 is unknown. No significant change could be seen between the fluid composition of 2007 and 2012 (sampled after drilling), which means the scientific drilling well CO2W55 (in June 2012) has no significnat influence on the spring composition.

Spatially, Ba/Ca and Mg/Ca ratio remain similar for these nine springs, while Mn/Ca shows bigger difference, which is higher in northern geysers (Airport Well and Crystal Geyser) than Salt Wash Fault system (espetially low ratio for Big Bubbling, Side Seep BBS and Pseudo-Tenmile); Na/Ca ratio increases southwardly from 1 to 10; Sr/Ca ratio shows especially high value in Pseudo-Tenmile and Tenmile springs, but remains relatively consistent for the rest springs.

In Fig. 4-35 the calculated paleo-fluid composition is compared with present day data from the springs in the vicinity of the Green River fault system and to the Ismay brine (location see Figure 4-1 in Greater Aneth oil field area) using box and whisker plots. The outliers of Side Seep Bubbling spring have been removed from the data. The geochemistry of Ismay brine is from Spangler et al. (1996).

From the comparisons between paleo-fluid and multiple springs, the composition of the paleo-fluid has more resemblance to the composition of the present springs of BBS, SSBB, PTG and TG (Big Bubbling Spring, Side Seep Big Bibbling, Pseudo-Tenmile Geyser and Tenmile Geyser) in terms of Mn/Ca and Sr/Ca (Fig. 4-35 (c) and (e)). These springs are all located by the side of Salt Wash Graben fault, to the south of the Little Grand Wash fault. In addition, the paleo-fluid composition has more similarity with the saline Ismay brine water than the very “fresh” Airport Well spring and the Crystal Geyser (which is composed of only 10-20% of Ismay brine and 80%-90% of Navajo fluid, Wilkinson et al. 2009), which suggests the paleo-fluid might be more saline than present Crystal Geyser spring.

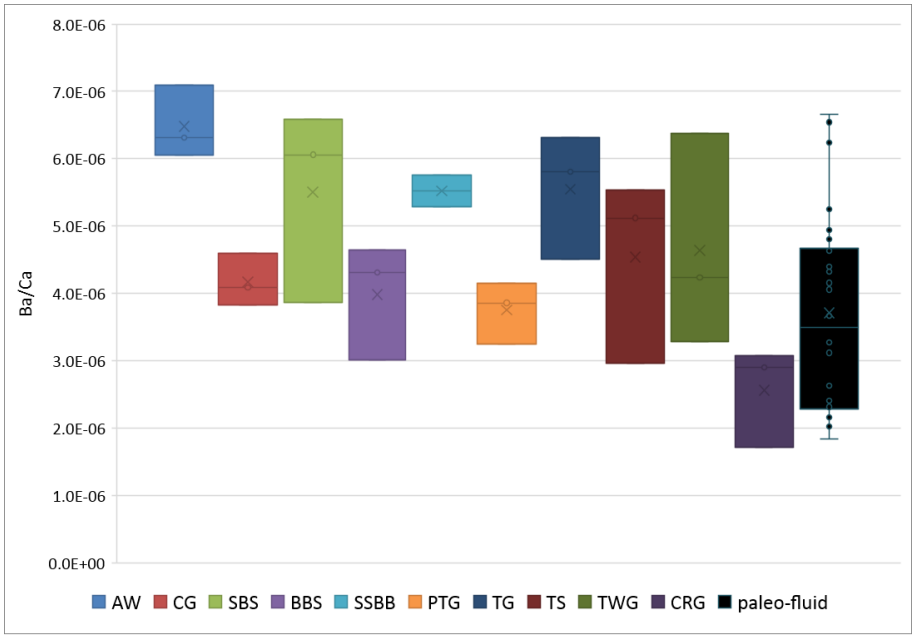

(a)

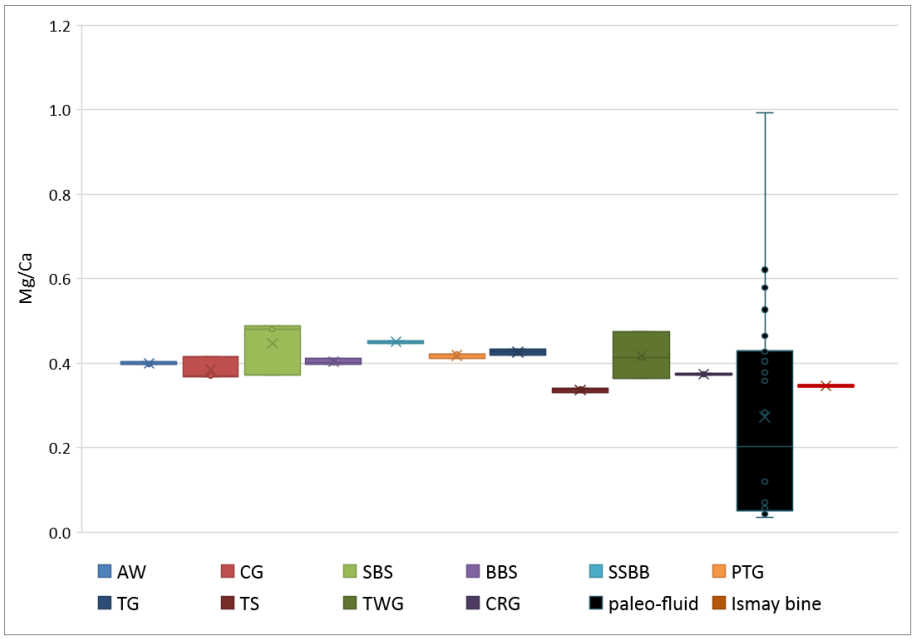
1.2
1.0
0.8
0.6
0.4
0.2
0.0
Mg/Ca
AW
CG
SBS
BBS
SSBB
PTG
TG
TS
TWG
CRG
paleo-fluid
Ismay bine

(b)

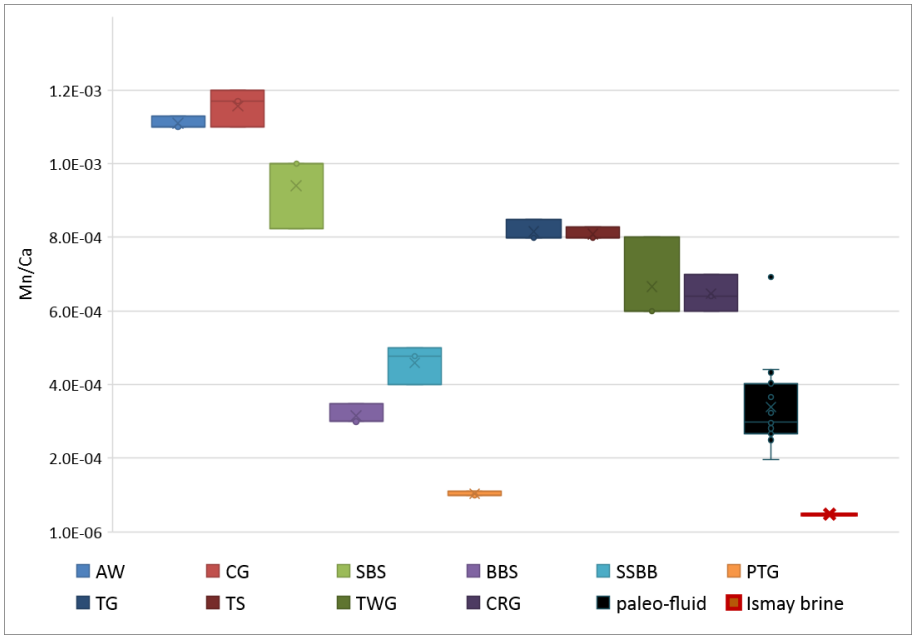
1.2E-03
1.0E-03
8.0E-04
6.0E-04
4.0E-04
2.0E-04
1.0E-06
Mn/Ca
AW
CG
SBS
BBS
SSBB
PTG
TG
TS
TWG
CRG
paleo-fluid
Ismay brine

(c)

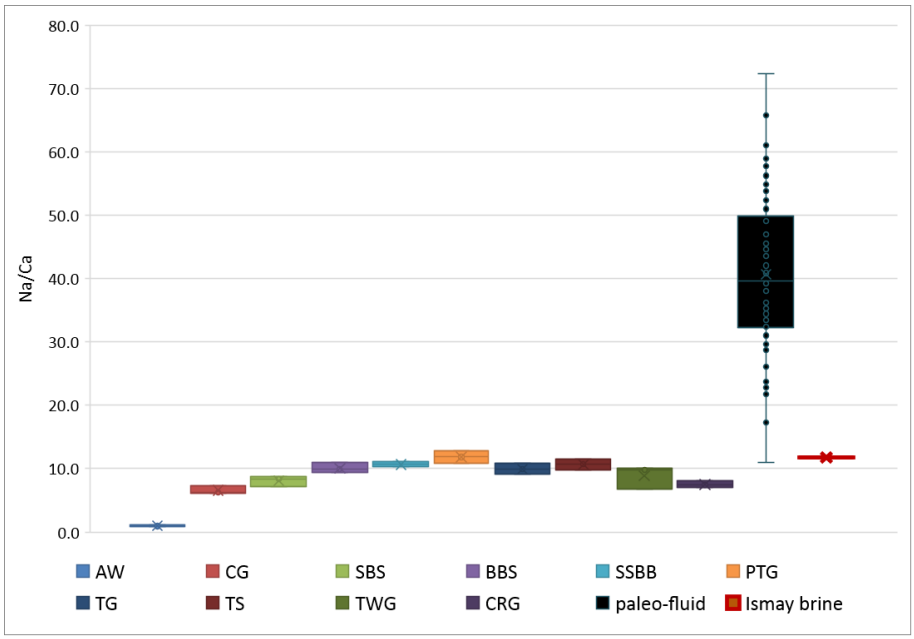

(d)

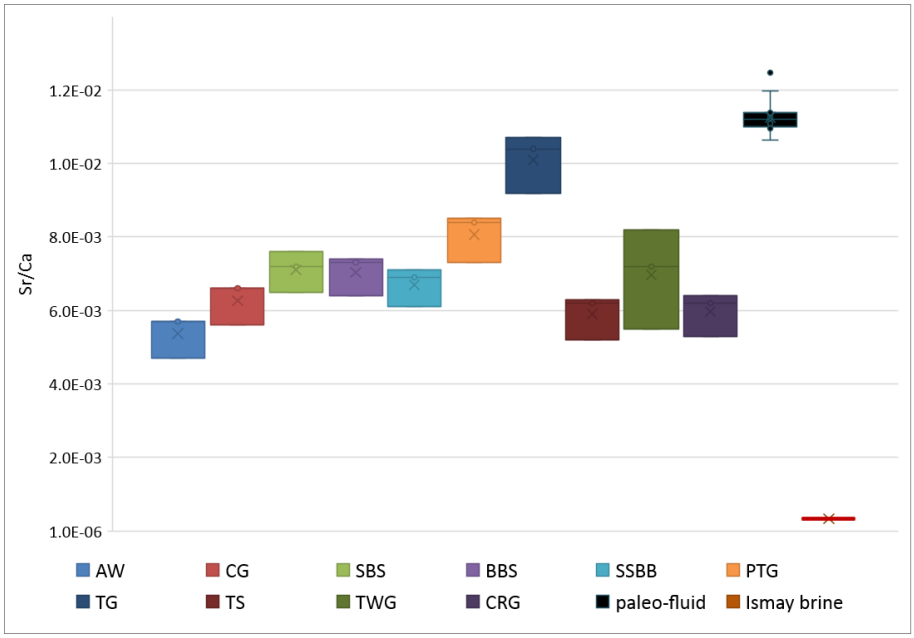

(e)

Figure 4- 34: elemental composition of paleo-fluid compared with 10 springs in the Green River region. The x-axis from the left to right are listed the geysers from the north to the south according to the latitude. AW=Airport well, CG=Crystal Geyser, SBS= Small Bubbling Spring, BBS= Big Bubbling Spring, SSBB= Side Seep Big Bubbling, PTG= Pseudo-Tenmile Geyser, TG= Tenmile Geyser, TS= Torrey's

Spring, TWG= Tumble Weed Geyser, CRG= Chaffin Rach Geyser (data see Appendix 9).

4.3.7 Fluid-fluid mixing model for the paleo-fluid

To estimate the percentage of the brine water intrusion, we cross-plotted the elemental ratio of Sr/Ca against Na/Ca to reflect the fluid mixing from two end members (Fig. 4-36): one end-member is Paradox brine (Rosenbauer et al., 1992), which is the most saline fluid collected from the layer that just above the a near-surface salt dome of the Paradox Formation, containing large amount of K, Na, Ca and Mg (location see Figure 4-1). The Paradox Basin contains thick evaporites deposit in the Pennsylvanian Paradox Formation and Mississippian Leadville Limestone, which comprise the major source of saline fluid (Rosenbauer et al., 1992). The other member that composes the paleo-fluid is the Airport Well spring, where is the recharged surface meteoric water which contains the least input of brine fluid, and it is the nearest geyser from the source of meteoric flow (see the meteoric charge trajectory in Figure 6-33).

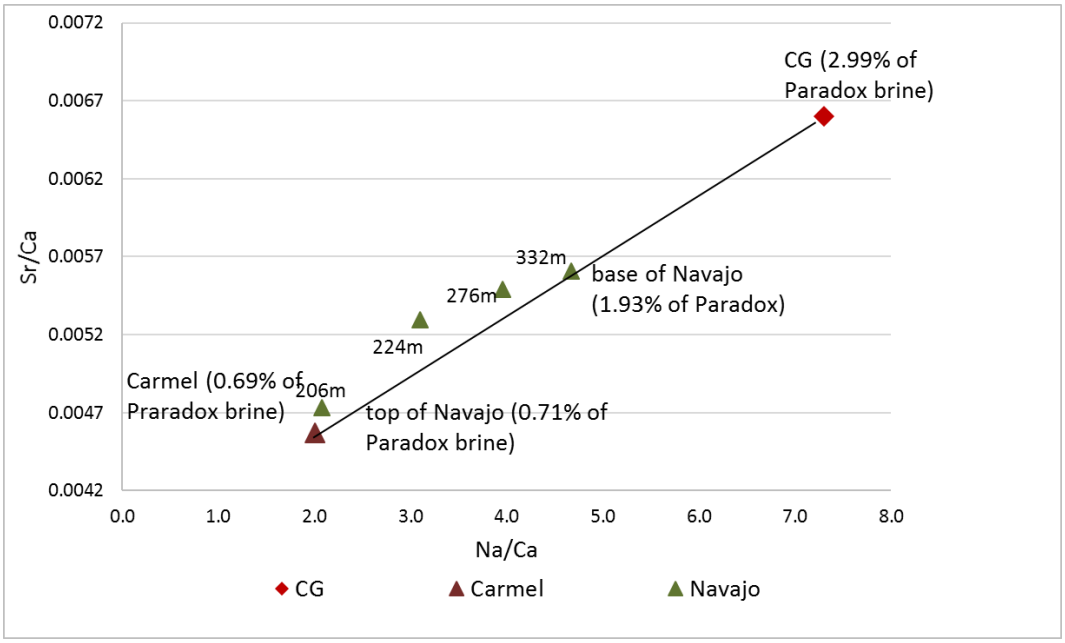

Figure 4- 35: Cross-plot of Sr/Ca against Na/Ca for fluid samples of the Crystal Geyser, and the samples of Entrada, Carmel, Navajo formations from well CO2W55

(data and percentage of the end-member fluids are from Kampman et al., 2014) (the location of well CO2W55 refers to Figure 3-1).

The fluid samples of Navajo formation (dark green triangle) was collected downhole from different depth (206m, 224m, 276m, 322m) at formation pressure and the sample of Carmel formation (fracture zone), respectively (Kampman et al., 2014) (data see Appendix 10). The salinity of the porewater of Navajo formation increases with the depth increase, accompanied with the increase of heavy oxygen isotope ratios, indicating the intrusion of saline water from deeper Paradox Formation by comparing the North American Meteoric Water Line (Kampman et al., 2014). The brine intrusion increases schematically from the top of the formation (0.71% of Paradox brine) to the bottom (1.93% of Paradox brine) (Fig. 4-36). Crystal Geyser spring contains slightly more of Paradox brine (2.99%) than the samples from well CO2W55, because the vent of Crystal Geyser is spatially farther from the meteoric source and nearer to the big fault than well CO2W55.

The general linear correlation of Sr/Ca vs. Na/Ca in Figure 4-36 demonstrates the inputs of meteoric water basically result from physical combination with not significant mineral reactions. This result is consistent with the conclusions of Kampman et al. (2014) who used Br and Sr against Cl as tracers, thus implying the cross-plot of Sr/Ca vs. Na/Ca is a valid tracer for Paradox brine intrusion.

The paradox brine consists about 3% of Crystal Geyser spring, and consists around 5-6% of other springs in the Green River area in the model of Kampman et al., (2014), while the proportion of Paradox brine is around 5-6% if we use Sr/Ca vs. Na/Ca as tracer (Figure 4-37). The deviation of the composition ratio is probably caused by mineral reactions concerning Calcium ion. Kampman et al. used Br and Cl instead to avoid the influence of fluid-rock reactions (Br and Cl could not be used in this study because no distribution coefficients are available for Na and trace the fluid composition).

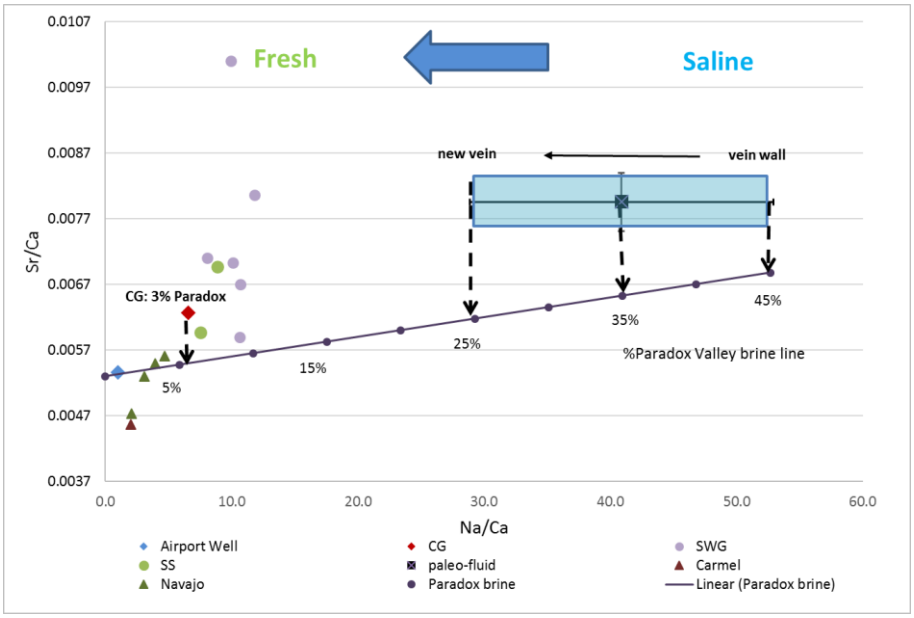

Figure 4- 36: Elemental ratio cross-plot of Sr/Ca vs. Sr/Ca to show the mixing of various fluids samples of the pleo-fluid (square), multiple springs in the flow path of Salt Wash Graben fault (round), Little Grand Wash fault flow path (diamond). fluid samples from CO2W55 drill hole (triangle). CG=Crystal Geyser; SWG=springs by Salt Wash Graben faut (Small Bubbling Spring, Big Bubbling Spring, Side Seep Big Bubbling, Pseudo-Tenmile Geyser, Tenmile Geyser, Torrey's Spring); SS=southern springs (Tumble Weed Geyser, Chaffin Rach Geyser). The data of CO2W55 is from Kampman et al., (2014).

The Na/Ca of the paleo-fluid shows a wide range with the proportion of Paradox brine water decreased during vein growth. The brine composes around 45% of the fluid at the beginning of the vein growth (old vein), while it gradually decreases to around 25% in the end (new vein). The decrease in Na/Ca during vein growth is presented in Figure 4-38 in comparison with the Paradox mixing line. The drop in Na/Ca of the paleo-fluid suggests the proportion of the Paradox brine decreases.

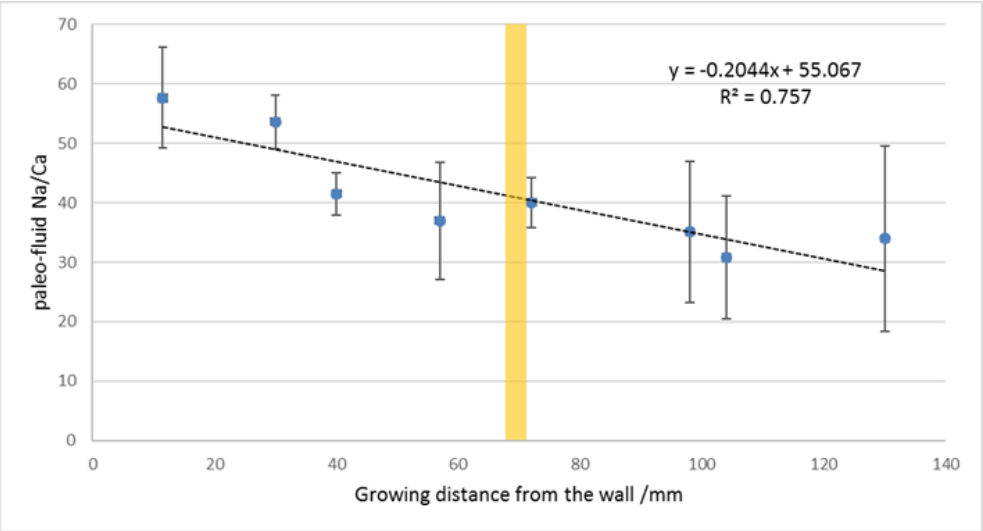

Figure 4- 37: Na/Ca of paleo-fluid against the vein growing distance from the wall. The vein here is sample T2-vein discussed in the previous sections. The yellow bends shows the location for colour variation on the vein.

4.3.8 Analysis of fluid source and deposition environment of the vein using isotopic methods

a. Sr isotope test for the formation process

There is no significant fractionation between the parent fluid and the precipitation for $^{87}Sr/^{86}Sr$, so that $^{87}Sr/^{86}Sr$ value was utilized to distinguish the veins formed by diagenetic or from CO_2-charged fluids. Measured Sr isotope values for different vein samples were displayed in Table 4-8. The result is compared with the $^{87}Sr/^{86}Sr$ value of fluids and carbonate veins in Paradox basin (compiled data in Figure 4-39). The result shows that two carbonate veins in T2 (T2-vein and sample YS014 -09) are formed by CO_2-charged fluid with $^{87}Sr/^{86}Sr$ greater than 0.712, while the rest calcite veins were from diagenetic processes with $^{87}Sr/^{86}Sr$ of around 0.708~0.710.

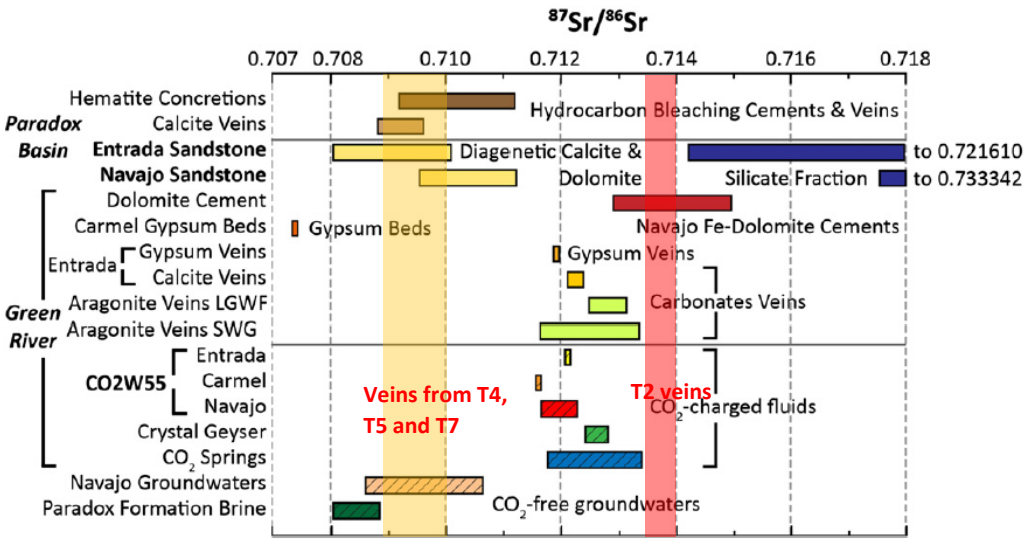

Figure 4- 38: $^{87}Sr/^{86}Sr$ ratio for fluids and minerals relevant to this study. The data were compiled from brine from the Paradox basin, Green River, and Navajo groundwater and Paradox formation brine by Kampman et al. (2014) using collective data (Spangler, 1996, Kampman et al., 2009, Truini, 2003, Goldstein et al., 2008, Chan et al., 2000).

Table 4- 8: $^{87}Sr/^{86}Sr$ value for veins in different locations (samples description see Table 4-3)

Sample No	$^{87}Sr/^{86}Sr$	% Std Err	Location	Description	Parent fluid
YS014 -09	0.7130	0.001	T2	Vein in Sst	CO_2-charged
YS014 -27	0.7094	0.0014	T5	Vein in Sst	diagenetic
YS014 -42	0.7081	0.0015	T7	Vein in Mancos shale	diagenetic
YS014 -65	0.7087	0.0012	T4	contact vein in Mancos shale	diagenetic
T2-Vein	0.7128	0.0017	T2	aragonite vein	CO_2-charged

b. Estimate the deposition environment using measured stable isotope

The proportion of warm to arid pollen taxa allows an estimate of the climate of the area through time (Fig. 4-40; Jimenez-Moreno et al., 2007). The deposition of T2-vein is between the Heinrich events H5 and H6 when the warm-arid taxa ratio is lower than the present ratio, which indicates the temperature when T2-vein deposit was probably colder compared to the present surface temperature of around 18-20 ˚C (Kampman et al., 2012, Kampman et al., 2014).

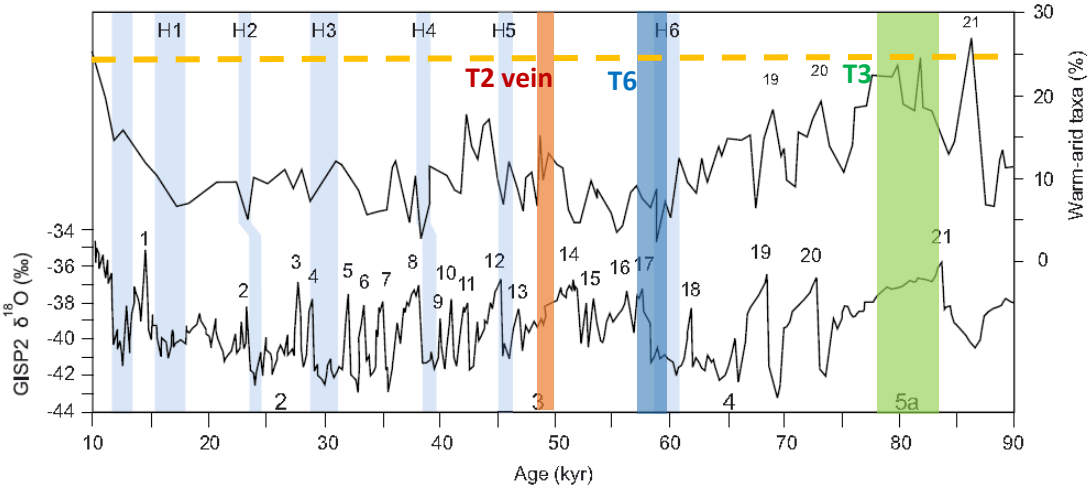

Figure 4- 39: Millennial-scale vegetation and climate change for the 10-90 ka interval at Bear Lake, Utah (Jiménez-Moreno et al., 2007). The red shaded zone shows the time period when T2-vein deposited; the blue shaded zone indicates the time period of T6 deposition; the green shaded zone shows the time when T3 deposited. The yellow dashed line indicates the present warm-arid taxa level.

As the aragonite vein (sample T2-vein) sample was demonstrated by formed by CO_2-charged fluid rather than diagenesis, the isotope could track the CO_2-rich paleo-fluid that precipitated the vein. The deposition mechanism that deposit the aragonite veins could be generalized as the CO_2-rich fluid migrates upwards to shallower depth that drives aragonite deposition and degassing at the same time as the fluid gets super-saturated at lower pressure (Kampman et al., 2014). The process is displayed as following equation:

$$2HCO_3^-(aq.) + Ca^{2+} \rightarrow CaCO_3(s) + CO_2\,(g) + H_2O \qquad \text{Equation 4-3}$$

As the equation progress to the rightward, $\delta^{18}O$ and $\delta^{13}C$ in bicarbonate in the fluid will preferentially deposit in aragonite, making which is more and more accumulated with heavy isotope. Therefore, the aragonite deposition can be used as tracer for the isotope values for bicarbonate in the paleo-fluid. The results of carbon isotope and oxygen isotope are displayed in table 4-10. The oxygen isotope fractionation equation between aragonite and H_2O is (Zhou and Zheng, 2003):

$$\Delta_{aragonite-H2O} = 20.44 \times \frac{10^3}{T} - 41.48\ (K) \qquad \text{Equation 4-4}$$

Where Δ_{ar-H2O} is the fractionation between aragonite and H_2O; T is the precipitation temperature. Oxygen isotope of T2-vein ranges from -12.32‰ to -12.49‰. A plot for oxygen isotope against carbon isotope was displayed in Figure 4-41.

Table 4- 9: Isotopic data of sub-samples of T2-vein (sub-samples CGA-CGF).

Sub-sample ID	Distance from the vein wall/mm	$\delta^{13}C$ VPDB‰	$\delta^{18}O$ VPDB‰	$d^{18}O$ SMOW‰
CG-A	8	5.28	-12.35	18.13
CG-B	15	5.31	-12.49	17.99
CG-C	30	5.40	-12.32	18.16
CG-D	55	5.40	-12.35	18.12
CG-E	70	5.43	-12.46	18.02
CG-F	95	5.52	-12.40	18.07
Average		5.39	-12.40	18.08

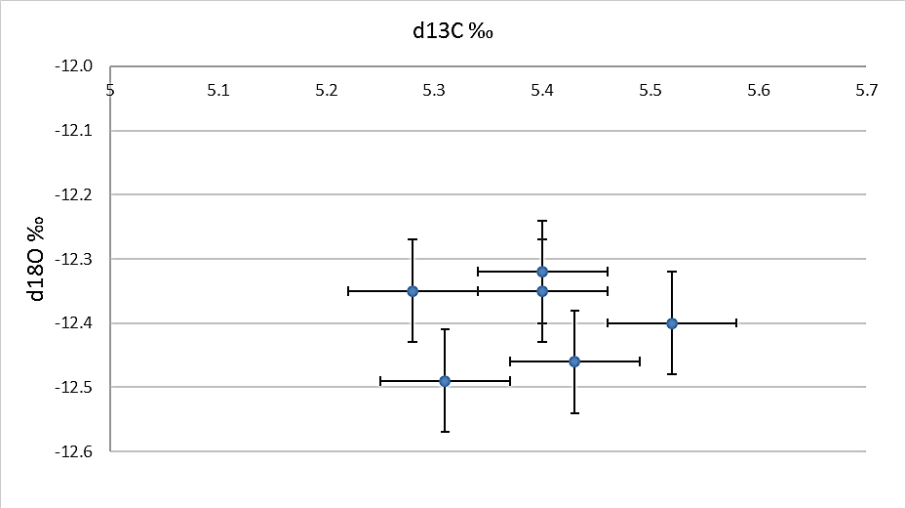

Figure 4- 40: Oxygen isotope vs. carbon isotope ratio for sub-samples of T2-vein (CGA-CGF).

Based on the conclusion of previous section, the paleo-fluid deposited the aragonite vein is a mixture of 25-45% of Paradox brine plus 55-75% of meteoric fluid. We can use oxygen isotope to test the reliability of the conclusion with the real measured oxygen isotope of the aragonite vein. The $\delta^{18}O$ of Paradox Valley brine ranges around -7.0‰ to -5.0‰ V-SMOW based on Morrison and Parry (1986). The late Cretaceous seawater has the $\delta^{18}O$ value of -1.2‰ (V-SMOW). The produced brine water from Ismay brine oil fields ranges from -7.6‰ V-SMOW to +2.0‰ V-SMOW (averaged at -5.0‰ V-SMOW for 5 samples, data see Appendix 11) (Spangler et al., 1996). We assumed -5.0‰ V-SMOW (-35‰ V-PDB) to be reasonable for representative value for Paradox brine water. The oxygen isotope of the Airport Well spring, which is the meteoric fluid end member of the fluid mixing, is -13.8‰ (V-SMOW) (Kampman et al., 2014).

The deposition temperature could be estimated when we confine the $\delta^{18}O$ value of aragonite within the range of the paleo-fluid oxygen isotope value from -12.2‰ to -12.6‰. The predicted temperature is around 12-18 ºC from the beginning to the end of the vein growth. The beginning of the vein growth is about 5-6 ºC below the present temperature (the temperature of present springs is 18-20 ºC in Green River, recorded by Kampman et al. (2014) and Heath (2004)). The calculated $\delta^{18}O$ of aragonite vein samples is shown in Table 4-10.

Table 4- 10: Estimated deposition temperature and $\delta^{18}O$ value for aragonite precipitated by mixed fluid of 25-45 % of Paradox Valley brine and 55-75% of meteoric fluid.

T/ ºC	Airport Well/ $\delta^{18}O$ (V-SMOW)	Paradox brine/ $\delta^{18}O$ (V-SMOW)	Mixing proportion	mixed fluid/ $\delta^{18}O$ (V-SMOW)	Aragonite/ $\delta^{18}O$ (V-SMOW)	Aragonite/ $\delta^{18}O$ (V-PDB)
18	-13.8	-5.0	45% Paradox: 55% Airport Well	-9.8	18.9	-11.9
		-6.0		-10.3	18.4	-12.4
		-7.0		-10.7	18.0	-12.8
16	-13.8	-5.0	35% Paradox: 65% Airport Well	-10.7	18.5	-12.3
		-6.0		-11.1	18.1	-12.7
		-7.0		-11.4	17.8	-13.0
12	-13.8	-5.0	25% Paradox: 75% Airport Well	-11.6	18.6	-12.2
		-6.0		-11.9	18.4	-12.4
		-7.0		-12.1	18.1	-12.7

The age of the vein is not analysed in this study, but previous studies have had insightful research on the deposition age of the travertines and veins using U-Th dating method (Burnside, 2010, Dockrill, 2006). The result shows the age of the white banded veins (T2-vein) is around 49,088 (±187) to 50,890 (±390) years old (Burnside, 2010). The study of Dockrill and Kampman et al. demonstrated the travertine age for our studied area is between 57, 000 to 60,000 yr (Dockrill, 2006, Kampman et al., 2012).

To sum up, the temperature and isotope estimation based on the fluid mixing model agrees with the probable environmental temperature and the measured isotope values, which demonstrates the fluid mixing model with 25-45% of Paradox brine and 55-75% of meteoric water could reasonably deposit the T2 vein under the temperature of 12 to 18˚C. The proportion of brine in the fluid decreased as the vein growth. The T2 aragonite vein was formed by CO_2-rich fluid moving upwards

degassing and precipitation at the same time. The paleo-fluid that deposited T2-vein at around 50k years ago was much more saline than the present Crystal Geyser spring water, which composes only around 3% of Paradox Valley brine (Kampman et al., 2014). A less proportion of Paradox brine at present day compared to the paleo-fluid suggests that a partial sealing of the fault zone might have happened during the past 50k years (and probably for a longer time), allowing less saline water to be incorporated in the Crystal Geyser fluids.

4.3.9 Geochemistry of the modelled paleo-fluid

Geochemistry composition of the paleo-fluid mixed by 25% to 45% of Paradox brine and 55% to 75% of meteoric water mixing is listed in Table 4-11. The element concentrations are compared with present day Crystal Geyser fluid. The modelled paleo-fluid is physical mixing of the two end members (geochemistry of end members see Appendix 12). In real facts, the compositions are likely be altered by fluid-rock reactions include carbonates (calcites, aragonites and dolomite) cementation and dissolution, gypsum deposition, Fe-dolomite cementation. In addition, large amount of CO_2 that majorly originated from the crust inflow the Carboniferous formations and oversaturated the fluids (Wilkinson et al., 2009a, Kampman et al., 2014). CO_2-saturated brine migrates upwards with free-phase CO_2 via fault and mixed with meteoric water in Navajo Fm. Therefore, the large amount of dissolved CO_2 should be considered when we reconstruct the geochemistry model of the paleo-fluid.

The amount of CO_2 from the crust also ascended through the fault dissolved in the fluid, making the paleo-fluid oversaturated with CO_2 (Wilkinson et al., 2009a, Kampman et al., 2014). The CO_2 concentrations have been measured by Kampman et al. during drilling from the present fluid samples, which increases from around 500mmol/l to 927mmol/l towards the base of the Navajo Formation, with pH decreasing from 5.3 to 5.1, and from CO_2 saturated statues at depth to CO_2 undersaturated statues at the surface (Kampman et al., 2014). As it is unable to estimate the amount of CO_2 dissolved in paleo-fluid, in this study it is assumed the paleo-fluid presented similar CO_2 saturation status as present fluid. In real fact, the paleo-fluid probably contains more free-phase CO_2 than the present fluid, as the carboniferous brine fluid carries more CO_2 comparing to the meteoric fluid. To make

a conservative estimation, the paleo-fluid is estimated to contain CO_2 concentrations of 100mmol/l, 500mmol/l, 800mmol/l and 1000mmol/l, based on the present CO_2 dissolution level in Navajo Fm (Kampman et al., 2014).

Table 4- 11: Element concentrations for Paradox brine, Airport Well spring, Crystal Geyser, mixed paleo-fluid with 25% ~45% of Paradox brine and 55%~75% of meteoric water and 500mmol/l of CO_2

Element	Mixed paleo-fluid /mmol/l (25% Paradox brine, 12 ˚C)	Mixed paleo-fluid/ mmol/l (45% Paradox brine, 18 ˚C)	Crystal Geyser /mmol/l (18 ˚C)
Na	8.52E+02	1.52E+03	1.64E+02
Mg	2.07E+01	3.03E+01	9.60E+00
Sr	6.28E-02	1.13E-01	1.47E-01
Mn	1.89E-02	1.48E-02	2.84E-02
Ba	9.87E-05	1.70E-04	1.00E-04
Ca	2.41E+01	2.56E+01	2.61E+01
SO_4	3.15E+01	3.80E+01	2.92E+01
K	2.58E+01	4.46E+01	9.30E+00
Cl	9.01E+02	1.62E+03	1.23E+02
Br	6.28E-01	4.12E-01	3.53E-02
SiO_2	2.60E-01	2.14E-01	6.40E-02
Fe	8.11E-02	6.12E-02	2.31E-01
Al	3.45E-03	2.53E-03	
CO_3^{2-}	8.15E+01	8.41E+01	

Table 4- 12: Saturation index for mixed paleo-fluid and Crystal Geyer spring after PHREEQCI (500mmol/l CO_2).

Minerals	Paleo-fluid 25% Paradox brine	Paleo-fluid 45% Paradox brine	Crystal Geyser
Aragonite	0.74	0.81	0.78
Calcite	0.89	0.97	0.93
Anhydrite	-0.77	-0.84	-0.36
Gypsum	-0.36	-0.44	0.01

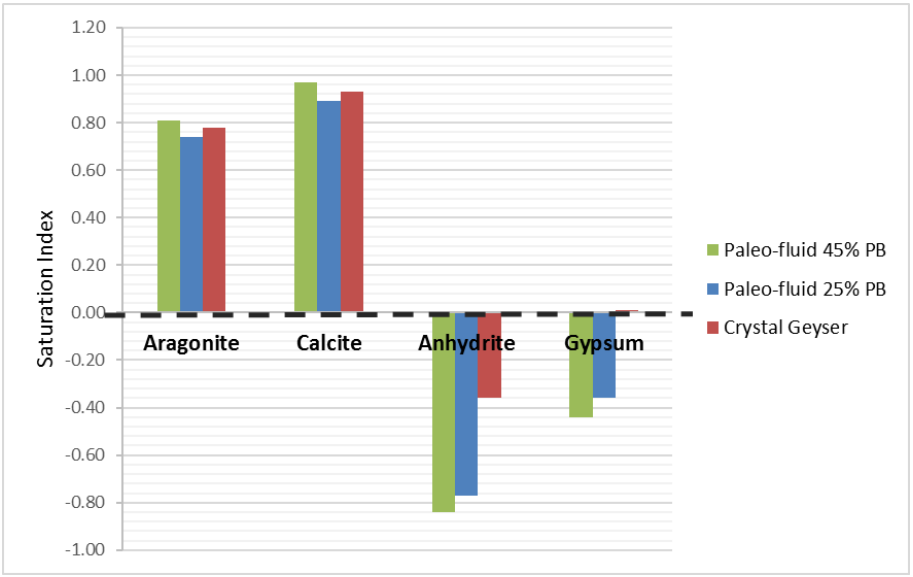

Figure 4- 41: saturation indices for carbonates and sulphates when 500mmol/l CO_2 dissolves in the paleo-fluid.

Table 4- 13: Saturation index for mixed paleo-fluid and Crystal Geyer spring after PHREEQCI (800 mmol/l CO_2).

Minerals	Paleo-fluid 25% Paradox brine	Paleo-fluid 45% Paradox brine	Crystal Geyser
Aragonite	0.85	0.97	0.78
Calcite	1.00	1.12	0.93
Anhydrite	-0.80	-0.89	-0.36
Gypsum	-0.39	-0.50	0.01

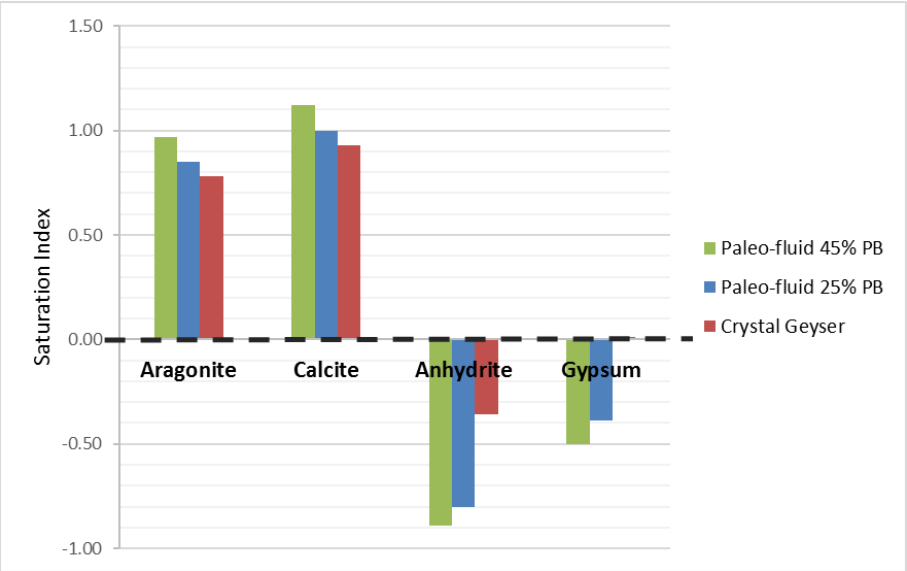

Figure 4- 42: saturation indices for carbonates and sulphates when 800mmol/l CO_2 dissolves in the paleo-fluid.

Table 4- 14: Saturation index for mixed paleo-fluid and Crystal Geyer spring after PHREEQCI (1000 mmol/l CO_2).

Minerals	Paleo-fluid 25% Paradox brine	Paleo-fluid 45% Paradox brine	Crystal Geyser
Aragonite	0.92	1.03	0.78
Calcite	1.08	1.19	0.93
Anhydrite	-0.82	-0.92	-0.36
Gypsum	-0.41	-0.533	0.01

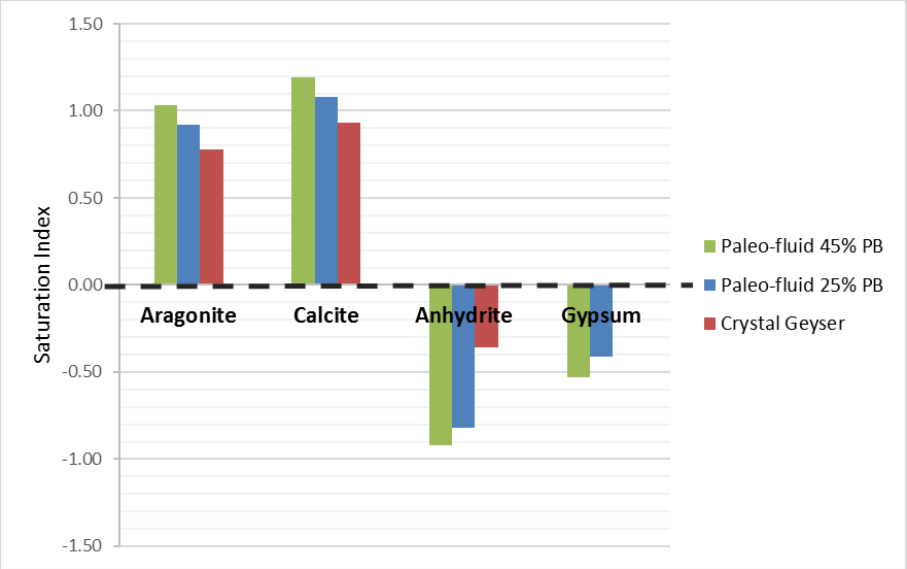

Figure 4- 43: saturation indices for carbonates and sulphates when 1000mmol/l CO_2 dissolves in the paleo-fluid.

The Mg/Ca ratio of the modelled paleo-fluid ranges from 0.86~1.18, which is much higher than that of Crystal Geyser (0.37). The Mg/Ca ratio of the paleo-fluid is beyond the aragonite formation ratio (Mg/Ca=0.8). This result reasonably explains why aragonite could deposit during cold spring.

PHREEQCI is utilized to simulate saturation statues of the paleo-fluid. The saturation indices for carbonates increase with the amount of CO_2 dissolving in the fluids from 500mmol/l to 1000mmol/l: the more CO_2 dissolves, the greater of the saturation indices of carbonates (Table 4-12 to 4-14, Fig. 4-42 to Fig. 4-44). When 500mmol/l of CO_2 dissolves in the fluid, the paleo-fluid and present Crystal Geyser show similar saturation level for carbonates (Fig. 4-42). When more CO_2 dissolves in the paleo-fluid, the saturation indices increase (Fig. 4-43 and Fig. 4-44).

Both the paleo-fluid under different CO_2 saturation statues and present Crystal Geyser fluid are undersaturated with anhydrite and gypsum (Crystal Geyser is slightly over saturation level for gypsum), which demonstrates the extensive gypsum veins in Mancos shale are not likely to precipitate from either present Crystal Geyser springs nor paleo-fluid. The dissolution of gypsum layer in Carmel Formation is not a

very convincing. The most possible explanation for the pyrite in Mancos shale is the weathered to gypsum veins with the reaction of (Garrels and Lerman, 1981):

$$4FeS + 8CaCO_3 + 7MgCO_3 + 7SiO_2 + 15H_2O \rightarrow 15CH_2O + 8CaSO_4 + 2Fe_2O_3 + 7MgSiO_3 \quad \text{Equation 5-5}$$

Pyrite could be oxidized to hematite and precipitate gypsum at the expense of carbonates. This assumption is facilitated by the field observation that gypsum veins are more commonly found in Mancos shale formation than sandstone formations that right above gypsum layer.

4.4 Conclusions

This chapter mainly investigates the paleo-fluid composition using carbonate veins. The major conclusions could be summarized as:

1) Three types of carbonate veins have been observed in the sandstone unit of T2, which are thick white-banded veins that seal fractures; millimetre thin, vertical veins with reduction zones in sandstones; and isolated thin veins that infills the fractures. Thick, banded aragonite and calcite veins are associated with the circulation of CO_2-rich fluids, while the millimetre thin, vertical veins in the sandstone unit are of diagenetic origin.

2) No thick carbonate veins have been observed in the Mancos shale unit. Only broken pieces of carbonate veins and thin, vertical veins formed are known to be present, and are of diagenetic produced veins. Extensive thin gypsum veins have been observed in Mancos shale unit of T3 just next to the fault plane. The gypsum veins are probably derived from weathering of pyrite in Mancos shale Fm.

3) A series of geochemical analysis have been carried out to study the thick, banded, white aragonite vein formed by CO_2-rich paleo-fluid. Different morphologies of crystals have been observed, but no significant elemental difference have been found between various morphologies. The different shapes and sizes of crystals might be owing to the change of flow rate. The colour variations (yellowish bands) do not correspond to compositional variations in the analysed elements.

4) Element distribution coefficients were used to calculate the composition of the paleo-fluid that deposited the vein, and the result has been compared with the

present Crystal Geyser. A mixing model is constructed to simulate the paleo-fluid elemental composition with two end members of Paradox Valley brine and Airport Well spring. The paleo-fluid is composed of 25% to 45% Paradox brine and 55% to 75% of meteoric water, and the deposition temperature is estimated to be around 12 to 18 ˚C. The mixing model is tested by Sr and stable isotope for the fluid source and the deposition temperature. The result agrees with historic environmental temperature, and supports the validity of the mixing model.

5) The modelled paleo-fluid is enriched with Mg/Ca ratio than that of present spring from Crystal Geyser (Mg/Ca=0.37). The ratio of the paleo-fluid is beyond the aragonite preferential ratio (Mg/Ca=0.8). The formation of aragonite rather than calcite also facilitates the conclusion the paleo-fluid is quite different from the present spring.

6) The paleo-fluid composition is compared with that of the present crystal geyser composition. The modelled paleo-fluid is much more saline than the present crystal geyser fluid (3% of Paradox brine and 97% of meteoric), and the percentage of brine that constitutes the fluid decreases as the vein growth. The smaller proportion of the Paradox brine is interpreted as gradual self-sealing of the fault zone, blocking the pathways for fluids ingress. The change of the shape of the carbonate crystals also facilitate the assumption, that the flow-rate of the fluid changed during the deposition of the thick aragonite vein.

6) The extensive gypsum veins found in the Mancos Formation should not be the result of the dissolution of gypsum layer in Carmel Formation, as neither of the paleo-fluid nor present Crystal Geyser spring is over-saturated with gypsum. The gypsum veins are more likely from the weathering of pyrite in Mancos Fm.

Chapter 5: Has the Mancos shale been altered by the CO_2-rich fluid?

The influence of the CO_2-charged fluid on sandstone unit has been extensively studied in previous studies. This chapter focuses on how the CO_2-rich fluid altered the shale unit on geological time scales. Shale is commonly used as caprock to prevent the injected CO_2 from migrating to other strata. Therefore, the influence of CO_2 on shales is of significance for the security of the geological CO_2 storage. Radiometric dating shows the leakage of the CO_2 in the Green River area has persist for more than 400k years (Kampman et al., 2012, Burnside et al., 2013) through the Little Grand Wash fault. We use the Mancos shale in the hanging wall of the Little Grand Wash fault as analogue to study the long-term behaviour of CO_2-rich fluid in a shale unit. We tackle the questions of what is the approximate volume of shales which would be changed by the CO_2-rich fluid? What reactions happen between the fluid and rock, and what are the impacts on the sealing capacity of the shales? And how the results of the Mancos shale study could contribute to practical CO_2 storage project?

5.1 Literature for stable isotopes

5.1.1 Stable isotope fractionation

As the fluid from deep formations ascends upwards, the degassing of CO_2 and the precipitation of calcium carbonate happen via the reaction:

$$2HCO_3^-(aq) + Ca^{2+} \leftrightarrow CaCO_3(s) + CO_2(g) + H_2O \qquad \text{Equation 5-1}$$

The stable isotopic composition of the CO_2-charged waters is recorded in the carbon and oxygen isotopic composition of precipitated veins and travertines. The light carbon ($\delta^{12}C$) and oxygen ($\delta^{16}O$) preferentially remain in the CO_2 gas, while the heavy carbon ($\delta^{13}C$) and oxygen ($\delta^{18}O$) are preferentially taken into the $CaCO_3$. The heavy isotope enrichment order follows: $CaCO_3 > HCO_3^- > CO_3^{2-} > H_2CO_3 \approx CO_2$ (g) (Michael A. Arthur, 1983).

The oxygen composition of the HCO_3^- is also controlled by O-exchange with water via reaction of:

$$CO_2(aq) + H_2O \leftrightarrow H_2CO_3 \leftrightarrow HCO_3^-(aq) + H^+ \quad \text{Equation 5-2}$$

When CO_2 dissolves in an aqueous fluid, the carbon isotope of the fluid is determined by the CO_2, while as the amount of oxygen in water is much larger than the amount in the dissolved CO_2, the change in oxygen isotopic ratio of the fluid is very limited.

A Rayleigh distillation model was constructed to model CO_2 removal (degassing and precipitation) from the system for carbon and oxygen isotopes (Kampman et al., 2012):

$$\delta = \delta_0 - [1000 \cdot ln\alpha_{p-r}(1-f)] \quad \text{Equation 5-3}$$

Where δ is the final carbon isotope of the fluid after CO_2 removal; δ_0 is the initial carbon isotope of the fluid; f is the fraction of HCO_3^- remaining in the system; α_{p-r} is carbon isotope fractionation factor between the removed product and HCO_3^-. For carbon isotope fractionation, according to Eq. 5-1, half of the C in HCO_3^- is removed as CO_2 and another half precipitates as carbonates. Therefore, $\alpha_{p-r} = \left(\frac{1}{2}\alpha_{CO2-HCO3}\right) + \left(\frac{1}{2}\alpha_{CaCO3-HCO3}\right)$. The fractionation factor between CO_2 and HCO_3^-, and $CaCO_3$ and HCO_3^- are controlled by temperature. For oxygen isotope fractionation, $\alpha_{p-r} = \left(\frac{2}{6}\alpha_{CO2-HCO3}\right) + \left(\frac{3}{6}\alpha_{CaCO3-HCO3}\right) + \left(\frac{1}{6}\alpha_{H2O-HCO3}\right)$ (Kampman et al., 2012).

a. Carbon isotope fractionation factor in dissolved CO_2-water system

Normally, dissolved inorganic carbon in natural waters is in the form of H_2CO_3, HCO_3^-, and CO_3^{2-}. The isotopic fractionation between dissolved inorganic carbon and CO_2 gas is a function of temperature (Deines et al., 1974) (Eq. 5-4 to Eq. 5-7).

$$\Delta_{H2CO3-CO2} = -0.91 + 0.0063\left(\frac{10^6}{T^2}\right) \quad \text{Equation 5-4}$$

$$\Delta_{HCO3^- - CO2} = -4.54 + 1.099\left(\frac{10^6}{T^2}\right) \quad \text{Equation 5-5}$$

$$\Delta_{CO3^{2-}-CO2} = -3.4 + 0.87\left(\frac{10^6}{T^2}\right)$$ Equation 5-6

$$\Delta_{CaCO3-CO2} = -3.63 + 1.194\left(\frac{10^6}{T^2}\right)$$ Equation 5-7

Where Δ equals to $10^3 ln\alpha$ which is the fractionation factor. T is in Kelvin. In natural fluids in most sedimentary rocks, the dominant species is bicarbonate.

The aragonite fractionation factor between temperatures of 10 to 40 ºC has been published by Romanek et al. in 1991. The aragonite-bicarbonate enrichment factor averaged 2.7 ± 0.6‰ and the aragonite-calcite fractionation is 1.7 ± 0.4‰, both of which are independent of temperature. The fractionation factor between aragonite and CO_2 is (Romanek et al., 1992):

$$\Delta_{ar-CO2} = 13.88(\pm 0.16) - 0.13(\pm 0.01)T$$ Equation 5-8

Where T in degrees Celsius.

b. Oxygen fractionation in calcite-H_2O system

The oxygen fractionation factor for the calcite-water system over a temperature of 10 to 40 °C with the following equation (Kim et al., 1997):

$$\Delta_{Calcite-H2O} = 18.03 \times \frac{10^3}{T} - 32.17$$ Equation 5-9

Where T in Kelvin.

Compared to calcite, aragonite is more enriched with heavy oxygen $\delta^{18}O$ for about 0.6±0.3 ‰, with no very significant temperature dependence (Grossman and Ku, 1986).

5.1.2 Mechanisms for carbon isotope variation

A range of diagenetic processes cause variations in carbon isotope composition in sedimentary rocks. Hudson (1977) explained the reason for the variations of isotopic ratios for carbonate cements. Organic carbon is usually depleted in $\delta^{13}C$ compared to oxidized carbon in the form of CO_2 or carbonates. The simplest reactions produce

carbonates with $\delta^{13}C$ of between about 0 ‰ (average marine carbonate) ~ -24 ‰ (average organic matter) V-PDB.

Irwin et al. (1977) summarized the major processes that contribute to modify carbon isotopic composition during the burial of organic-rich sediments. CO_2 is one product of organic matter degradation. The approximate range of carbon isotope ratios is related with the depth and burial processes (Figure 5-1).

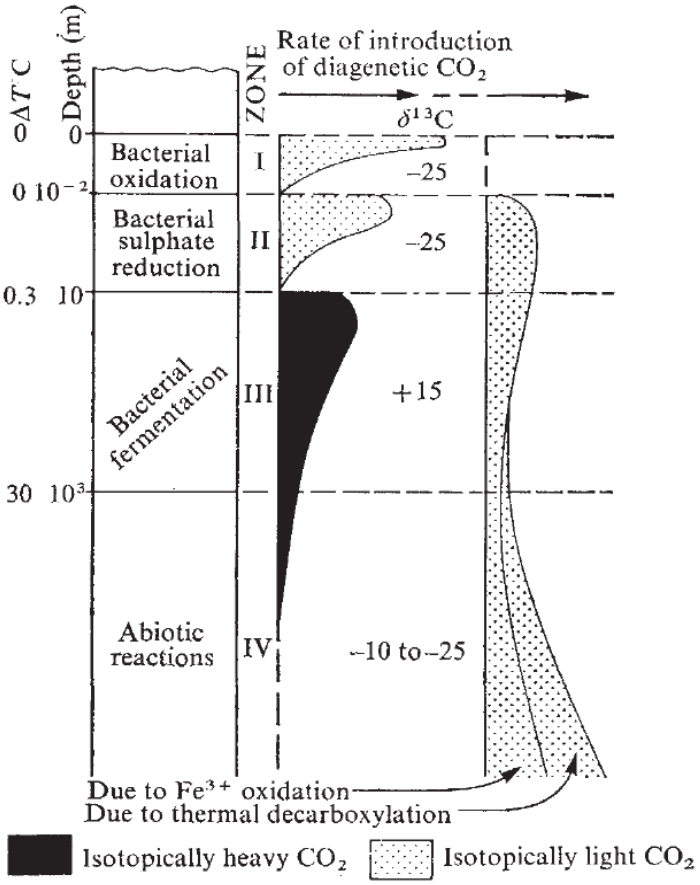

Figure 5- 1: Relationship between diagenetic CO_2 and depth, temperature and diagenetic zones (Irwin et al., 1977).

The burial processes include the mechanisms of (Irwin et al., 1977):

$$CH_2O + O_2 \rightarrow CO_2 + H_2O \quad Bacterial\ oxidation$$ Equation 5-10

$$2CH_2O + SO_4^{2-} \rightarrow 2CO_2 + S^{2-} + 2H_2O \quad Bacterial\ sulphate\ reduction$$

Equation 5-11

$$2CH_2O \rightarrow CH_4 + CO_2 \quad Bacterial\ fermentation$$ Equaion 5-12

$$R.CO_2H \rightarrow RH + CO_2 \;\; Abiotic\, reaction, decarboxylation$$ Equation 5-13

Bacteria oxidation and bacteria sulphate reduction are the first step at shallow burial that less than 10m in an aerobic environment. The CO_2 produced by this step inherits the light carbon in this step (Irwin et al., 1977, Hudson, 1977). Then fermentation starts as the sulphate reduction stops at deeper depth. The produced methane is usually extremely depleted with $\delta^{13}C$, thus making the produced CO_2 in this reaction very positive (~+15‰V-PDB). The reaction rate of the first three processes decreases as the rises of temperature and the diminishing of oxygen. Abiotic process starts at deep depth (~>1000m) and produces CO_2 of light carbon (Irwin et al., 1977). The anticipated marine reservoir bicarbonate is about $\delta^{13}C_{HCO3-} = 0‰$ V-PDB. The diagenetically produced CO_2 will dissolve in water to generate bicarbonate ions with different isotopic compositions.
Another important process is soil weathering, which is dominant in marine carbonate bedrocks where the CO_2 is of organic origin (Hudson, 1977). The reaction is:

$$CaCO_3 + H_2CO_3 \rightarrow Ca(HCO_3)_2$$ Equation 5-14

One carbon atom is contributed by the parent carbonate and one by organic sourced CO_2. The bicarbonate solution can interact with either organic-origin CO_2 or atmospheric CO_2, with a $\delta^{13}C$ of -7‰ V-PDB which is in equilibrium with dissolved bicarbonate of $\delta^{13}C$ of about +1 ‰ to +2 ‰ V-PDB at 20 °C. Hence, freshwater carbonates, formed as a result of this complex processes, show a wide range of $\delta^{13}C$ values of -12‰ to +3‰ V-PDB (Keith and Weber, 1964).

The Kimmeridge Clay Formation of the Dorset Coast section has been studied as an example of the variation of isotopic composition for the carbonate-producing diagenetic processes (Irwin et al., 1977). The studied section is generally organic rich with occasional cementstones (dolomitic calcilutites). Figure 5-2 is the plot of oxygen against carbon isotope. The diagenetic calcites show distinctive isotope ratios with very light carbon isotope and relatively heavy oxygen ($\delta^{13}C_{calcite} = -16‰;\;\; \delta^{18}O_{calcite} = -0.8‰$), and the precipitation temperature of around 15 ºC. The isotopic values indicate shallow burial within the bacterial sulphate reduction zone (zone II), and this conclusion is verified by the presence of pyrite in the samples.

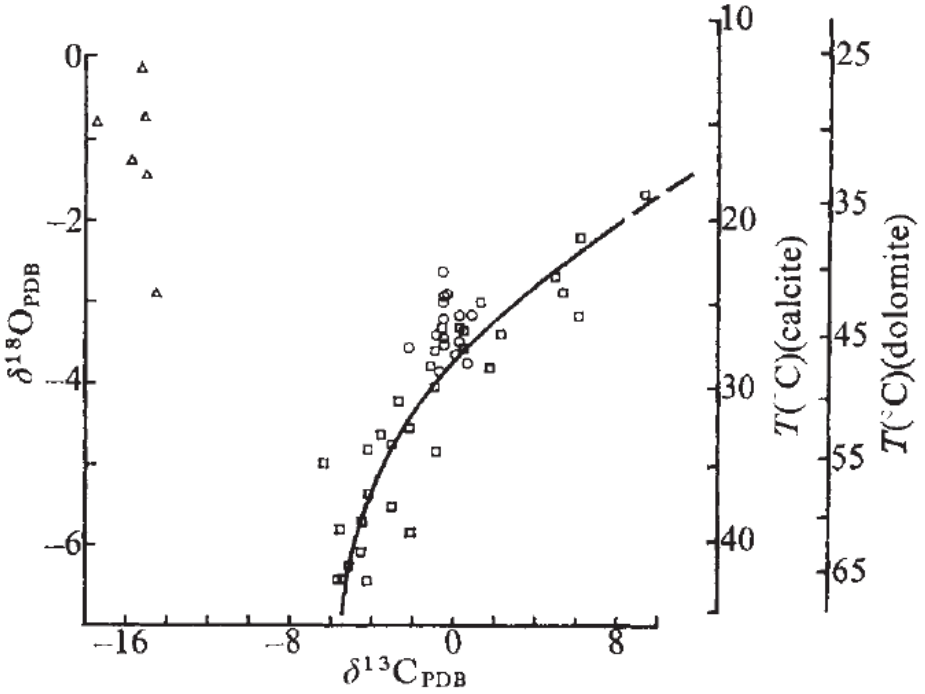

Figure 5- 2: Isotopic ratio against temperature for different carbonate samples. Triangles: diagenetic calcites; Squares: diagenetic dolomites; Circles: coccolithic calcites (Irwin et al., 1977).

The diagenetic dolomites (cementstones, squares in Figure 5-2) displays a relatively large temperature range from 34 ºC to 66 ºC. The oxygen and carbon isotope show correlation with the isotopically heaviest carbonates being precipitated at the lowest temperatures, indicating that the source fluid (bicarbonate) that precipitated carbonates is heavy in the shallow depth and becoming lighter at greater depth. When compared to the diagenetic zone in Fig. 5-1, the top part of the cementstones could be precipitation from bicarbonate produced by fermentation (zone III). With increasing depth, bicarbonate production changed from fermentation to abiotic oxidation and decarboxylation. The diagenetic zone model in Figure 5-1 was derived largely from this data (Irwin et al., 1977).

5.1.3 Oxygen isotope trends and variations

The fractionation of oxygen isotope between carbonates and water has been extensively studied, and is useful for studying the diagenetic history of sediments. The oxygen isotope ratio of a carbonate mineral is primarily controlled by

temperature of precipitation and fluid composition (Urey, 1947, Urey et al., 1951, Epstein, 1959). The temperature dependence of oxygen isotope fractionation between calcite and water is defined by the Eq. 5-9. Subsurface water is ultimately derived from the hydrological cycle as meteoric water, or from seawater. The isotopic variation of meteoric water is mostly owing to the processes of evaporation and condensation related to geographic factors such as temperature, altitude and latitude (Michael A. Arthur, 1983).

Underground formation fluids show a large variation in oxygen isotope ratio (Hudson, 1977). The general trends of oxygen isotope in carbonate rocks tend towards lighter oxygen with increasing geological age (Veizer, 1983, Veizer and Hoefs, 1976, Clayton and Degens, 1959). This trend has been explained as due to continuous re-equilibration with meteoric water (Veizer and Hoefs, 1976).

5.1.4 Mancos shale in the South and East Utah

5.1.4.1 Stratigraphy and lithology of Mancos Shale Formation

The Mancos Shale is a thick formation (about 3,500ft in the Book Cliffs area to about 2,000ft in southwestern Colorado) conformably overlying the Dakota Sandstones deposited in the Western Interior, or in other regions, unconformably overlying the Cedar Mountain formations (green-grey mudstones) where the Dakota Sandstone is absent (Molenaar and Cobban, 1991). The Mancos Shale Formation is mostly composed of uniform, dark-grey mudstone and siltstones (Nuccio and Condon, 1996).

Transgressive and regressive cycle caused the deposition of interlayers of shales and sandstones. The Mancos Shale Formation of the studied area is composed by three main members in eastern Utah and western Colorado: the Tununk Shale Member, Ferroan Sandstone Member and Upper Mancos Shale Member (Blue Gate) (Dockrill, 2006). The Tununk Shale Member is relatively thick (105-125m) blue-grey marine shale with sandy limestones; the Ferroan Sandstone is thin marine sandstones interbedded with grey shale (6-10m); the Upper Mancos shale (Blue Gate) is thick (>200m) grey shale with thin-bedded of sandstones and occasionally limestone lenses (Dockrill, 2006). Cole et al. added an additional member “Prairie

Canyon Member" that split the Blue Gate Member into an upper part and lower part (Cole et al., 1997).

The Tununk Shale Member of the Mancos Shale conformably overlies the Dakota Sandstone Formation, recording marine flooding and condensation during late Cenomanian time in southern Utah (Peterson, 1969, Peterson et al., 1980, Zelt, 1985). It represents the eustatic highstand of the Green Horn transgressive cycle (Kauffman, 1975). The Tununk Member could be separated into a lower part, Coon Spring Sandstone bed, and upper part of the member. Very thin layers (2-5cm) of chert-pebble conglomerates and sandy mudstones composes the lowest unit of Tununk Member in contacting with Dakota Sandstone, then grades upward to olive-grey, poorly bedded silty shale and thin sandy mudstone. The basal Mancos shale contains abundant gypsum and carbonate concretions (Nadeau and Reynolds, 1981). 20 to 75cm thick bentonite layers have been found, separated by silty mudstones. Biostratigraphic study shows fossil bivalves and ammonites in the lower Tununk Member (Kauffman, 1975, Cobban, 1976, Eaton, 1975, Eaton et al., 1990). The biostratigraphy is summarized in Figure 5-3.

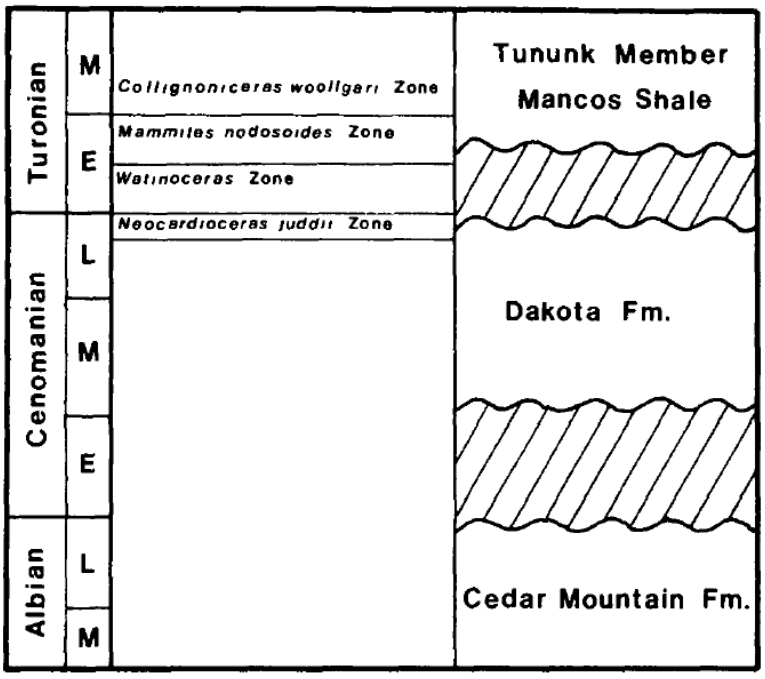

Figure 5- 3: Geological age and associated fossil zones for the mid-Cretaceous formations. The figure is from Eaton et al., (1990) based on studies of Cobban (1976). E=early; M=middle; L=late.

The silty unit turn into very fine-grained sandstone of Coon Spring Sandstone bed, which constitutes the middle part of Tununk Member of Mancos. The upper part of Tununk is thin (25cm) very fine grained, blue-grey, sandy mudstone bed, forming a slope beneath the resistant Ferron Sandstone Member on the east side of San Rafael Uplift (shown in solid lines of A-A' in Figure 5-3) (Molenaar and Cobban, 1991).

The Ferron Sandstone Member (as thick as 152m at the Clear Creek Gas field) overlying the Tununk Member crops out in the west side of the San Rafael uplift and grades into siltstone about 24km southeast of the Farham dome. The Member is overlain by the Blue Gate Mancos (main body of Mancos shale at the upper part of Mancos Fm). The lower part of the main body Mancos shale (Blue Gate) is dark-grey, noncalcareous fissile shale very poorly exposed to the surface, but it grades into a highly calcareous unit in the east of the Uinta basin. The increase in calcareous content gives a lighter colour (Molenaar and Cobban, 1991).

5.1.4.2 Diagenetic formation of carbonate cements in the Mancos shale and mudstones equivalent to the Mancos shale

Understanding the conventional diagenetic alteration of the Mancos Shale is important for this study, as it could assist in distinguishing the results of diagenesis versus alteration induced by CO_2-rich fluids. Studies on Mancos shale (or other mudstones) that are not associated with CO_2-rich fluid are reviewed in this section.

Taylor and Macquaker studied the impacts of diagenetic alterations of the Mancos shales using samples from the Blackhawk Member which is equivalent to the Mancos shale in the Book Cliffs, Utah (Taylor and Macquaker, 2014). The study demonstrated the microscopic mobility of carbonate, silica and aluminium in mudstones during the diagenesis, because abundant dolomite cements, quartz cements and kaolinite cements were observed. The precipitation of quartz cements and kaolinite that filled the septarian concretions demonstrated the mobility of Si and Al during diagenesis. Al was interpreted to be sourced from po r crystalline detrital aluminium oxides and clay minerals associated ...th the oxidation of organic matter (Fein, 1994, Mackin and Aller, 1984, Michalopoulos and Aller, 2004). The source of Si for quartz cements and kaolinite cements could be either from the recrystallization

of biogenetic silica (opal-A) (Thyberg et al., 2010), or from smectite-illite transformation (Thyberg et al., 2010, Thyberg and Jahren, 2011).

The formation of carbonate cements in mudstones has been studied by many researchers. Taylor and Macquaker (2014) and Klein et al. (2009) proposed the carbonate cements in organic-rich Mancos shale were associated with anaerobic/dysaerobic oxidation including the processes of sulphate -reduction, Fe-reduction and methanogenesis (Eq. 5-10, 5-11 and 5-12). Sulphate reduction was associated with the formation of pyrite, which is also a common mineral formed during mudstone diagenesis (Curtis, 1995). Pyrite often occurs as framboids, blocky masses or the replacement of primary calcite (e.g. microfossil walls) (Curtis, 1995).

Klein et at. studied the formation of carbonate concretions of Mancos shale using 324 samples from cemented zones of Mancos Shale in western Colorado (Klein et al., 1999). The carbonate cements show strong linear correlation isotopically between δ^{18}O and δ^{13}C. δ^{13}C value ranges from +10.7 to -9.7‰ V-PDB, and δ^{18}O values ranges from -0.4 to -9.9‰ V-PDB (Fig. 5-4). The strong isotopic correlation is interpreted as the formation of bicarbonate changed from bacteria fermentation in the centre of the concretions (zone III) to post-methanogenic thermally induced decarboxylation reactions in the edge of the concretions (zone IV). The isotope values of the host rock (δ^{13}C = 0‰ V-PDB; δ^{18}O = 24 ‰ V-SMOW) clustered near the middle of the concretion data, hence these values are likely to be the homogeneized mixtures of early and late cements (Klein et al, 1999).

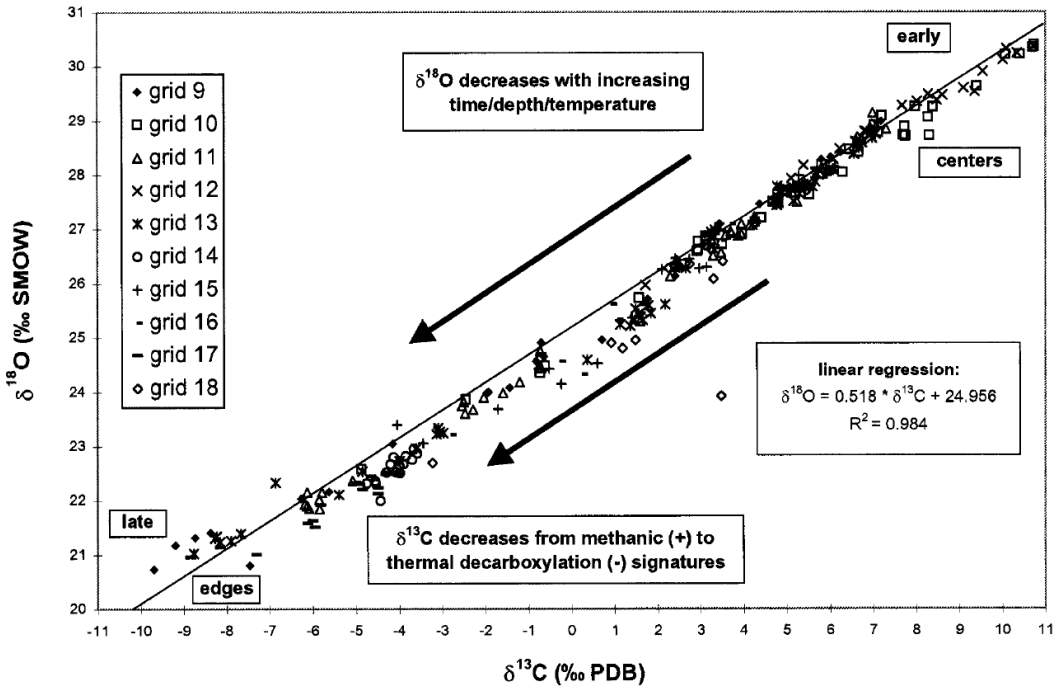

Figure 5- 4: Oxygen vs. carbon isotope correlation for carbonate concretions of the Mancos shale (Klein et al., 1999).

Taylor and Machent (2010) also studied the carbonate cements (ferroan dolomite of 30%-54% of the total rock volume) from sandstones and siltstones in the Book Cliffs that near the (Taylor and Machent, 2010). Oxygen isotope ratios suggested the precipitation of carbonate cements from a fluid with significant meteoric component. Most of the cements contain δ^{13}C around 0‰ V-PDB, suggesting marine carbon is the most common source, but some cements with negative carbon isotope indicates organic matter oxidation. The co-variant trend between carbon and oxygen isotope ratios has also been observed for dolomite cements here similar with the trend in the Klein et al. (1999) study (Figure 5-4). Apart from the thermal evolution explanation suggested by Klein et al. (1999), another possibility has been mentioned that two mineral phases could be mixed with differing proportions (Hendry et al., 2000). The later precipitates have been observed to be more Fe-rich (Taylor and Machent, 2010).

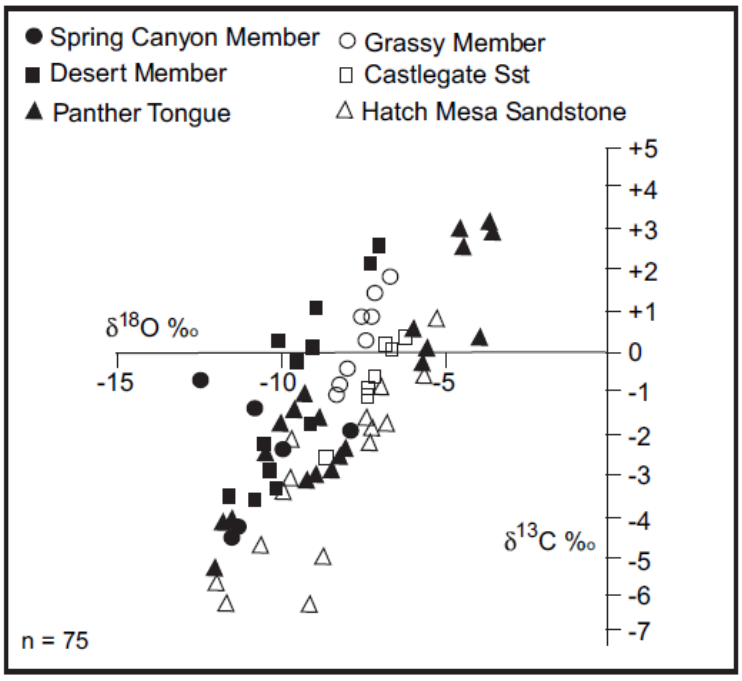

Figure 5- 5: Carbon and oxygen isotope for ferroan dolomite cements from Spring Canyon Member, Grassy Member, Desert Member, Castlegate Sandstone, Panther Tongue Member and the Hatch Mesabeds (Taylor and Machent, 2010).

5.2 Shale sampling and methodology

5.2.1 Shale sampling

Mancos shale samples have been collected from the host rock of T3, T4 and T6 in traverses (travertine location map see Fig. 3-4). The sampling was undertaken in a traverse in the same bed of the Mancos host rock to analyse the relationship between the proximity from the fault and the alterations of the Mancos Shale. Table 5-1 outlines the samples and analytical methods we used in this chapter. Figure 5-6, 5-7 and 5-8 are field pictures and schematic sketch to show how sampling has been undertaken.

Table 5- 1: Samples and the associated location description and analytical methods used in this chapter.

Sample name	Figure No.	Location	Analysis methods
YS014-66, 67, 68, 70	Figure 5-8	A traverse in T4 (not bedding parallel due to surface topography)	XRD, SEM, light microscope, stable isotope
YS014-16~25	Figure 5-6	A bedding parallel traverse below T3	
YS014-45~57	Figure 5-6	A bedding parallel traverse below T3	
YS014-28~39	Figure 5-6	A traverse away from T6 (not bedding parallel due to surface topography)	
YS014-40, 71, 72	Figure 5-7	Sandstone from the T6 fault zone	
YS014-76, 77	Figure 5-8	Control group: black Mancos shale about 100 m from YS014-39 (T6). The furthest from the fault and presumably the least influenced by CO_2	
YS-ZM1 to 4	Figure 3-4	Fault-perpendicular traverse, not close to any known travertine (location refers to Figure 3-4)	

5.2.1.1 Sample location and traverse sampling from T3

Mancos shale samples were collected from 2 bedding-parallel horizons (Bed 1 and Bed 2; Fig. 5-6(b)). Sample YS014-16 and YS014-45 locate around 15m away from the Little Grand Wash fault. The local displacement of this fault has been described in section 4.2.1. The shale sample locates furthest from the fault in T6 is sample YS014-25, which is 43m from the fault. Samples YS014-49, 19, 48, 50, 51, 52 form a vertical section at the north part of T6 (Figure 5-6(b)). All the Mancos shale samples were collected about 20 cm ~ 30 cm below the cliff surface, in an attempt to avoid the highly weathered surface layer.

Abundant gypsum was found filling the fractures below T3. The precipitation of gypsum ($CaSO_4.2H_2O$) in the Mancos Shale is proposed to be from the weathering of pyrite (section 4.3,9).

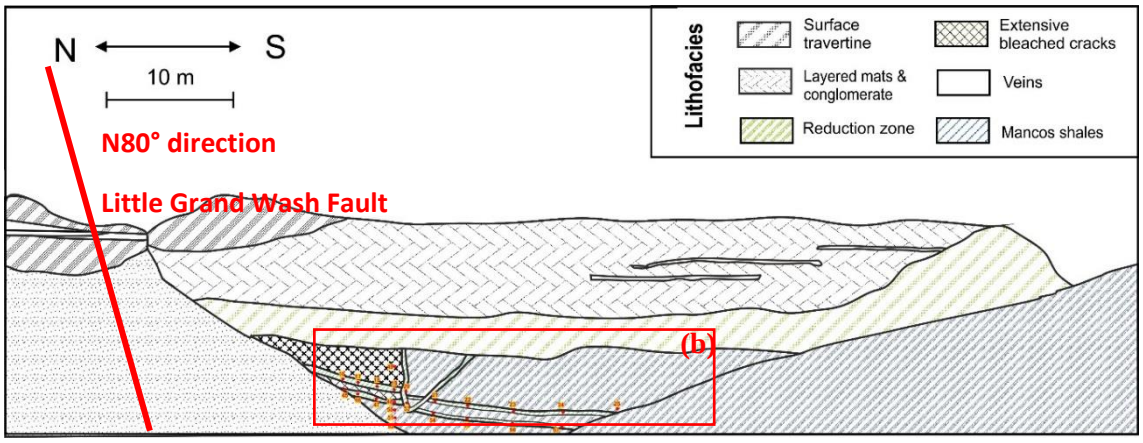
N
S
10 m
N80° direction
Little Grand Wash Fault
(b)
Lithofacies
Surface travertine
Extensive bleached cracks
Layered mats & conglomerate
Veins
Reduction zone
Mancos shales

(a)

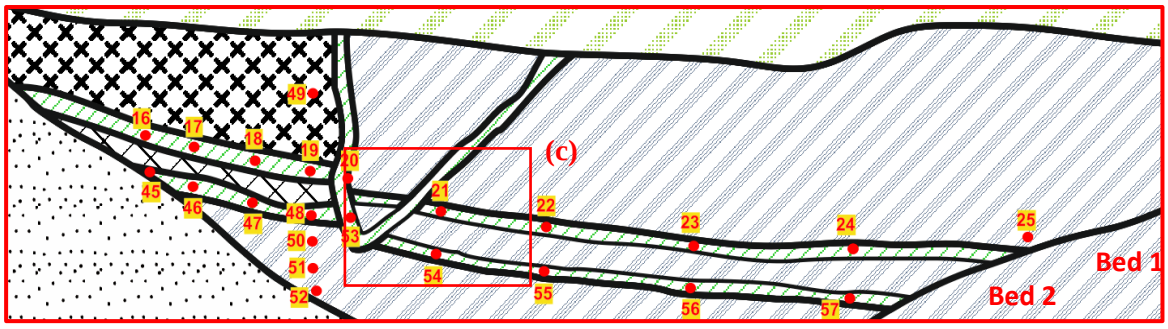
(c)
Bed 1
Bed 2

(b)


Sampling section

(c)

Figure 5- 6: (a) Schematic figure for T3; (b) the close-up of the sampling section of the red box in (a). The numbers are sample numbers; (c) field picture of Mancos shale sampling, rucksack for scale. The location shows in red box in (b).

Table 5- 2: The location of Mancos shale samples in the 2 bedding parallel traverses

Sample name	Location	Traverse
YS014-16	15m from main fault	Bed 1
YS014-17	18.5m from main fault	
YS014-18	20.5m from main fault	
YS014-19	22m from main fault	
YS014-20	24m from main fault	
YS014-21	29m from main fault	
YS014-22	31.3m from main fault	
YS014-23	33.8m from main fault	
YS014-24	37m from main fault	
YS014-25	43m from main fault	
YS014-45	15m from main fault	Bed 2 20cm below bed 1
YS014-46	18.5m from main fault	
YS014-47	20.5m from main fault	
YS014-48	22m from main fault	
YS014-53	24m from main fault	
YS014-54	29m from main fault	
YS014-55	31.3m from main fault	
YS014-56	33.8m from main fault	
YS014-57	37m from main fault	
YS014-49	22m from main fault; 0.2m above YS014-19	Vertical traverse
YS014-50	22m from main fault; 0.8m below YS014-19	

YS014-51	22m from main fault; 1.0m below YS014-19	
YS014-52	22m from main fault; 2.0m below YS014-19	

5.2.1.2 Sample location and traverse sampling from T6

T6 is a large travertine located around 1500m east of Green River. One fault-perpendicular traverse of Mancos shale samples and control group samples (i.e. those sufficiently distant from the fault to be potentially unaltered by CO_2-rich fluids) were collected. Sample YS014-28 is the Mancos shale sample located nearest to the main fault, which is around 20m from the surface travertine and main fault. The outcrop has a surface slope of 40°~50° degree, hence the horizontal distance from the fault is around 14m. Samples YS014-76 and 77 have been collected at the base of the outcrop (about 100m from sample YS014-39), which could be regarded as the least affected by the fault movement and CO_2-enriched fluid.

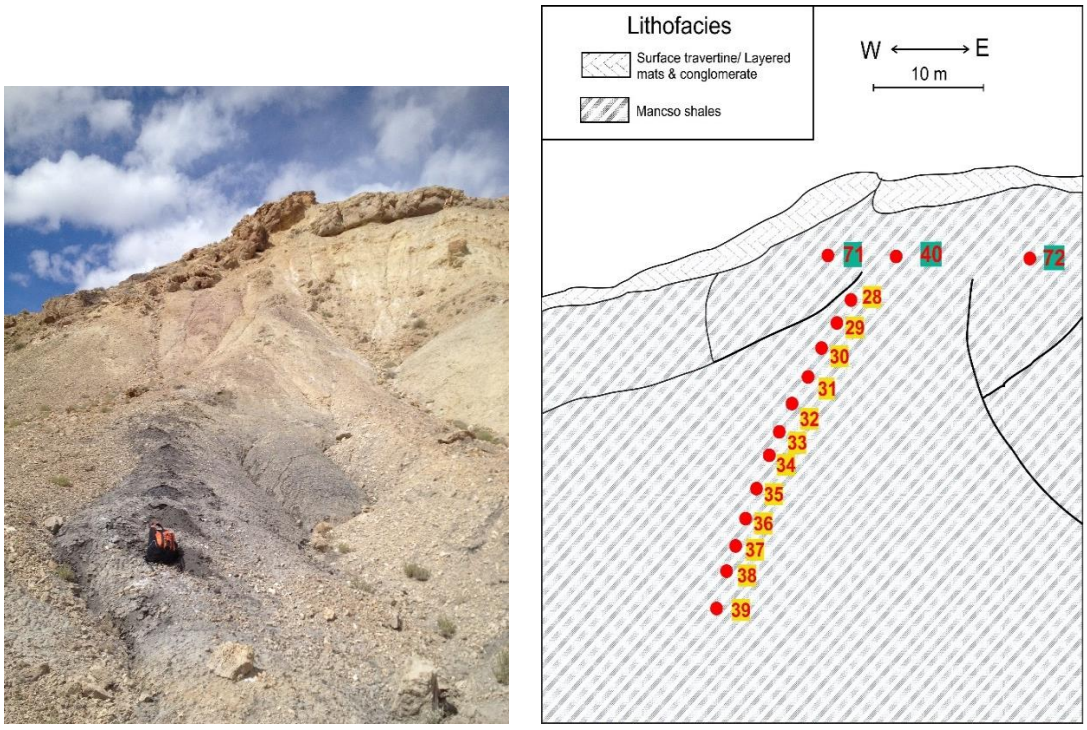

(a) (b)

Figure 5- 7: (a) Field picture of T6, rucksack for scale; (b) schematic sketch of T6 and sampling traverse with sample numbers. The numbers marked with

yellow background are shale traverse samples and marked with green background are sandstone samples.

Table 5- 3: Mancos shale and control group samples location

Sample name	Location (horizontal distance from the main fault)	Traverse
YS014-71, 72, 40	10m	Sandstones
YS014-28	14.1m	One shale traverse
YS014-29	15.0m	
YS014-30	16.4m	
YS014-31	17.0m	
YS014-32	19.0m	
YS014-33	20.1m	
YS014-34	20.9m	
YS014-35	21.3m	
YS014-36	22.6m	
YS014-37	23.3m	
YS014-38	24.1m	
YS014-39	24.8m	
YS014-76	>100m base of the outcrop	
YS014-77	>100m base of the outcrop	

Sample YS014-40, 71 and 72 were collected physically above the Mancos Shale exposures (i.e. to the north, close to the fault), and may be fault-bounded slivers of earlier sandstone formations (Dakota Sandstone or a Jurassic Formation) from the footwall of the fault, or of the Ferron Sandstone Member of the Mancos Shale that lies above the Tununk shale.

5.2.1.3 Sample location and traverse sampling from T4

Small travertine T4 (Location see Figure 3-4, around 50cm diameter size) has been discovered at the junction of two faults (Figure 5-8 (a)). Mancos Shale samples were collected in a single traverse (Figure 5-8 (b)) approximately perpendicular to the fault. The sample descriptions and the distance from the fault are listed in Table 5-4. An apparently cemented dark greenish rock has been discovered about 400m south of T4, i.e. within the general outcrop of the Mancos Shale.

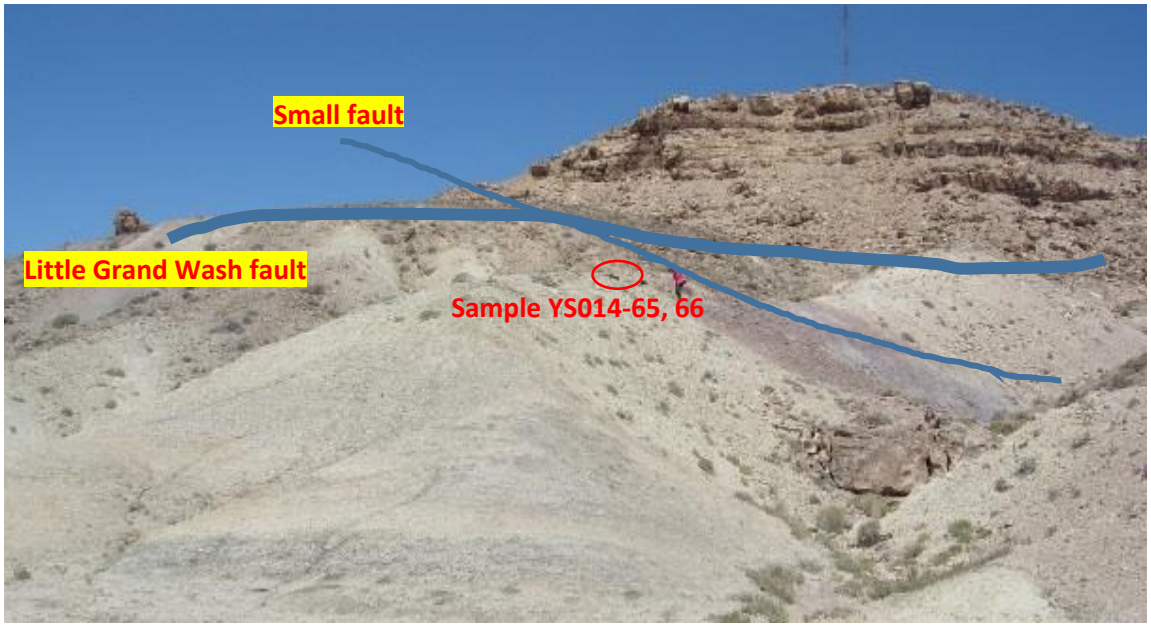

(a)

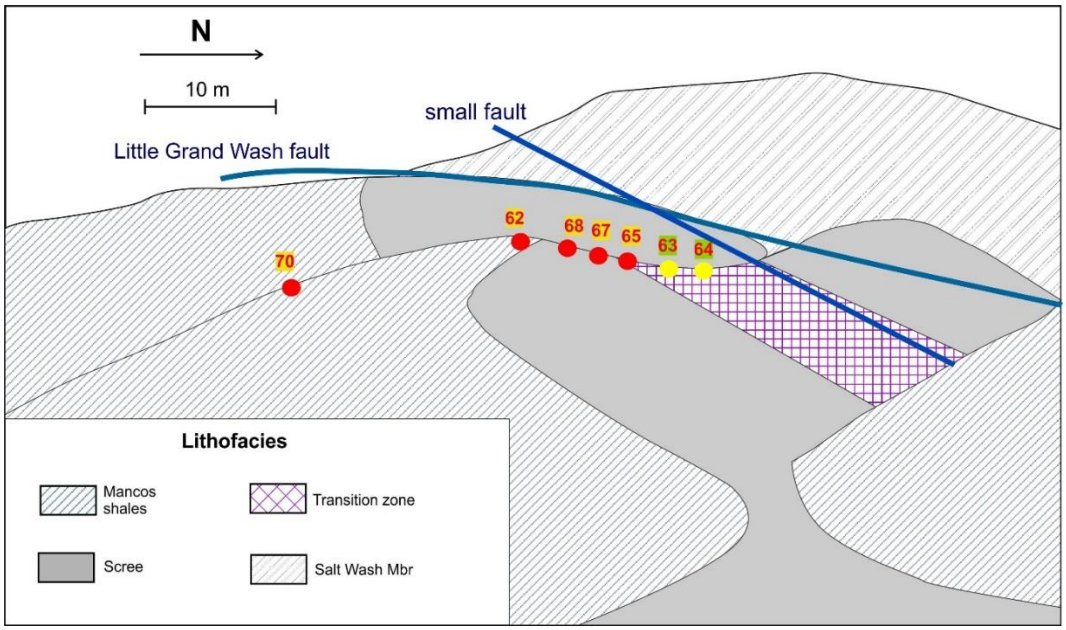

(b)

(c)

Figure 5- 8: (a) Location of T4 travertine is on the junction between the main fault of Little Grand Wash fault and a small cross fault. The bedded unit on the horizon is a sandstone in the footwall of the main fault. (b) Schematic sketch of T4. The yellow circle marks the travertine samples YS014-63 and YS014-64. YS014-62 is the vein

samples with evidence for 2 movement episodes (described in section 4.2.1). Sample YS014-66, 67, 68, 70 are Mancos Shale samples collected below T4. (c) Sample YS014-66: the contact of calcite vein and Mancos Shale.

Table 5- 4: Mancos shale and control group samples of T4

Sample name	Location (horizontal distance from the main fault)	Description
YS014-63, 64	0 m	Travertine samples
YS014-66	2.0m	Fault-perpendicular traverse
YS014-67	4.4m	
YS014-68	7.5m	
YS014-70	32.0m	

ZM traverse (YS-ZM1~ZM4) sampled between T7 and Locality 9 (Figure 3-4) (sample description see Table 5-5). These shale samples were collected by Prof. Zoe Shipton (or by someone on her behalf) approximately perpendicular to the main fault. The farthest sample from the fault (YS-ZM4) is around 200m away from YS-ZM1, and is apparently more cemented than the other samples, with much lighter colour than 'normal' Mancos Shale. ZM traverse samples are not from close to any known travertine, and are hence regarded as 'normal' Mancos Shale, i.e. are unlikely to have been altered by interaction with CO_2-rich porewaters, although YS-ZM4 is only 10m away from one of the fault segments.

Table 5- 5: Location and description of ZM traverse (note there is no known travertine at the fault at this location)

Sample name	Horizontal distance from the main fault	Description
YS-ZM4	10m	dark grey
YS-ZM3	70m	dark grey
YS-ZM2	130m	dark grey

YS-ZM1	200m	Light grey, hard, apparently cemented

5.2.2 Methodology

Major methodology used for the analysis of the Mancos Shale samples include XRD, SEM and stable isotope analysis (carbon and oxygen).

5.2.2.1 XRD analysis

The mineralogy of Mancos Shale samples and some control group samples have been analysed by XRD (X-ray powder diffraction). The equipment used for XRD measurement has been described in section 4.3.2. As the size of the sample is around 8cm * 8cm, only small proportions of the samples were prepared for analysis. For visually heterogeneous samples, multiple parts of the samples were prepared (YS014-28, 29), these are labelled as e.g. YS014-28-1/8~YS014-28-8/8 for a sample with 8 sub-samples.

5.2.2.2 SEM analysis

SEM (Scanning Electron Microscope) is used to study the morphology and the mineral alterations by the CO_2 fluid. The experiment was undertaken in School of Geosciences at the University of Edinburgh with Carl Zeiss SIGMA HD VP Field Emission SEM and Oxford AZtec ED X-ray analysis and Electron Backscatter Diffraction (EBSD) system. The polished thin sections of shale samples were coated with an electrically conductive material (gold).

5.2.2.3 Stable isotope analysis

Mancos Shale and control group samples were grounded into powder by hand using a mortar and pestle, for oxygen isotope and carbon isotope to trace the origins and the deposition environments of the carbonate cements. The experiment was undertaken at the University of Edinburgh (preparation steps described in section 4.2.5). As above, different sub-samples of one sample were analysed for visually

heterogeneous samples. The carbonate percentage was calculated from the mass of the sample and the mass of generated CO_2.

5.3 Results and discussion

The results of the petrographic experiments will be discussed in this section.

5.3.1 Results for T6 and YS-ZM traverse

5.3.1.1 XRD results

Figure 5-9 shows the results of XRD analysis on representative samples from T6 and ZM traverse (XRD traces see Appendix 13). YS014-28, 29, 30 and 31 are Mancos shale samples which are 14.1m, 15.0m, 16.4m and 17.0m from the fault. YS-ZM01 is about 10m from the fault however there is no known travertine at the fault at this location, so there is no reason to suspect that the sample has interacted with CO_2-rich porewater.

Samples further away (YS014-30, 31) from the fault are relatively enriched with feldspar minerals (anorthite, microcline, orthoclase) than the samples closer to the fault (YS014-28, 29, ZM04). Small amount of heulandite is found in samples that close to the fault, while none is found in samples further away. The source of Ca could be derived from the dissolution of orginal fossils and carboante cements by CO_2-enriched fluid.

YS014-28 (the sample closest to the main fault in T6) shows the most different mineralogy from the other Mancos shale samples, with much less proportion of calcite, but exceptional enriched with halite, and gypsum. It is likely that the halite and gypsum were precipitated, and original calcite dissolved away in YS014-28.

Table 5- 6: XRD for representative samples from T3 and ZM traverse

Sample name	Quartz	Calcite	Albite	Anorthite	Microcline	Orthoclase
YS014-28-7/8	6.9	1.8	2.3	4.1	5.1	4.3

YS014-28-6/8	21.4	7.0	4.0	4.5	4.7	3.4
YS014-29-6/8	7.3	65.2	2.5	1.8	3.1	3.3
YS014-29-7/8	17.4	41.3	3.6	2.8	3.9	3.3
YS014-30	23.4	35.6	3.1	2.7	3.4	2.6
YS014-31	19.3	44.9	2.8	2.6	4.2	2.8
YS-ZM04	4.0	41.0	3.3	1.7	4.2	3.8

Sample name	Muscovite	Halite	Dawsonite	Montmorillonite	Heulandite	Clay	Gypsum
YS014-28-7/8	4.6	40.5	2.5	0.0	3.0	10.4	13.2
YS014-28-6/8	5.6	28.4	1.7	0.2	2.4	9.1	2.05
YS014-29-6/8	1.9	1.1	1.3	0.7	2.8	5.4	0.69
YS014-29-7/8	4.5	4.7	1.9	0.2	2.4	9.3	1.29
YS014-30	7.8	4.8	2.1	0.6	0.1	9.4	1.06
YS014-31	6.5	0.2	4.4	0.4	0.1	7.6	1.16
YS-ZM04	6.0	7.0	3.0	0.1	4.3	7.4	1.65

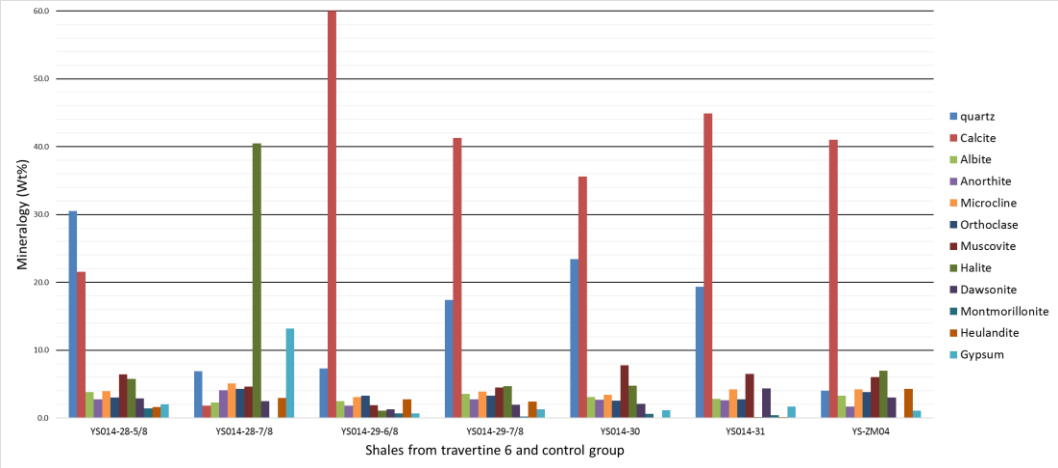

Figure 5- 9: Quantitative mineralogy measured by XRD on representative samples of Mancos shale from T6 and ZM.

5.3.1.2 SEM analysis

The results of SEM images for the Mancos Shale samples in T6 are presented as follows:

a. YS014-28: the sample closest to the fault

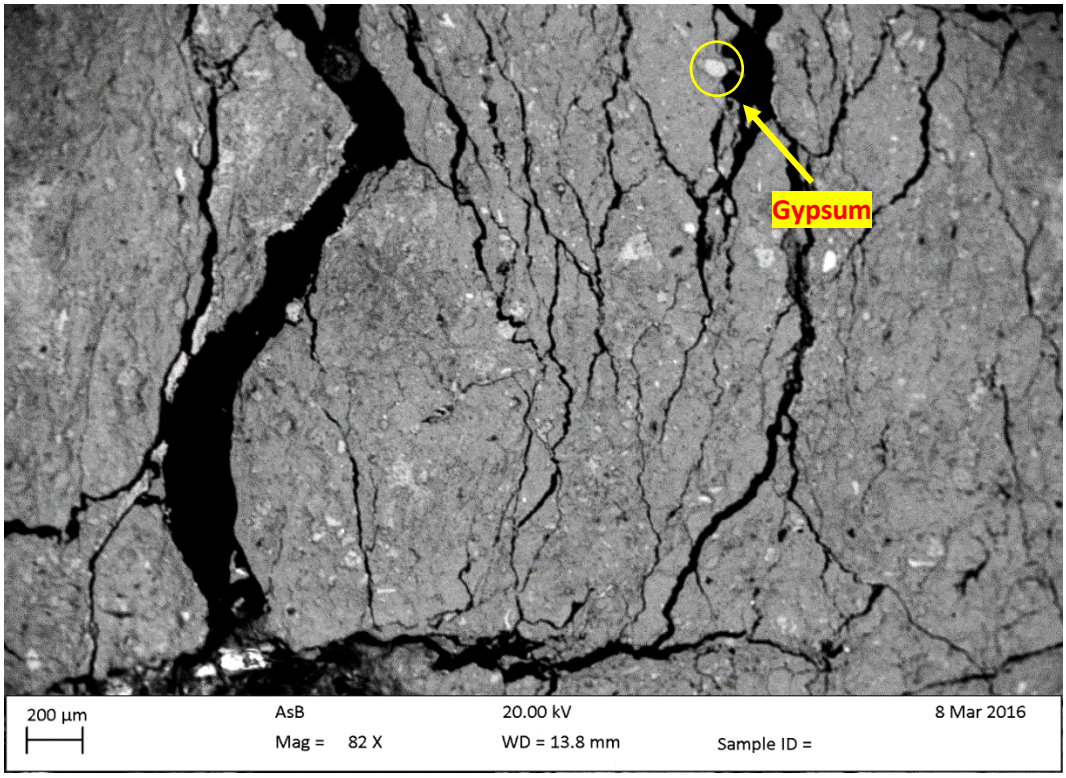

(a)

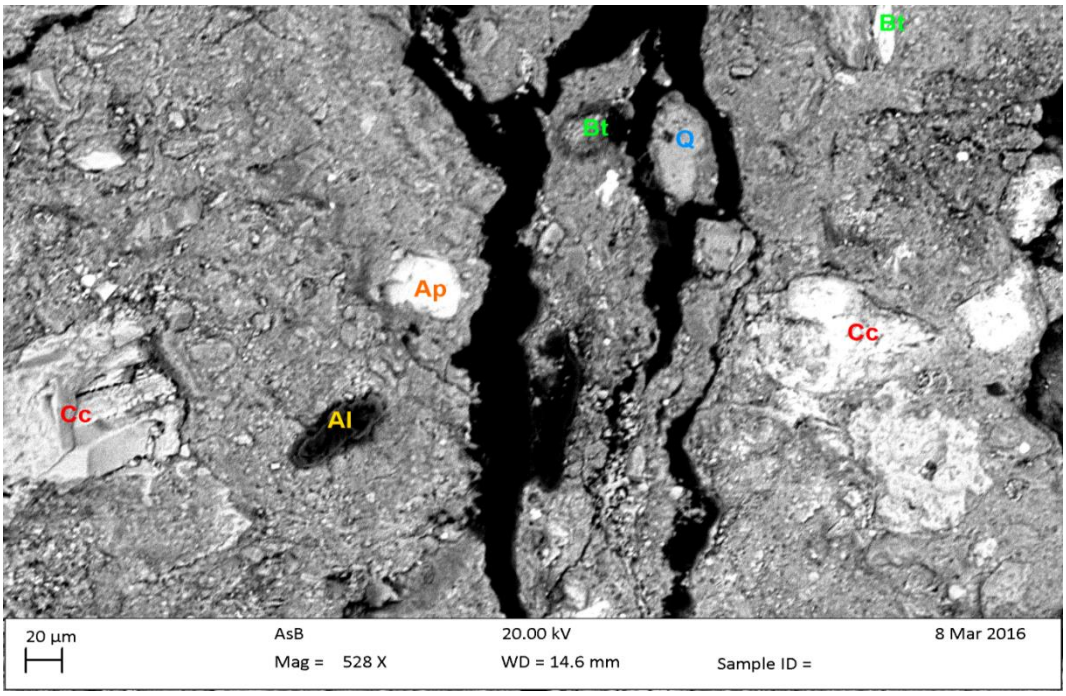

(b)

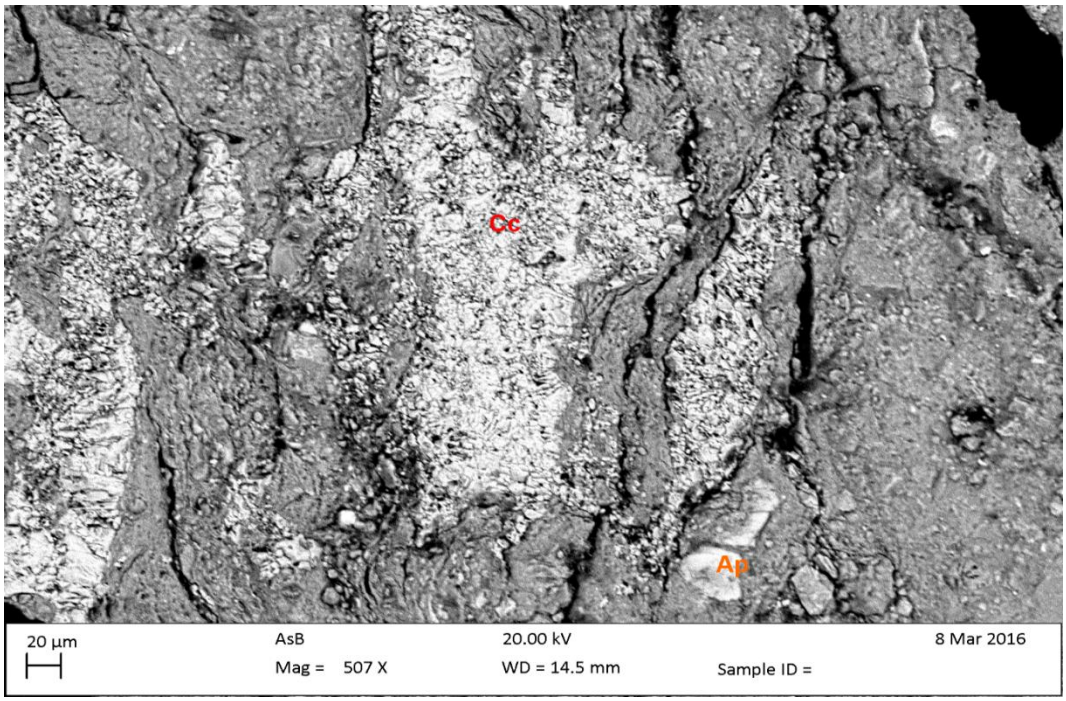

(c)

Figure 5- 10: SEM images of sample YS014-28, Cc=Calcite, Ap=Apatite, Al=albite, Bt=Biotite, Q=Quartz. (a) Sub-parallel fractures with gypsum. (b) Fractures with

calcite, albite, biotite and quartz. (c) The edge of the sample: calcite precipitate filling the pores and fractures.

Sample YS014-28 is the nearest to the Little Grand Wash fault. The SEM images of the sample present abundant open fractures. Both calcite and other grains after compaction could be observed in Figure 5-10(b). The existence of biotite, apatite and quartz with no clear crystal faces, suggesting they might be partly dissolved or physically deformed. Figure 5-10(c) is the close-up of a calcite-rich zone, which is parallel to the fractures, suggesting the precipitation of calcite might be related to the fractures. In sample YS014-28, much of the calcite cements appears to be deformed and fractured, so that apparently pre-dates at least some of the fault movement. Many of the calcite-rich areas are elongate parallel to the fractures.

b. Sample YS014-29: the sample 15m away from the main fault

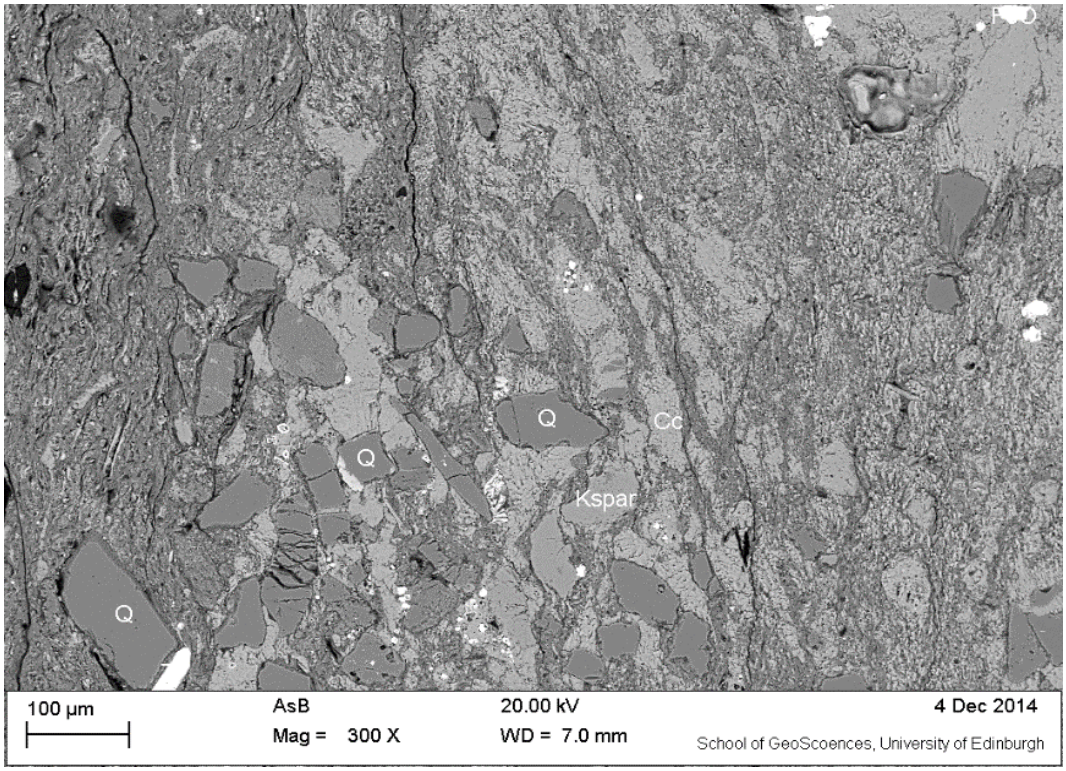

(a)

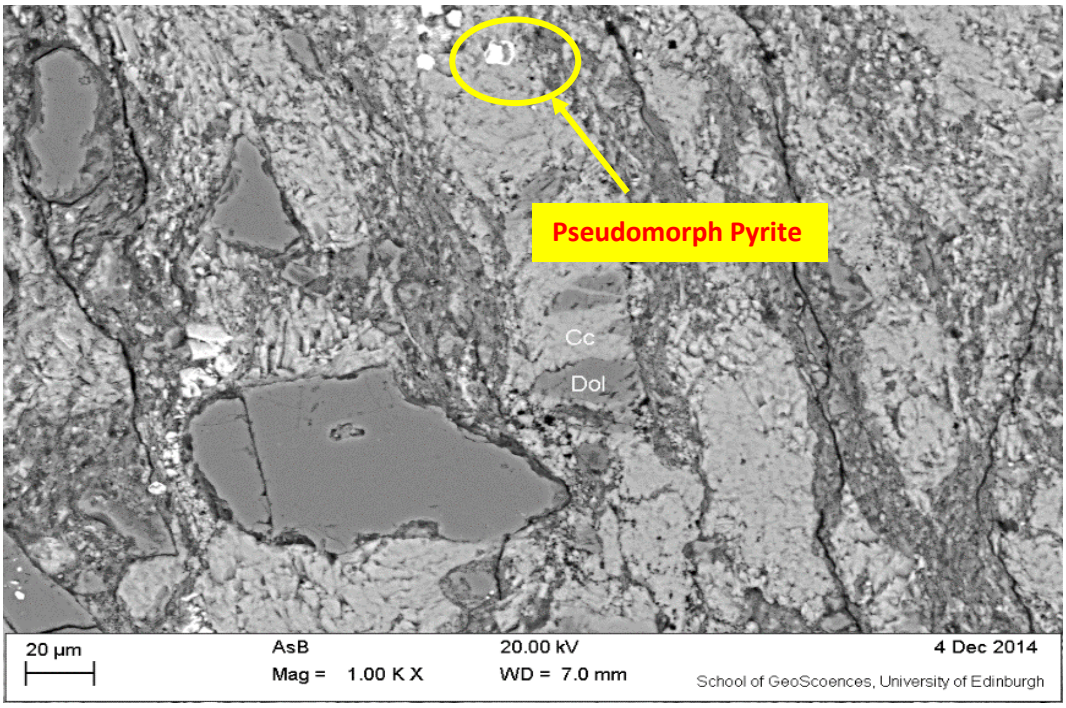

(b)

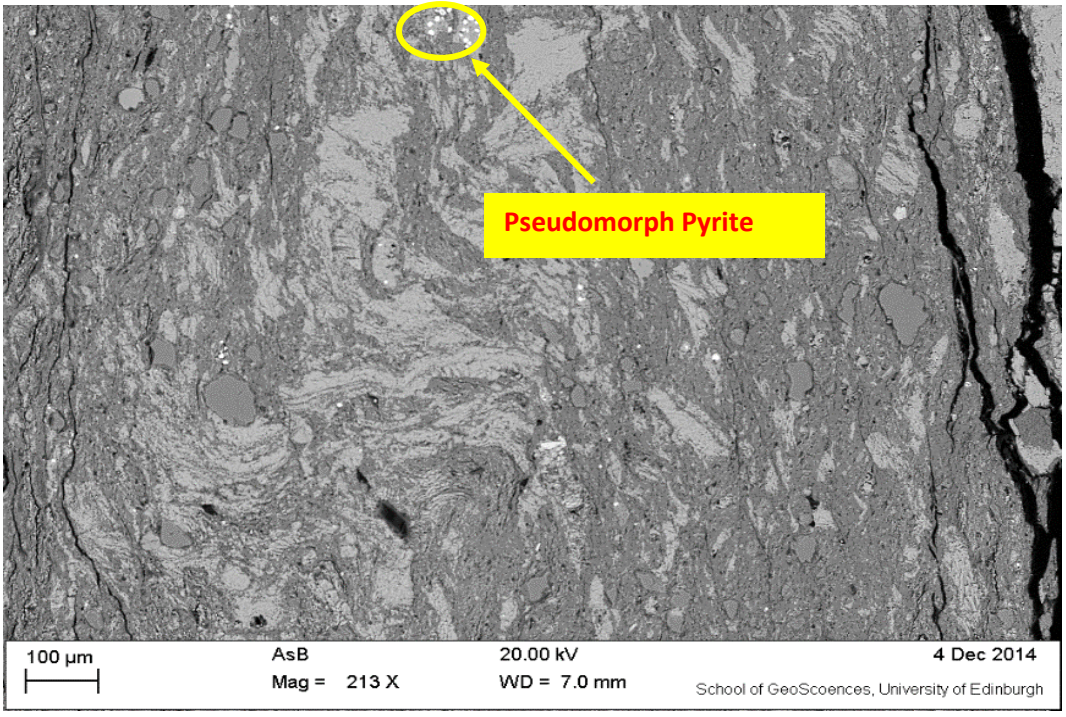

(c)

Figure 5- 11: SEM image of sample YS014-29. (a): calcite streaks parallel to fractures; (b) fractures have been fully cemented with secondary calcite. The circle

marks calcite inside a broken dolomite crystal; (c) irregular calcite cements suggesting deformation.

Figure 5-11 is the SEM image of sample YS014-29, which is the second nearest to the main fault. Diagenetic carbonate (streaky shaped carbonates) fills the open fractures compared with the highly porous sample YS014-28 (the sample closest to the fault). Pyrite (or pseudomorph after pyrite) has been observed in this sample. The precipitation of pyrite might be associated with the organic matter in Mancos shale via the reaction of:

$$CH_4 + SO_4^{2-} + Fe - mineral \xrightarrow{Bacteria} H_2S + FeS_2 + HCO_3^- \text{ (shallow burial)}$$

Equation 5-14

The dissolved CO_2 might contribute to the formation via the reactions of (Kampman et al., 2014):

$$4Fe_2O_3 + 15CO_2 + 6H_2O + CH_4 \rightarrow 8Fe^{2+} + 16HCO_3^-$$ Equation 5-15

$$Fe_2O_3 + 4CO_2 + H_2O + HS^- \rightarrow Fe^{2+} + FeS_2 + 4HCO_3^-$$ Equation 5-16

c. YS014-30: the sample 16.4m from the main fault

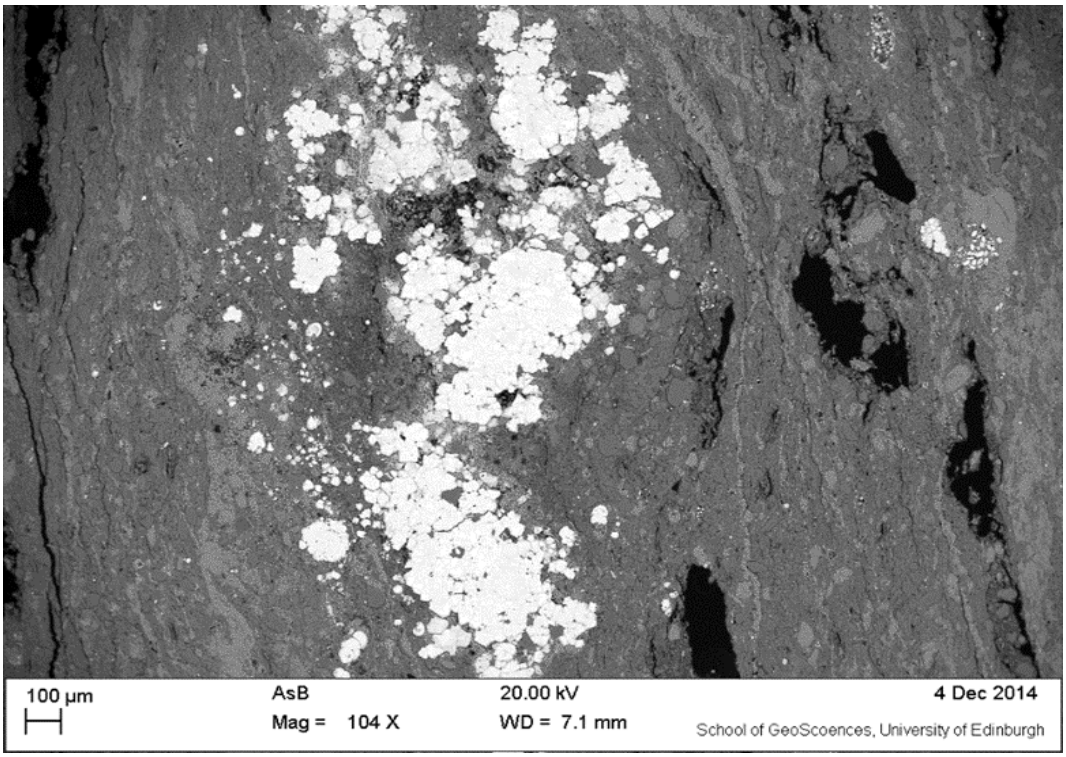
100 µm
AsB
Mag = 104 X
20.00 kV
WD = 7.1 mm
4 Dec 2014
School of GeoScoences, University of Edinburgh

(a)

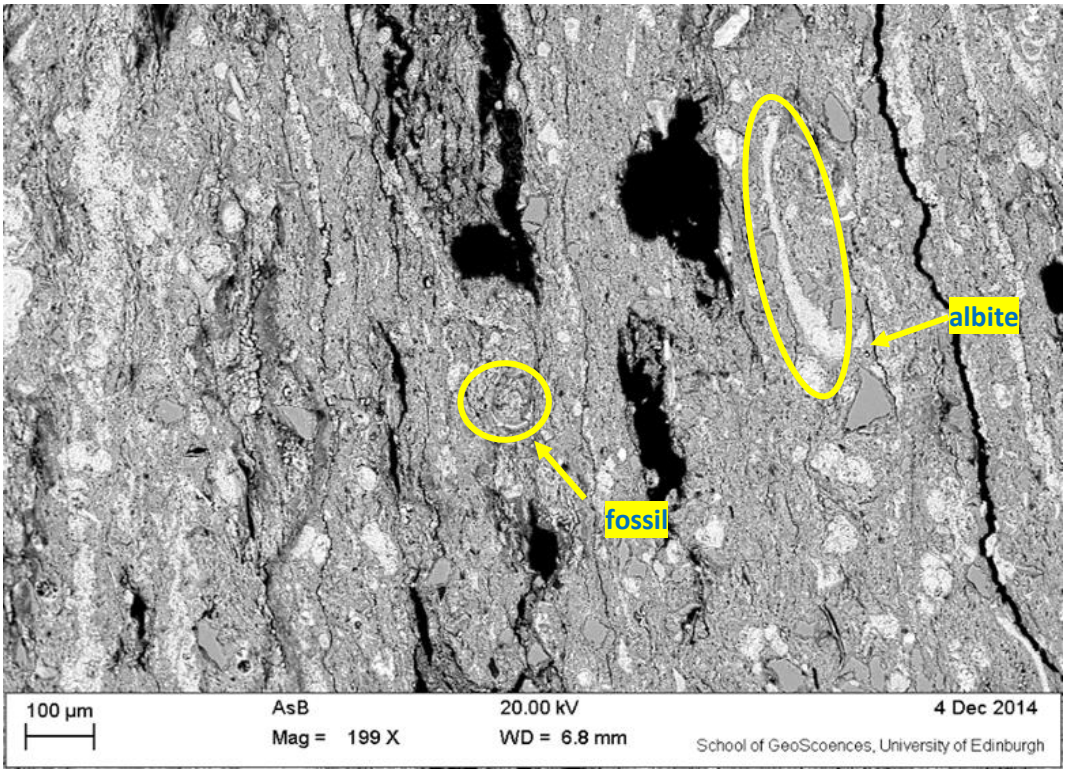
albite
fossil
100 µm
AsB
Mag = 199 X
20.00 kV
WD = 6.8 mm
4 Dec 2014
School of GeoScoences, University of Edinburgh

(b)

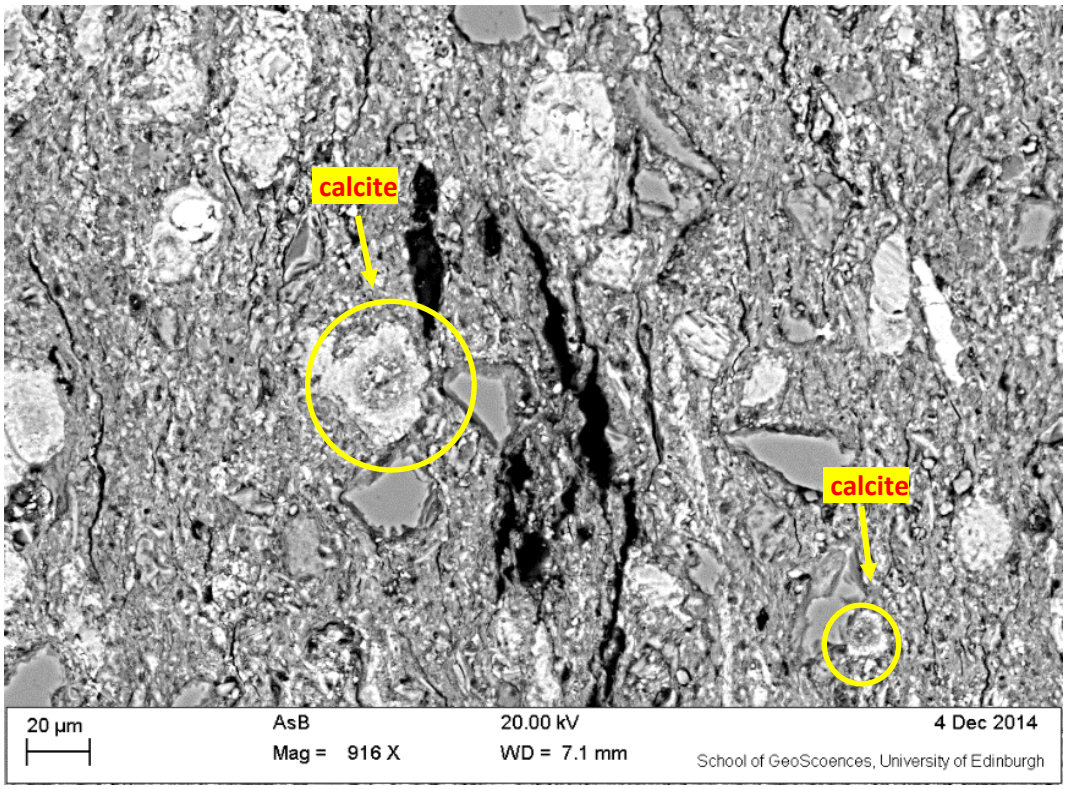
calcite
calcite
20 µm
AsB
Mag = 916 X
20.00 kV
WD = 7.1 mm
4 Dec 2014
School of GeoScoences, University of Edinburgh

(c)

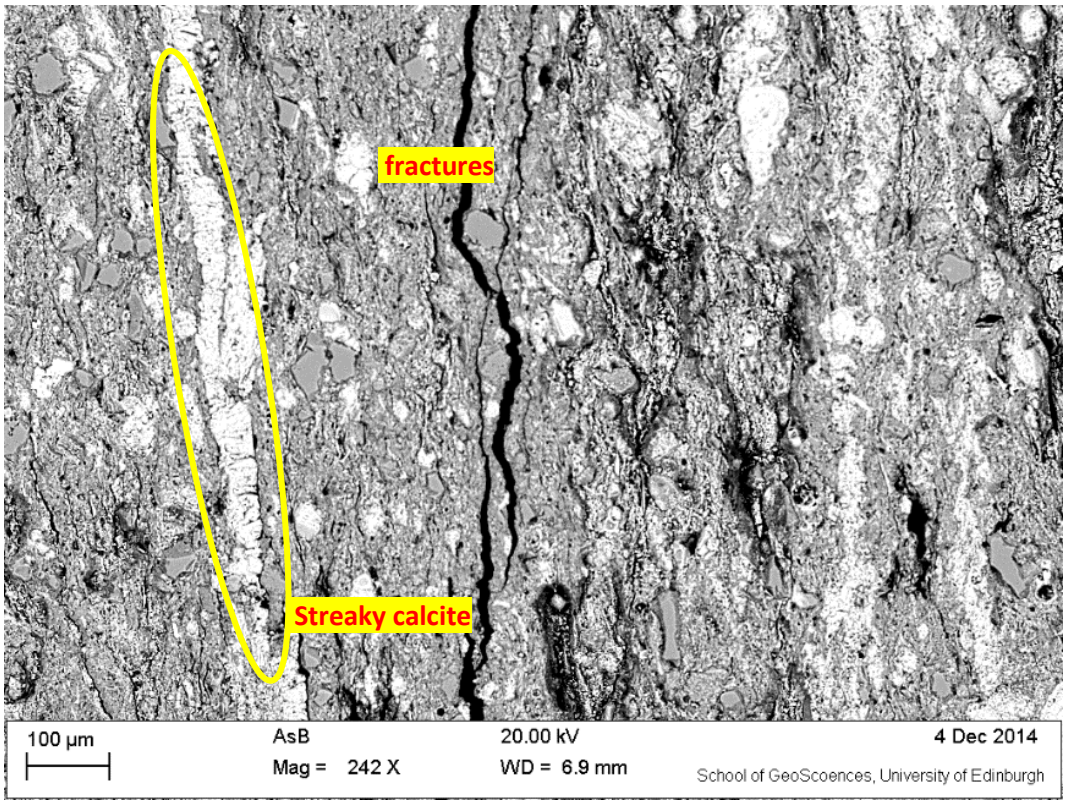
fractures
Streaky calcite
100 µm
AsB
Mag = 242 X
20.00 kV
WD = 6.9 mm
4 Dec 2014
School of GeoScoences, University of Edinburgh

(d)

Figure 5- 12: SEM scan images of sample YS014-30 from T6. (a) The edge of the sample: calcite streaks with big amount of framboid pyrite; (b) the middle of the sample: the blue circle marks remaining of fossil and albite (elongate); (c) the middle of the sample: the blue circle marks calcite; (d) the edge of the sample: calcite streaks filling the secondary pores.

The SEM image of YS014-30 sample shows calcite and clay streaks along with pyrite (white) (pore filling framboid pyrite). Pores in the Figure 5-12(a) (b) (c) might be the result of CO_2-rich fluid dissolution. The orientation of the secondary pores is similar the deformation fractures. Hence, the dissolution pores were probably formed during or after the deformation of the faults. The elongated albite (Figure 5-12(b)) filling the pores is the secondary precipitation from the fluid after the structure deformation. Figure 5-12(c) shows zoned calcites with clays in the middle and pure calcite in the edge. The edge of the sample has more deformation and pore filling calcite from secondary precipitation in Figure 5-12(d).

There are three types of calcite have been observed in sample YS014-30: fossil calcite, zoned calcite and pore filling calcite (elongate streaks). In addition, larger amount of pyrite has been found. However, almost no pyrite (less than 1%) has been detected by XRD and EDX analysis. The pyrite-like minerals are detected as FeO by EDX spectrum rather than FeS_2. The possible explanation for this replacement could be FeO pseudomorph after pyrite that substituted the original pyrite by weathering. The shape of the original pyrite remains unchanged, but sulphur has been weathered. The observation is consistent with the modelling result from paleo-fluid in section 4.3.9, that the large quantity of gypsum in Mancos Shale are from the weathering of pyrite.

d. Sample YS014-32: the sample 19m from the main fault

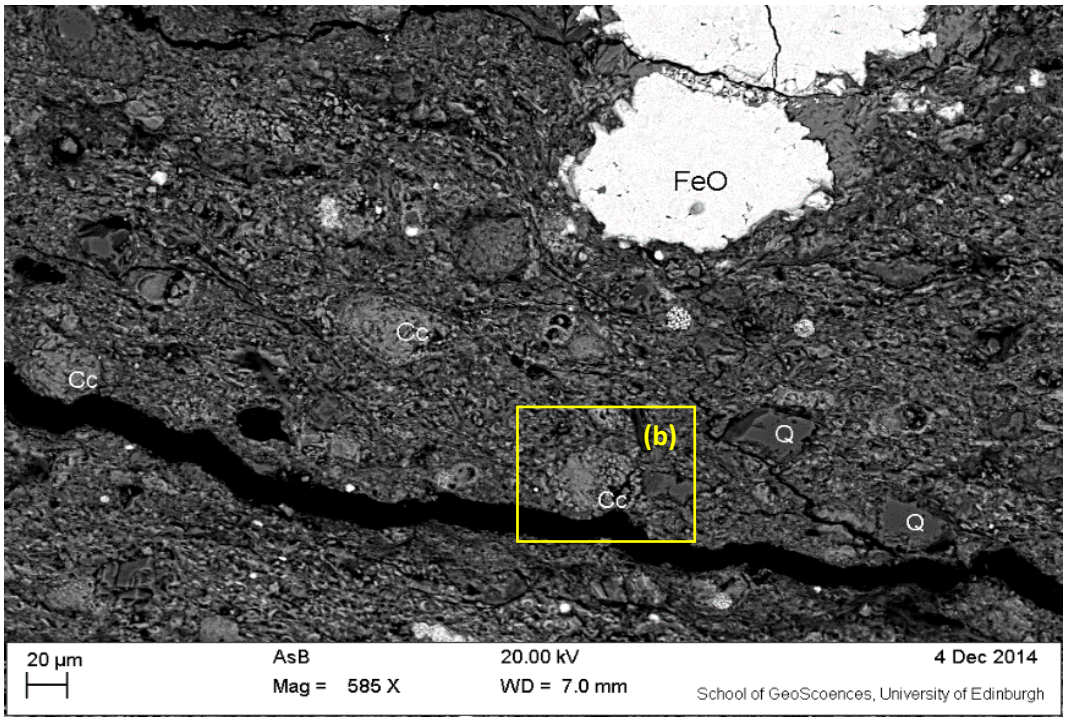
FeO
Cc
Cc
(b)
Cc
Q
Q
20 µm
AsB
Mag = 585 X
20.00 kV
WD = 7.0 mm
4 Dec 2014
School of GeoScoences, University of Edinburgh

(a)

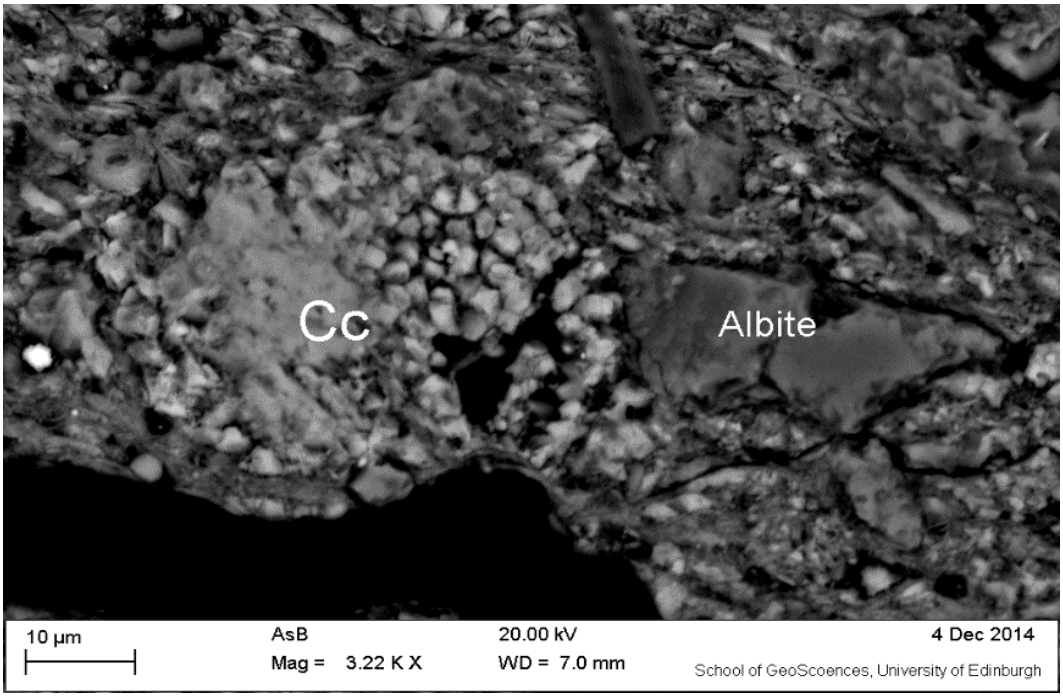
Cc
Albite
10 µm
AsB
Mag = 3.22 K X
20.00 kV
WD = 7.0 mm
4 Dec 2014
School of GeoScoences, University of Edinburgh

(b)

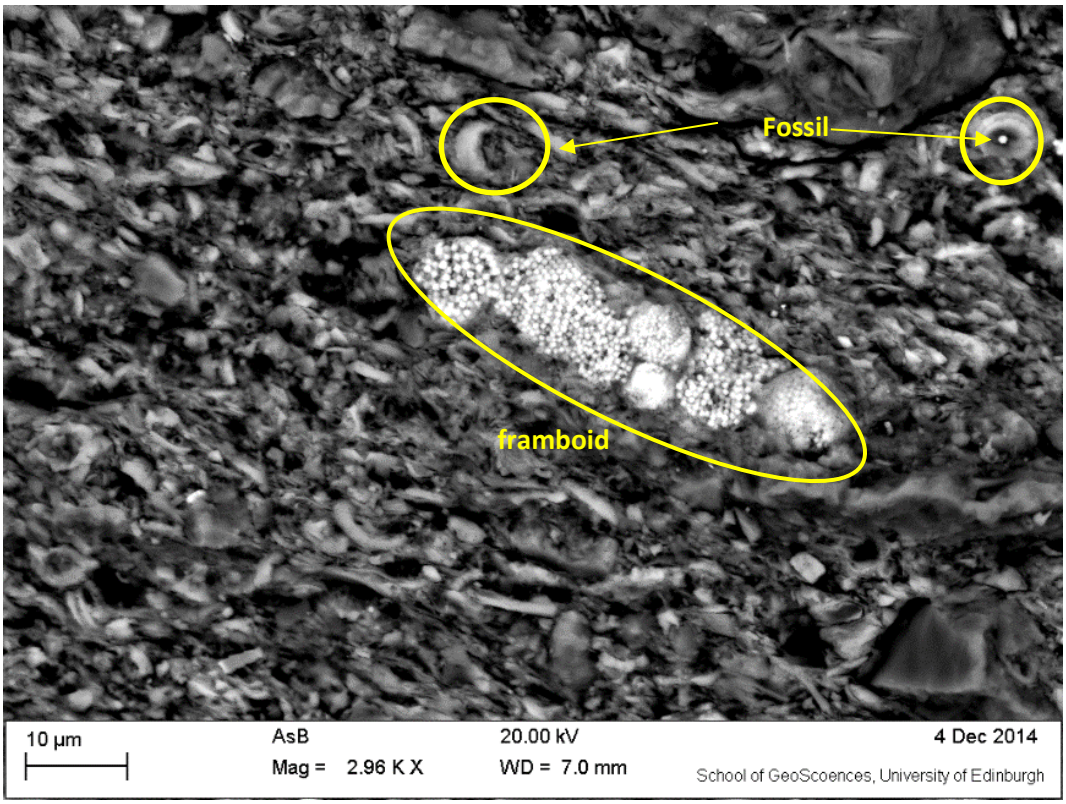
Fossil
framboid
10 µm
AsB
Mag = 2.96 K X
20.00 kV
WD = 7.0 mm
4 Dec 2014
School of GeoScoences, University of Edinburgh

(c)

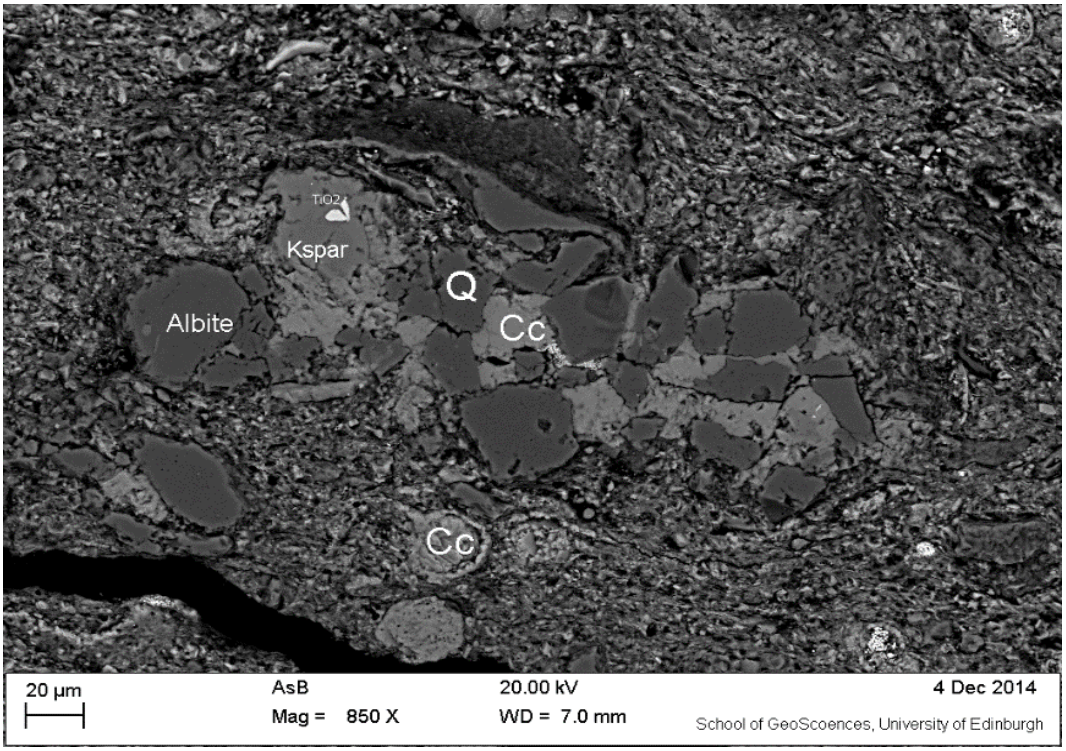
TiO2
Kspar
Q
Albite
Cc
Cc
20 µm
AsB
Mag = 850 X
20.00 kV
WD = 7.0 mm
4 Dec 2014
School of GeoScoences, University of Edinburgh

(d)

Figure 5- 13: SEM image of sample YS014-32: (a) the edge of the sample; (b) the close-up of the box zone in (a): euhedral calcite, albite and pyrite; (c) the close-up of the pyrite framboid (FeO pseudomorph) (>5um in diameter) occurring in the vicinity of calcareous fossil; (d) quartz cemented with calcite, K-feldpar and albite.

Small sized framboid (FeO pseudomorph) (>5um in diameter) has been observed in the shale samples 17m away from the main fault (Figure 5-13(c)). Few fractures could be found compared with sample YS014-28 and 29. The small sized framboid demonstrates euxinic conditions (H_2S-bearing, O_2-free water). Sweeney and Kaplan (1973) described the formation processes of pyrite framboid: the first iron sulphide is precipitated with highest Fe:S ratio (sometimes Mackinawite) as a spheroidal texture on transformation to greigite, then changed to framboid by continued internal nucleation of pyrite crystals (Sweeney and Kaplan, 1973, Raiswell and Brimblecombe, 1977).

Three types of calcite could be found in this sample: euhedral calcite, calcite cements between feldspar and quartz, and calcareous fossil. The formation of calcite cements might be related to feldspar dissolution and overgrowth with other diagenetic minerals. This type of cement still belongs to early cementation that un-associated with fault, because the fractures (parallel with the deformation fracture) that that penetrating the whole cementation indicating the formation of the cements should formed before the deformation (Fig. 5-13(d)).

e. Control group sample YS014-ZM04: the sample near the fault, not related with any travertine

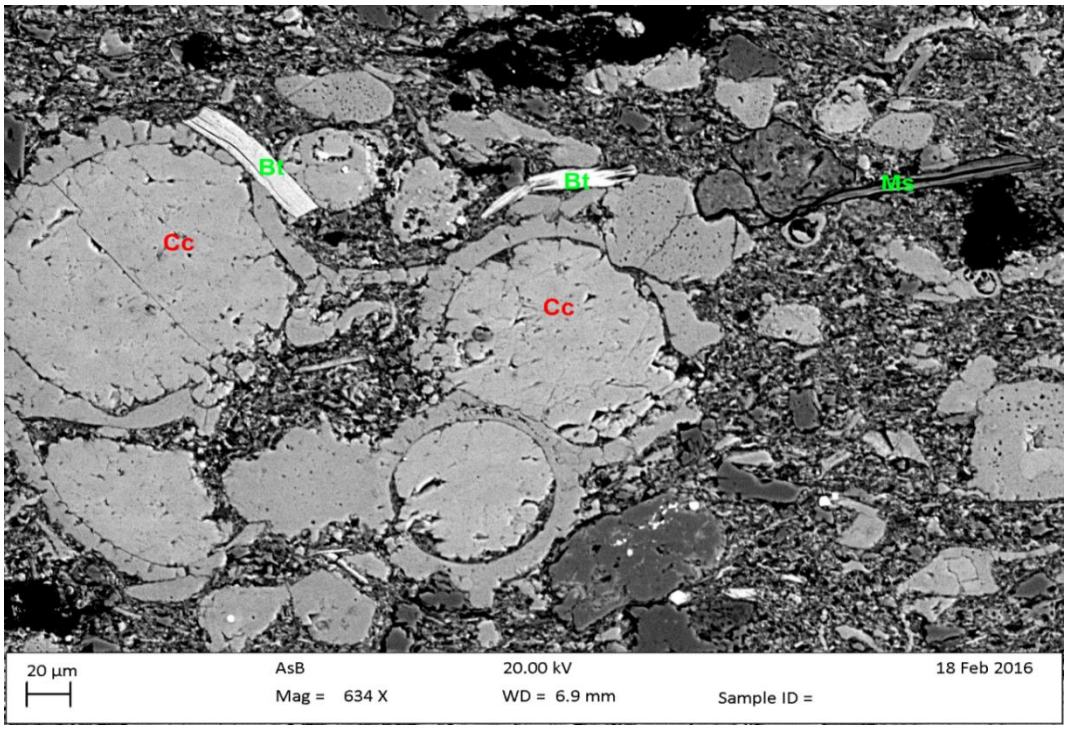

(a)

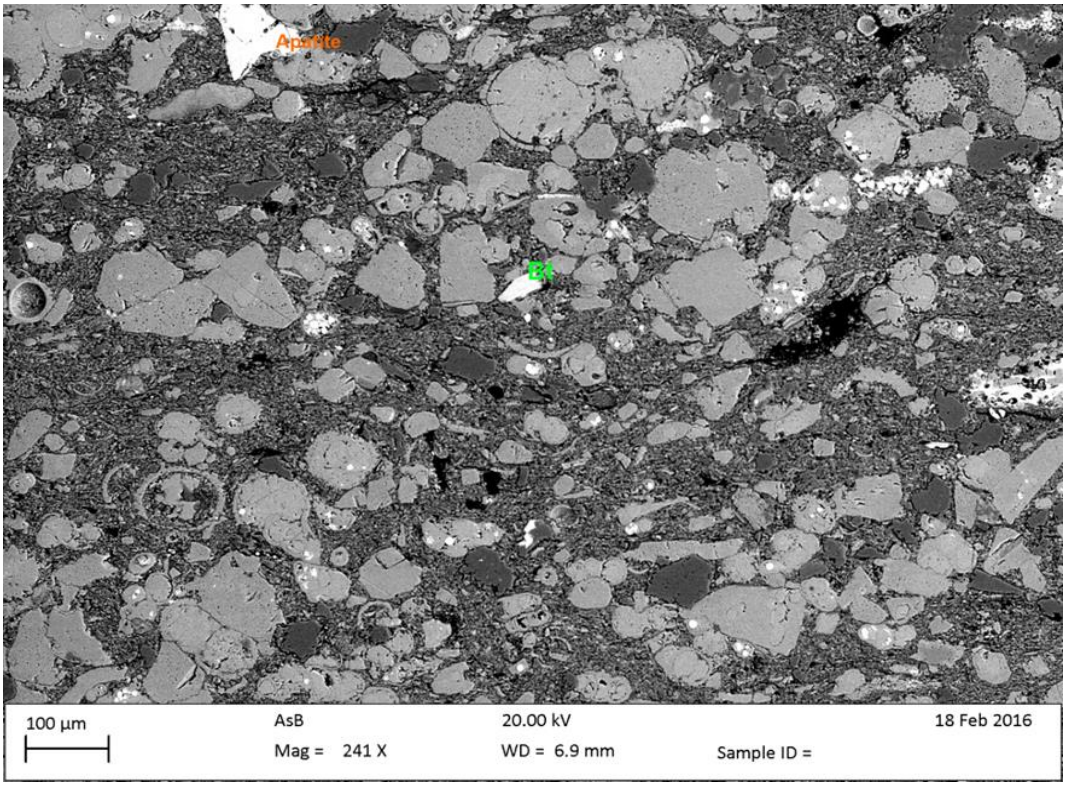

(b)

Figure 5- 14: SEM image of control group sample ZM-04: (a) apatite, biotite and pyrite associated with calcareous fossil; (b) the close-up of calcareous fossil with biotite and muscovite.

Most of carbonates in YS014-ZM04 are as foraminifera shells (called a 'test'; marine animals). The inside of the fossil usually forms framboid pyrite. Biotite forms at the dissolved edges of foraminifera, with very clear paralleled cleavage and easily split into thin flexible sheets. The bended cleavage suggests the growth of biotite was after the deposition of foraminifera calcite (Fig. 5-14(a)).

Comparatively, few framboid was observed in sample YS014-28 and 29 compared with sample YS014-30, 32 and YS014-ZM04 which are further away from the fault (Figure 5-13(a)). The earliest framboidal pyrite precipitated uniformly throughout the sediment prior to concretionary growth. But the addition of CO_2 into the fluid might inhibit the formation of framboid pyrite (Sweeney and Kaplan, 1973, Rickard, 1975). In a low pH system, the precipitation of metastable is impeded. The recrystallization will deposit pyrite but not in framboid feature (Sweeney and Kaplan, 1973). The absence of framboid pyrtie in the samples close to fault also faciliates the assumption that the CO_2-rich fluid react in sample YS014-28 and YS014-29.

In summary, the types of calcite and pyrite are described in Table 5-7. The morphology and the quantity of different types of calcite and pyrite are quite various for the samples with different proximity from the main fault. Sample YS014-28 and YS014-29 contain almost no fossil calcite and framboid pyrite. YS014-28 is highly fractured with undissolved gypsum, while the YS014-29 is seriously cemented with secondary calcite precipitation. The cementation formed post-dated to faulting, suggesting the fracture filling calcites should be associated with the inflow of CO_2-rich fluid. The YS014-30 and YS014-32 contain some fossil calcite and framboidal pyrite during the burial, and some fracture filling calcite as secondary precipitation. YS014-ZM04 contains the most fossil calcite and framboid but almost none of secondary pore filling calcite, which is the least affected by the secondary diagenesis (CO_2-rich fluid or physical compaction).

Table 5- 7: calcite and pyrite types in shale sample of T6 and ZM-04. Three check marks indicate a large amount; two check marks indicate a medium amount; one

check mark indicates a small amount; no check mark indicates none has been found.

Sample No.	Fossil calcite	euhedral/ sub-euhedral calcite	Fracture filling/ cementing calcite	Euhedral pyrite or FeO pseudomorph)	Framboidal pyrite or FeO pseudomorph)	Fractures/ pores
YS014-28		✓	✓			✓✓✓
YS014-29			✓✓✓	✓		
YS014-30	✓	✓	✓✓	✓✓	✓	✓
YS014-32	✓✓	✓	✓		✓✓	✓
YS014-ZM04	✓✓✓				✓✓✓	✓ (only dissolution pores)

5.3.1.3 Stable isotope analyse for T6 samples

Table 5-8 and Fig. 5-15 below show the isotopic results of the samples form T6 (location see Fig. 3-5). Sample T2-vein is separated for different sub-samples to study the variations (for example, YS014-28 is separated as 8 subsamples from YS014-28-1/8 to YS014-28-8/8).

Table 5- 8: Stable isotope and weight percentage of calcite of the samples from T6 and YS-ZM04

Sample ID	Description	δ^{13}C V-PDB‰	δ^{18}O V-PDB‰	% Calcite
YS014-27-1/2	Vein T5 filling the sandstone cracks	-5.3	-13.0	93.0
YS014-27-2/2		-5.3	-12.7	100.0
YS014-26-1/2		-4.9	-13.1	93.0
YS014-26-2/2		-5.0	-13.6	100.0
YS014-71-1/2	hard sandstone	0.7	-13.0	44.9
YS014-71-2/2		-6.5	-12.6	32.1

YS014-72-1/2		-4.4	-13.0	13.0
YS014-72-2/2		-5.7	-12.5	48.9
YS014-76-1/4	Control group: Normal black Mancos shale at the bottom of the outcrop	1.8	-7.4	37.0
YS014-76-2/4		1.8	-7.3	35.8
YS014-76-3/4		1.8	-7.3	38.0
YS014-76-4/4		1.6	-7.4	35.9
YS014-77-1/4		1.7	-7.5	29.4
YS014-77-2/4		1.7	-7.5	32.0
YS014-77-3/4		1.7	-7.5	30.4
YS014-77-4/4		1.7	-7.5	27.7
YS014-28-1/8	Bedrocks of Mancos shales from T6: Zone 3	0.5	-11.7	11.0
YS014-28-2/8		-0.2	-9.8	16.0
YS014-28-3/8		0.1	-11.7	37.0
YS014-28-4/8		-0.7	-11.3	37.0
YS014-28-5/8		-0.5	-12.4	17.1
YS014-28-6/8		-1.1	-13.0	9.5
YS014-28-7/8		-8.2	-14.8	5.4
YS014-28-8/8		-6.9	-13.4	5.7
YS014-29-1/8	Bedrocks of Mancos shales from T6: Zone 3	-0.6	-11.2	58.0
YS014-29-2/8		1.0	-11.6	50.0
YS014-29-3/8		-2.5	-12.2	60.0
YS014-29-4/8		1.4	-13.0	53.0
YS014-29-5/8		1.6	-12.7	9.4
YS014-29-6/8		1.4	-12.2	50.0
YS014-29-7/8		-0.1	-11.7	57.3
YS014-29-8/8		0.0	-10.8	67.2
YS014-30-1/4	Bedrocks of Mancos shales from T6: Zone 2	1.3	-9.0	31.0
YS014-30-2/4		1.4	-8.1	36.0
YS014-30-3/4		1.0	-9.2	33.0

YS014-30-4/4		0.9	-9.1	29.0
YS014-31-1/4	Bedrocks of Mancos shales from T6: Zone 1	1.9	-7.1	37.0
YS014-31-2/4		2.0	-7.0	40.0
YS014-31-3/4		2.0	-6.9	41.0
YS014-31-4/4		2.1	-6.6	41.0
YS014-32-1/4		1.9	-6.6	43.0
YS014-32-2/4		1.8	-7.0	46.0
YS014-32-3/4		1.9	-6.8	38.0
YS014-32-4/4		1.9	-6.7	40.0
YS014-33-1/4		2.1	-6.1	35.0
YS014-33-2/4		2.2	-5.9	34.0
YS014-33-3/4		2.1	-6.1	35.0
YS014-33-4/4		2.0	-6.5	38.0
YS014-34-1/4		2.0	-6.5	37.0
YS014-34-2/4		2.0	-6.8	37.0
YS014-34-3/4		2.0	-6.6	36.0
YS014-34-4/4		1.9	-6.8	35.0
YS014-35		1.8	-7.4	35.0
YS014-36-1/2		1.7	-7.5	41.4
YS014-36-2/2		1.7	-7.5	38.6
YS014-37-1/2		2.0	-6.8	34.3
YS014-37-2/2		2.0	-6.9	37.3
YS014-38-1/2		1.8	-7.2	42.0
YS014-38-2/2		1.8	-7.1	40.8
YS014-39-1/2		1.3	-7.1	55.5
YS014-39-2/2		1.3	-7.1	55.9
ZM04	ZM	1.5	-7.4	59.0
ZM04		1.8	-7.4	59.0

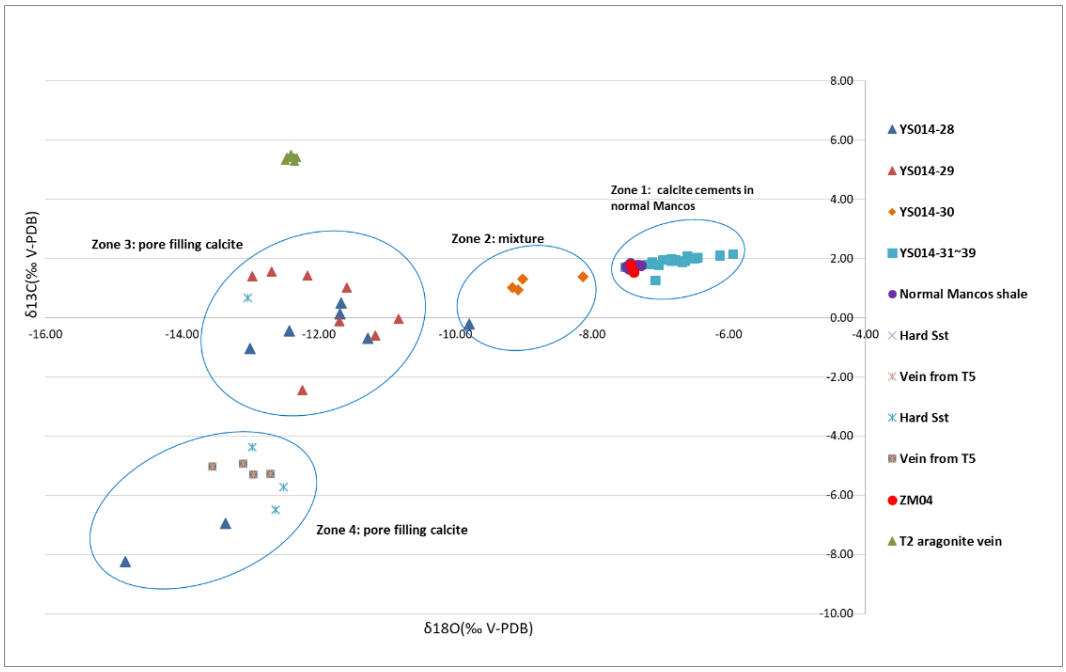

Figure 5- 15: Stable isotopic data for samples associated with Travertine 6 and YS-ZM traverse. Dark blue triangles represent sample YS014-28 which is the nearest to the fault; red triangles represent sample YS014-29 located second nearest to the fault; orange rectangles represent sample YS014-30; light blue rectangles represent sample YS014-31 to 34; solid purple circles are 'normal' Mancos shale; blue snowflakes are sandstones from on top of Mancos shales; orange snowflakes are veins in travertine 5, in fractures in the Mancos Shale; solid red circles are sample YS-ZM04.

The result displayed in Fig 5-15 shows the $\delta^{13}C$ values of the carbonate cement in Mancos shales range from -8.2‰ to +2.2‰ V-PDB and the $\delta^{18}O$ values range from -14.8‰ to -5.9‰ V-PDB (15.6‰ ~ 24.7‰ SMOW). The 2 samples that nearest to the fault (Sample YS014-28 and YS014-29) show big variations in carbon (from -8.2‰ to +1.6‰V-PDB) and oxygen (from -14.8‰ to -9.8‰ V-PDB). Sample YS014-30 is moderately scattered ranging from 0.93‰ to 1.4‰ in carbon isotope and -8.1‰ to -9.2‰ in oxygen. However, samples YS014-30, YS014-31, YS014-32 and YS014-33 form a tight correlation between carbon and oxygen isotope (1.9‰ to 2.2‰ in carbon and -5.9‰ to -7.1‰). Major sources of carbon carbonate cements were discussed in section 5.1.2. The highly uniform carbon isotopic values of the

cement could be either from single source of bicarbonate and fluid, or the average of a wide range.

The samples in T6 can be separated into 4 zones based on isotopic values (Figure 5-15): Zone 1 is thought to be 'normal' Mancos shale, i.e. unaffected by interaction with CO_2-rich water (i.e. the mixed fluid of meteoric and brine fluid with large quantity of CO_2 immigrated through the main fault); Zone 3 samples are close to the fault (and travertine), implying strong influence by the CO_2-rich fluid. The arithmetic mean and range of isotopic values of each zone has been listed in Table 5-9:

Table 5- 9: mean stable isotope values for different zones

Zone No.	$\delta^{13}C$ average ‰ V-PDB	$\delta^{13}C$ range ‰ V-PDB	$\delta^{18}O$ average ‰ V-PDB	$\delta^{18}O$ range ‰ V-PDB	% Calcite
Zone 1	1.9	1.3 ~ 2.2	-6.9	-7.5 ~ -5.9	41
Zone 2	1.2	-0.2 ~ 1.4	-8.9	-9.8 ~ -8.1	32
Zone 3	0.1	-2.5 ~ -1.6	-11	-13 ~ -11	40
Zone 4	-5.6	-8.2 ~ -4.9	-13	-13 ~ -15	31

a. The deposition temperature and fluid composition

An aim of interpreting the stable isotope is to model the temperature and fluid composition that deposited the calcite cements in the Mancos shale. The general trend of data is for the depletion of heavy carbon and heavy oxygen close to the fault, moving from Zone 1 to Zone 3 (Fig. 5-15). The change of carbon and oxygen isotope between samples in different zones could be the result of a) the change of temperature, b) the change of fluid composition, or c) a combination of these two. The temperature effect is much stronger for oxygen than for carbon.

Temperatures have varied widely during the geological history of the Manco Shale. The bottom water temperature for the Western Interior Seaway ranged from 15-30 °C (Kauffman, 1975). From the late Cretaceous to the early Tertiary, the Laramide Orogeny resumed to uplift the structure and reactivated or generated faults. The Colorado Plateau has undergone epeirogenic uplift since the late Cenozoic (Hunt, 1956, Lucchitta, 1979) accompanied with regional erosion that

resulted in salt beds uplifted to close to the surface, leading to the flushing of salt-rich fluid into ground water through fractures and faults (Doelling et al., 1988). Nuccio and Condon estimated the total erosion of the region is up to 8000ft (Nuccio and Condon, 1996). The paleo-temperatures of the Green River area shown in Figure 5-16 illustrates the highest temperature of Cretaceous sediments is about 200°F (93°C) and the deepest burial depth is 8000ft (~2400m). The deposition of travertine 6 occurred about 60 ky ago (Dockrill, 2006), and the paleo-surface temperature was about 10-20 °C (section 4.3.9).

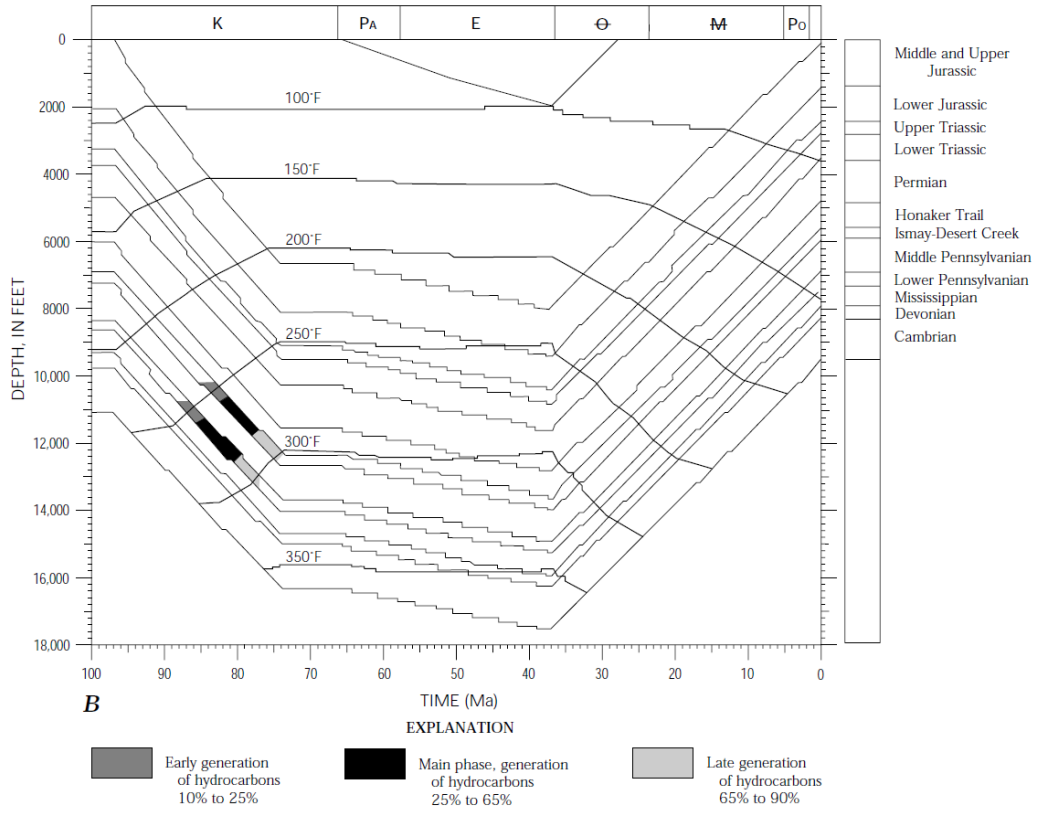

Figure 5- 16: Burial, thermal and petroleum generation model of the Green River area (Nuccio and Condon, 1996).

It is interesting to compare the data of this study to that of Klein et al. (1999)'s studies on the Prairie Canyon Member of the Mancos Shale to the northwest of the Grand Canyon. The blue crosses of Fig. 5-17 represent the values of concretions from the centre (upper right) to the edge (lower left), indicating a change from methanic process to thermal decarboxylation process, with an increase in temperature during burial. Most of the isotope values of the host-rock in Klein et al.

(1999)'s study cluster close to the middle of the concretion trend line (orange crosses on Fig. 5-17). It is interpreted as the host rock value represent a mixture of early and late cements. The outer edge of the concretions is proved to be formed under temperature of 95°C at depth of 3 km.

The Crystal Geyer cements are significantly different from the results of Klein et al. (1999). The uniform carbon isotopes in Zone 1 cannot be explained as the mean values of a wide spread of compositions. One reason for this is from the SEM images. No significant amount of zoned calcite could be found: most of the calcite cements observed in Zone 1 are fossil shells (tests). In addition, when we compare the calcite cements in Zone 1, Zone 2 and Zone 3, the oxygen isotope ratio is much more variable than the carbon isotope ratio (0.0 ~1.9‰ V-PDB for carbon; -6.9 ~ -11.0‰ V-PDB for oxygen), indicating that a change of fluid composition is more likely to be the reason for the variation than the temperature. The intrusion of meteoric water would strongly affect the oxygen isotope ratio of the pore fluids, but not the carbon isotopes.

Samples in Zone 3 (Fig. 5-15) are the most influenced by CO_2-rich fluid, the $\delta^{18}O$ of which resemble that of T2-vein (solid green triangle in Figure 5-15), indicating that Zone 3 cements should be deposited by CO_2-rich paleo-fluid. According to SEM analysis (section 5.2.2.2), the most common type of cements is secondary calcite filling pores and fractures that post-dated to main fault deformation, which suggest these pore filling calcites should be derived from the CO_2-rich fluid.

Samples in Zone 4 contain depleted $\delta^{18}O$ and $\delta^{13}C$ samples. The deposition of cements in Zone 4 is probably from thermal carboxylation during deep burial and high temperature (more than 90°C at the depth of >2000m). The difference in oxygen isotope from the deep buried dolomite concretion of Klein et al. (1999) (blue cross in Figure 5-17) is resulted from various oxygen fractionation of dolomite (Rosenbaum and Sheppard, 1986, Deines et al., 1974). Dolomite is more enriched with $\delta^{18}O$ rather than calcite under the same temperature, thus resulting in the calcite diagenetic line move left-ward (dashed line in Figure 5-17) about 3‰ V-PDB compared with the dolomite diagenetic line (solid line in Figure 5-17). Zone 2 is the physical mixture of Zone 1, Zone 3 and Zone 4, which is consistent with SEM study that sample YS014-30 contains both original marine carbonates and secondary pore filling carbonates.

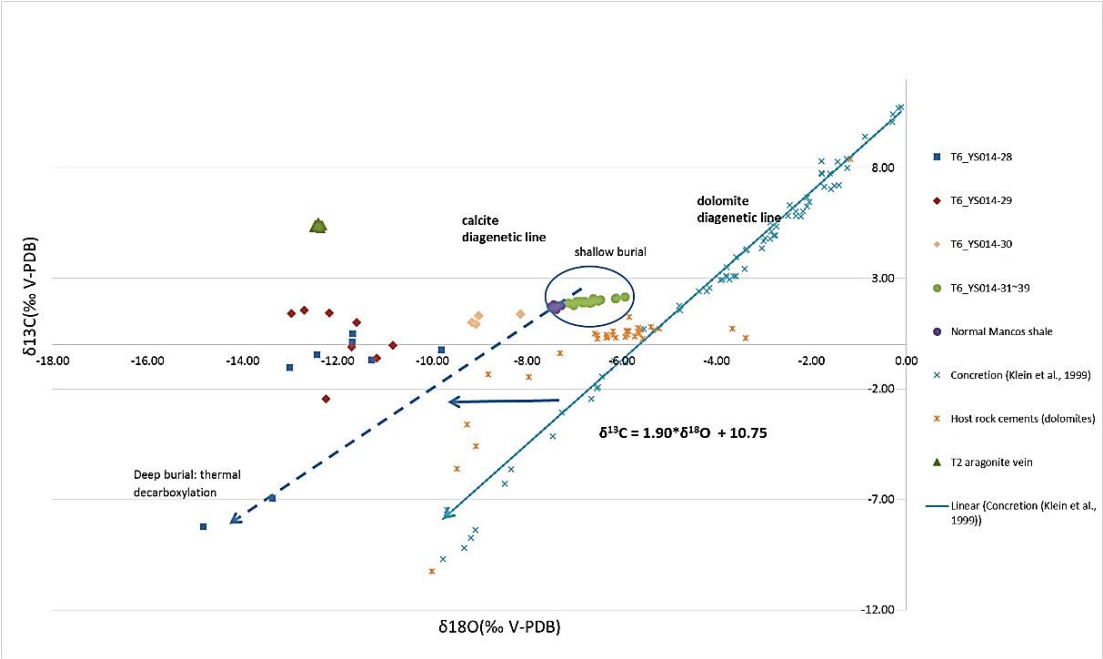

Figure 5- 17: Stable isotope of Mancos Shale cements of this study and the concretions and host rock cements of Klein et al., (1999).

The deposition condition for the formation of carbonate cements can be assessed using the carbonate-water fractionation factor equation for oxygen isotopes. The oxygen fractionation equation (Eq. 5-9) is from Kim and O'Neil (1997). The fractionation factor equals to the oxygen isotope of calcite cements minus that of the fluid. Paradox brine water ($\delta^{18}O$= -5 ~ -7‰ V-SMOW; Morrison and Parry, 1986) and Airport Well spring water ($\delta^{18}O$= -14‰ V-SMOW, Kampman et al., 2014; Assayag, et al., 2008) are used as end members to calculate the isotopic values of the mixed fluid (Table 5-10).

The oxygen isotopic values of the calcite cements in Zone 1 range from -6.9‰ to -12.7‰ V-PDB. As the calcites in Zone 1 are mostly depositional calcite or primary calcite cements formed in the early stage of burial, the deposition temperature should be similar to the sea temperature (15~25°C). Calcite cements in Zone 3, which are mostly secondary pore/fracture filling calcite, are probably deposited by the mixed fluid of around 30%-50% of brine water (Paradox brine) and 50%-70% of meteoric water (Airport Well spring water), which is similar with the paleo-fluid deposited T2-vein. The mixed fluid that deposited aragonite veins has been carefully studied in Chapter 4. The temperature of deposition is estimated to be close to the

surface temperature. The carbonate precipitates in Zone 4 (include calcite cements in Mancos in T6, veins in the cracks of T5 and T6) with depleted carbon isotope should be derived from thermal decarboxylation during deep burial. The cements in Zone 2 is a mixture of Zone 1, Zone 3 and Zone 4.

Table 5- 10: Calculated deposition temperature under different proportion of brine water. The underlined temperatures are the estimated deposition temperature.

Percentage of Paradox brine water	$\delta^{18}O$ of mixed fluid ‰V-PDB	Calculated deposition temperature (T in Celsius)		
		Zone 1	Zone 3	Zone 4
10%	-44.0	-12.8	6.8	11.0
20%	-43.1	-9.4	10.7	15.0
30%	-42.2	-6.0	14.7	19.1
40%	-41.3	-2.4	18.9	23.4
50%	-40.4	1.2	23.1	27.8
60%	-39.5	4.9	27.5	32.3
70%	-38.7	8.8	32.0	36.9
80%	-37.8	12.7	36.6	41.7
90%	-36.9	16.8	41.4	46.6
100%	-36.0	21.0	46.3	51.7

b. Carbon source for carbonate precipitates

The fractionation factors between carbonic ions and CO_2 are derived from Deines et al., (1974) (Eq. 5-4 ~ Eq. 5-7). The surface water of Crystal Geyser was measured as pH=6.4 (Mayo et al., 1991), and the average pH of Navajo aquifer in the Paradox Formation is about 8.0 (Spangler, 1992). Therefore, HCO_3^- ions should be the major components in the fluids.

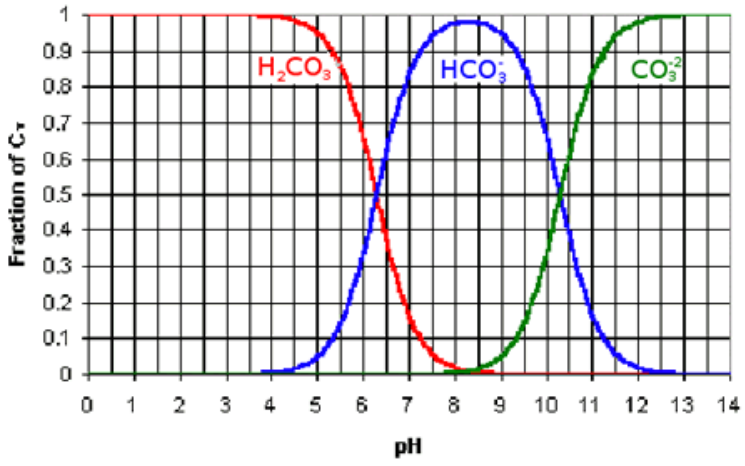

Figure 5- 18: The relationship between pH and the forms of carbonic ions

http://water.me.vccs.edu/courses/env211/lesson7_4.htm

Carbonate cements in Zone 1, Zone 2 and Zone 3 contain relatively positive $\delta^{13}C$, while Zone 4 cements are relatively depleted with $\delta^{13}C$ (Table 5-11). The change of carbon isotope is likely owing to the change in the carbon source. The source of light carbon could be bacterial oxidation, sulphate reduction during shallow burial or abiotic reactions during deeper burial (Figure 5-1).

Mancos Shales are generally depleted with heavy carbon compared to vein samples from the cracks of sandstone unit (~+5 ‰ V-PDB, chapter 4.3.8, T2-vein). Sample YS014-28 (14m from the main fault) and YS014-29 (15m from the main fault) show significant variations in carbon isotope values. The calcite cements of YS014-28 distribute very large variations in both carbon (-8.2 ~ 0.5‰ V-PDB), and the calcite cements in sample YS014-29 range from -2.4‰ to +1.6‰ V-PDB for carbon isotope (Figure 5-16). Cements with depleted $\delta^{13}C$ might be derived from abiotic reactions that happens in in depth of around 2500m to 3000m.

From investigating the isotope values of the carbonate cements in shales and veins of travertine 6 coupled with the studies of paleo-climate and tectonic history of the Paradox Basin, the environments for the formation of the cements could be predicted and listed in Table 5-11:

Table 5- 11: Summary for the formation environment of veins in T6

Sample	Major Zone	$\delta^{18}O$ ‰ (V-PDB)	Fluid composition	Precipitation temperature (°C)	$\delta^{13}C$ ‰ (V-PDB)	Formation mechanism
YS014-31~39, 76, 77, ZM	1	-7.5 ~ -5.9	Cretaceous brine	15~20	+1.3 ~ +2.2	Depositional carbonates or shallow burial diagenesis
YS014-30	2	-9.8~ -8.1	Mixture of Zone 1, Zone 3 and Zone 4	15~25	-0.22~ +1.3	Mixture
YS014-28,29	3	-13.0 ~ -10.8	30%~50% brine + 50%~70% meteoric	15~25	-2.5~ +1.6	Mixture
YS014-28,71,72, 26,27	4	-14.8~ -12.7	Contemporary brine	90~100	-8.2~ -4.9	Thermal carboxylation , deep burial

5.3.1.4 Three-source mixing model to calculate the proportion of calcite formed by CO_2-rich fluid

Based on the isotope studies and deposition environment analysis in the previous section, coupled with the SEM studies on the morphologies of different types of calcite cements, end-members of the calcite cements that are from three different mechanisms are proposed.

a) The average isotope of the depositional/diagenetic calcite during early deposition with $\delta^{18}O$ of -7.0‰ V- PDB and $\delta^{13}C$ of +1.8 ‰ V- PDB, that are not influenced by the CO_2-rich fluid. These are primary carbonate cements that are commonly found in Mancos shale that are free from the influence of the faults and CO_2-rich fluid.
b) Calcite cements formed by the CO_2-rich water containing around 50%~70% meteoric water plus 30%~50% Paradox Brine under low temperature (the fluid deposited travertines). The average values for T2 aragonite veins are used with $\delta^{18}O$ of -12.4‰ V- PDB and $\delta^{13}C$ of +5.4 ‰ V- PDB.
c) Cements deposited from abiotic reactions under the temperature of around 90 °C at depth of over 2000m. Zone 4 cement with the most depleted isotope

values are used as end member (YS014-28-7/8), with $\delta^{18}O$ of -14.8‰ V-PDB and $\delta^{13}C$ of -8.2‰ V- PDB.

Table 5- 12: Carbon and oxygen isotope for end members from three sources (Paradox brine: $\delta^{18}O$= -5‰ V-SMOW (Morrison and Parry,1986); meteoric: $\delta^{18}O$= -13.8‰ V-SMOW (Kampman et al., 2014); $\delta^{13}C$ of the degassed CO_2 is -6.4‰ V-PDB from Heath, (2008); $\delta^{18}O$ of Cretaceous brine= -31.2‰ V-SMOW (Shackleton and Kennett, 1975). The end-members from three different mechanisms are identified as three different sources

	Source description	$\delta^{13}C$ of CO_2 ‰ V-PDB	$\delta^{18}O$ of fluid ‰V-PDB	Average $\delta^{13}C$ ‰V-PDB	Average $\delta^{18}O$ ‰V-PDB
Source A	Depositional/early diagenetic marine carbonates	/	-31.2	+1.8	-7.0
Source B	Mixed fluid (70% meteoric+ 30% Paradox brine) CO_2 under 25°C (fluid deposited T2 vein)	-6.4	-42.2	+5.4	-12.4
Source C	Late-diagenetic calcite under 90°C	-25.0	-31.2	-8.2	-14.8

It is impossible to determine the exact depositional temperature using the stable isotope. The depositional temperature would alter the isotopic fractionation factors, especially for oxygen. Hereby, we arbitrarily use 25°C for shallow deposition and 90°C for deep burial. The thermal carboxylation derived CO_2 (~ -25‰ V-PDB) dissolves in fluid and generate calcite with very depleted $\delta^{13}C$ (c. ~ -20 ‰ V-PDB).

Figure 5-19 shows the relationship between calcite cements and three source members. Most of samples are included in the triangle defined by the 3 sources. It is evident that the calcite cements in normal Mancos shale samples (shale that far from the fault) are basically from source A (depositional or early diagenetic calcite). Cements in Zone 3 are mostly from source B, the CO_2-rich fluid with meteoric fluid in

charge, and the calcite cements in Zone 4 is mainly derived from source C, where carbon is modified by δ^{13}C-depleted CO_2 originated from deep burial.

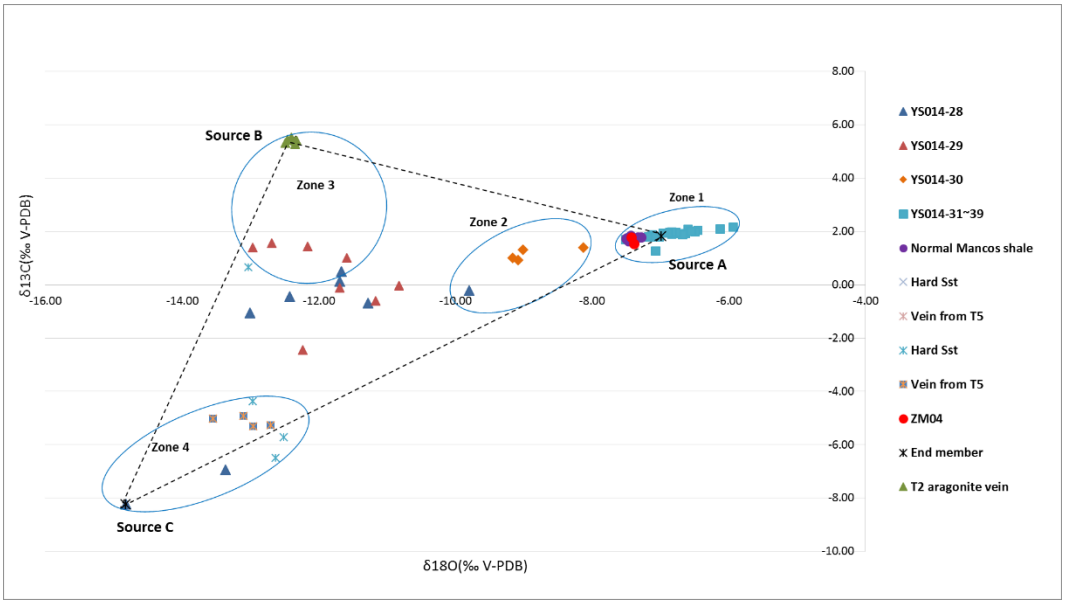

Figure 5- 19: Carbon and oxygen isotope for samples in travertine 6. The black triangle envelopes the area for the mixture of the three end-members.

A simple linear mixing model is used to determine the contribution of each source (Ben-David et al., 1997, Szepanski et al., 1999, Phillips, 2001) following mass balance equations. For example, for three source and dual element system, the equations could be established as:

$$\delta^{13}C_D = f_A\delta^{13}C_A + f_B\delta^{13}C_B + f_C\delta^{13}C_C \quad \text{Equation 5-17}$$

$$\delta^{18}O_D = f_A\delta^{18}O_A + f_B\delta^{18}O_B + f_C\delta^{18}O_C \quad \text{Equation 5-18}$$

$$1 = f_A + f_B + f_C \quad \text{Equation 5-19}$$

Where A, B, C are subscripts represent three different sources of carbonate cements; D represents the measured cements; f_A, f_B and f_C are proportion of each carbonate source. Then, the contribution of each source could be calculated with Eq. 5-17 to 5-19. In this study, the end member of A, B and C are listed in Table 5-12.

Table 5- 13: Proportion of calcite cements that derived from different source using 3-source mixing model.

Sample ID	Sample type	% of source A	% of source B	% of source C
'YS014-76-1/4'	Shale	93	6	2
'YS014-76-2/4'	Shale	95	3	2
'YS014-76-3/4'	Shale	95	4	2
'YS014-76-4/4'	Shale	94	2	3
'YS014-77-1/4'	Shale	92	5	3
'YS014-77-2/4'	Shale	92	5	3
'YS014-77-3/4'	Shale	93	4	3
'YS014-77-4/4'	Shale	92	5	3
'YS014-31-1/4'	Shale	98	2	0
'YS014-31-2/4'	Shale	100	1	-1
'YS014-31-3/4'	Shale	102	0	-1
'YS014-31-4/4'	Shale	106	-2	-3
'YS014-32-1/4'	Shale	106	-3	-2
'YS014-32-2/4'	Shale	100	0	0
'YS014-32-3/4'	Shale	103	-2	-1
'YS014-32-4/4'	Shale	105	-3	-2
'YS014-33-1/4'	Shale	113	0	-5
'YS014-33-2/4'	Shale	116	0	-7
'YS014-33-3/4'	Shale	113	0	-6
'YS014-33-4/4'	Shale	108	-4	-4
'YS014-34-1/4'	Shale	108	-4	-3
'YS014-34-2/4'	Shale	103	-1	-2
'YS014-34-3/4'	Shale	107	-4	-3
'YS014-34-4/4'	Shale	102	-1	-1
'YS014-ZM02'	Shale	97	0	3
'YS014-ZM02'	Shale	99	-2	2

'YS014-ZM02'	Shale	101	-5	4
'YS014-ZM03'	Shale	100	-2	2
'YS014-ZM03'	Shale	84	9	7
'YS014-ZM03'	Shale	94	2	4
'YS014-ZM04'	Shale	93	5	2
'YS014-ZM04'	Shale	81	17	3
'YS014-35'	Shale	93	5	2
'YS014-36-1/2'	Shale	93	5	3
'YS014-36-2/2'	Shale	92	5	3
'YS014-37-1/2'	Shale	102	0	-2
'YS014-37-2/2'	Shale	101	0	-1
'YS014-38-1/2'	Shale	97	2	1
'YS014-38-2/2'	Shale	99	1	1
'YS014-39-1/2'	Shale	100	-4	4
'YS014-39-2/2'	Shale	100	-4	4
Average		**99**	**1**	**1**
Zone 2				
'YS014-30-1/4'	Shale	68	20	12
'YS014-30-2/4'	Shale	82	10	8
'YS014-30-3/4'	Shale	66	19	15
'YS014-30-4/4'	Shale	68	17	15
Average		**71**	**16**	**12**
Zone 3				
'YS014-28-1/8'	Shale	60	15	26
'YS014-28-2/8'	Shale	27	41	31
'YS014-28-3/8'	Shale	36	28	35
'YS014-28-4/8'	Shale	17	45	38
'YS014-28-5/8'	Shale	9	46	45
'YS014-29-1/8'	Shale	38	28	34

'YS014-29-2/8'	Shale	26	48	25
'YS014-29-3/8'	Shale	26	23	51
'YS014-29-4/8'	Shale	2	69	29
'YS014-29-5/8'	Shale	6	67	26
'YS014-29-6/8'	Shale	16	59	25
'YS014-29-7/8'	Shale	28	39	33
'YS014-29-8/8'	Shale	42	29	29
'YS014-71-1/2'	Sst	3	63	34
Average		**22**	**40**	**37**
Zone 4				
'YS014-27-1/2'	Vein	22	5	73
'YS014-27-2/2'	Vein	26	2	71
'YS014-26-1/2'	Vein	19	10	71
'YS014-26-2/2'	Vein	12	15	73
'YS014-71-2/2'	Sst	31	-10	79
'YS014-72-1/2'	Sst	19	14	66
'YS014-72-2/2'	Sst	31	-4	73
'YS014-28-8/8'	Shale	6	41	53
Average		**21**	**9**	**70**

The proportion of calcite from each source has been presented in Table 5-13. Source B represents the calcite deposited by CO_2-rich fluid, which occupies 1%, 16%, 40% and 9% in samples within Zone 1, Zone 2, Zone 3 and Zone 4, respectively. Sample YS014-28 (14m from the fault), YS014-29 (15m from the fault) and YS014-30 (16.4m from the fault) present clear evidence of being affected by the CO_2-rich fluid. Sample YS014-29-4/8 contains the most CO_2-seqeustered calcite with a proportion of 69% (against the total calcite). Starting from sample YS014-31, which is 17m from the fault, to samples that are further away (sample YS014-32 to YS014-39, YS014-ZM02 to YS014-ZM04) from the main fault are demonstrated to be little or not influenced by the CO_2-rich fluid.

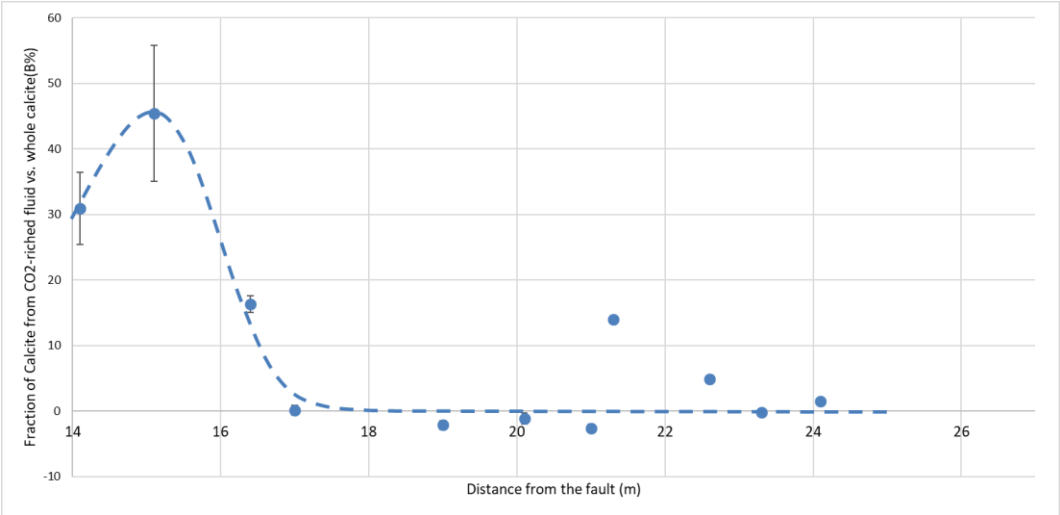

Figure 5- 20: Average percentage of carbonate derived from CO_2-rich fluid against distance from the fault. The standard error of carbonate percentage is illustrated by the error bars.

The proportion of calcite contributed by CO_2 sequestration drastically dropped from 45% at 15m from the fault to 0% at 17m away from the fault (Figure 5-20). Samples further away from the fault are un-altered by CO_2-rich fluid with the calcite fraction fluctuated around 0%.

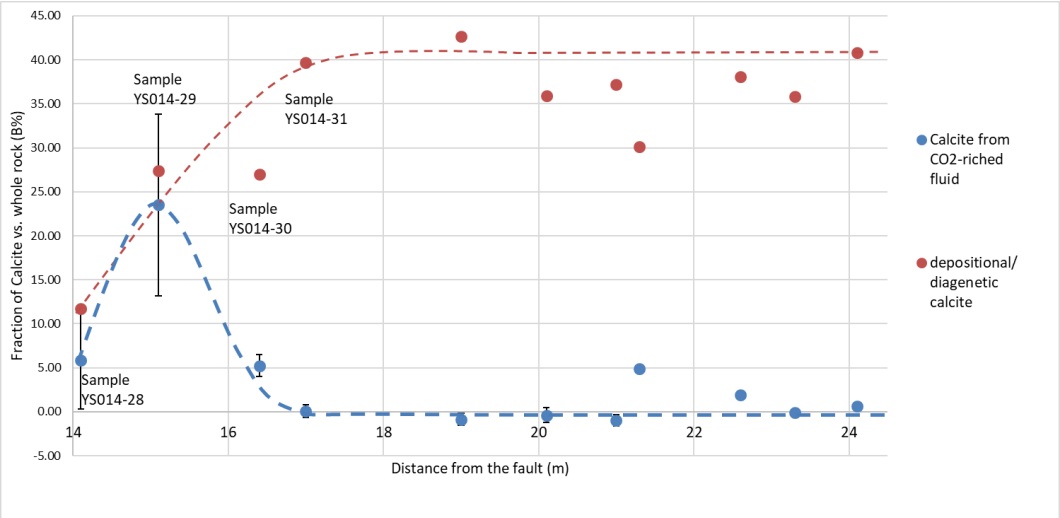

Figure 5- 21: Comparisons of calcite precipitated by CO_2-rich fluid (B%) against the weight of the whole rock (blue dots), and the fraction of depositional/diagenetic calcite against the whole rock volume (red dots). The blue-dashed line represents

the general trend for the calcite deposited from the CO_2-rich fluid; the red dashed line represents the change of primary depositional/diagenetic calcite

Figure 5-21 presents the proportion of calcite derived from CO_2-rich fluid or depositional/early diagenetic against the whole rock (%weight) change with the distance. Dramatic change happens between 14m to 17m from the fault. The total calcite fraction for the normal Mancos shale in T6 is relatively uniformed with calcite fraction around 30% to 45% (Figure 5-22, green shaded area), while two samples that closest to the main fault, sample YS014-28 and YS014-29, present big difference in total calcite fraction. Sample YS014-28 contains especially low total calcite, with the lowest fraction of 5% and the highest of 30%, while the total calcite proportion ranges from 32% to 69% for Sample YS014-29. The especially low depositional/diagenetic calcite proportion in YS014-28 could be the result of dissolution caused CO_2-rich fluid. Sample YS014-29 contains the most secondary calcite, that 24% (on average) of the total rock is derived from CO_2 sequestered calcite. In general, Samples located closer than 17m from the main fault that have been demonstrated to be altered by CO_2-rich fluid.

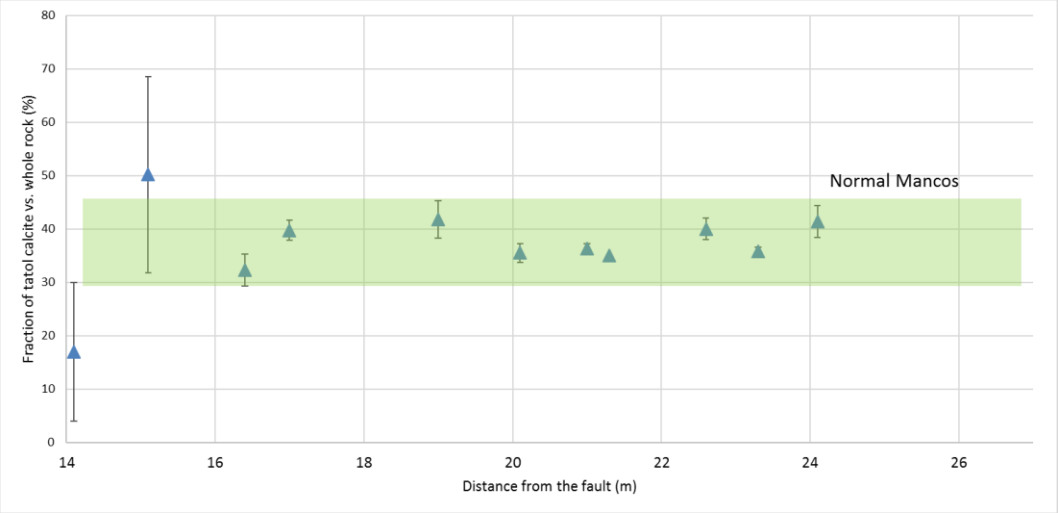

Figure 5- 22: Total calcite fraction vs. distance from the main fault. The green shaded area represents the fraction of the total calcite for normal Mancos shale.

5.3.2.5 Summary for calcite precipitation in T6

a. The sample closest to the fault (YS014-28) shows most petrographic variation compared with other Mancos Shale samples, with significant amounts of halite and gypsum and a low quantity of calcite. Sample YS014-29 (15m from the main fault) is especially enriched with calcite (up to 69%) with most of the calcite deposited by the CO_2-rich fluid. These findings indicate the CO_2-rich fluid could either dissolve the original calcite cements (YS014-28) or deposit new cements (YS014-29) close to the fault plane.
b. Three types of calcite cements have been observed in samples in T6: fossil calcite formed during early burial; euhedral and sub-euhedral calcite cements formed during sediment diagenesis; and fracture filling calcite formed during from CO_2-rich fluid.
c. Two types of pyrite have been observed in samples in T6: euhedral pyrite and framboidal pyrite. The absence of framboidal pyrite in samples YS014-28 and 29 might suggest the addition of the CO_2-rich fluid.
d. Isotopically, the samples could be separated into 4 zones: Zone 1 is cements of normal Mancos Shale with uniformed isotopic values. The carbon is from depositional calcite and the oxygen is contemporary seawater; Zone 3 contains cements influenced by CO_2-rich fluid migrated through the fault and fractures; Zone 4 include veins formed by thermal decarboxylation CO_2; Zone 2 is the mixture.
e. Three-source model has been established to calculate the proportion of calcite cements derived from CO_2-rich fluid. Sample YS014-29 (15m from the main fault) contains the biggest proportion of calcite that influenced by CO_2-rich fluid, with 24% (%weight on average) of the whole rock that deposited from CO_2-rich fluid.
f. Sample closest to the fault with clear evidence of deformation fractures have demonstrated to be interacted with CO_2-rich fluid. CO_2 in the fluid was sequestered by secondary calcite deposited filling the fractures and open spaces of the deformed Mancos shale.

5.3.2 Results for T3

The sampling map and sketch have been illustrated in section 5.2.1.1. The results of petrographic studies will be discussed in this section.

5.3.2.1 XRD results for T3

The XRD results for representative samples in T3 have been outlined in Figure 5-24. Sample YS014-16 and 17 are located closest to the fault (15m laterally) where extensive fractures and bleached cracks are present. Samples YS014-21 and 22 are close to a very small fault (Figure 5-6). Sample YS014-25 is located the furthest from the fault (43m). There are no obvious quantitative mineralogy variations among these samples (Figure 5-23). The mineralogy composition of samples at T3 is similar with the sample YS014-30 and YS014-31 in T6 (Figure 5-9). There is no significant halite or gypsum deposition observed in samples in T3, but extensive gypsum veins have been found in fractures in the outcrop, especially in the section near the main fault.

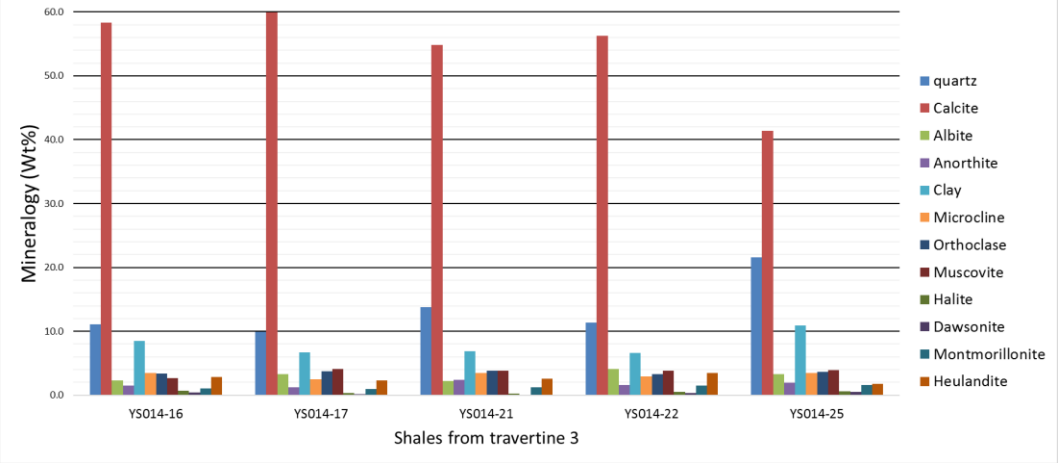

Figure 5- 23: Quantitative mineralogy measured by XRD on representative samples of Mancos shale from T3

5.3.2.2 SEM analysis for T3

Sample YS014-19, 29 and 24 have been selected for SEM study to observe the texture of the samples. All these 3 samples are from bedding 1 (field picture see Figure 5-6).

- Sample YS014-19: 22m from the main fault

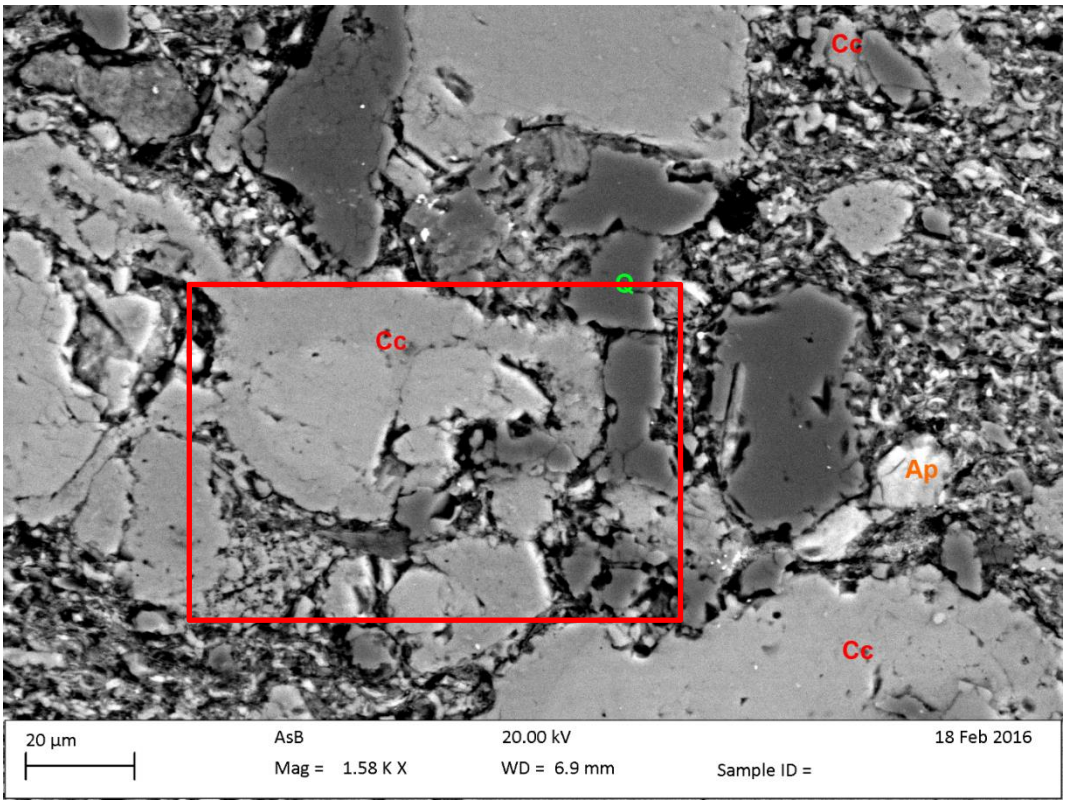

(a)

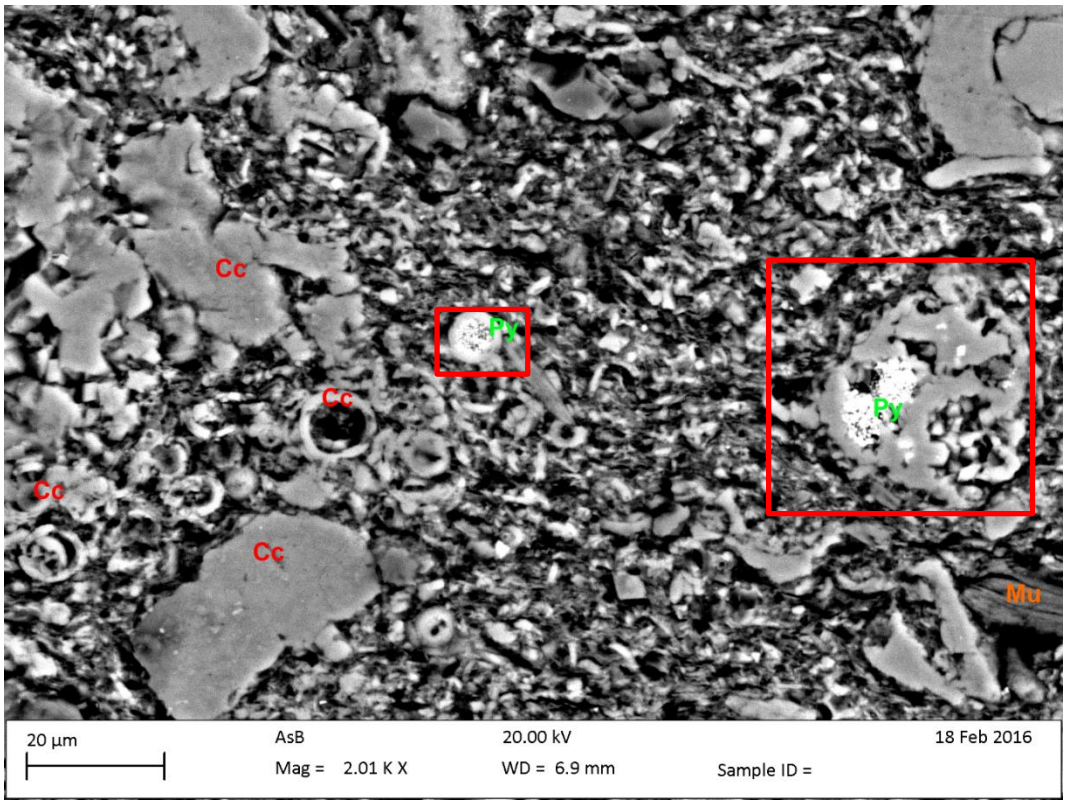
Cc
Py
Cc
Py
Cc
Cc
Mu
20 µm
AsB
Mag = 2.01 K X
20.00 kV
WD = 6.9 mm
Sample ID =
18 Feb 2016

(b)

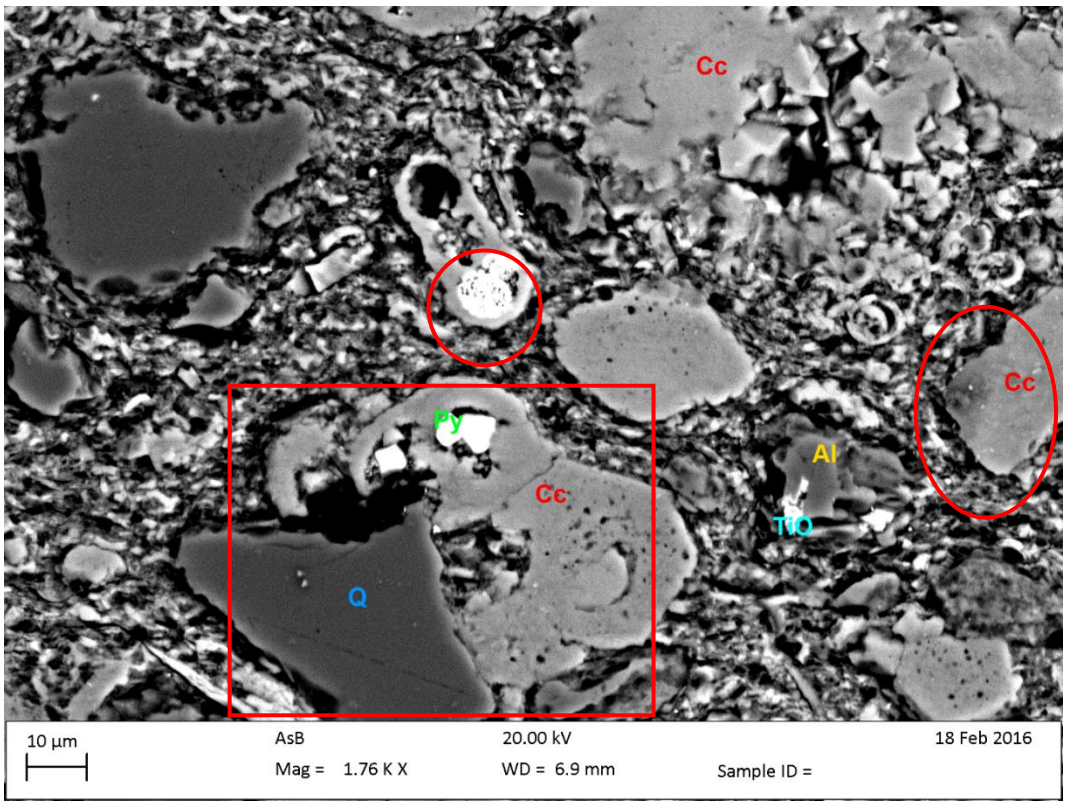
Cc
Py
Cc
Q
Al
TiO
Cc
10 µm
AsB
Mag = 1.76 K X
20.00 kV
WD = 6.9 mm
Sample ID =
18 Feb 2016

(c)

Figure 5- 24: The SEM images of Sample YS014-19 from T3. Cc=calcite, Q=quartz, Py=pyrite, AP=Apatite, Al=albite, Mu=Muscovite. (a) The remaining of foraminifera shells (red rectangle) with quartz and apatite; (b) pyrite framboid (Pseudomorph) deposited inside the remaining foraminifera (red rectangle); (c) quartz in contact with the foraminifera calcite (red rectangle) and euhedral/ sub-euhedral calcite (red circle)

The carbonates observed in the image are the remaining of foraminifera shells and euhedral calcite formed by depositional or diagenetic processes. Framboidal pyrite (Pseudomorph) is frequently found grows in the centre of the fossil calcite.

- Sample YS014-20: 24m from the main fault, situated at the local small fault

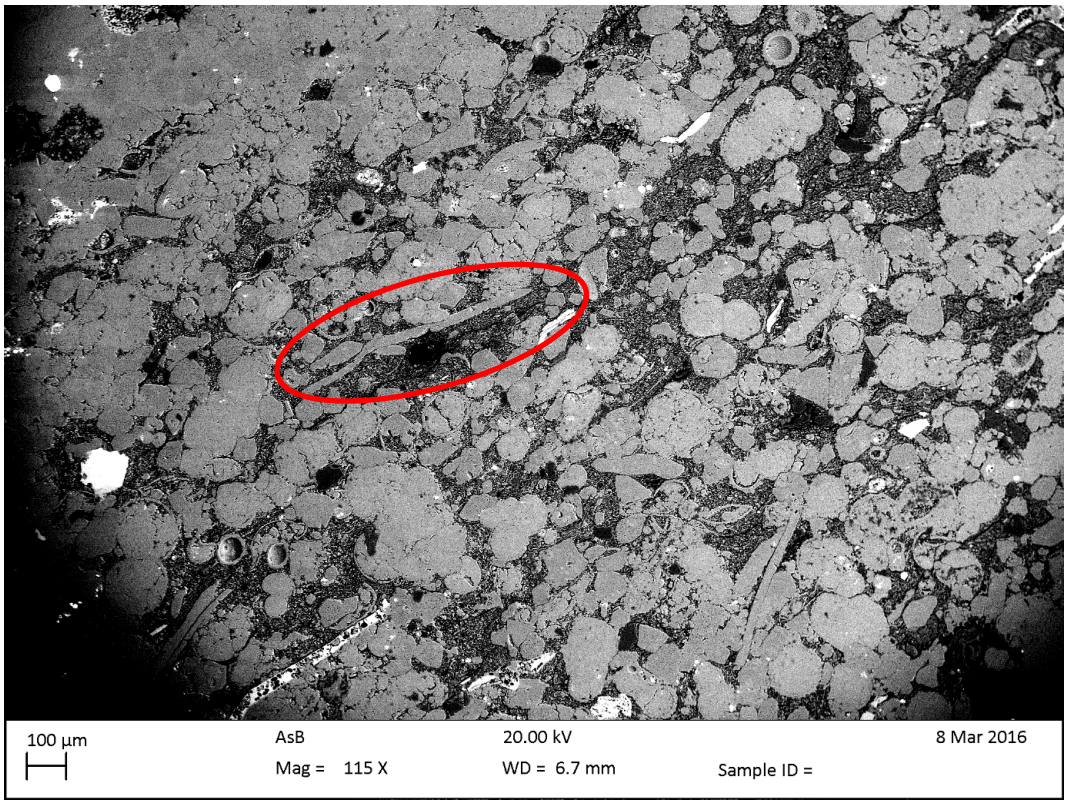

(a)

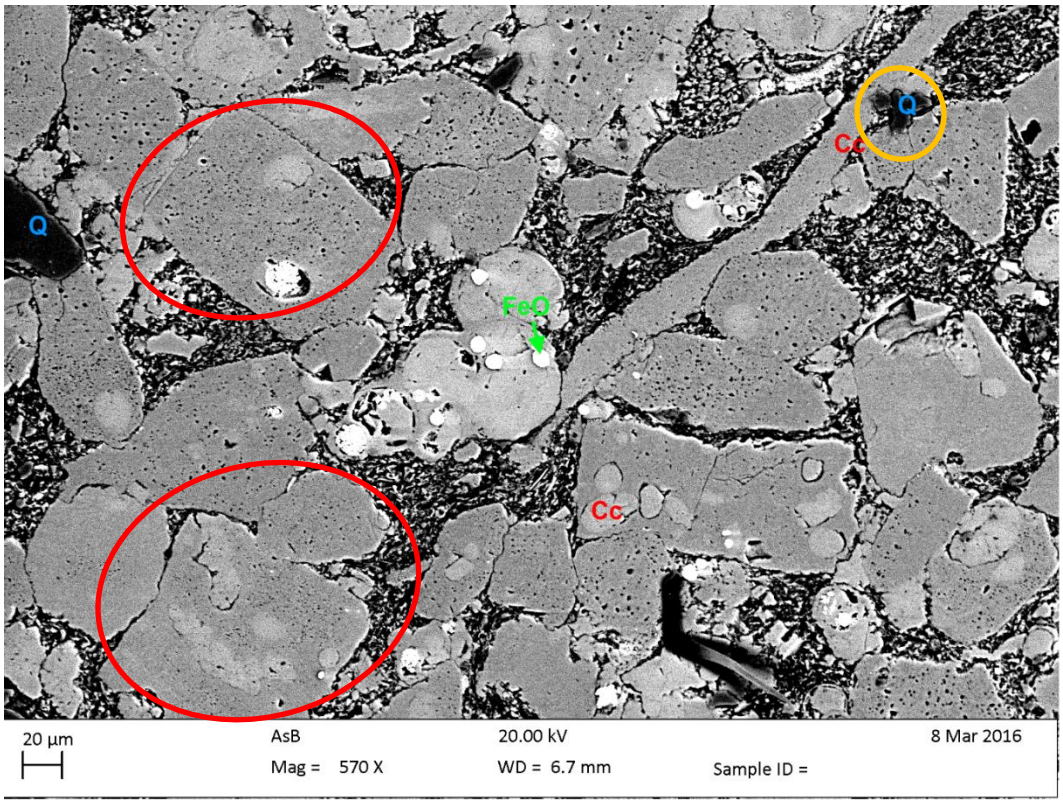

(b)

Figure 5- 25: SEM images for YS014-20. (a) Low magnification view of the sample, with enlongated calcite cements in length of around 500 µm in length; (b) calcite with pyrite framboid (Pseudomorph). The streaky calcite might be the dissolution and re-precipitation of the primary fossil calcite and deposit to fill the pores and fractures (big red circle).

Sample YS014-20 is located at the minor fault which is 24m from the main fault (see the location of micro fault in Figure 5-6(b)). There exists more cemented with calcite filling the pores and fractures (the elongate streak in Fig. 5-25(b), around 200µm in length). The dissolution and re-precipitation processes are probably occurred in-situ, since the dissolved elements are unable to be transported long distance in the low-permeable shale. Diagenetic quartz formed prior to the re-precipitation of calcite cements (small yellow circle on upper right of Figure 5-25(b)) hence the streaky-shaped re-precipitated calcite wraps around the euhedral quartz crystals. This also support the view that the movement of the minor fault probably caused the dissolution of depositional/ diagenetic calcite and re-precipitated in-situ.

- Sample YS014-24: 37m from the main fault, at the distal end of the Mancos outcrop

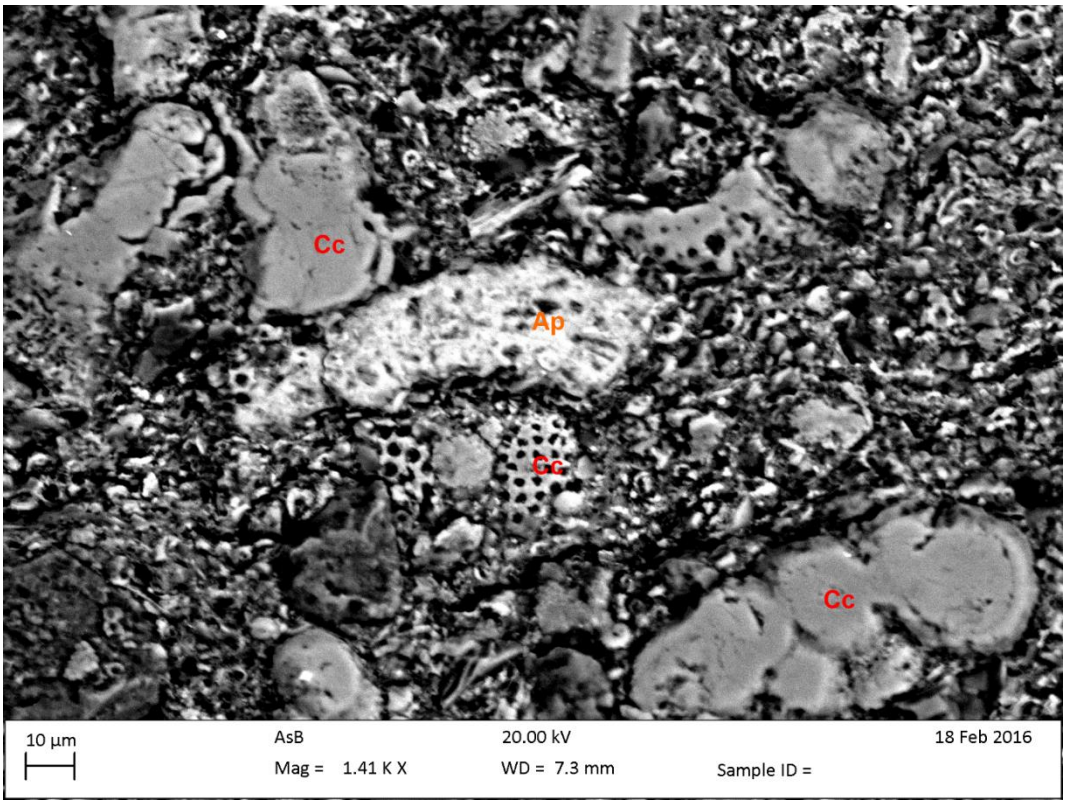

(a)

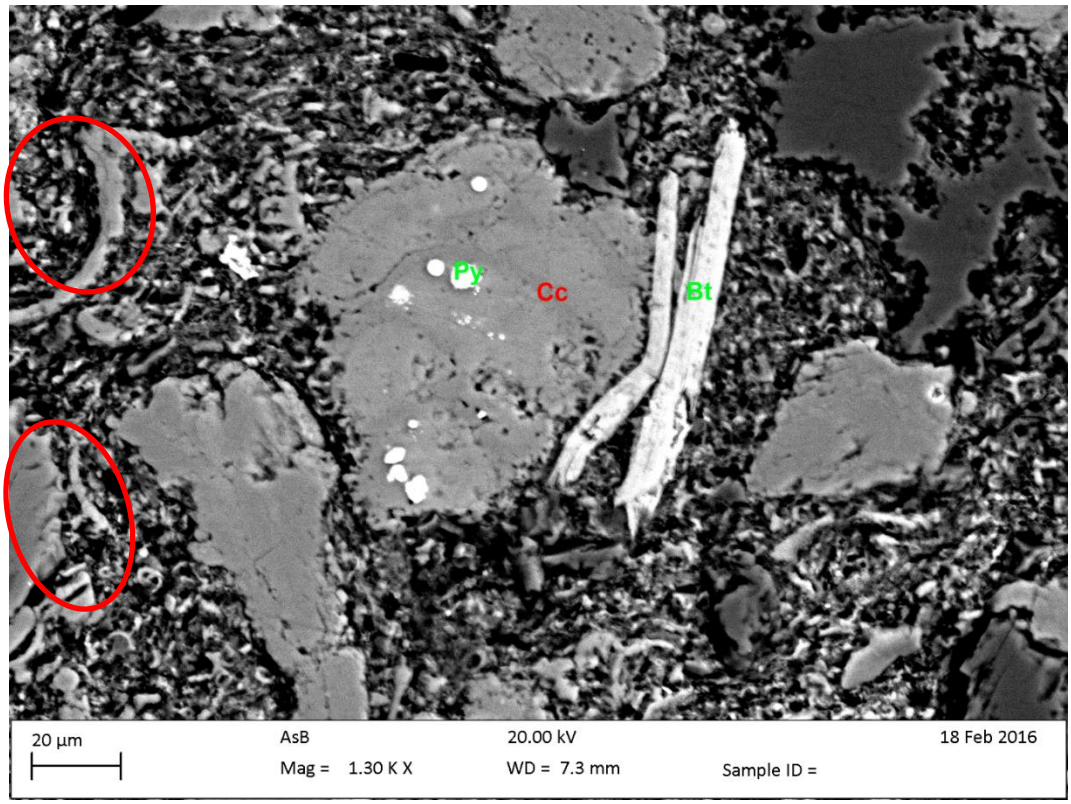
Py
Cc
Bt
20 µm
AsB
20.00 kV
18 Feb 2016
Mag = 1.30 K X
WD = 7.3 mm
Sample ID =

(b)

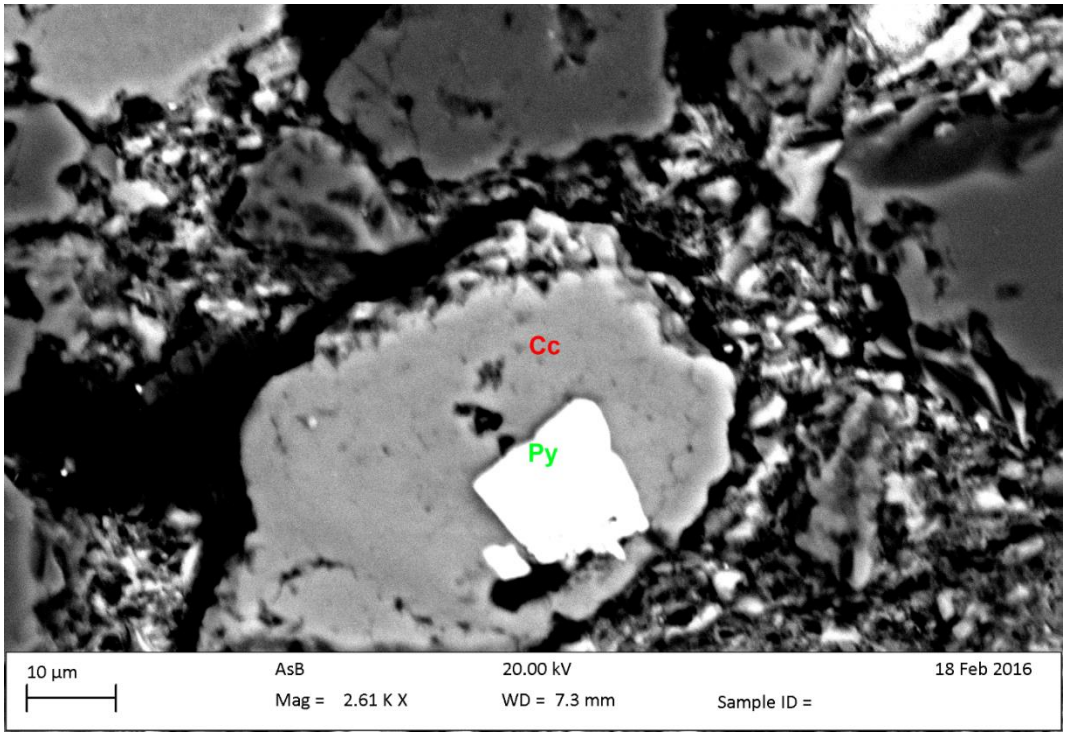
Cc
Py
10 µm
AsB
20.00 kV
18 Feb 2016
Mag = 2.61 K X
WD = 7.3 mm
Sample ID =

(c)

Figure 5- 26: SEM images for Sample YS014-24. (a) The remaining fossil calcite, apatite and detrital grains; (b) fossil calcite, framboid pyrite, quartz and biotite; (c) the close-up of calcite, associated pyrite (Pseudomorph), quartz and dissolved pores among the grains.

Sample YS014-24 situates at the distal of the Mancos outcrop of T3. Not many re-precipitated calcite cementations could be observed compared with sample YS014-20 in the displacement area. Both fossil calcite and euhedral/ sub-euhedral calcite could be observed that associated with euhedral and framboidal pyrite.

In summary of the SEM analysis for T3, the sample in the minor fault (YS014-20) shows the most variation from pristine Mancos Shale because of the local micro fault: significant amount of the primary calcite has been replaced with re-precipitated calcite cements. The dissolution and re-precipitation occurred in-situ, since no big-scale calcite cementation could be observed compared with sample YS014-29 and 30 in T6. The generalized types of calcite and pyrite in Mancos shale sample in T3 are displayed in Table 5-14:

Table 5- 14: calcite and pyrite types in shale sample of T3. Three check marks indicate large amount; two check marks indicate medium amount; one check mark indicates a small amount; no check mark indicates none has been found.

Sample No.	Fossil calcite	euhedral/ sub-euhedral calcite	Fracture filling/ cementing calcite	Euhedral pyrite (Pseudomorph)	Framboidal pyrite (Pseudomorph)
YS014-19	✓✓✓	✓		✓	✓✓
YS014-20	✓	✓	✓✓	✓	✓
YS014-24	✓	✓		✓	✓

5.3.2.3 Stable isotope analyse for T3 samples

Mancos shale from 2 horizontal beddings and 1 vertical traverse have been collected (sampling position and field picture in section 5.2.1.1. The results of stable isotope have been listed in Table 5-15.

Table 5- 15: Stable isotope and carbonate percentage for Mancos shale samples below T3

	Distance (m)	δ^{13}C V-PDB (‰)	δ^{18}O V-PDB (‰)	Carbonate percentage (%)
Bed 1	Horizontal distance from the main fault			
YS014-16	15.1	1.5	-7.3	59
YS014-17	18.5	1.3	-7.7	64
YS014-18	20.5	1.3	-7.6	56
YS014-19	22	0.9	-7.5	69
YS014-20	24	1.5	-7.7	55
YS014-21	29	1.5	-7.6	48
YS014-22	31.3	1.3	-7.5	62
YS014-23	33.8	1.8	-7.4	43
YS014-24	37	1.8	-7.1	43
YS014-25	43	1.7	-7.0	39
Bed 2	Horizontal distance from the main fault; 30cm below Bed 1			
YS014-45	15.1	1.5	-7.0	44
YS014-46	18.5	1.5	-7.0	44
YS014-47	20.5	1.6	-7.1	42
YS014-48	22	1.8	-7.0	39
YS014-53	24	1.4	-7.3	60
YS014-54	29	1.6	-7.2	44
YS014-55	31.3	1.6	-6.9	45
YS014-56	33.8	1.1	-7.3	61
YS014-57	37	1.5	-7.0	56
Vertical traverse	Distance from the base of the outcrop (m)			
YS014-49	2	1.5	-7.4	56

YS014-19	1.8	0.9	-7.5	69
YS014-48	1.5	1.8	-7.0	39
YS014-50	1.2	0.7	-7.2	36
YS014-51	1	1.3	-7.3	45
YS014-52	0	2.1	-7.1	24

The stable isotope feature for Mancos Shale samples at T3 are quite uniform compared with samples at T6. The carbon isotope ranges from +0.7‰ to +2.1‰ V-PDB and oxygen isotope ranges from -7.7‰ to -6.9‰ V-PDB. All of the T3 samples are located in Zone 1 (see section 5.3.1.3) (Figure 5-27).

The presence of visible reduction zones below T3 has been assumed to be related to CO_2-rich fluid in some previous studies (Haszeldine et al., 2005, Dockrill, 2006, Kampman et al., 2014). However, since the carbonates show no evidence of being influenced by the CO_2-rich fluid, the formation of reduction zone is more likely to be owing to other reducing species such as H_2S (Garden et al., 2001, Chan et al., 2000). The leaching reactions might be:

$$Fe_2O_3 + 2H_2S + 2H^+ \rightarrow FeS_2 + 3H_2O + Fe^{2+} \quad \text{Equation 5-20}$$

Or with the involvement of CO_2 via the reaction of:

$$Fe_2O_3 + 4CO_2 + H_2O + 2HS^- \rightarrow Fe^{2+} + 4HCO^- + FeS_2 \quad \text{Equation 5-21}$$

Whether the CO_2 is actually involved in the reduction is unproven.

The stable isotope study combined with SEM analysis demonstrated shale samples in T3 have not been altered by CO_2-rich fluid starting from 15m furthering away from the fault. No evidence to show the fluid has interacted with the shale unit. Therefore, the overlying travertine unit should be deposited from the flow of the CO_2-rich fluid in the footwall of the main fault. Abundant vertical thick veins in the cracks of sandstone of the footwall (section 4.2.1) proved the vertical flow of the CO_2-rich fluid.

However, we have demonstrated in section 5.3.1 that CO_2-rich fluid result in variations for the samples closer than 17m away from the fault in T6. The reason for the alteration happen in T6 samples (YS014-28, 29 and 30) are probably because

they situate in the fault zone or in the adjacent to the fault zone. Clear deformation fractures could be observed in fault zone samples of T6, while none can be observed in T3 samples. Therefore, the conclusion is, CO_2-rich fluid is not likely to penetrate or react with shale, only except where deformation and fracturing happen to create pathways for the fluid, CO_2 mineral sequestration would happen.

In summary of the CO_2-rich fluid transportation in the fossil travertine of the Crystal Geyser, the fluid will initially flow up-dip through sand-rich carrier unit and deposit as carbonate layered mats on top of cemented, conglomerate layers. CO_2-rich fluid cannot interact with Mancos shale unless the deformation already exists. Deformation fractures in the damaged zone or the associated zone in the shale unit could enable the transport and cementation of the fluid. The local minor fault could cause in-situ dissolution and re-precipitation of the calcite, but no long-term transportation of the fluid occurred.

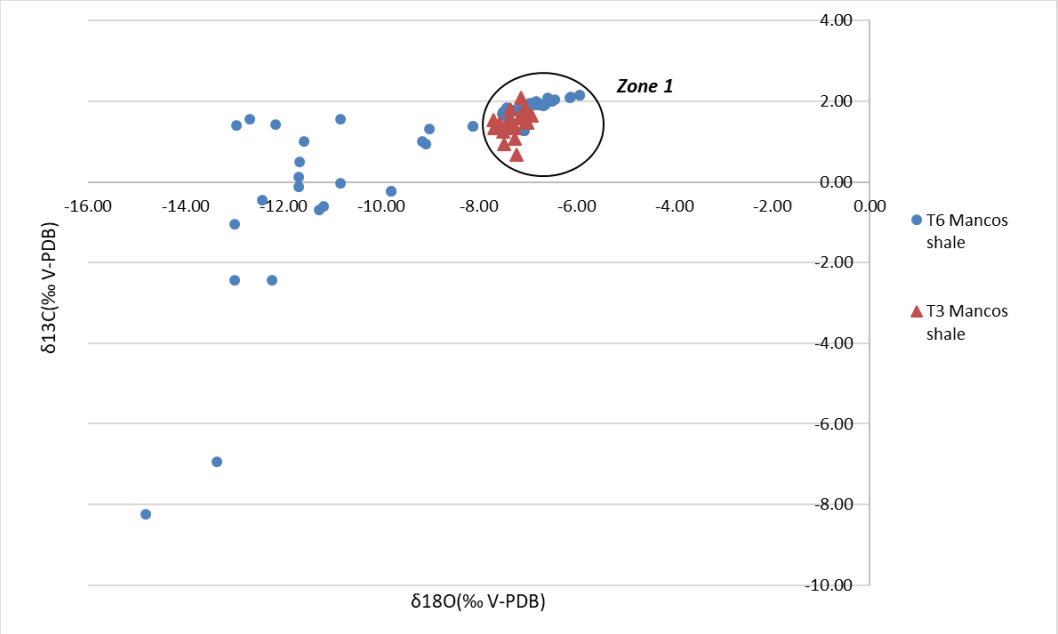

Figure 5- 27: Stable isotope for Mancos shale samples in T6 (solid blue circle) and T3 (solid red triangle)

5.3.2.4 Summary for the calcite precipitation in T3

a. Samples in T6 are little influenced by the CO_2-rich fluid compared with samples in T6. The isotopic values and the petrographic studies show very uniform for the samples from two horizontal beds and one vertical traverse.
b. Sample in the local displacement area shows massive dissolution and re-precipitation of primary fossil calcite. But the reactions occurred in-situ, as no big scale of permeable fractures cementation have been observed.
c. Stable isotope signatures the samples are unaltered by the CO_2-rich fluid. The relatively positive carbon isotope excludes the involvement of organic-source carbon, thus indicating the light-coloured reduction zones are not likely to be related to the organic matters or CO_2. It is possible from the reduction of hydrogen sulphide.
d. CO_2-rich fluid did not interact with the un-deformed Mancos shale in T6.

5.3.3 Results for T4

Mancos Shale samples were collected from close to the small travertine T4, for sample map see section 5.2.1.3, Figure 6-12. The location and description of vein samples have been discussed in section 5.2.1. T4 is different from T3 and T4, as it is located in the junction of two mapped faults. Sample YS014-66, 67, 68, 69, 70 were sampled in an approximately fault-perpendicular traverse to examine the variation away from the faults.

5.3.3.1 XRD results

The results of XRD shows in Figure 5-28. Sample YS014-67 and 68 contain similar mineralogy with normal Mancos shale samples in T6 (YS014-31) and T3 (YS014-25), with very small amount of clays, feldspars, no halite, 50% calcite and 20% ~30% of quartz. Sample YS014-70, that is relatively distant from the small travertine, contains relatively less calcite (16%) but more of the other minerals (feldspar, clays, mica and heulandite).

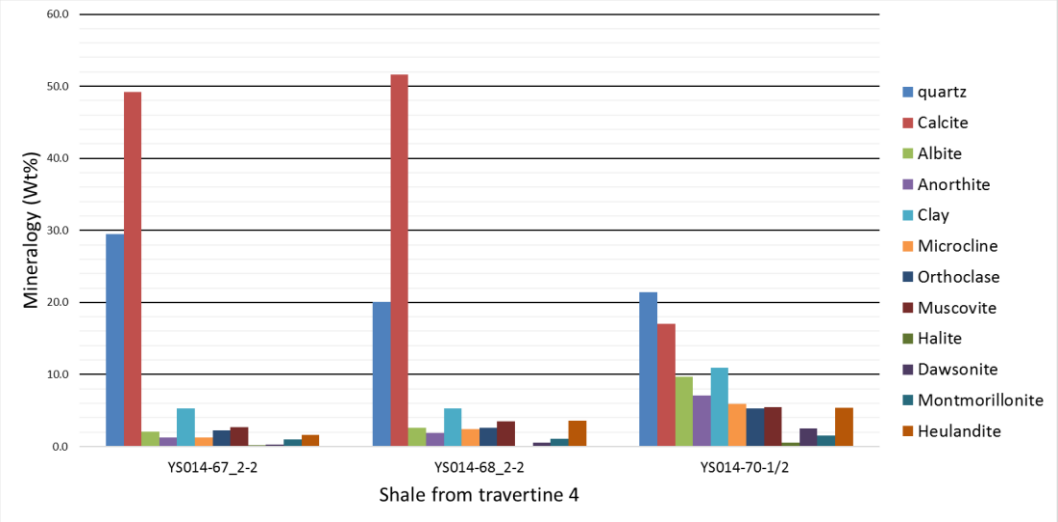

Figure 5- 28: Quantitative mineralogy measured by XRD on representative samples of Mancos shale from T4.

5.3.3.2 SEM analysis

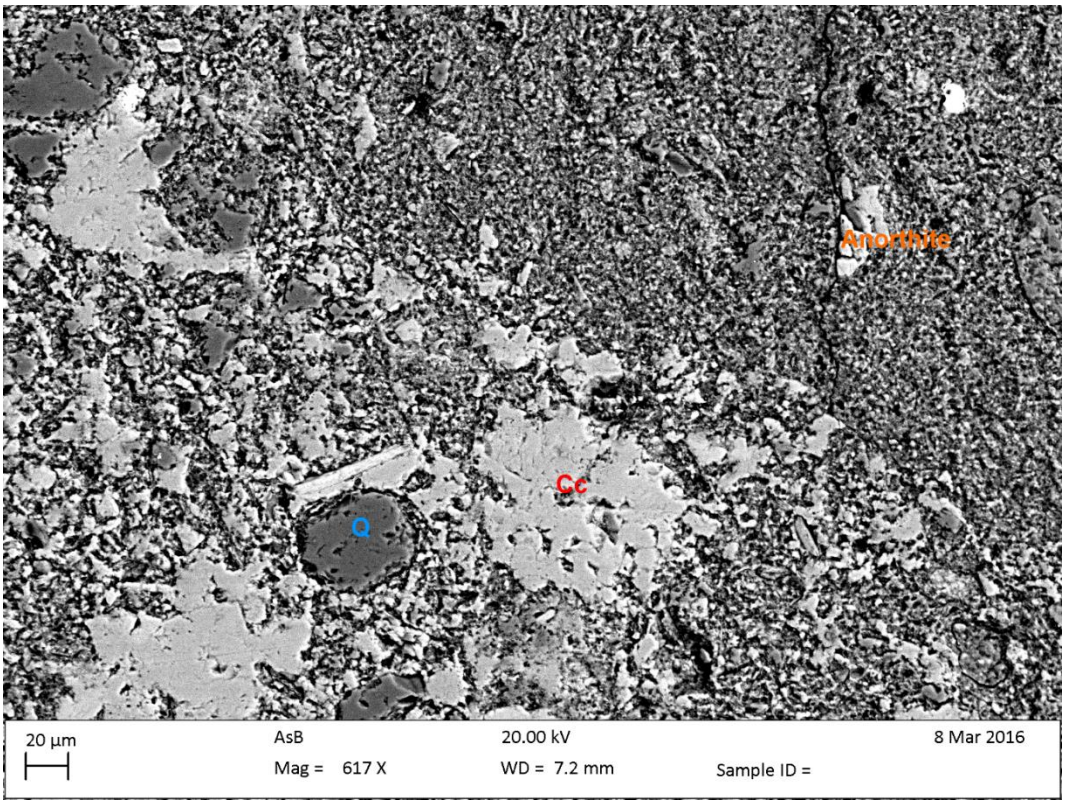

(a)

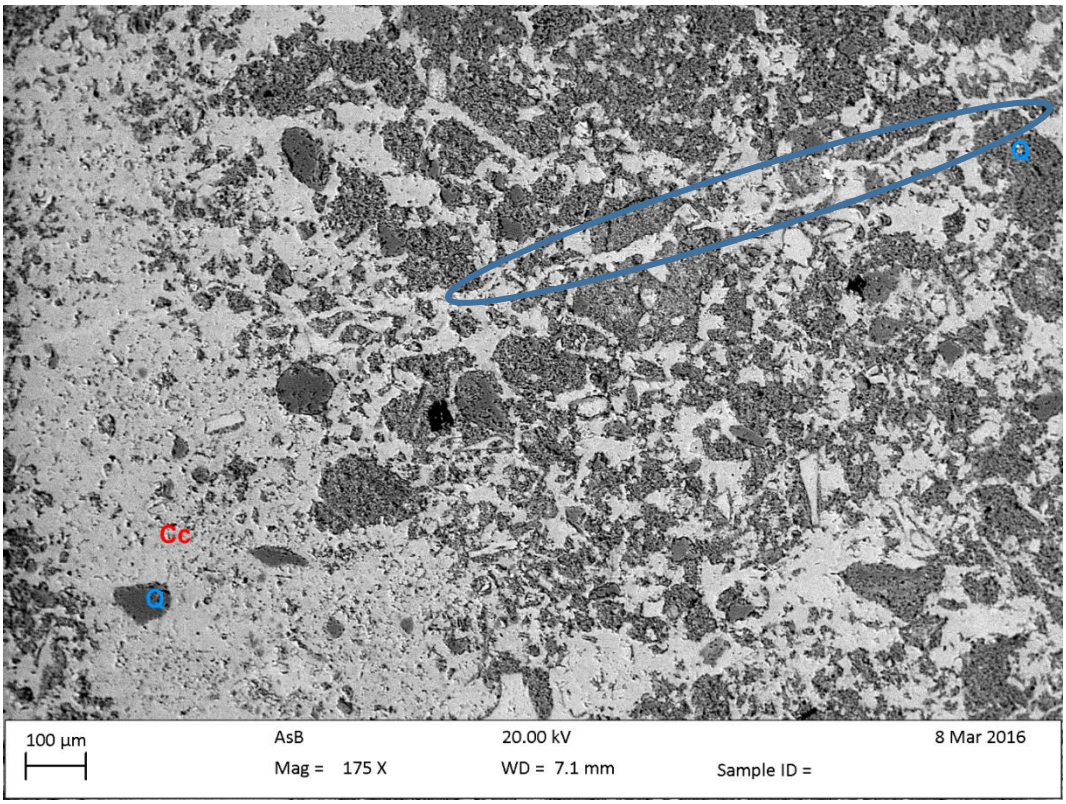
Q
Cc
Q
100 µm
AsB
Mag = 175 X
20.00 kV
WD = 7.1 mm
Sample ID =
8 Mar 2016

(b)

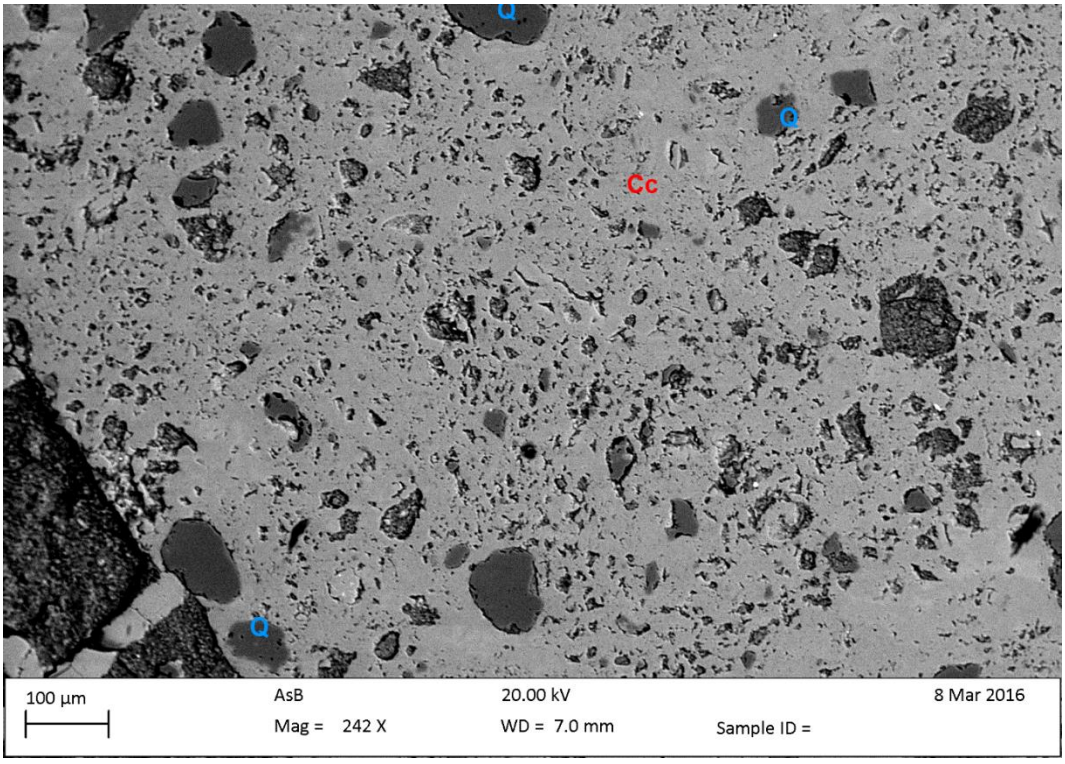
Q
Q
Cc
Q
100 µm
AsB
Mag = 242 X
20.00 kV
WD = 7.0 mm
Sample ID =
8 Mar 2016

(c)

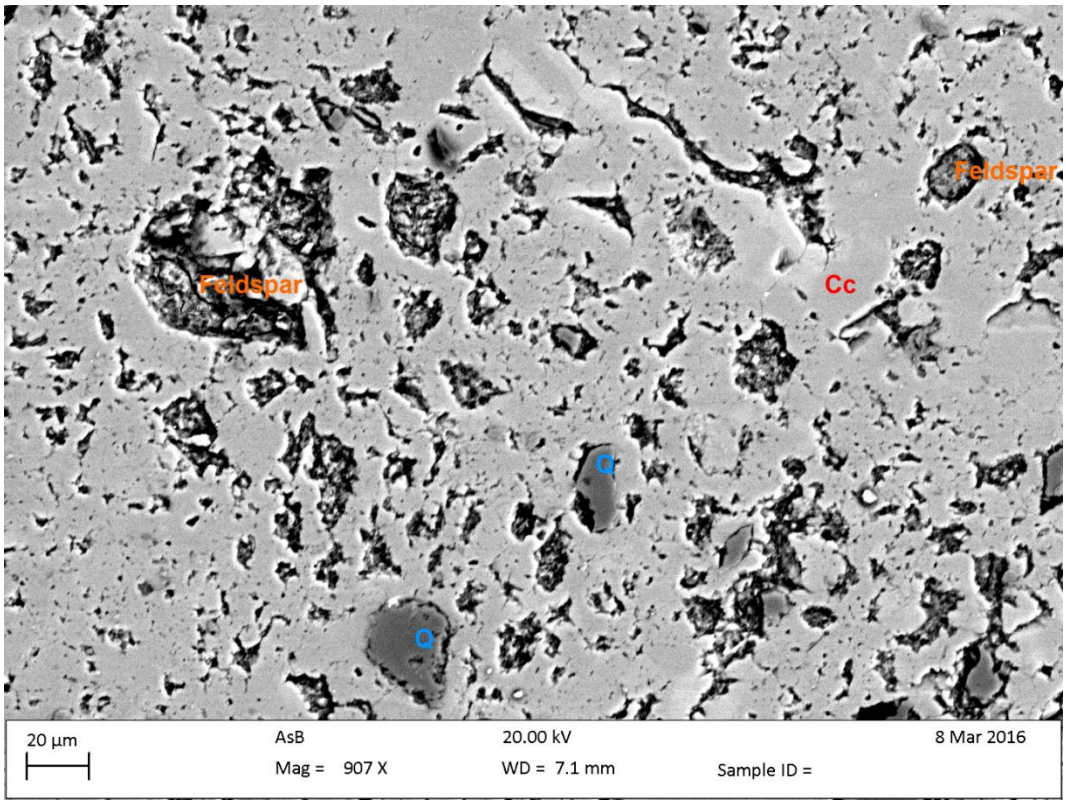

(d)

Figure 5- 29: SEM image of sample YS014-66 and 68. (a)&(b): Sample YS014-66 which is the cemented Mancos shale in the transaction of two faults; (c)&(d): the magnificent view of the calcite cemented sample YS014-68.

The precipitation of calcite fills the pores in samples from T4. Elongated cementations suggest the fluid that deposited the calcite is likely to be transported from elsewhere (Figure 5-29(b)). The primary calcite is recrystallized, and the shale is well-cemented.

5.3.3.3 Stable isotope analysis for T4

The T4 samples display in a range between -7.8‰ to +1.6‰ V-PDB for carbon and -7.6 ‰ to -12.6 ‰ V-PDB for oxygen. Sample YS014-70, about 32m from T4, is normal Mancos shale, with $\delta^{13}C$ of +1.5‰ V-PDB and $\delta^{18}O$ of -7.5‰ ~ -7.8‰ V-PDB (Zone 1, Figure 5-16).

The sample that is nearest to the travertine (YS014-66) contains an extremely high proportion of calcite cement (66%~71%). It is isotopically similar to samples in the Zone 4 of T6, with relatively depleted carbon isotope of -5.6‰ V-PDB and oxygen isotope of -12.9‰ ~ -12.0‰ V-PDB. Calcite vein YS014-65 that is situated about 2m away from T4 has similar stable isotopic feature as Sample YS014-66 ($\delta^{18}O$= -13.5‰ V-PDB, $\delta^{13}C$= -5.8‰ V-PDB). The $^{87}Sr/^{86}Sr$ of vein sample YS014-65 (0.7087+/- 0.0012) is depleted with heavy Sr compare to CO_2-rich fluid originated calcite (discussed in section 4.3.8), but similar to measured diagenetic carbonates, indicating the formation of the calcite vein should be derived by diagenesis rather than modern CO_2-rich fluid through the fault.

Samples in the middle of the sampling traverse (sample YS014-67, 68, 4.4m and 7.5m from T4 respectively, Zone 5 in Figure 5-30) are not included in the envelope of three-source model described in section 5.3.1.4. The oxygen isotope values for sample YS014-67 and 68 are comparable with the normal Mancos, while carbon isotope is much more depleted with $\delta^{13}C$. These peculiar isotopic values have not been found in other Mancos or vein samples, implying the carbonate cements of the T4 Mancos shale were deposited under different scheme with other travertines.

The existence of the Travertine 4 demonstrates CO_2-rich fluid could indeed penetrate the damaged Mancos shale unit and precipitated travertine on the top surface. However, T4 has distinct isotopic feature compared with other big travertines of the region. T4 is enriched with $\delta^{18}O$ (-7.5‰ V-PDB ~ -6.1‰ V-PDB) and depleted with $\delta^{13}C$ (-4.8‰ V-PDB ~ -5.3‰ V-PDB). The enriched $\delta^{18}O$ and depleted $\delta^{13}C$ should be derived from the dissolution and re-precipitation of the Zone 4 cements (cements derived from thermal decarboxylation at deep burial) under lower temperature. The interacted deposition fluid should be CO_2-rich brine water without the input of meteoric fluid (around $\delta^{18}O$ = -5‰ V-SMOW), and the deposition occurred post-dated to the leakage of the CO_2 (~400ka).

Table 5- 16: Stable isotope for veins and Mancos shale samples in one traverse in T4.

Sample No.	Description	Distance from the local travertine (m)	$\delta^{13}C$ V-PDB	$\delta^{18}O$ V-PDB	Calcite percentage (%)
YS014-62-1/2	twice-movement veins in the contact of the two faults	10	1.55	-11.77	89.25
YS014-62-2/2		10	1.46	-11.85	93.82
YS014-65-1/2	veins in the contact of the two-coloured Mancos shale	2	-5.69	-13.66	77.29
YS014-65-2/2		2	-5.79	-13.49	81.88
YS014-63-1/2	Local travertine	0	-4.96	-6.68	87.16
YS014-63-2/2		0	-4.85	-6.12	85.86
YS014-64-1/2		0	-5.35	-6.90	71.43
YS014-64-2/2		0	-5.23	-7.54	62.81
YS014-66-1/2	Mancos shale in a traverse	2.0	-5.62	-12.55	66.58
YS014-66-2/2		2.0	-5.65	-12.09	71.52
YS014-67-1/2		4.4	-7.81	-8.24	49.88
YS014-67-2/2		4.4	-7.37	-9.00	44.52
YS014-68-1/2		7.5	-6.06	-9.31	56.81
YS014-68-2/2		7.5	-5.59	-8.43	45.07
YS014-70-1/2		32.0	1.53	-7.54	17.14
YS014-70-2/2		32.0	1.59	-7.84	19.54

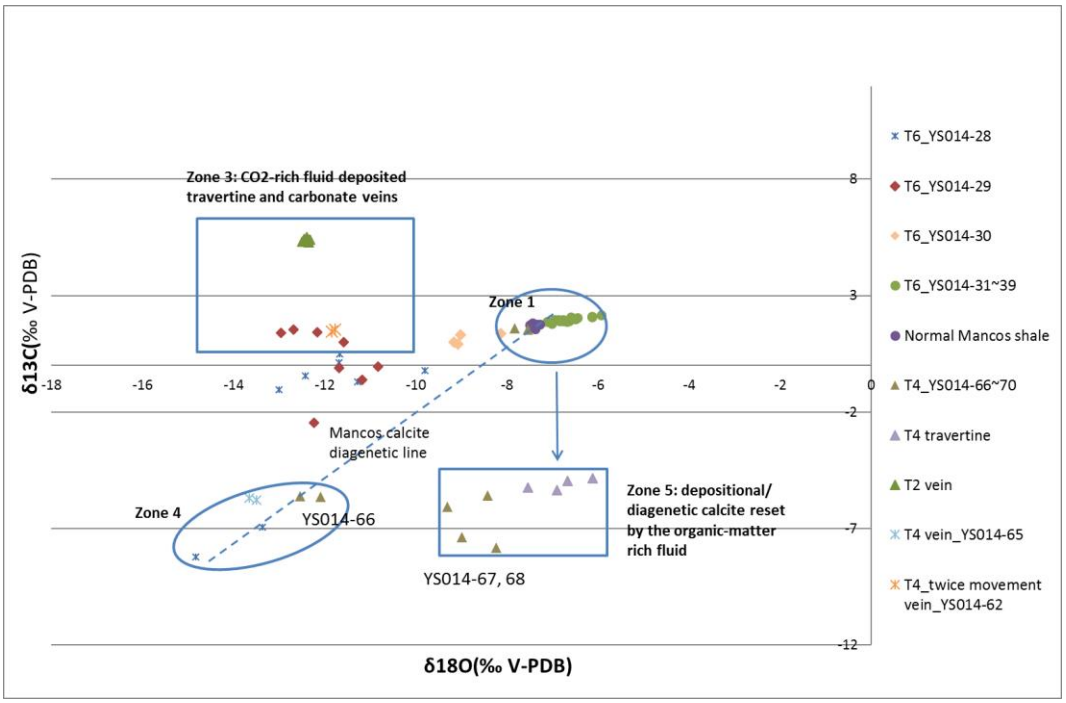

Figure 5- 30: Plot of stable isotope for T4 (dark green triangles stand for Mancos shale; dark purple triangles stand for T4 travertine), T6 samples and T2-vein.

5.3.2.5 Summary for the calcite precipitation for T4

The stable isotopic features of the local travertine should be fully interaction and inherit from the host Mancos. The shale sample which is 2m from T4 (YS014-66) and adjacent to vertical foliated vein in the fault zone of the small fault, has been completely cemented by the fluid deposited the vein. The depositional/ diagenetic carbonates in the samples further away from the travertine (YS014-67, 68) have be completely recrystalized by the infill of the contemporary fluid. Sample YS014-70 that is 30m away from the local fault is normal Mancos shale has not been altered by the fault movement.

The small-scale travertine T4 that is located at the junction of the main fault and a subsidiary small fault, was derived by the CO_2-rich brine under low temperature. The dissolved bicarbonate in the fluid should be derived from the dissolution and re-precipitation of the deep buried diagenetic calcite cements (Zone 4), because there is no other possible source for the $\delta^{13}C$ depleted bicarbonate. The CO_2-rich fluid

enabled to penetrate the deformed Mancos shale and deposit travertines on the top surface. The saturation of CO_2 into the brine suggest the formation of travertine should be post-dated to the formation of the two faults and the start of the CO_2 leakage. There is no ingress of the meteoric fluid, that implies the meteoric fluid cannot flow across the fault zone to mix with the formation brine.

5.4 The rock-water interaction model

Both of the fluid composition and the initial rock contribute to the isotope composition of the precipitated carbonates, hence the isotope ratio should be influenced by the ratio between the rock and the water. If the amount of water compared in the aquifer is small compared to the contacted rock (at least the carbonate fraction), the isotope values of the precipitated carbonates are dominated by the rock; while in a very porous aquifer with high flow rates, the water composition will be the dominant factor.

Equations to calculate the water/rock interaction curves between water and rock has been presented by Morrison and Parry (1986):

$$\delta^{18}O_w^f = \frac{\frac{W}{R}(\delta^{18}O_w^i) - 3(\Delta^{18}O_{rw} - \delta^{18}O_r^i)}{3+\frac{W}{R}} \qquad \text{Equation 5-22}$$

$$\delta^{13}C_w^f \cong \frac{\frac{W}{R}\left(\frac{m_{HCO_3}}{m_{H2O}}\right)(\delta^{13}C_w^i) + \delta^{13}C_r^i - \Delta^{13}C_{r-HCO_3}}{\frac{W}{R}\left(\frac{m_{HCO_3}}{m_{H2O}}\right)+1} \qquad \text{Equation 5-23}$$

Where $\delta^{18}O_w^f$ and $\delta^{13}C_w^f$ are the calculated dissolved bicarbonate values; $\delta^{18}O_w^i$ and $\delta^{13}C_w^i$ are initial dissolved bicarbonate values; $\delta^{18}O_r^i$ and $\delta^{13}C_r^i$ are initial rock carbonate values; $\Delta^{18}O_{rw}$ and $\Delta^{13}C_{r-HCO_3}$ are fractionation of oxygen and carbon at a particular temperature; m_{HCO_3} is bicarbonate molality (m_{H2O}= 55mol/L) ; $\frac{W}{R}$ is the molar ratio of water to carbonate minerals.

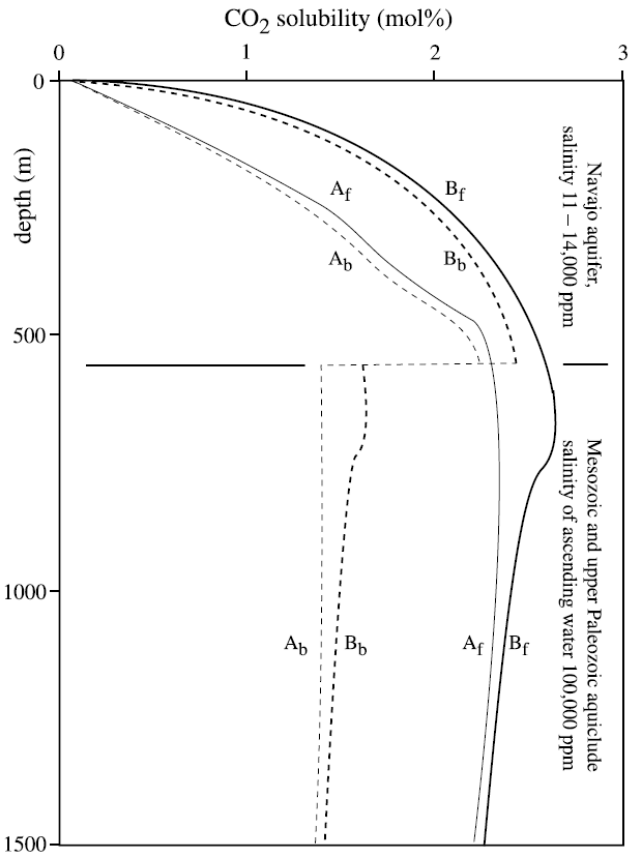

Figure 5- 31: Solubility of CO_2 in fresh water (A_f and B_f) and brine water (A_b and B_b) compiled by Wilkinson et al., (2009) after aquifer data (Rush et al., 1982, Baer and Rigby, 1978).

Normally, m_{HCO_3} is extremely small compared to water molality. The mole fraction between dissolved bicarbonate and water ($\frac{m_{HCO_3}}{m_{H2O}}$) ranges from 1% to 1.5% for thermal brine.

Water-rock ratio describes in the mole ratio between the fluid in the open spaces against the calcite in the rocks that interacts with the fluid. Porosity of the shales is usually less than 10% (Nelson, 2009) and for porous sandstones is over 20%. The proportion of calcite in the initial Mancos shale is around 30% to 45%, then the calculated W/R should be ranging from 0.2~0.3 for shales and from 0.7~1.1 for porous sandstones for static system. However, in real cases, the W/R ratio could be much larger than these values due to the flow of water. Therefore, the range for W/R is expanded from 0.1 to 50 in this study.

The oxygen isotope for the initial rock is that of depositional/diagenetic normal Mancos shale, which is the average value for Zone 1 in Figure 5-15 ($\delta^{18}O_r^i$= -6.9‰ V-PDB), and the oxygen isotope for the initial fluid is the Cretaceous brine with $\delta^{18}O_w^i$= -31.2‰ V-PDB. The water-rock ratio (W/R) ranges from 0.1 (rock with very little pore space for fluid) to 50 (rock with through-flowing fluid). When W/R less is than 0.1, the oxygen isotope of the precipitated calcite is almost entirely inherited from the initial rock (normal Mancos shale). As W/R increases, the precipitated calcite tends to be dominated by the fluid.

The Mancos shale samples that are not influenced by the meteoric can be used to define the trend of diagenesis during deep burial (diagenetic line in Fig. 5-30). The diagenetic line starts where only depositional carbonates exist without any fluid/rock interaction (W/R=0.1). When it reaches the depth of deeper than 1000m, abiotic reactions began that resulted in δ^{13}C-depleted carbon. The highest temperature reached by the Mancos as c. 93°C (Nuccio and Condon, 1996) at the deepest burial (8000ft) at the end of Eocene (burial history Figure 5-16). The sediments started to be uplifted from the Laramide orogeny happened around 40Ma ago until the present day. The time of the deepest burial for Cretaceous formation coincides with the formation of Little Grand Wash fault (Dockrill, 2006).

The CO_2 sequestration model for T6 (red dashed line in Figure 5-32) represents when the CO_2 in the modern fluid was sequestered as carbonates at different W/R interaction ratio. The initial rock is normal Mancos shale in Zone 1. Since there is no record for the δ^{13}C of the paleo-fluid, hence we use δ^{13}C of the present-day Crystal Geyser spring (~ 0‰ V-PDB) instead. The precipitation of the carbonates in Zone 3 happened during shallow burial at low temperature with the intrusion of great amount of meteoric fluid mixing with brine water near the vicinity of the main fault (less than 17m). The W/R ratio is greater than 50, suggesting big flow rate of the paleo-fluid penetrating the deformed Mancos unit. The deposition happened post-dated to the leakage of CO_2 (400 ka, Kampman et al., 2012) at the same time with the deposition of fossil travertines. Cements in seriously deformed Mancos, and veins in sandstone units (footwall of the main fault) were formed by this mechanism.

The CO_2 sequestration path for T4 Mancos (Zone 5) (Figure 5-33) is different from the sequestration path for Zone 3 due to different initial rock and water

compositions. The initial rock in the T4 model is the deep burial diagenetic calcite cements (Sample YS014-65 and 66). Then followed by the uplift of the sediments to the surface until the in-charge of the CO_2-rich modern brine migrated through the fault and fractures. The low permeable fault zone effectively inhibited the in-flow of meteoric fluid from the source of the ground-water to the southwest of the Crystal Geyser. The deposition of cements in Mancos shale happened at the W/R ratio of 4~10, and the travertine deposited at of W/R ratio of 20. The flow-rate of the penetrating fluid to form T4 is much lower than that of T6, which result in the isotope of the deposited cements is dominant by the initial rock rather than the fluid. The depositional time should be similar with that of T6, which is post-dated to the commencement of the CO_2 leakage. The CO_2 sequestration pathway model and diagenetic model have been generalized in Table 5-17. Thick aragonite veins (T2 vein) and other travertines are especially enriched with heavy carbon, which is probably owing to the involvement of bacteria preferentially removing light carbon.

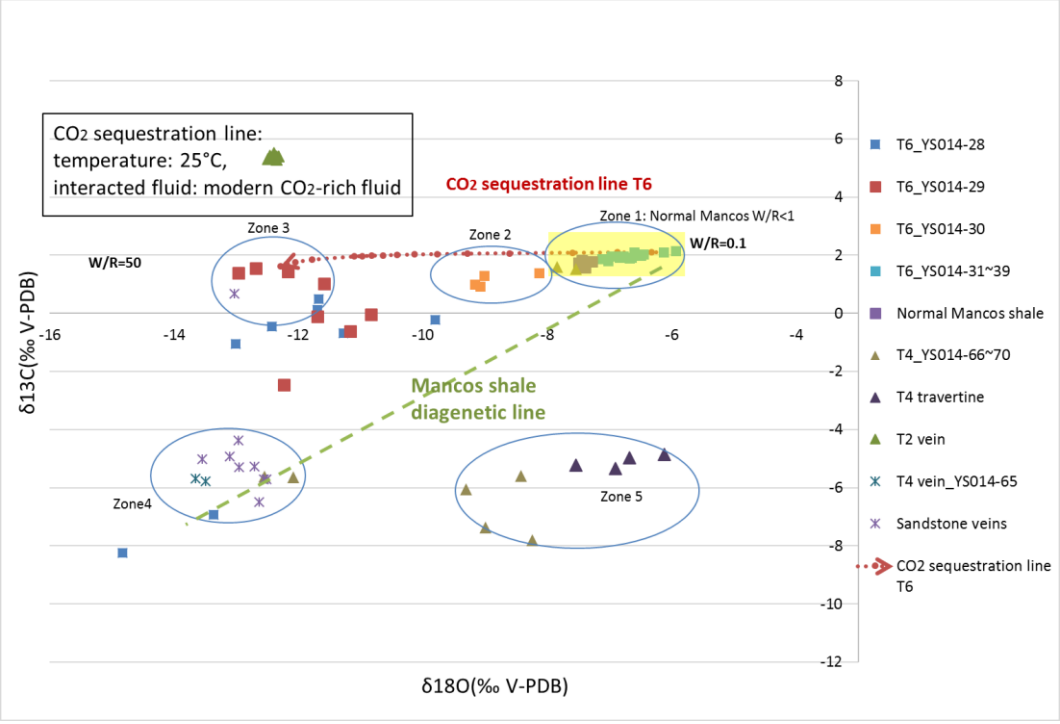

Figure 5- 32: Mancos shale CO_2 sequestration line during the surface deposition at the temperature of 25°C.

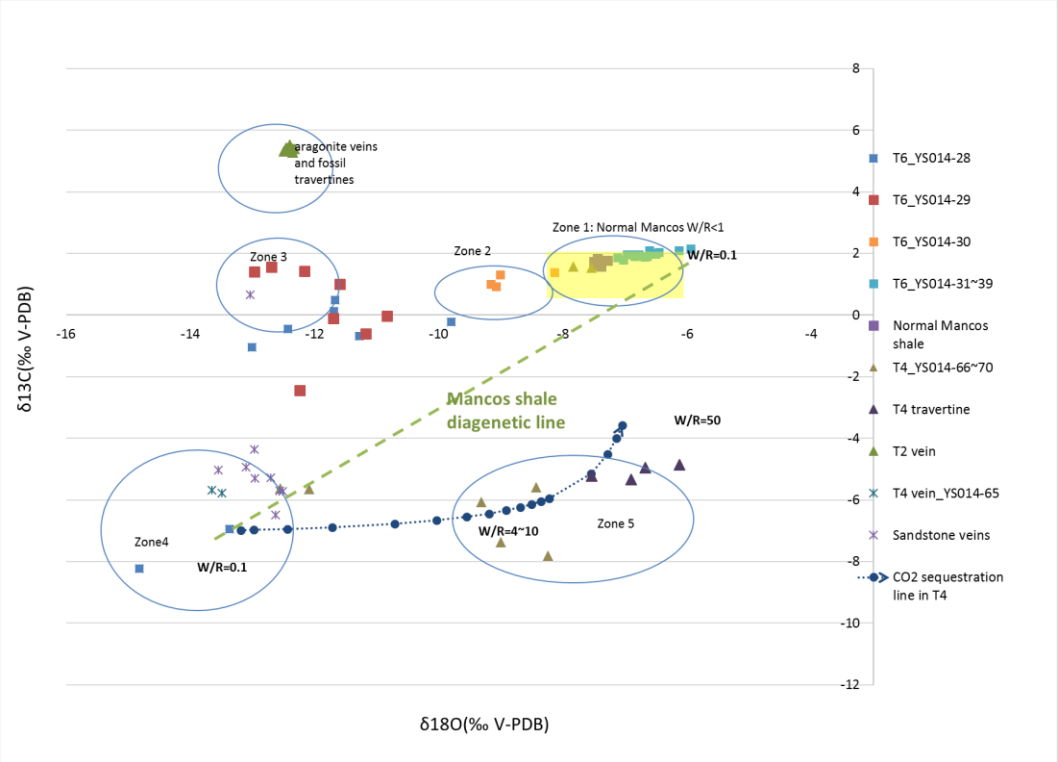

Figure 5- 33: Mancos shale CO_2 sequestration line for T4 during the surface deposition at the temperature of 25°C.

Table 5- 17: Interaction paths models for rock-fluid reactions and the deposition temperature and involved processes

Mode	$\delta^{13}C_w^i$ ‰ V-PDB	$\delta^{18}O_w^i$‰ V-PDB	$\delta^{13}C_r^i$‰ V-PDB	$\delta^{18}O_r^i$ ‰ V-PDB	T /°C	Process
Mode 1	~ 0 (CO_2-rich fluid from Assaya g et al., (2008))	-41.0 (CO_2-rich paleo-fluid from the model in Chapter 5)	+2.1 (depositional/diagenetic normal Mancos)	-5.9 (depositional/diagenetic normal Mancos)	25	Carbon sequestration from CO_2-rich fluid for T6
Mode 2	~0 (CO_2-rich	-35.0	-7.0 (deep buried	-13.4 (deep buried	25	Carbon sequ

	fluid from Assaya g et al., 2008)	(CO_2-rich brine fluid from Morrison and Parry, 1986)	diageneti c calcite cements)	diagen etic calcite cement s)		estrat ion from CO_2-rich fluid for T4

The interaction path model enables to explained different deposition model that formed the dispersed isotopic feature of the cements in Mancos shales, travertines and veins in shales and sandstones. The time of deposition, temperature, burial depth and the interacted fluid have been summarized in Figure 5-34.

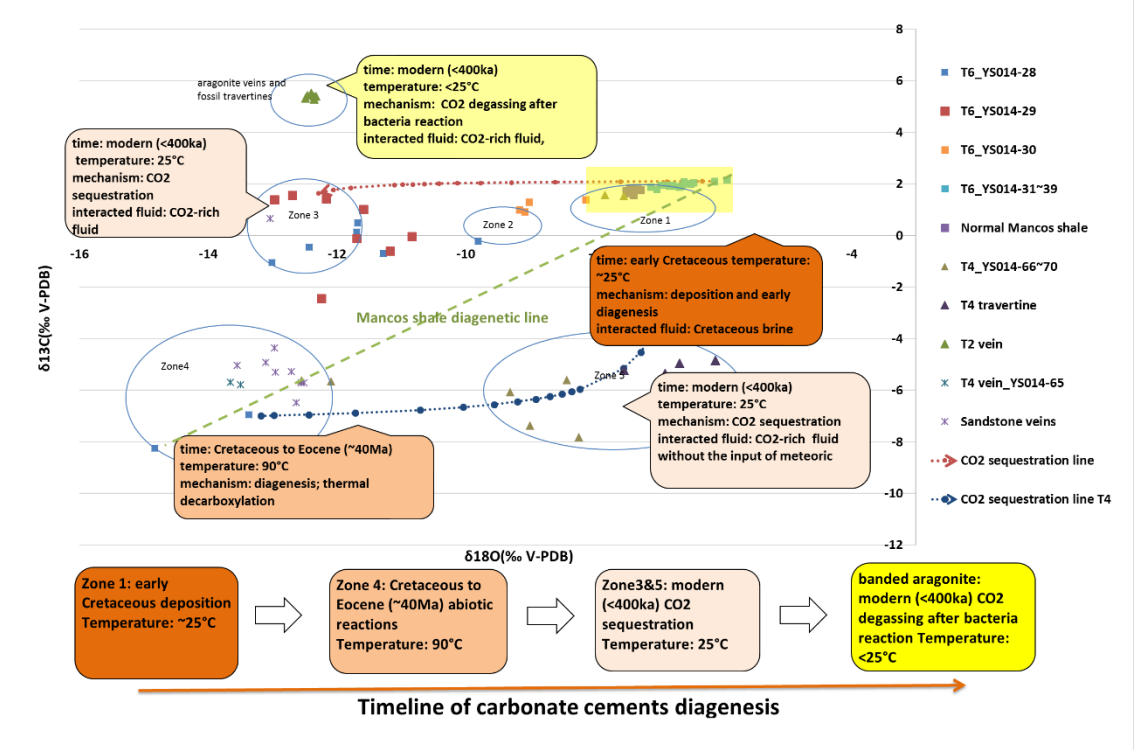

Figure 5- 34: Formation mechanisms for cements, veins and travertines in T3, T4 and T6 explained by interaction model

5.5 CO_2-rich fluid circulation model in Mancos shale

Features of the three studied travertines (T3, T4 and T6) and the associated Mancos shale samples have been studied using petrographic methods and stable isotope analysis in order to investigate whether the fault-associated CO_2-rich fluids

have altered the Mancos shale on the hanging wall of the Little Grand Wash Fault (conceptual model in Figure 5-36). The composition and saturation state of CO_2-enriched fluid have been intensively studied in chapter 4, using aragonite vein sample that records the fluid features. The fluid that deposited the aragonite veins contains around 25% to 45% brine plus 55% to 75% meteoric fluid, which is much more saline than present Crystal Geyser spring water (around 3% of Paradox brine). In this chapter, the CO_2-rich fluid that deposited the veins and carbonate cements of the Mancos is assumed to contain 30% to 50% of Paradox brine and 50% to 70% meteoric.

Three major travertines and the shale/vein samples in the vicinity of the travertines have been sampled for analysis. T3 and T6 are large fossil travertines, and T4 is a small travertine with fluid penetrating the Mancos shale in the intersection of the LGWF and a subsidiary small fault (location see Figure 5-12). Samples in T6 that close to the fault shows evidence of been altered by CO_2-rich fluid, with up to 27% (weight percentage) of the total rock deposited by the CO_2-rich fluid. The Mancos further than 17m away from the main fault are little influenced by the fluid.

Samples from T3 with similar proximity from LGWF is demonstrated to be little influenced by the CO_2-rich fluid. Only in-situ dissolution and re-precipitation of primary fossil carbonate have been observed. Extensive thin gypsum veins inside the fractures near the fault might be from the weathering of pyrite. The reduction zone is probably from reduction by hydrogen sulphide.

Samples from the small travertine T4 shows quite different petrographic and isotopic features compared with the Mancos shale from the other travertines. This small travertine (T4) formed from the CO_2-rich brine fluid without the interaction of meteoric water. This fluid penetrated the Mancos shale and deposited the small travertine at very low flow-rate (W/R=4~10) (around 20cm in diameter). The travertine post-dated the uplift of the basin and the leakage of CO_2.

By analysing the morphology and the stable isotopes of the cements, most carbonate cements in shale samples are from three origins: a) the depositional and/or diagenetic carbonates; b) the CO_2-rich fluid with meteoric ingress; c) the dissolution and re-precipitation of deep burial diagenetic calcite cements without the interaction of meteoric fluid. Given the distinctive stable isotope of each derivation,

the proportion of carbonate cements from each source has been calculated and compared spatially. As consequence, the behaviour of the CO_2-rich fluid to the Mancos shale from the primary deposition until present day have been illustrated in the schematic diagram in Figure 5-35.

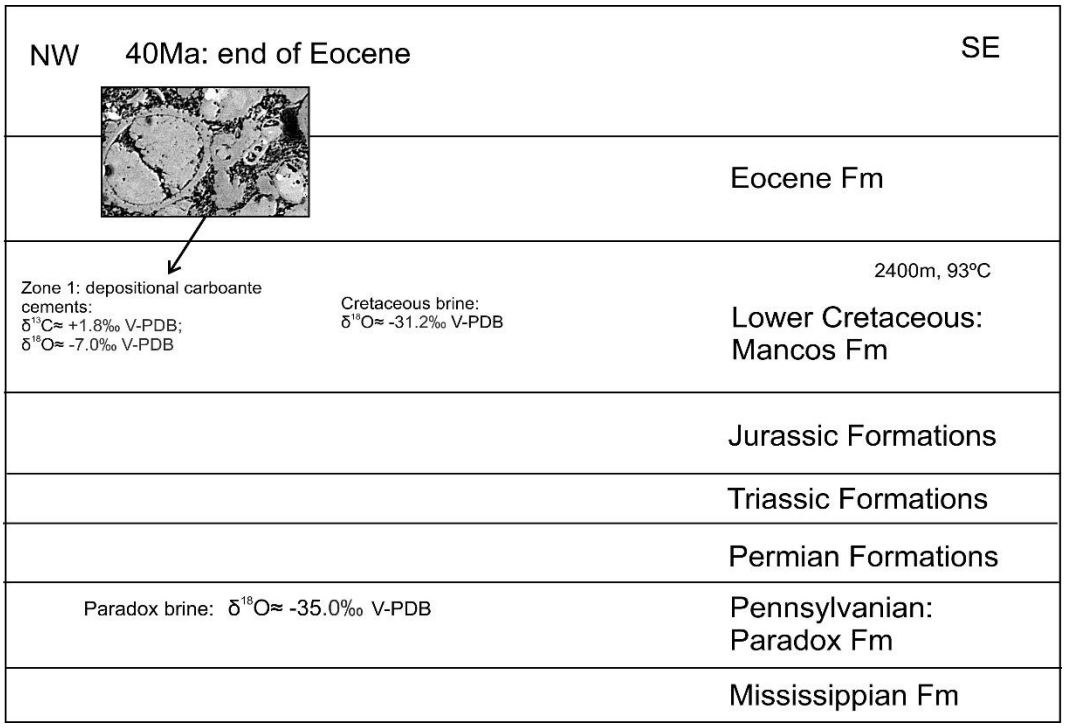

(a)

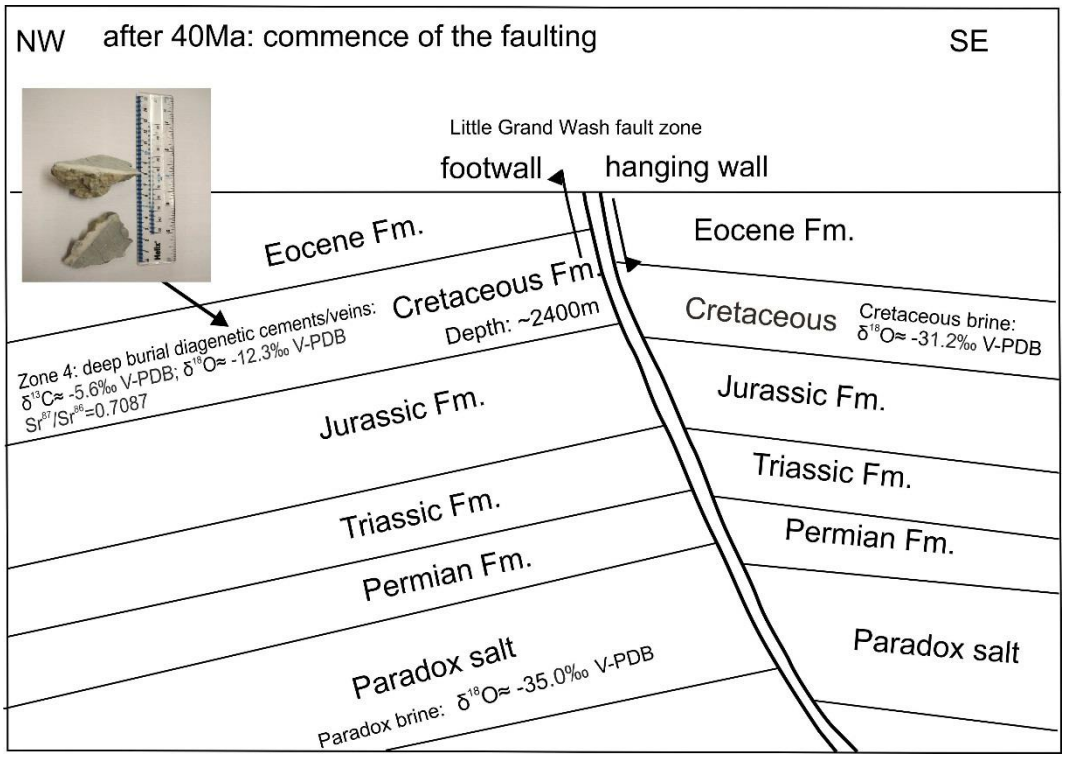
NW
after 40Ma: commence of the faulting
SE
Little Grand Wash fault zone
footwall
hanging wall
Eocene Fm.
Cretaceous Fm.
Depth: ~2400m
Zone 4: deep burial diagenetic cements/veins:
δ13C≈ -5.6‰ V-PDB; δ18O≈ -12.3‰ V-PDB
Sr87/Sr86=0.7087
Jurassic Fm.
Triassic Fm.
Permian Fm.
Paradox salt
Paradox brine: δ18O≈ -35.0‰ V-PDB
Eocene Fm.
Cretaceous
Cretaceous brine:
δ18O≈ -31.2‰ V-PDB
Jurassic Fm.
Triassic Fm.
Permian Fm.
Paradox salt

(b)

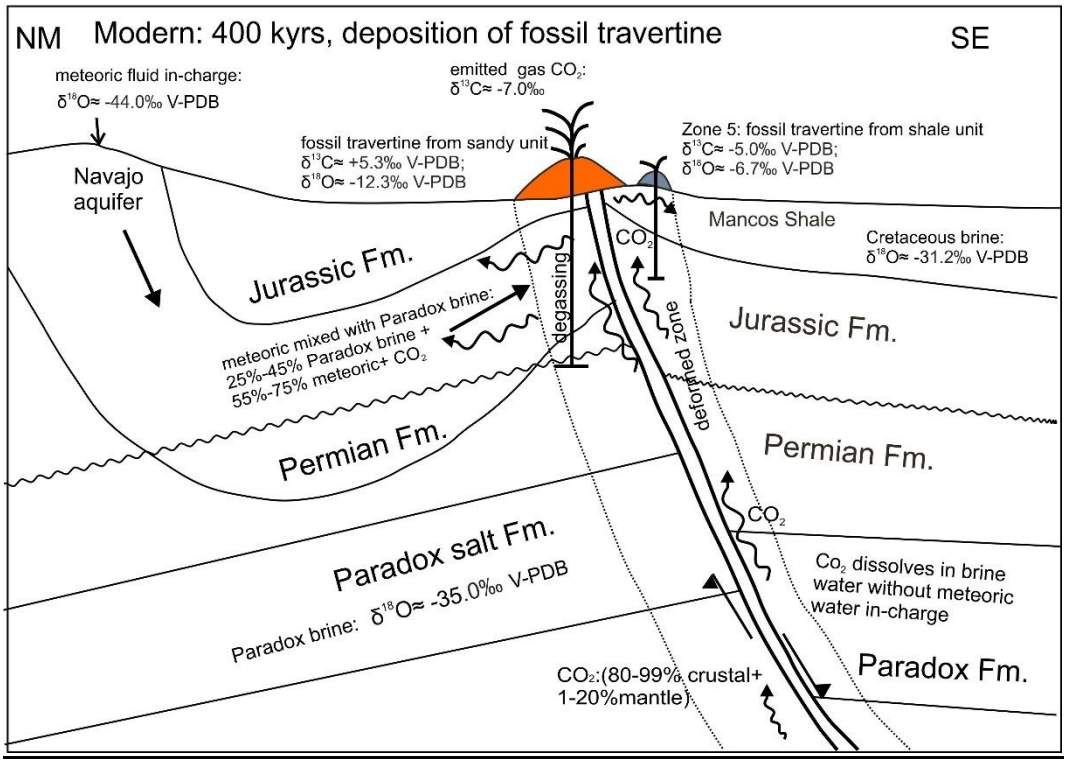
NM
Modern: 400 kyrs, deposition of fossil travertine
SE
meteoric fluid in-charge:
δ18O≈ -44.0‰ V-PDB
emitted gas CO2:
δ13C≈ -7.0‰
fossil travertine from sandy unit
δ13C≈ +5.3‰ V-PDB;
δ18O≈ -12.3‰ V-PDB
Zone 5: fossil travertine from shale unit
δ13C≈ -5.0‰ V-PDB;
δ18O≈ -6.7‰ V-PDB
Navajo aquifer
Jurassic Fm.
Mancos Shale
Cretaceous brine:
δ18O≈ -31.2‰ V-PDB
CO2
degassing
meteoric mixed with Paradox brine:
25%-45% Paradox brine +
55%-75% meteoric+ CO2
deformed zone
Jurassic Fm.
Permian Fm.
Permian Fm.
CO2
Paradox salt Fm.
Paradox brine: δ18O≈ -35.0‰ V-PDB
Co2 dissolves in brine
water without meteoric
water in-charge
Paradox Fm.
CO2:(80-99% crustal+
1-20%mantle)

(c)

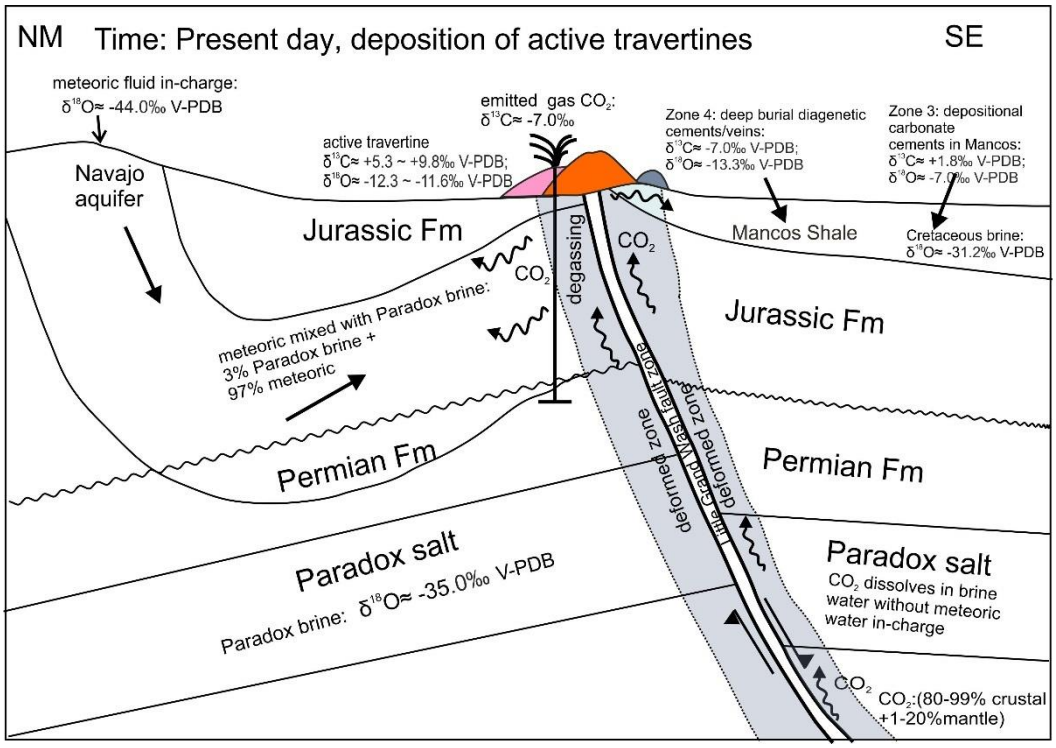

(d)

Figure 5- 35: Schematic diagram showing different stages of the development of the Little Grand Wash fault and the associated deposition of travertines and carbonate cements of Mancos shale. (a) The deposition of early Cretaceous Mancos Fm; (b) faulting commenced from the end of Eocene (~40Ma) and at the same time, the deposition of Mancos reached the deepest burial of around 2400m and started uplift afterwards; (c) surface meteoric fluid entered Jurassic Fm and mixed with CO_2-rich brine water, and deposited fossil travertines and thick carbonate veins; (d) active travertines deposited at by present day Crystal Geyser spring.

To sum up, the deposition of carbonate cements/travertines in relationship with the formation of the faults experienced four major stages, which are:

Stage 1: The Mancos shale sediment deposited with fossil carbonates and early diagenetic carbonate cements during early Cretaceous.

Stage 2: The deposition continued until the Eocene (reached a depth of ~8000ft at 40Ma), followed by the Laramide orogeny and the initiated of the Little Grand Wash

fault and the uplift of the area. Sediment that post-dates the Cretaceous is absent due to erosion.

Stage 3: The leakage of CO_2 started at least from 400ka ago. CO_2 (mostly crustal originated) saturated the Carboniferous Formations brine at the depth of over 2km (Kampman et al., 2014) and migrated upward through the fault zone. In the Permian, Triassic and Jurassic Formations, the CO_2-rich brine mixed with meteoric fluid in-charged from the surface. The CO_2-rich, mixed fluid penetrated the deformed rocks and precipitated travertines and carbonate veins and cements in the host rocks while it migrated upward through the fault/fractures and laterally within the strata. The deposition fluid of the aragonite veins is composed of 25% to 45% of Carboniferous brine and 55% to 75% of meteoric.

Stage 4: The main fault and fractures that providing the migration pathways for the mixed fluid experienced self-sealing during the past hundreds of thousands of years. Less proportion of the brine fluid from the depth entered shallow formations and the flow-rate decreased, until there is only 3% Paradox brine in the present-day Crystal Geyser spring water. Only deformed Mancos has been influenced by the CO_2-rich fluid. The CO_2 sequestered carbonates could compose up to 27% of the whole rock (% weight).

Faults and the associated fractures have been proved to have significant influence on the flow of the CO_2-rich fluid according to the breaching of sandstones, carbonate veins and hydrocarbon staining on the footwall in the previous studies (Dockrill and Shipton, 2010).

CO_2-rich fluid with meteoric fluid ingress did alter the Mancos shale in the hanging wall of the LGWF, but the distance of influence is very limited (normally less than 20m). The CO_2-rich fluid could result in precipitation in high porous or deformed shale samples. The fluid could penetrate the deformed area, deposit small-scale travertine and interact with the pristine cement in the Mancos at low flow-rate. The conceptual model for how the CO_2-rich fluid could influence the host units and in relationship with the main fault has been summarized in Figure 5-36.

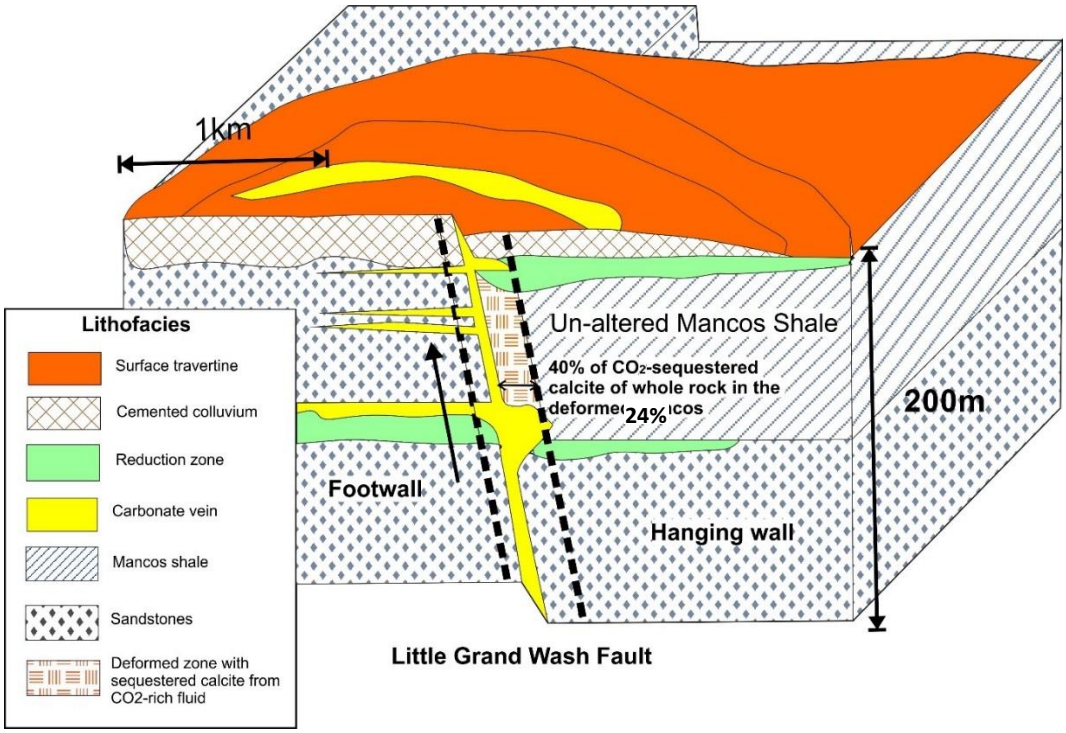

Figure 5- 36: Conceptual model for CO_2-rich fluid circulation in relation to Little Grand Wash fault.

Chapter 6: Conclusions and future work

6.1 Conclusions for this research.

6.1.1 Calculation model for pore throat radii and the generic distribution for UK North Sea

A new statistical model has been established for effective pore throat radii calculation using the back-calculation method in chapter 2. The data of hydrocarbon fields of the UK North Sea has been utilised to build the new model, and the calculated pore throat radius has been demonstrated to be comparable with those of worldwide mudstones derived from commonly used Mercury Injection Porosimetry method. The calculated effective pore throat radius is not the real pore throat radius of caprocks, but the calculated pore throat radius at the critical point of leakage when the buoyancy force equals to the capillary pressure. The calculated effective pore throat radius derived from the new method conquered the shortcomings of the conventional experimental method because: a) it represents a field-scale condition; b) no caprock samples are required, and c) the calculated pore throat radii includes the effects of fracturing and faulting.

Mudstone caprocks of hydrocarbon fields have been used as analogues for mudstones of the UK North Sea. In total, 140 reservoirs of UK North Sea have been studied, and 53 of which have both sufficient data to allow calculation and the capillary pressure is plausibly the controlling factor for hydrocarbon sealing. Fields with column height controlled by spill point (lowest closing contour is the same as oil-water contact) have been excluded from analysis. The cumulative distribution and the probability distribution of the effective pore throat radii of the mudstone caprocks in the UK North Sea oil fields were obtained, which could be applied as a reference for storage siting for saline aquifers. Monte Carlo simulation has been utilized to get a more reliable distribution of the effective pore throat radii with various distributions of the input parameters.

The probability distribution has been compared to the distribution of Yang and Aplin (1998) that derived from the conventional experiment using the mudstones from the North Sea. The results derived from the new model show a similar shape of the curve (Figure 2-33), but narrowed down the range to 37nm ~ 1700nm (the most

probable effective pore throat radius is 50 nm). The correlation between the possible controlling factors of burial depth of the reservoir (the top of the reservoir to the crest), the degree of faulting, the caprock thickness and the effective pore throat radii have been tested. The burial depth is inversely proportional to the pore throat radius providing the burial depth is less than 3000m, when the mechanical compaction is the dominant factor of the pore throat radii. This correlation disappeared at the burial depth greater than 3000m, where the diagenetic processes becomes the dominant factor for the pore throat radii.

6.1.2 CO_2 migration and interaction model for Mancos shale

The Crystal Geyser in Utah acts as an ideal natural analogue to study the behaviour of CO_2 in a geological time. The leakage of CO_2 has been demonstrated to be last for at least 400kyrs (Burnside et al., 2013). The generated CO_2 originated from the crust (1%-20%) and the mantle (16%-99%) (Wilkinson et al., 2009a) dissolves in the brine and rises upward through the main fault zone to enter the overlying aquifers and mixed with meteoric fluid in Jurassic formations. The deposit of travertine distributed alongside the main fault zone suggest the CO_2 leakage through the fault or fault related fractures. Carbonate veins were deposited as the record of the CO_2-rich fluid (named as “paleo-fluid” in chapter 5 to distinguish with present spring) migrated up-dip through fault.

Vein samples were observed and sampled to investigate the migration pattern and the geochemistry of the paleo-fluid. Thick, banded aragonite veins from T2 travertine mound were intensively studied in Chapter 4 to model the change of the paleo-fluid with time, and the deposition environment in the Crystal Geyser area. The paleo-fluid is a mixture of two end members: the CO_2-saturated brine fluid migrated up-dip from fault, and the meteoric fluid in-charged from northwest of the Crystal Geyser. The distribution coefficients are utilized to convert the composition of veins to the fluid. The paleo-fluid is composed of 25% to 45% of Paradox brine plus 55% to 75% of meteoric, under the temperature of approximately 12 ~18 °C. This mixing result suggests the paleo-fluid is much more saline compared to the present Crystal Geyser spring, which contains only 3% of Paradox brine. The proportion of saline water decreases as the vein grew, which might be owing to the gradual self-healing of the fault.

By studying the alterations of petrographic features of the Mancos shale samples in the hanging wall of the fault, the CO_2-rich fluid alteration model and migration pattern of the fluid have been illustrated in chapter 5. The CO_2-rich fluid can only penetrate and interact with the deformed Mancos that caused by faulting. No evidence show the intact Mancos has been affected by the CO_2-rich fluid.

The CO_2-rich fluid could deposit up to 27% of calcite against the whole rock (%weight) at where the deformed Mancos is approximately 15m from the main fault, while the Mancos further than 17m from the main fault has no CO_2-rich fluid induced calcite precipitation. The water/rock interaction model was established to quantitatively illustrate the stable isotope pathways under different water-rock contact schemes (Figure 5-34). Small-scale travertine (T4), with distinctive stable isotope features compared with other fossil travertines, was deposited by the CO_2-rich brine that penetrating the Mancos shales at slow flow-rate. The deposition fluid contains no meteoric fluid, indicating the meteoric flow was inhibited by the faults.

6.1.3 Apply the study results into CO_2 storage siting procedures

For a real geological carbon storage project, the workflow could be intersected into four major stages (Cooper, 2009):

- Site selection and development: this phase includes site screening, selection and characterisation. It usually takes about three to ten years to carry out the pre-operation work. The construction begins as long as the suitable site has been selected. Some infrastructures could be re-used after modification for the carbon storage in the depleted hydrocarbon fields.
- Operation: inject supercritical CO_2 into subsurface under monitoring and simulation to ensure the safety injection.
- Case closure: the monitoring work should be continued until to verify the injection is well managed with no potential danger for leakage before the closure of the project. Then the plug wells and infrastructures could be removed from the sites.
- Post closure: the future performance of the injected CO_2 is estimated to acknowledge the potential migration pathways and leakage potential in geological time.

Site selection and development phase could be divided into site screening, selection and characterization. Site screening focuses on the evaluation of potential sub-regions for carbon storage according to basinal data. The evaluation will rank the potential of the storage sites from highest to lowest preferable, and pick the most suitable site to process to the second stage. The analysed data include regional geological data, regional proximity data and social data. Site selection phase is the further evaluation of the screened regional with geological data, regulatory requirements, modelled data and social data. Initial characterization aims at gaining more information and understanding the most promising area with existing geological, seismic and well logs data.

The site selection phase is especially important for the whole project to ensure the injectivity, storage potential and security. Various siting criteria has been implemented to practical carbon storage project. One of the most prevalent criterial was proposed by Chadwick et al. (2008), which has been widely used for storage potential study, such as the carbon storage potential for the UK North Sea by Scottish Centre for Carbon Storage (2009) (Chadwick et al., 2008). A table of compiled criteria for storage siting from various institutions shows in Table 6-1 (the criteria related to the quality of caprock is underlined).

Table 6- 1: Site screening and selection criteria from the compilation of literatures (IEA, 2008, Bachu, 2003, Chadwick et al., 2008)

	Criterion type	Criterion	Not Suitable/Unfavorable	Suitable/Desirable
1	Critical	Depth	Less than 1000m or deeper than 4000m	1000m to 4000m
2		Reservoir-seal pairs and stratigraphic sequences	Poor (few, discontinuous, faulted and or breached	Intermediated and excellent. At least one major extensive competent seal
3		Pressure regime	Over-pressured	Hydrostatic or sub-hydrostatic
4		Legal accessibility	Forbidden	Possible

5		CO_2 source within economic distance	More than 300km	Less than 300km
6		Data availability	Not available or old 2D seismic data	Available (new 3D seismic data, uniform coverage)
7	Essential	Seismicity (basin tectonic setting)	High and very high (subduction zones; syn-rift and strike-slip basins)	Very low to moderate (foreland, passive margin and cratonic basins)
8		Faulting and fracturing intensity	Extensive	Limited to moderate
9		Hydrogeology	Shallow, short flow system, or compaction flow	Intermediate and regional-scale flow; topography and erosional-rebound flow
10		Surface areal extent	Less than 2500 km^2	Greater than 2500 km^2
11	Selection	Within fold belts	Yes	No
12		Significant diagenesis	Present	Absent
13		Geothermal Regime	Warm basin (Gradient >0.04 °C/m)	Cold or moderate basin (Gradient >0.04 °C/m)
14		Evaporites (salt)	Absent	Domes and beds
15		Hydrocarbon potential	Absent or small	Medium to giant
16		Industry maturity	Immature	Mature
17		Climate	Harsh	Moderate
18		Infrastructure	Absent or rudimentary	Developed
19		Reservoir thickness	Very thin (<20m)	Thick (>20m)
20		Average porosity	<10%	>10%
21		Maximum permeability	<200mD	>200mD
22		Salinity	<10g/l	>10g/l

23		Reservoir stratigraphy	Complex lateral variations and connectivity	Uniform
24		Caprock thickness	<20m	>20m
25		Capillary entry pressure	Similar or smaller than the injection pressure	Much greater than the injection-induced pressure
26		Igneous rock	Little knowledge about the existence	Appreciation of the existence, geometry and effect on the surrounding rocks
27		Static capacity	<20 million tonnes of CO_2	>20 million tonnes of CO_2

Criteria concerning the sealing rocks include the thickness, the lateral continuity and the capillary entry pressure when we evaluate the quality of the caprock. The conventional way to measure the capillary entry pressure is to use high pressure Mercury Injection Porosimitry method on core samples by converting the mercury intrusion pressure into gas-brine intrusion (see section 2.2.4). This research enables us to use the existing hydrocarbon field data to get the distribution of the effective pore throat radii of the region, which could be used to predict the capillary entry pressure of the caprocks of the saline aquifers without using core samples. The calculated effective pore throat radius could be used to calculate the maximum height of the CO_2 column, and then to predict the sealing capacity of the caprocks. The procedure of using effective pore throat radii for site screening and selection is shown in the diagram below (Figure 6-1).

Another important leakage potential is from the pre-existing or induced faults and fractures. Normally, faults could act as roles of either conduits or barriers for the regional flow. Geochemical reactions could either “improve” or “inhibit” the leakage by dissolution or precipitation filling the faults/fractures. Previous studies have proved the faults/fractures act as conduits for regional CO_2-rich fluid to migrate upward and deposited veins in the cracks of sandstone units. This study focuses on Mancos shale that associated with the Little Grand Wash fault, and the result has proved the CO_2-rich fluid could only influence the damaged host rocks (deformed and fractured), with very limited influencing radius (less than 20m)..

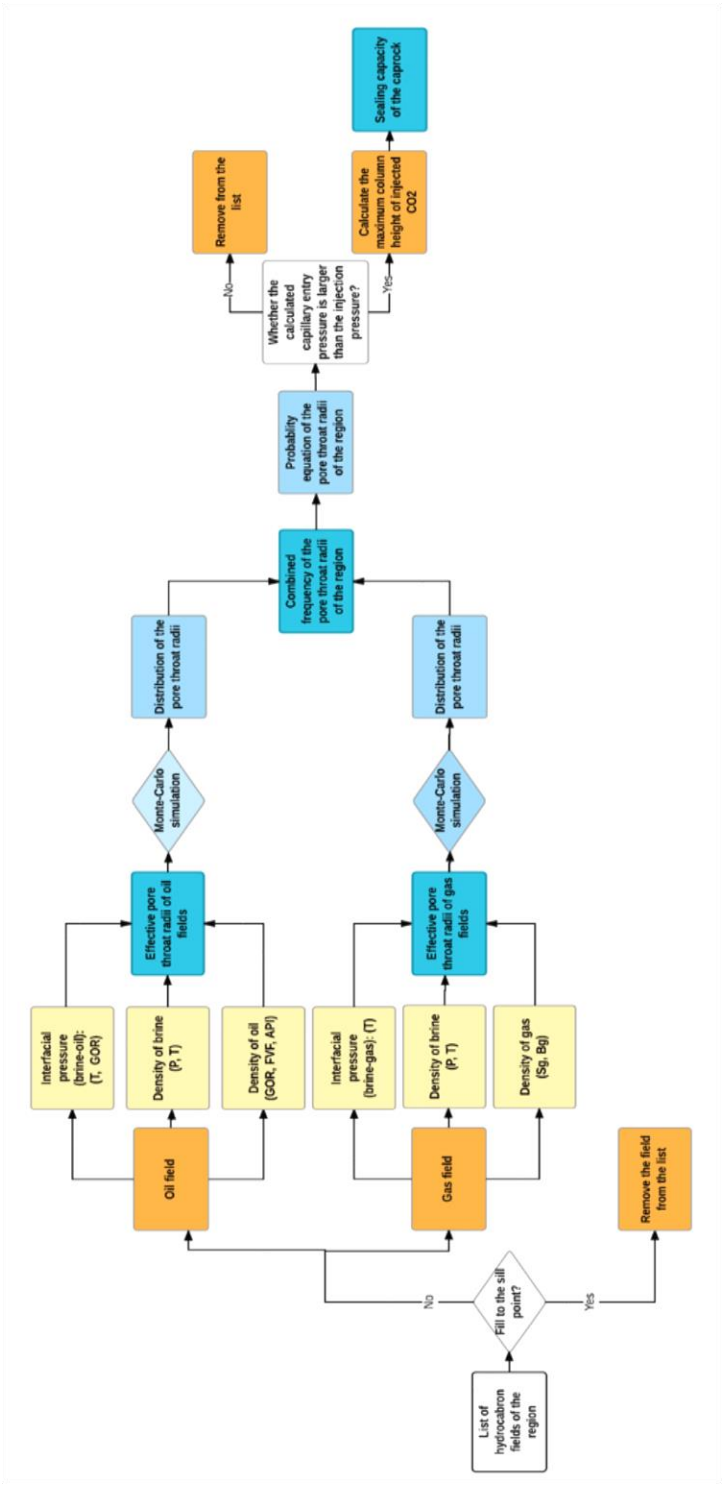
List of hydrocabron fields of the region
Fill to the sill point?
No
Yes
Remove the field from the list
Oil field
Gas field
Interfacial pressure (brine-oil): (T, GOR)
Density of brine (P, T)
Density of oil (GOR, FVF, API)
Interfacial pressure (brine-gas): (T)
Density of brine (P, T)
Density of gas (Sg, Bg)
Effective pore throat radii of oil fields
Effective pore throat radii of gas fields
Monte-Carlo simulation
Monte-Carlo simulation
Distribution of the pore throat radii
Distribution of the pore throat radii
Combined frequency of the pore throat radii of the region
Probability equation of the pore throat radii of the region
Whether the calculated capillary entry pressure is larger than the injection pressure?
No
Yes
Remove from the list
Calculate the maximum column height of injected CO2
Sealing capacity of the caprock

Figure 6- 1: The workflow for using hydrocarbon fields as analogue to estimate the capillary entry pressure, maximum column height of the injected CO_2, and the caprock sealing capacity.

6.2 Future work

- The range of pore throat radii is too wide compared with the possible column height. A method is required to narrow the range using data that is easily get from the exploration work. Since well-logs data relate to the macroscopic properties of rocks (porosity, permeability, water content, etc.), and these properties relate to effective pore throat radii and retention capacity, in this study it is assumed to be a correlation between well-logs data and pore throat radii. With expanded dataset, it is assumed a reliable, fixed relationship could be found between well-logs data and pore throat radii. With this correlation, a more precise sealing capacity of caprocks could be predicted. Mathematical models will be established to link the pore throat radius and well logging data in the future work.

- Overpressure has two distinctive effects on seal effectiveness: firstly, any overpressure in a mudstone will inhibit compaction resulting in higher porosities, larger pore throats and hence lower seal efficiency at any given depth. Secondly, differences in overpressures between the reservoirs and overlying seal will affect the critical balance between buoyancy and capillary resistance. This can dramatically increase seal efficiency. The investigations on how the overpressure could react on the effective pore throat radii could be included in the future work plan, to test whether overpressure is enhancing or damaging the effective pore throat radii and the sealing capacity.

- The correlation between faulting degree and the effective pore throat radii is merited further discussion. More details are required rather than just the presence or absence of faults. Other parameters should also be taken into account, such as conductivity, formation, age, displacement and compartmentation.

- Although using natural analogues for geological carbon storage enables us to investigate and predict the leakage potential from a storage site in a geological spatial and temporal scale, the leakage potential from other pathways need to be carefully investigated, such as the leakage potential from injection wells and other wells. The configurations for injection wells, the rate and pressure of injection, the pressure/temperature conditions of the storage sites, etc are significant parameters to check for the leakage potential. The choice for material should consider about the corrosion condition and desired injection rate. The integrity of wells should be monitored and tested during and post injection to ensure the CO_2 is sealed with cement and plugs. Previous study highlight that abandoned wells have greater leakage potential than faults (Burnside et al., 2013).

- For a real storage project, the thermal effects on field stress and fracturing need to be analysed because the injected CO_2 is normally much cooler than reservoir temperature. The temperature drop gives rise to changes of field stress around well boles and results in thermal fracturing. In real injection cases, other impurities produced from the industrial processes (hydrogen, nitrogen and sulphur oxides) might also cause deviations from pure SC-CO_2 regime.

Reference

ABBOTTS, I. 1991. United Kingdom oil and gas fields: 25-years commemorative volume.

ABDUL-MAJEED, G. H. & ABU AL-SOOF, N. B. 2000. Estimation of gas–oil surface tension. *Journal of Petroleum Science and Engineering,* 27**,** 197-200.

ADAMSON, A. W. & GAST, A. P. 1967. Physical chemistry of surfaces.

AMANN, A., WASCHBÜSCH, M., BERTIER, P., BUSCH, A., KROOSS, B. M. & LITTKE, R. 2011. Sealing rock characteristics under the influence of CO< sub> 2</sub>. *Energy Procedia,* 4**,** 5170-5177.

AMANN-HILDENBRAND, A., BERTIER, P., BUSCH, A. & KROOSS, B. M. 2013. Experimental investigation of the sealing capacity of generic clay-rich caprocks. *International Journal of Greenhouse Gas Control,* 19**,** 620-641.

AMUNDSON, R. & KELLY, E. 1987. The chemistry and mineralogy of a CO2-rich travertine depositing spring in the California Coast Range. *Geochimica et Cosmochimica Acta,* 51**,** 2883-2890.

ANDERSON, W. G. 1987. Wettability literature survey-part 4: Effects of wettability on capillary pressure. *Journal of Petroleum Technology,* 39**,** 1,283-1,300.

ASCHENBRENNER, B. C. & ACHAUER, C. W. 1960. Minimum conditions for migration of oil in water-wet carbonate rocks. *AAPG Bulletin,* 44**,** 235-243.

ASSAYAG, N., BICKLE, M., KAMPMAN, N. & BECKER, J. 2009. Carbon isotopic constraints on CO< sub> 2</sub> degassing in cold-water Geysers, Green River, Utah. *Energy Procedia,* 1**,** 2361-2366.

BACCI, G., KORRE, A. & DURUCAN, S. 2011. An experimental and numerical investigation into the impact of dissolution/precipitation mechanisms on CO 2 injectivity in the wellbore and far field regions. *International Journal of Greenhouse Gas Control,* 5**,** 579-588.

BACHU, S. 2002. Sequestration of CO 2 in geological media in response to climate change: road map for site selection using the transform of the geological space into the CO 2 phase space. *Energy Conversion and management,* 43**,** 87-102.

BACHU, S. & BENNION, B. 2008. Effects of in-situ conditions on relative permeability characteristics of CO2-brine systems. *Environmental Geology,* 54**,** 1707-1722.

BADLEY, M., PRICE, J., DAHL, C. R. & AGDESTEIN, T. 1988. The structural evolution of the northern Viking Graben and its bearing upon extensional modes of basin formation. *Journal of the Geological Society,* 145**,** 455-472.

BAER, J. L. & RIGBY, J. K. 1978. Geology of the Crystal Geyser and environmental implications of its effluent, Grand County, Utah. *Utah Geology,* 5**,** 125-130.

BAINES, S. J. & WORDEN, R. H. 2004. The long-term fate of CO2 in the subsurface: natural analogues for CO2 storage. *Geological Society, London, Special Publications,* 233**,** 59-85.

BAKER, O. & SWERDLOFF, W. 1956. Finding surface tension of hydrocarbon liquids. *Oil & Gas Journal,* 2**,** 125-128.

BALDWIN, B. & O. BULTER, C. 1985. Compaction Curves. *The American Association of Petroleum Geologists Bulletin,* 69**,** 622-626.

BARBEAU, D. 2003. A flexural model for the Paradox Basin: implications for the tectonics of the Ancestral Rocky Mountains. *Basin Research,* 15**,** 97-115.

BARNARD, P. & COOPER, B. 1981. Oils and source rocks of the North Sea area. *Petroleum geology of the Continental shelf of North West Europe,* 169**,** 75.

BARTH, J. A. 2012. Crystal Geyser, Utah: Active Travertine Deposits of a Cold-water Carbon Dioxide-driven Geyser and Related Ancient Deposits of the Little Grand Wash Fault.
BAUMGARTNER, L. P. & VALLEY, J. W. 2001. Stable isotope transport and contact metamorphic fluid flow. *Reviews in Mineralogy and Geochemistry,* 43**,** 415-467.
BEN-DAVID, M., FLYNN, R. & SCHELL, D. 1997. Annual and seasonal changes in diets of martens: evidence from stable isotope analysis. *Oecologia,* 111**,** 280-291.
BENSON, S. M. & COLE, D. R. 2008. CO2 sequestration in deep sedimentary formations. *Elements,* 4**,** 325-331.
BERG, R. R. 1975. Capillary pressures in stratigraphic traps. *AAPG bulletin,* 59**,** 939-956.
BERNER, R. A. 1984. Sedimentary pyrite formation: an update. *Geochimica et Cosmochimica Acta,* 48**,** 605-615.
BLAKEY, R. C. 1974. Stratigraphic and depositional analysis of the Moenkopi Formation, southeastern Utah.
BORST, R. L. 1982. Some effects of compaction and geological time on the pore parameters of argillaceous rocks. *Sedimentology,* 29**,** 291-298.
BOULIN, P., BRETONNIER, P., GLAND, N. & LOMBARD, J. Low water permeability measurements of clay sample. Contribution of steady state method compared to transient methods. International Symposium of the Society of Core Analysts, Halifax, Nova Scotia, Canada, 2010.
BRACKBILL, J., KOTHE, D. B. & ZEMACH, C. 1992. A continuum method for modeling surface tension. *Journal of computational physics,* 100**,** 335-354.
BRAND, U. & VEIZER, J. 1983. Origin of coated grains: trace element constraints. *Coated Grains.* Springer.
BRUCE, W. & WELGE, H. The Restored-State Method for Determination of Oil in Place and Connate Water. Drilling and Production Practice, 1947. American Petroleum Institute.
BURNSIDE, N. 2010. U-Th dating of travertine on the Colorado Plateau: Implications for the leakage of geologically stored CO2 [Ph. D. thesis].
BURNSIDE, N. M., SHIPTON, Z. K., DOCKRILL, B. & ELLAM, R. M. 2013. Man-made versus natural CO2 leakage: A 400 ky history of an analogue for engineered geological storage of CO2. *Geology,* 41**,** 471-474.
BURRUSS, R. C. 2009. Development of a probabilistic assessment methodology for evaluation of carbon dioxide storage.
BUSCH, A. & AMANN-HILDENBRAND, A. 2013. Predicting capillarity of mudrocks. *Marine and petroleum geology,* 45**,** 208-223.
BUSENBERG, E. & NIEL PLUMMER, L. 1985. Kinetic and thermodynamic factors controlling the distribution of SO< sub> 3</sub>< sup> 2−</sup> and Na< sup>+</sup> in calcites and selected aragonites. *Geochimica et Cosmochimica Acta,* 49**,** 713-725.
BÉNÉZETH, P., PALMER, D. A., ANOVITZ, L. M. & HORITA, J. 2007. Dawsonite synthesis and reevaluation of its thermodynamic properties from solubility measurements: Implications for mineral trapping of CO 2. *Geochimica et Cosmochimica Acta,* 71**,** 4438-4455.
CAILLY, B., LE THIEZ, P., EGERMANN, P., AUDIBERT, A., VIDAL-GILBERT, S. & LONGAYGUE, X. 2005. Geological storage of CO2: A state-of-the-art of injection processes and technologies. *Oil & gas science and technology,* 60**,** 517-525.
CAINE, J. S., EVANS, J. P. & FORSTER, C. B. 1996. Fault zone architecture and permeability structure. *Geology,* 24**,** 1025-1028.

CAPPA, J. A. & RICE, D. D. 1995. Carbon dioxide in Mississippian rocks of the Paradox Basin and adjacent areas, Colorado, Utah, New Mexico, and Arizona.
CAROTHERS, W. W. & KHARAKA, Y. K. 1978. Aliphatic acid anions in oil-field waters--implications for origin of natural gas. *AAPG Bulletin,* 62**,** 2441-2453.
CATER, F. W. & CRAIG, L. C. 1970. Geology of the Salt Anticline region in southwestern Colorado, with a section on stratigraphy. US Govt. Print. Off.
CHADWICK, A., ARTS, R., BERNSTONE, C., MAY, F., THIBEAU, S. & ZWEIGEL, P. 2008. *Best Practice for the Storage of CO2 in Saline Aquifers-Observations and Guidelines from the SACS and CO2STORE projects*, British Geological Survey.
CHALMERS, G. R. & BUSTIN, R. M. 2012. Geological evaluation of Halfway–Doig–Montney hybrid gas shale–tight gas reservoir, northeastern British Columbia. *Marine and Petroleum Geology,* 38**,** 53-72.
CHAN, M. A., PARRY, W. & BOWMAN, J. 2000. Diagenetic hematite and manganese oxides and fault-related fluid flow in Jurassic sandstones, southeastern Utah. *AAPG bulletin,* 84**,** 1281-1310.
CHIQUET, P., BROSETA, D. & THIBEAU, S. 2007. Wettability alteration of caprock minerals by carbon dioxide. *Geofluids,* 7**,** 112-122.
CHOU, L., GARRELS, R. M. & WOLLAST, R. 1989. Comparative study of the kinetics and mechanisms of dissolution of carbonate minerals. *Chemical Geology,* 78**,** 269-282.
CLARK, I. D. & FRITZ, P. 1997. *Environmental isotopes in hydrogeology*, CRC press.
CLAYTON, C. & HAY, S. 1994. Gas migration mechanisms from accumulation to surface. *Bulletin of the Geological Society of Denmark,* 41**,** 12-23.
CLAYTON, R. N. & DEGENS, E. T. 1959. Use of carbon isotope analyses of carbonates for differentiating fresh-water and marine sediments. *AAPG Bulletin,* 43**,** 890-897.
COBBAN, W. 1976. Ammonite record from the Mancos Shale of the Castle Valley-Price-Woodside area, east-central Utah. *Brigham Young University Geology Studies,* 22**,** 117-26.
COLE, R. D., YOUNG, R. G. & WILLIS, G. C. 1997. The Prairie Canyon Member, a New Unit of the Upper Cretaceous Mancos Shale, West-Central Colorado and East-Central Utah (MP-97-4).
COLLINS, M., KNUTTI, R., ARBLASTER, J., DUFRESNE, J.-L., FICHEFET, T., FRIEDLINGSTEIN, P., GAO, X., GUTOWSKI, W., JOHNS, T. & KRINNER, G. 2013. Long-term climate change: projections, commitments and irreversibility.
CONDON, S. M. & HUFFMAN, A. 1997. Geology of the Pennsylvanian and Permian cutler group and Permian Kaibab limestone in the Paradox Basin, southeastern Utah and southwestern Colorado.
COOPER, C. 2009. A Technical Basis for Carbon Dioxide Storage CO2 Capture Project. Energy Procedia.
CRANGANU, C. & VILLA, M. A. 2005. Capillary sealing as an overpressure mechanism in the Anadarko basin. *AAPG Ann Conv Calgary, Alberta*.
CROWLEY, S. S., STANTON, R. W. & RYER, T. A. 1989. The effects of volcanic ash on the maceral and chemical composition of the C coal bed, Emery Coal Field, Utah. *Organic Geochemistry,* 14**,** 315-331.
CUREWITZ, D. & KARSON, J. A. 1997. Structural settings of hydrothermal outflow: Fracture permeability maintained by fault propagation and interaction. *Journal of Volcanology and Geothermal Research,* 79**,** 149-168.
CURTIS, C. D. 1995. Post-depositional evolution of mudstones l: early days and parental influences. *Journal of the Geological Society,* 152**,** 577-586.

DA ROCHA, S. R., HARRISON, K. L. & JOHNSTON, K. P. 1999. Effect of surfactants on the interfacial tension and emulsion formation between water and carbon dioxide. *Langmuir,* 15**,** 419-428.
DANESH, A. 1998. *PVT and phase behaviour of petroleum reservoir fluids*, Elsevier.
DANIEL, R. F. & KALDI, J. G. Evaluating seal capacity of caprocks and intraformational barriers for the geosequestration of CO2. Eastern Australasian Basins Symposium (3rd: 2008: Sydney, Australia) EABS III, 2008.
DEINES, P., LANGMUIR, D. & HARMON, R. S. 1974. Stable carbon isotope ratios and the existence of a gas phase in the evolution of carbonate ground waters. *Geochimica et Cosmochimica Acta,* 38**,** 1147-1164.
DEWHURST, D. N., JONES, R. M. & RAVEN, M. D. 2002. Microstructural and petrophysical characterization of Muderong Shale: application to top seal risking. *Petroleum Geoscience,* 8**,** 371-383.
DNV 2010. Design and operation of CO2 pipelines: recommended practice DNV-RP-J202. Norway.
DOCKRILL, B. 2006. *Understanding leakage from a fault-sealed CO2 reservoir in East-Central Utah: a natural analogue applicable to CO2 storage.* Trinity College Dublin.
DOCKRILL, B. & SHIPTON, Z. K. 2010. Structural controls on leakage from a natural CO< sub> 2</sub> geologic storage site: Central Utah, USA. *Journal of Structural Geology,* 32**,** 1768-1782.
DOELLING, H. H., OVIATT, C. G. & HUNTOON, P. W. 1988. *Salt deformation in the Paradox region*, Utah Geological Survey.
DOREMUS, R. 1958. Precipitation kinetics of ionic salts from solution. *The Journal of Physical Chemistry,* 62**,** 1068-1075.
DUCHATEAU, C. & BROSETA, D. 2012. A simple method for determining brine–gas interfacial tensions. *Advances in Water Resources,* 42**,** 30-36.
DUCHI, V., GIORDANO, M. & MARTINI, M. 1978. Riesame del problema della precipitatzione di calcite od aragonite da soluzioni naturali. *Rend. Soc. Ital. Mineral. Petrol,* 34**,** 605-618.
DULLIEN, F. A. 2012. *Porous media: fluid transport and pore structure*, Academic press.
EATON, B. A. The equation for geopressure prediction from well logs. Fall meeting of the Society of Petroleum Engineers of AIME, 1975. Society of Petroleum Engineers.
EATON, J. G., KIRKLAND, J. I. & KAUFFMAN, E. G. 1990. Evidence and dating of mid-Cretaceous tectonic activity in the San Rafael Swell, Emery County, Utah. *The Mountain Geologist*.
EICHHUBL, P., GREENE, H., NAEHR, T. & MAHER, N. 2000. Structural control of fluid flow: offshore fluid seepage in the Santa Barbara Basin, California. *Journal of Geochemical Exploration,* 69**,** 545-549.
ENEYOK, G., BUSSINK, P. & MAAN, A. 2003. The Curlew Field, Block 29/7, UK North Sea. *Geological Society, London, Memoirs,* 20**,** 509-522.
EPSTEIN, S. 1959. The variations of the 18O/16O ratios in nature and some geologic implications. *Researches in Geochemistry. Wiley, New York***,** 217-240.
ESCHNER, T. B. & KOCUREK, G. 1986. Marine destruction of eolian sand seas: origin of mass flows. *Journal of Sedimentary Research,* 56.
ESPINOZA, D., KIM, S. & SANTAMARINA, J. 2011. CO2 geological storage—geotechnical implications. *KSCE Journal of Civil Engineering,* 15**,** 707-719.

ESPINOZA, D. N. & SANTAMARINA, J. C. 2010. Water-CO2-mineral systems: Interfacial tension, contact angle, and diffusion—Implications to CO2 geological storage. *Water resources research,* 46**,** W07537.

FAULKNER, D., JACKSON, C., LUNN, R., SCHLISCHE, R., SHIPTON, Z., WIBBERLEY, C. & WITHJACK, M. 2010. A review of recent developments concerning the structure, mechanics and fluid flow properties of fault zones. *Journal of Structural Geology,* 32**,** 1557-1575.

FEIN, J. B. 1994. Porosity enhancement during clastic diagenesis as a result of aqueous metal-carboxylate complexation: Experimental studies. *Chemical Geology,* 115**,** 263-279.

FIROOZABADI, A. & RAMEY JR, H. J. 1988. Surface tension of water-hydrocarbon systems at reservoir conditions. *Journal of Canadian Petroleum Technology,* 27.

FOLK, R. L. 1994. Interaction between bacteria, nannobacteria, and mineral precipitation in hot springs of central Italy. *Géographie physique et Quaternaire,* 48**,** 233-246.

FRERY, E., GRATIER, J.-P., ELLOUZ-ZIMMERMAN, N., LOISELET, C., BRAUN, J., DESCHAMPS, P., BLAMART, D., HAMELIN, B. & SWENNEN, R. 2015. Evolution of fault permeability during episodic fluid circulation: Evidence for the effects of fluid–rock interactions from travertine studies (Utah–USA). *Tectonophysics,* 651**,** 121-137.

GARDEN, I., GUSCOTT, S., BURLEY, S., FOXFORD, K., WALSH, J. & MARSHALL, J. 2001. An exhumed palaeo‐hydrocarbon migration fairway in a faulted carrier system, Entrada Sandstone of SE Utah, USA. *Geofluids,* 1**,** 195-213.

GARRELS, R. M. & LERMAN, A. 1981. Phanerozoic cycles of sedimentary carbon and sulfur. *Proceedings of the National Academy of Sciences,* 78**,** 4652-4656.

GEORGIADIS, A., MAITLAND, G., TRUSLER, J. M. & BISMARCK, A. 2010. Interfacial tension measurements of the (H2O+ CO2) system at elevated pressures and temperatures. *Journal of Chemical & Engineering Data,* 55**,** 4168-4175.

GILLETT, N. P., ARORA, V. K., MATTHEWS, D. & ALLEN, M. R. 2013. Constraining the ratio of global warming to cumulative CO2 emissions using CMIP5 simulations. *Journal of Climate,* 26**,** 6844-6858.

GIVEN, R. K. & WILKINSON, B. H. 1985. Kinetic control of morphology, composition, and mineralogy of abiotic sedimentary carbonates. *Journal of Sedimentary Research,* 55.

GLENNON, J. A. & PFAFF, R. M. 2005. The operation and geography of carbon dioxide-driven, cold-water “geysers”. *GOSA Trans,* 9**,** 184-192.

GLUYAS, J. G. & HICHENS, H. M. 2003. *United Kingdom oil and gas fields: commemorative millennium volume*, Geological Society.

GOLDSTEIN, H. L., REYNOLDS, R. L., REHEIS, M. C., YOUNT, J. C. & NEFF, J. C. 2008. Compositional trends in aeolian dust along a transect across the southwestern United States. *Journal of Geophysical Research: Earth Surface,* 113.

GOUVEIA, F. & FRIEDMANN, S. 2006. *Timing and prediction of CO2 eruptions from Crystal Geyser, UT*, United States. Department of Energy.

GRATIER, J.-P., FRERY, E., DESCHAMPS, P., RØYNE, A., RENARD, F., DYSTHE, D., ELLOUZ-ZIMMERMAN, N. & HAMELIN, B. 2012. How travertine veins grow from top to bottom and lift the rocks above them: The effect of crystallization force. *Geology,* 40**,** 1015-1018.

GRIFFITH, C. A., DZOMBAK, D. A. & LOWRY, G. V. 2011. Physical and chemical characteristics of potential seal strata in regions considered for demonstrating geological saline CO2 sequestration. *Environmental Earth Sciences,* 64**,** 925-948.

GROSSMAN, E. L. & KU, T.-L. 1986. Oxygen and carbon isotope fractionation in biogenic aragonite: temperature effects. *Chemical Geology: Isotope Geoscience section,* 59**,** 59-74.

GUNTER, W., WIWEHAR, B. & PERKINS, E. 1997. Aquifer disposal of CO2-rich greenhouse gases: extension of the time scale of experiment for CO2-sequestering reactions by geochemical modelling. *Mineralogy and Petrology,* 59**,** 121-140.

HAN, W. S., LU, M., MCPHERSON, B. J., KEATING, E., MOORE, J., PARK, E., WATSON, Z. & JUNG, N. H. 2013. Characteristics of CO2-driven cold-water geyser, Crystal Geyser in Utah: experimental observation and mechanism analyses. *Geofluids,* 13**,** 283-297.

HANCOCK, P., CHALMERS, R., ALTUNEL, E. & CAKIR, Z. 1999. Travitonics: using travertines in active fault studies. *Journal of Structural Geology,* 21**,** 903-916.

HASSLER, G. & BRUNNER, E. 1945. Measurement of capillary pressures in small core samples. *Transactions of the AIME,* 160**,** 114-123.

HASZELDINE, R., QUINN, O., ENGLAND, G., WILKINSON, M., SHIPTON, Z., EVANS, J. P., HEATH, J., CROSSEY, L., BALLENTINE, C. & GRAHAM, C. 2005. Natural geochemical analogues for carbon dioxide storage in deep geological porous reservoirs, a United Kingdom perspective. *Oil & gas science and technology,* 60**,** 33-49.

HAZEL JR, J. E. 1994. Sedimentary response to intrabasinal salt tectonism in the Upper Triassic Chinle Formation, Paradox basin, Utah. USGPO; For sale by US Geological Survey, Map Distribution.

HEATH, J. E., LACHMAR, T. E., EVANS, J. P., KOLESAR, P. T. & WILLIAMS, A. P. 2009. Hydrogeochemical Characterization of Leaking, Carbon Dioxide-Charged Fault Zones in East-Central Utah, With Implications for Geologic Carbon Storage. *Carbon Sequestration and Its Role in the Global Carbon Cycle***,** 147-158.

HEATH, J. E., LACHMAR, T. E., EVANS, J. P., KOLESAR, P. T., WILLIAMS, A. P. & NELSON, S. T. 2004. Hydrogeochemical characterization of leaking carbon dioxide-charged fault zones in east-central Utah.

HENDRY, J. P., WILKINSON, M., FALLICK, A. E. & TREWIN, N. H. 2000. Disseminated 'jigsaw piece'dolomite in Upper Jurassic shelf sandstones, Central North Sea: an example of cement growth during bioturbation? *Sedimentology,* 47**,** 631-644.

HILDENBRAND, A., SCHLÖMER, S. & KROOSS, B. 2002. Gas breakthrough experiments on fine-grained sedimentary rocks. *Geofluids,* 2**,** 3-23.

HILDENBRAND, A., SCHLÖMER, S., KROOSS, B. & LITTKE, R. 2004. Gas breakthrough experiments on pelitic rocks: comparative study with N2, CO2 and CH4. *Geofluids,* 4**,** 61-80.

HILLS, G. & HØILAND, H. 1984. Pressure dependence of the surface tension of mercury. *Journal of colloid and interface science,* 99**,** 463-467.

HITCHON, B., GUNTER, W., GENTZIS, T. & BAILEY, R. 1999. Sedimentary basins and greenhouse gases: a serendipitous association. *Energy Conversion and Management,* 40**,** 825-843.

HOLLAND, H., HOLLAND, H. & MUNOZ, J. 1964. The coprecipitation of cations with CaCO 3—II. The coprecipitation of Sr+ 2 with calcite between 90° and 100° C. *Geochimica et Cosmochimica Acta,* 28**,** 1287-1301.

HOOD, J. W. & PATTERSON, D. J. 1984. Bedrock aquifers in the northern San Rafael Swell area, Utah, with special emphasis on the Navajo Sandstone. Utah Department of Natural Resources.

HUDSON, J. 1977. Stable isotopes and limestone lithification. *Journal of the Geological Society,* 133**,** 637-660.
HUNT, C. B. 1956. Cenozoic geology of the Colorado Plateau.
ICHIKUNI, M. 1973. Partition of strontium between calcite and solution: effect of substitution by manganese. *Chemical Geology,* 11**,** 315-319.
IEA 2008. Energy technology perspectives. *In:* IEA/OECD (ed.). Paris.
IPCC 2005. Carbon Dioxide Capture and Storage: special report of the intergovernmental panel on climate change. Cambridge, UK and New York: Cambridge University Press.
IRWIN, C. D. 1971. Stratigraphic analysis of Upper Permian and Lower Triassic strata in southern Utah. *AAPG Bulletin,* 55**,** 1976-2007.
IRWIN, H., CURTIS, C. & COLEMAN, M. 1977. Isotopic evidence for source of diagenetic carbonates formed during burial of organic-rich sediments.
JIMÉNEZ-MORENO, G., SCOTT ANDERSON, R. & FAWCETT, P. J. 2007. Orbital-and millennial-scale vegetation and climate changes of the past 225ka from Bear Lake, Utah–Idaho (USA). *Quaternary Science Reviews,* 26**,** 1713-1724.
JOHNSON, J., NITAO, J., STEEFEL, C. & KNAUSS, K. Reactive transport modeling of geologic CO 2 sequestration in saline aquifers. The Influence of Intra-Aquifer Shales and the Relative Effectiveness of Structural, Solubility, and Mineral Trapping During Prograde and Retrograde Sequestration. Washington: First National Conference on Carbon Sequestration, 2001.
KALDI, J. & ATKINSON, C. 1997. Evaluating seal potential: example from the Talang Akar Formation, offshore northwest Java, Indonesia. *MEMOIRS-AMERICAN ASSOCIATION OF PETROLEUM GEOLOGISTS***,** 85-102.
KAMPMAN, N., BICKLE, M., BECKER, J., ASSAYAG, N. & CHAPMAN, H. 2009. Feldspar dissolution kinetics and Gibbs free energy dependence in a CO 2-enriched groundwater system, Green River, Utah. *Earth and Planetary Science Letters,* 284**,** 473-488.
KAMPMAN, N., BICKLE, M., WIGLEY, M. & DUBACQ, B. 2014. Fluid flow and CO 2–fluid–mineral interactions during CO 2-storage in sedimentary basins. *Chemical Geology,* 369**,** 22-50.
KAMPMAN, N., BURNSIDE, N. M., SHIPTON, Z. K., CHAPMAN, H. J., NICHOLL, J. A., ELLAM, R. M. & BICKLE, M. J. 2012. Pulses of carbon dioxide emissions from intracrustal faults following climatic warming. *Nature Geoscience,* 5**,** 352.
KATSUBE, T. & ISSLER, D. 1993. Pore-size distributions of shales from the Beaufort-Mackenzie Basin, northern Canada. *PAPERS-GEOLOGICAL SURVEY OF CANADA***,** 123-123.
KATSUBE, T., MUDFORD, B. S. & BEST, M. 1991. Petrophysical characteristics of shales from the Scotian shelf. *Geophysics,* 56**,** 1681-1689.
KAUFFMAN, E. G. 1975. Dispersal and biostratigraphic potential of Cretaceous benthonic Bivalvia in the Western Interior. *The Cretaceous System in the Western Interior of North America. Geological Association of Canada Special Paper,* 13**,** 311-381.
KEITH, M. & WEBER, J. 1964. Carbon and oxygen isotopic composition of selected limestones and fossils. *Geochimica et Cosmochimica Acta,* 28**,** 1787-1816.
KELLEY, V. C. 1958. Tectonics of the region of the Paradox Basin.
KIM, S.-T., AMP, AMP, APOS & NEIL, J. R. 1997. Equilibrium and nonequilibrium oxygen isotope effects in synthetic carbonates. *Geochimica et Cosmochimica Acta,* 61**,** 3461-3475.

KITANO, Y. 1963. Geochemistry of calcareous deposits found in hot springs. *The Journal of earth sciences, Nagoya University,* 11**,** 68-100.
KITANO, Y., KANAMORI, N. & OOMORI, T. 1971. Measurements of distribution coefficients and barium between carbonate precipitate—Abnormally high values of distribution measured at early stages of carbonate of strontium and solution coefficients formation. *Geochemical Journal,* 4**,** 183-206.
KITANO, Y., KANAMORI, N., TOKUYAMA, A. & COMORI, T. Factors controlling the trace-element contents of marine carbonate skeletons. Proceeding of Symposium on Hydrogeochemistry and Biogeochemistry, The Clarke Co, Washington, DC, 1973. 484-499.
KITANO, Y., OKUMURA, M. & IDOGAKI, M. 1975. Incorporation of sodium, chloride and sulfate with calcium carbonate. *Geochemical Journal,* 9**,** 75-84.
KITANO, Y., TOKUYAMA, A. & KANAMORI, N. 1968. Measurement of the distribution coefficient of zinc and copper between carbonate procipitate and solution. *The Journal of earth sciences, Nagoya University,* 16**,** 1-102.
KLEIN, J. S., MOZLEY, P., CAMPBELL, A. & COLE, R. 1999. Spatial distribution of carbon and oxygen isotopes in laterally extensive carbonate-cemented layers: implications for mode of growth and subsurface identification. *Journal of Sedimentary Research,* 69.
KOLODZIE JR, S. Analysis Of Pore Throat Size And Use Of The Waxman-Smits Equation To Determine Ooip In Spindle Field Colorado. SPE Annual Technical Conference and Exhibition, 1980. Society of Petroleum Engineers.
LAHANN, R. W. 1978. A chemical model for calcite crystal growth and morphology control. *Journal of Sedimentary Research,* 48**,** 337-347.
LASH, G. G. 2006. Top seal development in the shale-dominated Upper Devonian Catskill delta complex, western New York state. *Marine and Petroleum Geology,* 23**,** 317-335.
LENORMAND, R. & ZARCONE, C. Role of roughness and edges during imbibition in square capillaries. SPE annual technical conference and exhibition, 1984. Society of Petroleum Engineers.
LI, S., DONG, M., LI, Z., HUANG, S., QING, H. & NICKEL, E. 2005. Gas breakthrough pressure for hydrocarbon reservoir seal rocks: implications for the security of long-term CO2 storage in the Weyburn field. *Geofluids,* 5**,** 326-334.
LIU, B. 2011. *Development of China oil and gas fields commemorative millennium volume-East South China Sea,* Beijing, Petroleum industry.
LOUCKS, R. G., REED, R. M., RUPPEL, S. C. & JARVIE, D. M. 2009. Morphology, genesis, and distribution of nanometer-scale pores in siliceous mudstones of the Mississippian Barnett Shale. *Journal of Sedimentary Research,* 79**,** 848-861.
LU, J., WILKINSON, M., HASZELDINE, R. S. & FALLICK, A. E. 2009. Long-term performance of a mudrock seal in natural CO2 storage. *Geology,* 37**,** 35-38.
LUCCHITTA, I. 1979. Late cenozoic uplift of the southwestern colorado plateau and adjacent lower colorado river region. *Tectonophysics,* 61**,** 63-95.
MACKIN, J. E. & ALLER, R. C. 1984. Diagenesis of dissolved aluminum in organic-rich estuarine sediments. *Geochimica et Cosmochimica Acta,* 48**,** 299-313.
MALESANI, P. & VANNUCCI, S. 1975. Precipitazione di calcite o di aragonite dalle acque termominerali in relazione alla genesi e all'evoluzione dei travertini. *Accademia Lincell, Rendiconti Scienze fisica, matematica e naturale,* 58**,** 761-776.
MARTINEZ, S. 1976. Reports of hot spring activity in theYellowstone National Parck for 1976.

MAYO, A. L., SHRUM, D. B. & CHIDSEY JR, T. C. 1991. Factors contributing to exsolving carbon dioxide in ground water systems in the Colorado Plateau, Utah.
MCCULLOUGH, J., ALBAUGH, F. & JONES, P. Determination of the interstitial-water content of oil and gas sand by laboratory tests of core samples. Drilling and Production Practice, 1944. American Petroleum Institute.
MCINTIRE, W. 1963. Trace element partition coefficients—a review of theory and applications to geology. *Geochimica et Cosmochimica Acta,* 27**,** 1209-1264.
MICHAEL A. ARTHUR, T. F. A., ISAAC R. KAPLAN, JAN VEIZER, LYNTON S. LAND 1983. *Stable isotopes in sedimentary geology,* Dallas, SEPM.
MICHAEL, K., GOLAB, A., SHULAKOVA, V., ENNIS-KING, J., ALLINSON, G., SHARMA, S. & AIKEN, T. 2010. Geological storage of CO< sub> 2</sub> in saline aquifers—A review of the experience from existing storage operations. *International Journal of Greenhouse Gas Control,* 4**,** 659-667.
MICHALOPOULOS, P. & ALLER, R. C. 2004. Early diagenesis of biogenic silica in the Amazon delta: alteration, authigenic clay formation, and storage. *Geochimica et Cosmochimica Acta,* 68**,** 1061-1085.
MICKLETHWAITE, S. & COX, S. F. 2004. Fault-segment rupture, aftershock-zone fluid flow, and mineralization. *Geology,* 32**,** 813-816.
MOLENAAR, C. 1981. Mesozoic stratigraphy of the Paradox Basin-an overview.
MOLENAAR, C. M. & COBBAN, W. A. 1991. Middle Cretaceous stratigraphy on the south and east sides of the Uinta Basin, northeastern Utah and northwestern Colorado.
MURRAY, C. 1989. The cold water geyser of Utah, II: observation of Crystal Geyser. *The Geyser Observation and Study Association,* 2**,** 133-9.
NADEAU, P. 2011. Earth's energy "Golden Zone": a synthesis from mineralogical research. *Clay Minerals,* 46**,** 1-24.
NADEAU, P. H. & REYNOLDS, R. C. 1981. Burial and contact metamorphism in the Mancos Shale. *Clays and Clay Minerals,* 29**,** 249-259.
NAYLOR, M., WILKINSON, M. & HASZELDINE, R. 2011. Calculation of CO< sub> 2</sub> column heights in depleted gas fields from known pre-production gas column heights. *Marine and Petroleum Geology,* 28**,** 1083-1093.
NELLEON, M. 1952. *Mechanics and properties of matter,* London.
NELSON, P. H. 2009. Pore-throat sizes in sandstones, tight sandstones, and shales. *AAPG bulletin,* 93**,** 329-340.
NOIRIEL, C., RENARD, F., DOAN, M.-L. & GRATIER, J.-P. 2010. Intense fracturing and fracture sealing induced by mineral growth in porous rocks. *Chemical Geology,* 269**,** 197-209.
NUCCIO, V. F. & CONDON, S. M. 1996. Burial and thermal history of the Paradox Basin, Utah and Colorado, and petroleum potential of the Middle Pennsylvanian Paradox Basin.
OLDENBURG, C. M. 2007. Joule-Thomson cooling due to CO 2 injection into natural gas reservoirs. *Energy Conversion and Management,* 48**,** 1808-1815.
PENTECOST, A. 2005a. Mineralogy and Elemental Composition. *Travertine.* London: Springer.
PENTECOST, A. 2005b. *Travertine,* Dordrecht, Springer Netherlands: Dordrecht.
PETERSON, F. 1969. Cretaceous sedimentation and tectonism in the southeastern Kaiparowits region, Utah. US Geological Survey].
PETERSON, F., RYDER, R. & LAW, B. 1980. Stratigraphy, sedimentology, and regional relationships of the Cretaceous system in the Henry Mountains region, Utah.

PEVEAR, D., VROLIJK, P. & LONGSTAFFE, F. 1997. Timing of Moab fault displacement and fluid movement integrated with burial history using radiogenic and stable isotopes. *Geofluids II,* 97**,** 42-45.
PHILLIPS, D. L. 2001. Mixing models in analyses of diet using multiple stable isotopes: a critique. *Oecologia,* 127**,** 166-170.
PITTMAN, E. D. 1992. Relationship of porosity and permeability to various parameters derived from mercury injection-capillary pressure curves for sandstone (1). *AAPG Bulletin,* 76**,** 191-198.
PITTMAN, E. D. & DUSCHATKO, R. W. 1970. Use of pore casts and scanning electron microscope to study pore geometry. *Journal of Sedimentary Research,* 40.
PURCELL, W. 1949. Capillary pressures-their measurement using mercury and the calculation of permeability therefrom. *Journal of Petroleum Technology,* 1**,** 39-48.
RAISWELL, R. & BRIMBLECOMBE, P. 1977. The partition of manganese into aragonite between 30 and 60 C. *Chemical Geology,* 19**,** 145-151.
RASTALL, R. H. 1926. Note on the geology of the Bath springs. *Geological Magazine,* 63**,** 98-104.
REN, Q.-Y., CHEN, G.-J., YAN, W. & GUO, T.-M. 2000. Interfacial tension of (CO2+ CH4)+ water from 298 K to 373 K and pressures up to 30 MPa. *Journal of Chemical & Engineering Data,* 45**,** 610-612.
RENARD, F., DYSTHE, D., FEDER, J., MEAKIN, P., MORRIS, S. & JAMTVEIT, B. 2009. Pattern formation during healing of fluid-filled cracks: an analog experiment. *Geofluids,* 9**,** 365-372.
REZAEE, M., JAFARI, A. & KAZEMZADEH, E. 2006. Relationships between permeability, porosity and pore throat size in carbonate rocks using regression analysis and neural networks. *Journal of Geophysics and Engineering,* 3**,** 370.
RICKARD, D. T. 1975. Kinetics and mechanism of pyrite formation at low temperatures. *American Journal of Science,* 275**,** 636-652.
RISACHER, F. & EUGSTER, H. P. 1979. Holocene pisoliths and encrustations associated with spring-fed surface pools, Pastos Grandes, Bolivia. *Sedimentology,* 26**,** 253-270.
RITCHIE, J. 2003. The Dunbar, Ellon and Grant Fields (Alwyn South Area), Blocks 3/8a, 3/9b, 3/13a, 3/14, 3/15, UK North Sea. *Geological Society, London, Memoirs,* 20**,** 265-281.
ROCHELLE, C., BATEMAN, K. & PEARCE, J. 2002. Geochemical interactions between supercritical CO2 and the Utsira Formation: an experimental study. *British Geological Survey Commissioned Report, CR/02/060,* 62.
ROMANEK, C. S., GROSSMAN, E. L. & MORSE, J. W. 1992. Carbon isotopic fractionation in synthetic aragonite and calcite: Effects of temperature and precipitation rate. *Geochimica et Cosmochimica Acta,* 56**,** 419-430.
ROSENBAUER, R., BISCHOFF, J. & KHARAKA, Y. 1992. Geochemical effects of deep-well injection of the Paradox Valley brine into Paleozoic carbonate rocks, Colorado, USA. *Applied geochemistry,* 7**,** 273-286.
ROSENBAUM, J. & SHEPPARD, S. 1986. An isotopic study of siderites, dolomites and ankerites at high temperatures. *Geochimica et cosmochimica acta,* 50**,** 1147-1150.
RUSH, F. E., WHITFIELD, M. & HART, I. 1982. Regional hydrology of the Green River-Moab area, northwestern Paradox basin, Utah. Geological Survey, Denver, CO (USA). Water Resources Div.
RYER, T. A. 1981. Deltaic coals of Ferron Sandstone Member of Mancos Shale: predictive model for Cretaceous coal-bearing strata of Western Interior. *AAPG Bulletin,* 65**,** 2323-2340.

SCHMIDT, K. A., FOLAS, G. K. & KVAMME, B. 2007. Calculation of the interfacial tension of the methane–water system with the linear gradient theory. *Fluid Phase Equilibria,* 261**,** 230-237.

SCHOLL, D. W. & TAFT, W. H. 1964. Algae, contributors to the formation of calcareous tufa, Mono Lake, California. *Journal of Sedimentary Research,* 34.

SCHOWALTER, T. T. 1979. Mechanics of secondary hydrocarbon migration and entrapment. *AAPG bulletin,* 63**,** 723-760.

SELLEY, R. C. 1998. *Elements of petroleum geology*, Gulf Professional Publishing.

SHACKLETON, N. & KENNETT, J. 1975. Late Cenozoic oxygen and carbon isotopic changes at DSDP Site 284: implications for glacial history of the Northern Hemisphere and Antarctica. *Initial reports of the deep sea drilling project,* 29**,** 801-807.

SHAH, V., BROSETA, D., MOURONVAL, G. & MONTEL, F. 2008. Water/acid gas interfacial tensions and their impact on acid gas geological storage. *International Journal of Greenhouse Gas Control,* 2**,** 594-604.

SHIPTON, Z. K., EVANS, J. P., DOCKRILL, B., HEATH, J., WILLIAMS, A., KIRCHNER, D. & KOLESAR, P. T. 2005. Natural Leaking CO< sub> 2</sub>-Charged Systems as Analogs for Failed Geologic Storage Reservoirs.

SHIPTON, Z. K., EVANS, J. P., KIRSCHNER, D., KOLESAR, P. T., WILLIAMS, A. P. & HEATH, J. 2004. Analysis of CO2 leakage through 'low-permeability'faults from natural reservoirs in the Colorado Plateau, east-central Utah. *Geological Society, London, Special Publications,* 233**,** 43-58.

SOLLIE, F. O. & RODGERS, S. G. Towards better measurements of logging depth. SPWLA 35th Annual Logging Symposium, 1994. Society of Petrophysicists and Well-Log Analysts.

SOLUM, J. G., DAVATZES, N. C. & LOCKNER, D. A. 2010. Fault-related clay authigenesis along the Moab Fault: Implications for calculations of fault rock composition and mechanical and hydrologic fault zone properties. *Journal of Structural Geology,* 32**,** 1899-1911.

SONG, J. & ZHANG, D. 2012. Comprehensive Review of Caprock-Sealing Mechanisms for Geologic Carbon Sequestration. *Environmental science & technology,* 47**,** 9-22.

SPANGLER, L. E. 1992. Records of wells in sandstone and alluvial aquifers and chemical data for water from selected wells in the Navajo aquifer in the vicinity of the Greater Aneth Oil Field, San Juan County, Utah. *Available from Books and Open File Report Section, USGS, Box 25425, Denver, CO 80225. USGS Open-File Report 92-124, 1992. 44 p, 10 fig, 8 tab, 6 ref. USGS Project*.

SPANGLER, L. E. 1996. *Hydrology, chemical quality, and characterization of salinity in the Navajo aquifer in and near the Greater Aneth Oil Field, San Juan County, Utah*, Salt Lake City, Utah: U.S. Dept. of the Interior, U.S. Geological Survey ; Denver, Colo.: U.S. Dept. of the Interior, U.S. Geological Survey.

SPEIGHT, J. G. 2005. *Lange's handbook of chemistry*, McGraw-Hill New York.

STEWART, J. H., POOLE, F. G., WILSON, R. F. & CADIGAN, R. 1972. Stratigraphy and origin of the Triassic Moenkopi Formation and related strata in the Colorado Plateau region, with a section on sedimentary petrology.

SWEENEY, R. & KAPLAN, I. 1973. Pyrite framboid formation; laboratory synthesis and marine sediments. *Economic Geology,* 68**,** 618-634.

SZEPANSKI, M., BEN-DAVID, M. & VAN BALLENBERGHE, V. 1999. Assessment of anadromous salmon resources in the diet of the Alexander Archipelago wolf using stable isotope analysis. *Oecologia,* 120**,** 327-335.

TABER, S. 1916. The growth of crystals under external pressure. *American Journal of Science*, 532-556.
TAGUCHI, K., HASEGAWA, K. & SUZUKI, T. 1988. The relationship between silica minerals and organic matter diagenesis: Its implication for the origin of oil. *Organic geochemistry,* 13, 97-107.
TAYLOR, K. & MACQUAKER, J. 2014. Diagenetic alterations in a silt-and clay-rich mudstone succession: an example from the Upper Cretaceous Mancos Shale of Utah, USA. *Clay Minerals,* 49, 213-227.
TAYLOR, K. G. & MACHENT, P. G. 2010. Systematic sequence-scale controls on carbonate cementation in a siliciclastic sedimentary basin: Examples from Upper Cretaceous shallow marine deposits of Utah and Coloradao, USA. *Marine and Petroleum Geology,* 27, 1297-1310.
THORNTON, O. & MARSHALL, D. 1947. Estimating interstitial water by the capillary pressure method. *Transactions of the AIME,* 170, 69-80.
THYBERG, B. & JAHREN, J. 2011. Quartz cementation in mudstones: sheet-like quartz cement from clay mineral reactions during burial. *Petroleum Geoscience,* 17, 53-63.
THYBERG, B., JAHREN, J., WINJE, T., BJØRLYKKE, K., FALEIDE, J. I. & MARCUSSEN, Ø. 2010. Quartz cementation in Late Cretaceous mudstones, northern North Sea: changes in rock properties due to dissolution of smectite and precipitation of micro-quartz crystals. *Marine and Petroleum Geology,* 27, 1752-1764.
TRIMBLE, L. M. & DOELLING, H. H. 1978. *Geology and uranium-vanadium deposits of the San Rafael River mining area, Emery County, Utah*, Utah Geological Survey.
TRUINI, M. 2003. *Hydrogeology of the D aquifer and movement and ages of ground water determined from geochemical and isotopic analyses, Black Mesa area, northeastern Arizona*, Tucson, Ariz.: U.S. Dept. of the Interior, U.S. Geological Survey ; Denver, CO: U.S. Dept. of the Interior, U.S. Geological Survey.
TRUONG, J. G. & WAYNER JR, P. C. 1987. Effects of capillary and van der Waals dispersion forces on the equilibrium profile of a wetting liquid: Theory and experiment. *The Journal of chemical physics,* 87, 4180-4188.
TUCKER, M. E. & WRIGHT, V. P. 1990. Carbonate mineralogy and chemistry. *Carbonate Sedimentology*, 284-313.
TURNER, C. E. & FISHMAN, N. S. 1991. Jurassic Lake T'oo'dichi': A large alkaline, saline lake, Morrison Formation, eastern Colorado Plateau. *Geological Society of America Bulletin,* 103, 538-558.
UREY, H. C. 1947. The thermodynamic properties of isotopic substances. *Journal of the Chemical Society (Resumed)*, 562-581.
UREY, H. C., LOWENSTAM, H. A., EPSTEIN, S. & MCKINNEY, C. R. 1951. Measurement of paleotemperatures and temperatures of the Upper Cretaceous of England, Denmark, and the southeastern United States. *Geological Society of America Bulletin,* 62, 399-416.
VAN DER PLUIJM, B. A., HALL, C. M., VROLIJK, P. J., PEVEAR, D. R. & COVEY, M. C. 2001. The dating of shallow faults in the Earth's crust. *Nature,* 412, 172-175.
VEIZER, J. 1983. Chemical diagenesis of carbonates: theory and application of trace element technique.
VEIZER, J. & HOEFS, J. 1976. The nature of O 18/O 16 and C 13/C 12 secular trends in sedimentary carbonate rocks. *Geochimica et Cosmochimica Acta,* 40, 1387-1395.

WASHBURN, E. W. 1921. Note on a method of determining the distribution of pore sizes in a porous material. *Proceedings of the National Academy of Sciences of the United States of America*, 115-116.
WHITE, A. F. 1977. Sodium and potassium coprecipitation in aragonite. *Geochimica et Cosmochimica Acta,* 41, 613-625.
WIEGAND, G. & FRANCK, E. 1994. Interfacial tension between water and non-polar fluids up to 473 K and 2800 bar. *Berichte der Bunsengesellschaft für physikalische Chemie,* 98, 809-817.
WILKINSON, M., CHEN, Z. & SHU, Y. 2014. Retention capacity of seals from hydrocarbon field analogues for appraisal of saline aquifers. *International Journal of Greenhouse Gas Control,* 28, 126-133.
WILKINSON, M., GILFILLAN, S. M., HASZELDINE, R. S. & BALLENTINE, C. J. 2009a. Plumbing the depths: testing natural tracers of subsurface CO2 origin and migration, Utah.
WILKINSON, M. & HASZELDINE, R. S. 2002. Fibrous illite in oilfield sandstones–a nucleation kinetic theory of growth. *Terra Nova,* 14, 56-60.
WILKINSON, M., HASZELDINE, R. S. & FALLICK, A. E. 2006. Hydrocarbon filling and leakage history of a deep geopressured sandstone, Fulmar Formation, United Kingdom North Sea. *AAPG bulletin,* 90, 1945-1961.
WILKINSON, M., HASZELDINE, R. S., FALLICK, A. E., ODLING, N., STOKER, S. J. & GATLIFF, R. W. 2009b. CO2–mineral reaction in a natural analogue for CO2 storage—implications for modeling. *Journal of Sedimentary Research,* 79, 486-494.
WINLAND, H. 1972. Oil accumulation in response to pore size changes, Weyburn field, Saskatchewan. *Amoco Production Company Research Department, F72-G-25*.
WOLLENWEBER, J., ALLES, S., BUSCH, A., KROOSS, B., STANJEK, H. & LITTKE, R. 2010. Experimental investigation of the CO< sub> 2</sub> sealing efficiency of caprocks. *International Journal of Greenhouse Gas Control,* 4, 231-241.
WOPFNER, H. & HÖCKER, C. F. 1987. *The Permian Groeden Sandstone between Bozen and Meran (northern Italy), a habitat of dawsonite and nordstrandite*, Schweizerbart.
XU, T., APPS, J. A. & PRUESS, K. 2005. Mineral sequestration of carbon dioxide in a sandstone–shale system. *Chemical geology,* 217, 295-318.
YAN, W., ZHAO, G.-Y., CHEN, G.-J. & GUO, T.-M. 2001. Interfacial tension of (methane+ nitrogen)+ water and (carbon dioxide+ nitrogen)+ water systems. *Journal of Chemical & Engineering Data,* 46, 1544-1548.
YANG, Y. & APLIN, A. C. 1998. Influence of lithology and compaction on the pore size distribution and modelled permeability of some mudstones from the Norwegian margin. *Marine and Petroleum Geology,* 15, 163-175.
YANG, Y. & APLIN, A. C. 2004. Definition and practical application of mudstone porosity–effective stress relationships. *Petroleum Geoscience,* 10, 153-162.
YANG, Y. & APLIN, A. C. 2007. Permeability and petrophysical properties of 30 natural mudstones. *Journal of Geophysical Research: Solid Earth (1978–2012),* 112.
YANG, Y., APLIN, A. C. & LARTER, S. R. 2004. Quantitative assessment of mudstone lithology using geophysical wireline logs and artificial neural networks. *Petroleum Geoscience,* 10, 141-151.
ZELT, F. B. 1985. Natural gamma-ray spectrometry, lithofacies, and depositional environments of selected Upper Cretaceous marine mudrocks, western United States, including Tropic Shale and Tununk Member of Mancos Shale. Princeton Univ., NJ (USA).

ZHANG, L., BAO, Y., LIU, Q., ZHANG, S., ZHU, R. & ZHANG, L. 2010. Effects of hydrocarbon physical properties on caprock's capillary sealing ability. *Science China Earth Sciences,* 53**,** 665-671.

ZHANG, S. & DEPAOLO, D. J. 2017. Rates of CO2 Mineralization in Geological Carbon Storage. *Accounts of Chemical Research*.

ZHOU, G.-T. & ZHENG, Y.-F. 2003. An experimental study of oxygen isotope fractionation between inorganically precipitated aragonite and water at low temperatures. *Geochimica et Cosmochimica Acta,* 67**,** 387-399.

ZICKFELD, K., EBY, M., MATTHEWS, H. D. & WEAVER, A. J. 2009. Setting cumulative emissions targets to reduce the risk of dangerous climate change. *Proceedings of the National Academy of Sciences,* 106**,** 16129-16134.

ZUO, Y.-X. & STENBY, E. H. 1998. Calculation of interfacial tensions of hydrocarbon-water systems under reservoir conditions. *In Situ,* 22**,** 157-180.

付广. 2006. *泥质岩盖层对各种相态天然气封存机理及定量研究*. 博士研究生学位论文, 大庆石油学院.

付广 & 许凤鸣 2003. 盖层厚度对封闭能力控制作用分析. *天然气地球科学,* 14**,** 186-190.

吕延防，张绍臣，王亚明 2000. 盖层封闭能力与盖层厚度的定量关系. *石油学报,* 21**,** 21-31.

庞雄奇, 付广 & 万龙贵 1998. 盖层封油气性综合定量评价——盆地模拟在盖层评价中的应用. 北京: 地质出版社.

田宜灵, 肖衍繁, 朱红旭, 董习靖, 任晓文 & 张凤才 1997. 高温高压下水与非极性流体间的界面张力. *物理化学学报,* 13**,** 89-95.

童晓光，牛嘉玉 1989. 区域盖层在油气聚集中的作用. *石油勘探与开发,* 16**,** 1-8.

蒋有录 1998. 油气藏盖层厚度与所封盖烃柱高度关系问题探讨. *天然气工业,* 18**,** 20-23.

Appendix

Appendix 1: Field list of the UK North Sea

Calculated limiting pore throat radii for all fields for which sufficient information was available. Also listed are the fields with hydrocarbon columns that are not limited by capillary leakage.

Field Name	Pore throat radius (nm) or limiting factor	Fault bounded?	Fault type	Lithology
Douglas	waste zone			
Hamilton Field	waste zone			
Hamilton North Field	waste zone			
Lennox	waste zone			
North Morecambe	waste zone			
South Morecambe	waste zone			
Foinaven	filled to spill			
Andrew	filled to spill			
Fleming	42	no	no/small	shale
Hawkins (well curves NA)	44	yes	moderate	shale
Beryl Lewis Reservoir	165	yes	no / small	shale
Beryl Nansen Reservoir	77	yes	no / small	shale
Beryl Linnhe (Beryl A)	51	yes	no / small	shale
Beryl Linnhe (Beryl B)	133	yes	no / small	shale
Central Brae	43	yes	large	shale
East Brae	28	no	no / small	shale
South Brae	44	yes	moderate	shale
North Brae	53	no	large	shale
West Brae	filled to spill			
Sedgwick	filled to spill			
Deveron	filled to spill	yes	?	shale

Don	199	?	no / small	shale
Dunbar (Brent, West Flank)	47	yes	no / small	shale
Dunbar (Brent, Frontal)	57	yes	no / small	shale
Dunbar (Statfjord)	37	yes	no / small	shale
Dunbar (Lunde)	37	yes	no / small	shale
Ellon	69	yes	no / small	shale
Grant	38	yes	no / small	shale
Harding Central	60	no	no / small	shale
Harding South	thin reservoir			shale
Harding	thin reservoir			shale
Brae, Heather reservoir	filled to spill			
Kingfisher, Brae unit 1	filled to spill			
Kingfisher, Brae unit 2	filled to spill			
Kingfisher	filled to spill			
Statfjord (Brent) reservoir	127	yes	moderate	shale
Statfjord (Dunlin) reservoir	242	yes	moderate	shale
Statfjord (Statfjord) Reservoir	121	yes	moderate	shale
Strathspey Brent reservoir	filled to spill			
Tiffany	54	yes		shale
Toni	52	yes		shale
Thelma	174	yes		shale
SE Thelma	82	yes		shale
Thistle	157	yes		shale
Captain	filled to spill			

Ivanhoe (Supera)	270	yes	large	shale
Ivanhoe (Main)	279	yes	large	shale
Rob Roy (Supera)	204	yes	large	shale
Rob Roy (Main)	255	yes	large	shale
Hamish	458	yes	?	shale
MacCulloch	filled to spill			
Scott	62	yes	moderate	shale
Auk	leaking at present	yes		
Curlew B	409	no	no / small	shale
Curlew D	54	no	no / small	shale
Curlew D South	99	no	no / small	shale
Erskine Erskine reservoir	filled to spill			
Erskine Pentland reservoir	298	yes	no / small	shale
Erskine Heather reservoir	no lower fluid contact			
Fife	601	no	no / small	shale
Flora	filled to spill			
Forties and Brimmond	filled to spill			
Forties and Brimmond	filled to spill			
Fulmar	83	no	moderate	shale
Maureen	filled to spill	no	moderate	shale
Maureen (Mary)	184	no	moderate	shale
Maureen (Morag)	60	no	moderate	shale
Moira	filled to spill		moderate	
Montrose	369	no	moderate	shale
Arbroath	filled to spill			
Arkwright	filled to spill			

Nelson	333	no	no / small	shale
Pierce	filled to spill			
Barque	22	yes	moderate	evaporites
Boulton	filled to spill			
Camelot	filled to spill			
Clipper	34	yes	moderate	evaporites
Corvette	36	?	moderate	evaporites
Davy	75	yes	moderate	carbonates + anhydrite
Bessemer	134	yes	moderate	evaporites and dolomites
Beaufort	153	yes	moderate	evaporites and dolomites
Brown	139	yes	moderate	carbonates + anhydrite
Gawain	filled to spill			
Guinevere	filled to spill			
Indefatigable	25	yes	moderate	halite
Johnston	79	yes	moderate	shale
Leman	45	no	moderate	evaporites
Malory	filled to base			
Murdoch	filled to spill			
Schooner	24		no / small	evaporites
V-Fields	at / close spill			
Waveney	very low relief			
Hatfield Gas Storage Field	filled to spill			shale
Saltfleetby	filled to spill			
Herriard	715			limestone
Storrington	filled to spill			
Singleton	345			limestone

Horndean	filled to spill			
Palmers Wood	791			limestone

Appendix 2: Parameters of the studied fields used for effective pore throat calculation

The parameters used in the statistical model has been described in section 5.2.1.

Field's name	Reservoir Formation	Oil column height (m)	Depth (m)	Faults type	Sealing Formation
Beryl	Lewis Unit III	174	3108.96	Medium faults	Kimmeridge Clay Formation
Beryl	Nansen	351	3035.50	Medium faults	Kimmeridge Clay Formation
Beryl	Linnhe (Beryl A)	472	3048.00	Medium faults	Kimmeridge Clay Formation
Beryl	Linnhe (Beryl B)	183	3413.76	Medium faults	Kimmeridge Clay Formation
Central Brae	Brae	511	3581.40	Medium faults	Kimmeridge Clay Formation (shales)
Curlew B	Upper Fulmar	52	3215.64	Medium faults	Kimmeridge Clay Formation (shales)
Curlew D South	Fulmar	180	3139.44	Medium faults	Kimmeridge Clay Formation (shales)
Deveron	Brent	64	2651.76	Medium faults	Humber Group shale section
Don	Brent	152	3322.32	Medium faults	Heather and Kimmeridge Clay Formation (Unconformably overlain by mudstones)
Dunbar (West Flank)	Brent	350	3300.00	Medium faults	Heather Formation
Dunbar (Frontal/Central)	Brent	297	3500.00	Medium faults	Heather Formation

Dunbar (Statfjord)	Statfjord	490	3130.00	Medium faults	Heather Formation
Dunbar (Lunde)	Lunde	490	3130.00	Medium faults	Heather Formation
Ferfus	Fife	43	2633.47	Medium faults	Kimmeridge Clay Formation (shales)
Fife	Fife	80	2514.60	Medium faults	Kimmeridge Clay Formation (shales)
Fulmar	Fulmar	283	3017.52	Medium faults	Kimmeridge Clay (Shales) and Upper Creraceous chalks
Ivanhoe (supera)	Piper sands	140.8	2313.43	Medium faults	Kimmeridge Clay Formation
Ivanhoe (main)	Piper sands	140.8	2313.43	Medium faults	Kimmeridge Clay Formation
Maureen	Maureen Formation	237.74	2423.16	Medium faults	Lista Formation mudstones
Maureen (Mary)	Hugin Formation	182.88	3063.24	Medium faults	Heather and Kimmeridge Clay Formation (mudstones)
Maureen (Morag)	Morag Member	426.72	2804.16	Medium faults	Triassic and Middle Jurassic mudstones
Montrose	Forties	64	2450.59	NA	Sele Formation (mudstones)
Nelson	Forties	85	2192.12	Large faults	Balder Formation shales and Sele Formation Mudstones
Rob Roy (Supera)	Piper sands	116.13	2301.24	Large faults	Kimmeridge Clay Formation
Rob Roy (Main)	Piper sands	116.13	2301.24	Large faults	Kimmeridge Clay Formation

Scott	Sgiath & Piper Formations	380.7	3169.92	Medium faults	Kimmeridge Clay Formation (shales)
South Brae	Brae	509	2651.76	Small or no faults	Organic rich mudstones of the Kimmeridge Clay and Brea Formation
Statfjord (Brent)	Brent Group/sandstone	226	2360.00	Large faults	Middle to Upper Jurassic and Cretaceous shales
Statfjord (Dunlin)	Cook formation (Dunlin II)/sandstone	129	2475.00	Large faults	Middle to Upper Jurassic and Cretaceous shales
Statfjord (Statfjord)	Statfjord formation/sandtstone	239	2575.00	Large faults	Middle to Upper Jurassic and Cretaceous shales
T-Block (Tiffany)	Brae	426.72	3816.10	Medium faults	Kimmeridge Clay Formation (Shale)
T-Block (Toni)	Brae	358.75	3582.92	Medium faults	Kimmeridge Clay Formation (Shale)
T-Block (Thelma)	Brae	96.32	3590.54	Medium faults	Kimmeridge Clay Formation (Shale)
T-Block (SE Thelma)	Brae and Sand Shale	256.95	3627.12	Medium faults	Kimmeridge Clay Formation (Shale)
Thistle	Brent	250.55	2590.80	Medium fauts	Mudstones of the Humber Group,Shale of Heather and Kimmeridge Clay Formation

Field's name	Reservoir Formation	min API	max API	API (avg.)	min Rs(m3/m3)	max Rs (m3/m3)	Rs (avg.)
Beryl	Lewis Unit III	36.0	36.0	36.0	132.08	132.08	132.08

Beryl	Nansen	27.0	27.0	27.0	169.06	169.06	169.06
Beryl	Linnhe (Beryl A)	38.0	38.0	38.0	169.06	169.06	169.06
Beryl	Linnhe (Beryl B)	38.0	38.0	38.0	169.06	169.06	169.06
Central Brae	Brae	33	37	35	249.18	249.18	249.18
Curlew B	Upper Fulmar	39	39	39	189.84	189.84	189.84
Curlew D South	Fulmar	40	40	40	387.42	387.42	387.42
Deveron	Brent	38	38	38	26.42	26.42	26.42
Don	Brent	37	42	40	58.99	175.04	117.01
Dunbar (West Flank)	Brent	43	43	43	500.00	500.00	500.00
Dunbar (Frontal/Central)	Brent	42	42	42	300.00	300.00	300.00
Dunbar (Statfjord)	Statfjord	41	41	41	250.00	250.00	250.00
Dunbar (Lunde)	Lunde	41	41	41	250.00	250.00	250.00
Ferfus	Fife	36.4	36.4	36.4	96.00	96.00	96.00
Fife	Fife	36.4	36.4	36.4	96.00	96.00	96.00
Fulmar	Fulmar	40	40	40	108.13	108.13	108.13
Ivanhoe (supera)	Piper sands	31	31	31	63.40	63.40	63.40
Ivanhoe (main)	Piper sands	29	29	29	63.40	63.40	63.40
Maureen	Maureen Formation	36	36	36	69.21	69.21	69.21

Maureen (Mary)	Hugin Formation	32	32	32	96.86	96.86	96.86
Maureen (Morag)	Morag Member	31.3	31.3	31.3	132.08	132.08	132.08
Montrose	Forties	40	40	40	105.66	140.88	123.27
Nelson	Forties	40.6	40.6	40.6	97.74	97.74	97.74
Rob Roy (Supera)	Piper sands	41	41	41	244.96	244.96	244.96
Rob Roy (Main)	Piper sands	39	39	39	107.95	107.95	107.95
Scott	Sgiath & Piper Formations	36	36	36	101.78	246.19	173.98
South Brae	Brae	35	35	35	236.50	236.50	236.50
Statfjord (Brent)	Brent Group/sandstone	38.4	38.4	38.4	185.00	185.00	185.00
Statfjord (Dunlin)	Cook formation (Dunlin II)/sandstone	36.4	36.4	36.4	147.00	147.00	147.00
Statfjord (Statfjord)	Statfjord formation/sandtstone	39.6	39.6	39.6	156.60	156.60	156.60
T-Block (Tiffany)	Brae	35.6	35.6	35.6	155.85	155.85	155.85
T-Block (Toni)	Brae	34.8	34.8	34.8	382.14	382.14	382.14
T-Block (Thelma)	Brae	38.5	38.5	38.5	475.47	475.47	475.47
T-Block (SE Thelma)	Brae and Sand Shale	34.7	34.7	34.7	211.32	211.32	211.32
Thistle	Brent	38.4	38.4	38.4	51.07	51.07	51.07

Field's name	Reservoir Formation	T(avg,C)	P(bar)	FVF (RB/STB)	Salinity (avg.%)

Beryl	Lewis Unit III	102	366	1.41	7.00
Beryl	Nansen	97	338	1.55	8.50
Beryl	Linnhe (Beryl A)	97	338	1.60	8.50
Beryl	Linnhe (Beryl B)	97	338	1.60	8.50
Central Brae	Brae	119	487	1.77	7.90
Curlew B	Upper Fulmar	121	503	1.50	20.00
Curlew D South	Fulmar	122	502	1.90	20.00
Deveron	Brent	105	324	1.13	2.35
Don	Brent	129.4	507	1.36	2.16
Dunbar (West Flank)	Brent	128	570	3.00	2.10
Dunbar (Frontal/Central)	Brent	128	570	2.70	3.50
Dunbar (Statfjord)	Statfjord	130	575	2.40	2.10
Dunbar (Lunde)	Lunde	130	575	2.40	2.10
Ferfus	Fife	108	390	1.10	6.13
Fife	Fife	108	390	1.10	6.13
Fulmar	Fulmar	140.5	393	1.43	13.80
Ivanhoe (supera)	Piper sands	79	242	1.19	9.10
Ivanhoe (main)	Piper sands	79	242	1.19	9.10
Maureen	Maureen Formation	119	261	1.29	3.00
Maureen (Mary)	Hugin Formation	134	432	1.33	3.00
Maureen (Morag)	Morag Member	132	421	1.61	3.00
Montrose	Forties	125	258	1.51	11.10
Nelson	Forties	107	229	1.36	8.40
Rob Roy (Supera)	Piper sands	79	242	1.68	9.10
Rob Roy (Main)	Piper sands	79	242	1.34	9.10
Scott	Sgiath & Piper Formations	104	543.40-646.90	1.54	11.00
South Brae	Brae	123	491	1.73	7.50

Statfjord (Brent)	Brent Group/sandstone	89	384	1.53	1.400
Statfjord (Dunlin)	Cook formation (Dunlin II)/sandstone	98	384	1.43	1.40
Statfjord (Statfjord)	Statfjord formation/sandtstone	97	405	1.48	1.36
T-Block (Tiffany)	Brae	135	514	1.57	9.50
T-Block (Toni)	Brae	121	483	2.20	9.50
T-Block (Thelma)	Brae	127	459	2.58	9.50
T-Block (SE Thelma)	Brae and Sand Shale	127	479	1.79	9.50
Thistle	Brent	104	418	1.18	1.30

Field's name	Reservoir Formation	δ (air-dead oil); mN/m	δ (air-lo T); mN/m	δ (air-lo GOR); mN/m	δ (air-water); mN/m	$\Delta\delta$ mN/m
Beryl	Lewis Unit III	28.73	23.12	2.88	60.77	57.89
Beryl	Nansen	31.06	25.47	2.39	61.51	59.11
Beryl	Linnhe (Beryl A)	28.21	23.14	2.17	61.51	59.33
Beryl	Linnhe (Beryl B)	28.21	23.14	2.17	61.51	59.33
Central Brae	Brae	28.99	21.83	1.32	58.26	56.94
Curlew B	Upper Fulmar	27.95	20.88	1.72	57.96	56.24
Curlew D South	Fulmar	27.70	20.60	0.75	57.81	57.06
Deveron	Brent	28.21	22.45	13.14	60.32	47.19
Don	Brent	27.70	19.97	2.85	56.72	53.87
Dunbar (West Flank)	Brent	26.92	19.53	0.54	56.93	56.39
Dunbar (Frontal/Central)	Brent	27.18	19.72	0.97	56.93	55.96
Dunbar (Statfjord)	Statfjord	27.44	19.74	1.19	56.63	55.44
Dunbar (Lunde)	Lunde	27.44	19.74	1.19	56.63	55.44
Ferfus	Fife	28.63	22.52	4.03	59.88	55.85

Fife	Fife	28.63	22.52	4.03	59.88	55.85
Fulmar	Fulmar	27.70	19.04	2.97	55.08	52.11
Ivanhoe (supera)	Piper sands	30.03	26.27	7.53	64.16	56.63
Ivanhoe (main)	Piper sands	30.54	26.72	7.66	64.16	56.50
Maureen	Maureen Formation	28.73	21.63	5.61	58.26	52.64
Maureen (Mary)	Hugin Formation	29.77	21.05	3.73	56.04	52.31
Maureen (Morag)	Morag Member	29.95	21.36	2.66	56.34	53.68
Montrose	Forties	27.70	20.35	2.74	57.37	54.63
Nelson	Forties	27.54	21.74	3.81	60.03	56.22
Rob Roy (Supera)	Piper sands	27.44	24.01	1.48	64.16	62.68
Rob Roy (Main)	Piper sands	27.95	24.46	3.83	64.16	60.34
Scott	Sgiath & Piper Formations	28.73	22.95	2.09	60.47	58.38
South Brae	Brae	28.99	21.47	1.38	57.66	56.29
Statfjord (Brent)	Brent Group/sandstone	28.11	23.74	2.01	62.69	60.67
Statfjord (Dunlin)	Cook formation (Dunlin II)/sandstone	28.63	23.39	2.58	61.36	58.78
Statfjord (Statfjord)	Statfjord formation/sandtstone	27.80	22.80	2.34	61.51	59.17
T-Block (Tiffany)	Brae	28.83	20.30	2.09	55.89	53.80
T-Block (Toni)	Brae	29.04	21.69	0.81	57.96	57.15
T-Block (Thelma)	Brae	28.08	20.46	0.59	57.07	56.48
T-Block (SE Thelma)	Brae and Sand Shale	29.07	21.18	1.54	57.07	55.53
Thistle	Brent	28.11	22.45	8.23	60.47	52.24

Field's name	Reservoir Formation	$\cos\theta$	ρw (std, kg/m^3))	ΔVwp	ΔVwt	Bw
Beryl	Lewis Unit III	1	65.45	-1.15E-02	4.43E-02	1.0323
Beryl	Nansen	1	66.11	-1.00E-02	4.11E-02	1.0306

Beryl	Linnhe (Beryl A)	1	66.11	-1.00E-02	4.11E-02	1.0306
Beryl	Linnhe (Beryl B)	1	66.11	-1.00E-02	4.11E-02	1.0306
Central Brae	Brae	1	65.85	-1.93E-02	5.62E-02	1.0359
Curlew B	Upper Fulmar	1	71.17	-2.05E-02	5.77E-02	1.0360
Curlew D South	Fulmar	1	71.17	-2.05E-02	5.84E-02	1.0368
Deveron	Brent	1	63.40	-9.53E-03	4.64E-02	1.0364
Don	Brent	1	63.32	-2.11E-02	6.40E-02	1.0415
Dunbar (West Flank)	Brent	1	63.29	-2.57E-02	6.29E-02	1.0356
Dunbar (Frontal/Central)	Brent	1	63.91	-2.57E-02	6.29E-02	1.0356
Dunbar (Statfjord)	Statfjord	1	63.29	-2.62E-02	6.44E-02	1.0366
Dunbar (Lunde)	Lunde	1	63.29	-2.62E-02	6.44E-02	1.0366
Ferfus	Fife	1	65.07	-1.30E-02	4.84E-02	1.0348
Fife	Fife	1	65.07	-1.30E-02	4.84E-02	1.0348
Fulmar	Fulmar	1	68.44	-1.41E-02	7.27E-02	1.0575
Ivanhoe (supera)	Piper sands	1	66.37	-5.60E-03	2.99E-02	1.0242
Ivanhoe (main)	Piper sands	1	66.37	-5.60E-03	2.99E-02	1.0242
Maureen	Maureen Formation	1	63.69	-7.03E-03	5.62E-02	1.0488
Maureen (Mary)	Hugin Formation	1	63.69	-1.63E-02	6.75E-02	1.0502

Maureen (Morag)	Morag Member	1	63.69	-1.56E-02	6.60E-02	1.0494
Montrose	Forties	1	67.25	-7.00E-03	6.06E-02	1.0532
Nelson	Forties	1	66.07	-5.56E-03	4.77E-02	1.0419
Rob Roy (Supera)	Piper sands	1	66.37	-5.60E-03	2.99E-02	1.0242
Rob Roy (Main)	Piper sands	1	66.37	-5.60E-03	2.99E-02	1.0242
Scott	Sgiath & Piper Formations	1	67.21	-2.62E-02	4.57E-02	1.0183
South Brae	Brae	1	65.67	-1.98E-02	5.91E-02	1.0382
Statfjord (Brent)	Brent Group/sandstone	1	62.98	-1.21E-02	3.60E-02	1.0235
Statfjord (Dunlin)	Cook formation (Dunlin II)/sandstone	1	62.98	-1.23E-02	4.17E-02	1.0288
Statfjord (Statfjord)	Statfjord formation/sandtstone	1	62.97	-1.34E-02	4.11E-02	1.0271
T-Block (Tiffany)	Brae	1	66.55	-2.18E-02	6.83E-02	1.0450
T-Block (Toni)	Brae	1	66.55	-1.91E-02	5.77E-02	1.0375
T-Block (Thelma)	Brae	1	66.55	-1.77E-02	6.21E-02	1.0433
T-Block (SE Thelma)	Brae and Sand Shale	1	66.55	-1.91E-02	6.21E-02	1.0419
Thistle	Brent	1	62.94	-1.44E-02	4.57E-02	1.0306

Field's name	Reservoir Formation	ρw (sur., kg/m^3)	ρ (res. methane, kg/m^3)	ρ (surf. methane, kg/m^3)	ρo (surf., kg/m^3)	ρo (res. kg/m^3)	$\Delta\rho$ kg/ m$^{3)}$
Beryl	Lewis Unit III	1015.57	188.25	0.678	843.94	662.05	353.52

Beryl	Nansen	1027.50	176.19	0.678	891.87	649.35	378.15
Beryl	Linnhe (Beryl A)	1027.50	176.19	0.678	833.99	592.88	434.62
Beryl	Linnhe (Beryl B)	1027.50	176.19	0.678	833.99	592.88	434.62
Central Brae	Brae	1018.22	239.62	0.678	849.01	575.12	443.11
Curlew B	Upper Fulmar	1100.44	246.24	0.678	829.10	638.54	461.90
Curlew D South	Fulmar	1099.65	245.13	0.678	824.26	572.07	527.58
Deveron	Brent	979.95	165.32	0.678	833.99	751.89	228.06
Don	Brent	973.81	242.66	0.678	824.26	664.41	309.40
Dunbar (West Flank)	Brent	979.00	274.1695	0.678	810.09	383.03	595.97
Dunbar (Frontal/Central)	Brent	988.53	274.17	0.678	814.76	377.10	611.43
Dunbar (Statfjord)	Statfjord	978.09	275.20	0.678	819.48	412.08	566.01
Dunbar (Lunde)	Lunde	978.09	275.20	0.678	819.48	412.08	566.01
Ferfus	Fife	1007.22	197.43	0.678	841.93	823.22	184.00
Fife	Fife	1007.22	197.43	0.678	841.93	823.22	184.00
Fulmar	Fulmar	1036.71	183.32	0.678	824.26	627.67	409.04
Ivanhoe (supera)	Piper sands	1038.11	132.60	0.678	869.91	767.14	270.97
Ivanhoe (main)	Piper sands	1038.11	132.60	0.678	880.75	777.55	260.56
Maureen	Maureen Formation	972.74	128.42	0.678	843.94	690.59	282.15
Maureen (Mary)	Hugin Formation	971.46	204.73	0.678	864.59	699.44	272.02
Maureen (Morag)	Morag Member	972.19	200.50	0.678	868.31	593.47	378.72

Montrose	Forties	1022.88	125.03	0.678	824.26	600.42	422.45
Nelson	Forties	1015.71	116.23	0.678	821.39	654.13	361.59
Rob Roy (Supera)	Piper sands	1038.11	132.60	0.678	819.48	586.99	451.12
Rob Roy (Main)	Piper sands	1038.11	132.60	0.678	829.10	671.34	366.77
Scott	Sgiath & Piper Formations	1057.30	304.41	0.678	843.94	622.79	434.51
South Brae	Brae	1013.19	239.15	0.678	849.01	583.45	429.74
Statfjord (Brent)	Brent Group/sandstone	985.79	204.59	0.678	832.02	626.61	359.18
Statfjord (Dunlin)	Cook formation (Dunlin II)/sandstone	980.62	204.59	0.678	841.93	659.38	321.24
Statfjord (Statfjord)	Statfjord formation/sandtstone	982.06	211.12	0.678	826.19	628.28	353.78
T-Block (Tiffany)	Brae	1020.13	242.99	0.678	845.97	604.59	415.54
T-Block (Toni)	Brae	1027.50	236.45	0.678	850.03	504.61	522.90
T-Block (Thelma)	Brae	1021.78	221.33	0.678	831.53	447.25	574.53
T-Block (SE Thelma)	Brae and Sand Shale	1023.15	230.97	0.678	850.55	555.21	467.95
Thistle	Brent	978.27	214.36	0.678	832.02	734.45	243.83

Appendix 3: R script for Monte Carlo simulation

```
#Monte Carlo simulation#
#For one dimension model#
# Read in table of parameters where each line is a different field#
EPR <- matrix(rep(0, 33000), nrow=33, ncol=1000)
H <- EPR_MC$Height.m
n <- 1000
# Loop over all fields #
for (i in 1:33)
{
   Hmc <- runif(1, min = H[i]-6, max = H[i]+6)
   APImc <- rnorm(n, mean = API[i], sd = 0.05)
   T.Cmc <- rnorm(n, mean = T.C[i], sd = 0.05)
   Pmc <- rnorm(n, mean = P[i], sd = 0.05)
   Rsmc <- rnorm(n, mean = Rs[i], sd = 0.05)
   FVFmc <- rnorm(n, mean = FVF[i], sd = 0.05)
   Wsmc <- rnorm(n, mean = Ws[i], sd = 0.05)
   cosqmc <- runif(1, min = 0.9, max = 1.0)
   #define IFTwa: IFT between water and air#
   IFTwa <- -0.1477*T.Cmc + 75.832

   #define IFTao: IFT between air and oil#
   ifelse (Rsmc < 50,
```

{IFTao <- (1.11591-0.00305*T.Cmc)*(38.085-0.259*APImc)/(1+0.02549*Rsmc^1.0157)},

{IFTao <- (1.11591-0.00305*T.Cmc)*(38.085-0.259*APImc)*32.0436*Rsmc^(-1.1367)})

#define IFT#

IFT <- IFTwa - IFTao

#water density calculation according to Danesh, A.2007#

#standard saline water#

rws <- 62.368 + 0.438603*Wsmc + 1.60074*10^(-3)*Wsmc

#pressure and temperature correction factor#

dVwp <- -Pmc*(3.58922E-7 + 1.953E-9*T.Fmc) - Pmc^2*(2.25341E-10 + 1.72834E-13*T.Fmc)

dVwt <- -1.001E-2 + 1.33391E-4*T.Fmc + 5.50654E-7*T.Fmc^2

#formation volume factor#

Bw <- (1 + dVwp)*(1 + dVwt)

#corrected water density#

rwr <- rws/Bw *16.018463 #convert bm/ft3 to kg/m3#

#oil density calculation according to volume and mass change#

ros <- 141.5*999.016/(APImc + 131.5)

ror <- (ros + 0.678*Rsmc)/FVFmc

```
#density difference#

dd <- rwr - ror


#Effective porethroat radii#

EPR[i,] <-2*cosq*IFT/(dd*9.8*Hmc)*10^6

}


hist(EPR, n=300, xlab="Effective Porethroat Radii/nm", ylab="Frequency",
xlim=c(0,1000), ylim=c(0,3000))
```

Appendix 4: Results of Monte Carlo simulation

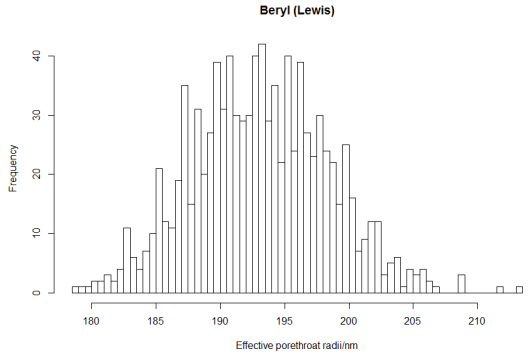

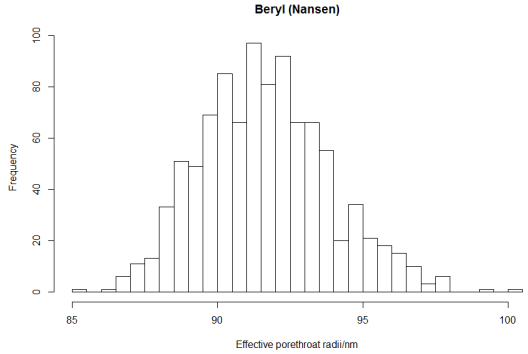

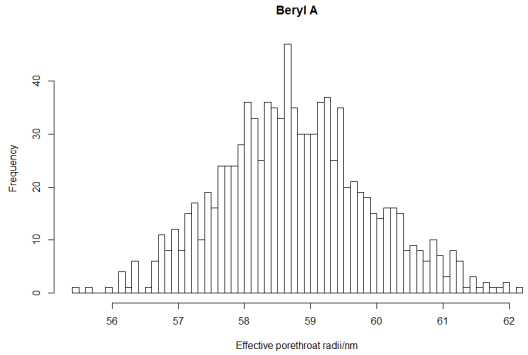

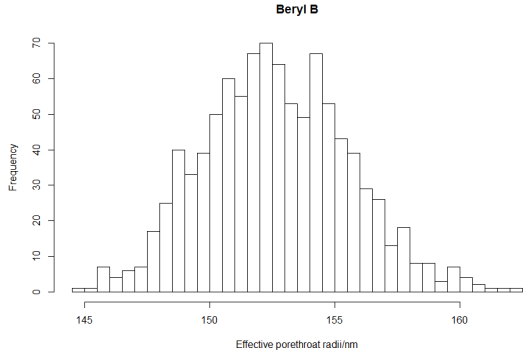

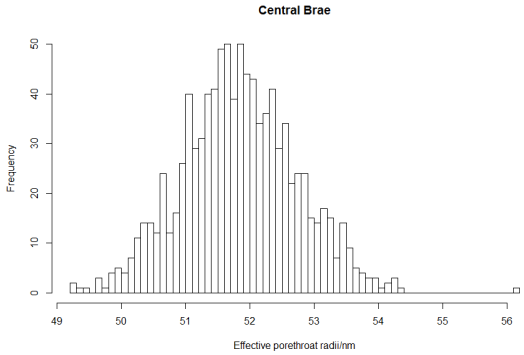
Central Brae
Frequency
0
10
20
30
40
50
49
50
51
52
53
54
55
56
Effective porethroat radii/nm

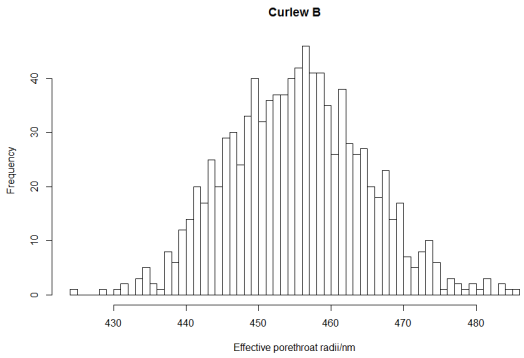
Curlew B
Frequency
0
10
20
30
40
430
440
450
460
470
480
Effective porethroat radii/nm

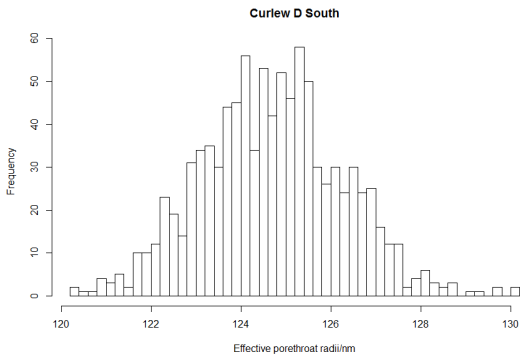
Curlew D South
Frequency
0
10
20
30
40
50
60
120
122
124
126
128
130
Effective porethroat radii/nm

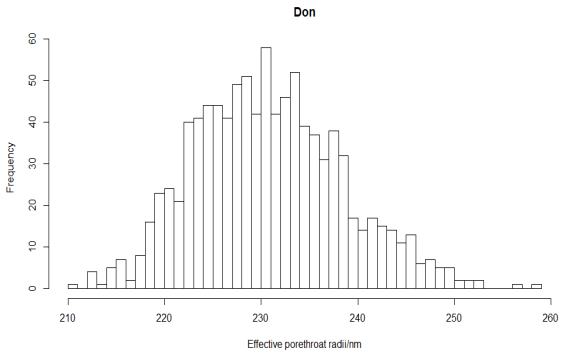
Don
Frequency
0
10
20
30
40
50
60
210
220
230
240
250
260
Effective porethroat radii/nm

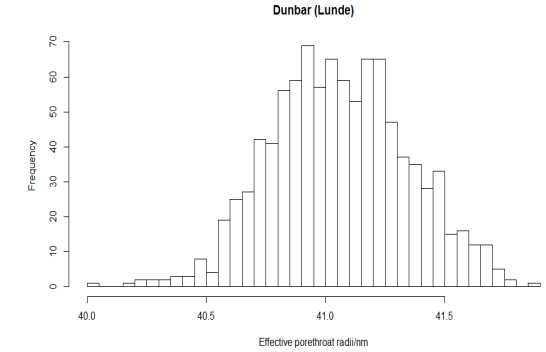
Dunbar (Lunde)
Frequency
0
10
20
30
40
50
60
70
40.0
40.5
41.0
41.5
Effective porethroat radii/nm

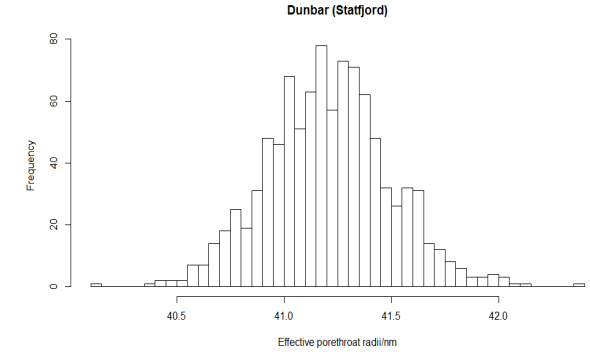
Dunbar (Statfjord)
Frequency
0
20
40
60
80
40.5
41.0
41.5
42.0
Effective porethroat radii/nm

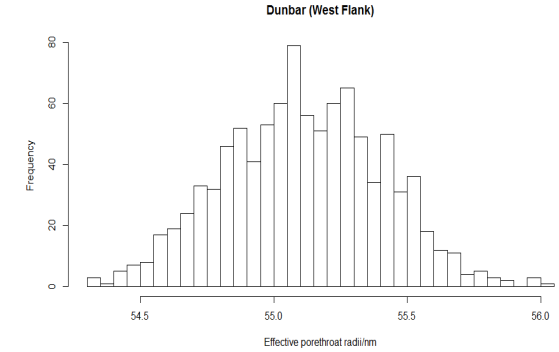
Dunbar (West Flank)
Frequency
0
20
40
60
80
54.5
55.0
55.5
56.0
Effective porethroat radii/nm

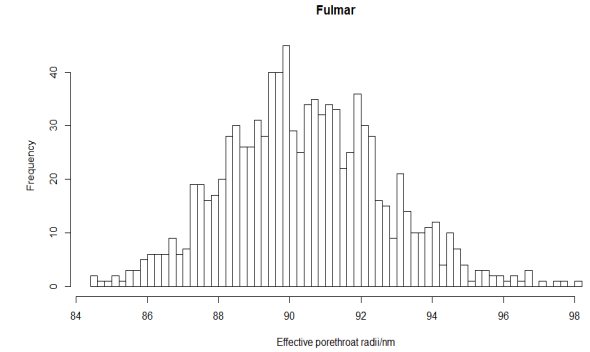
Fulmar
Frequency
0
10
20
30
40
84
86
88
90
92
94
96
98
Effective porethroat radii/nm

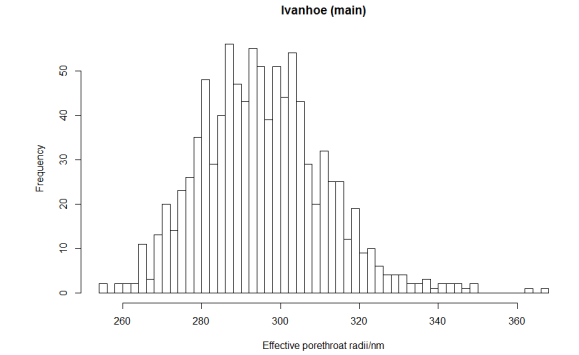
Ivanhoe (main)
Frequency
0
10
20
30
40
50
260
280
300
320
340
360
Effective porethroat radii/nm

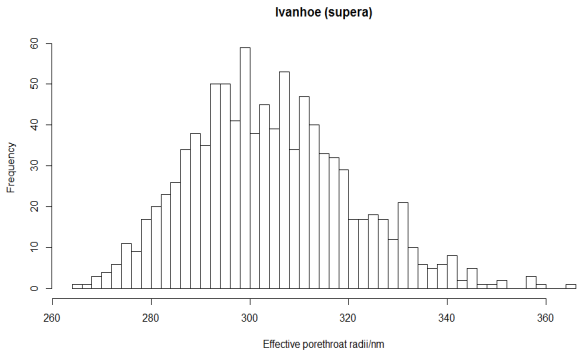
Ivanhoe (supera)
Frequency
0
10
20
30
40
50
60
260
280
300
320
340
360
Effective porethroat radii/nm

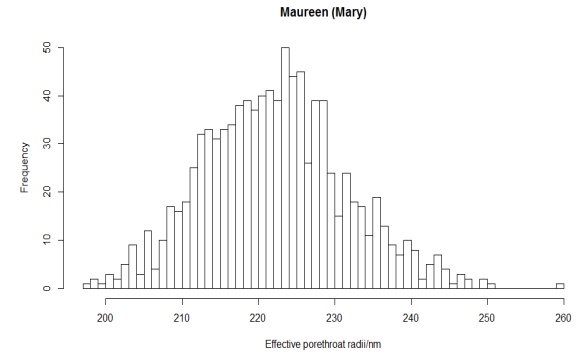
Maureen (Mary)
Frequency
0
10
20
30
40
50
200
210
220
230
240
250
260
Effective porethroat radii/nm

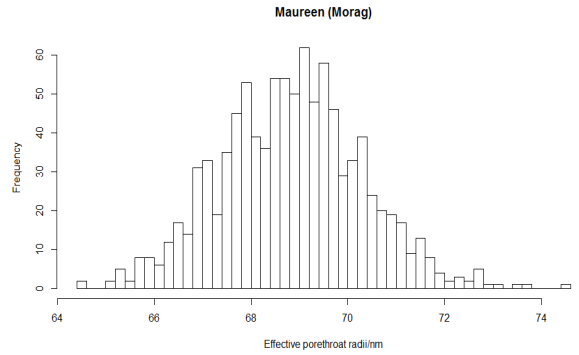
Maureen (Morag)
Frequency
0
10
20
30
40
50
60
64
66
68
70
72
74
Effective porethroat radii/nm

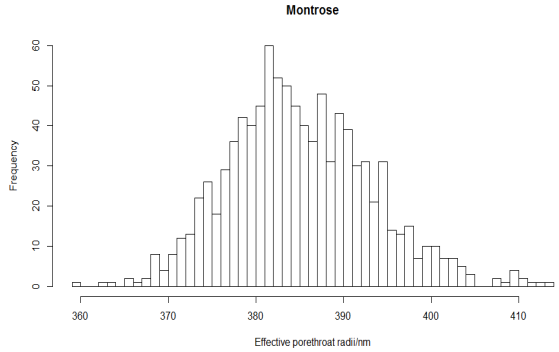
Montrose
Frequency
0
10
20
30
40
50
60
360
370
380
390
400
410
Effective porethroat radii/nm

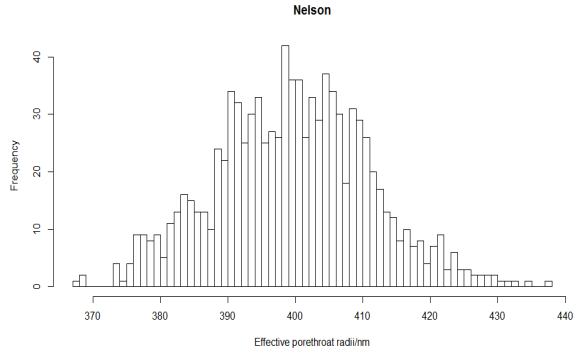
Nelson
Frequency
0
10
20
30
40
370
380
390
400
410
420
430
440
Effective porethroat radii/nm

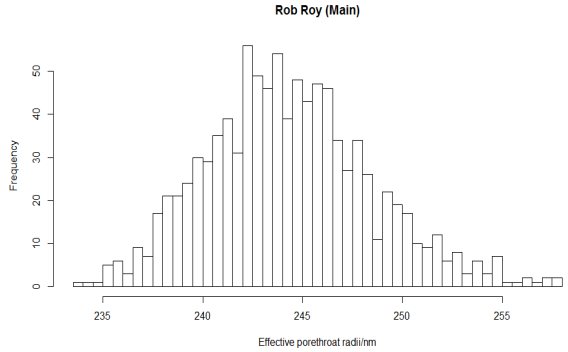
Rob Roy (Main)
Frequency
0
10
20
30
40
50
235
240
245
250
255
Effective porethroat radii/nm

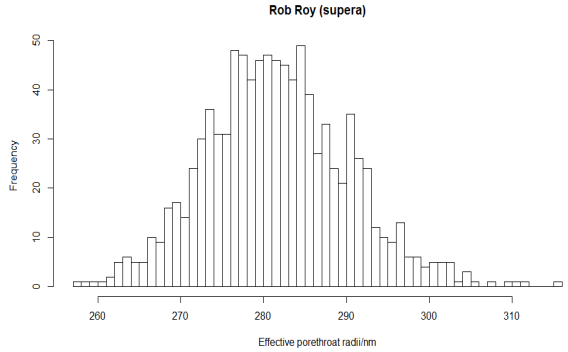
Rob Roy (supera)
Frequency
0
10
20
30
40
50
260
270
280
290
300
310
Effective porethroat radii/nm

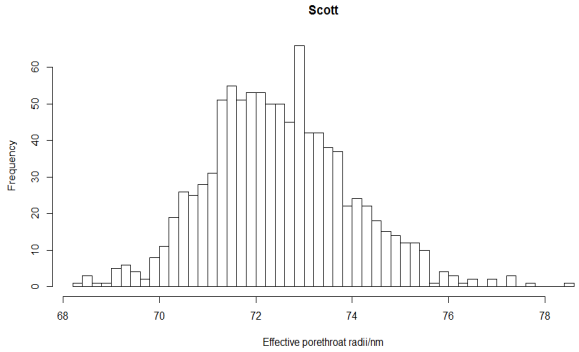
Scott
Frequency
0
10
20
30
40
50
60
68
70
72
74
76
78
Effective porethroat radii/nm

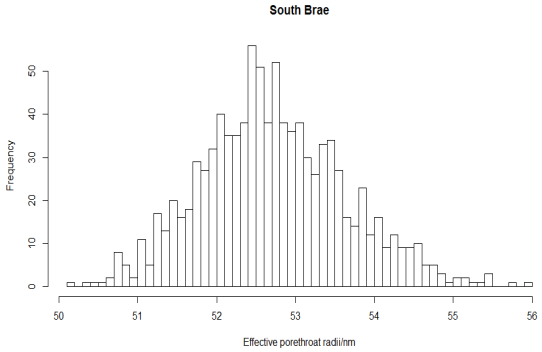
South Brae
Frequency
0
10
20
30
40
50
50
51
52
53
54
55
56
Effective porethroat radii/nm

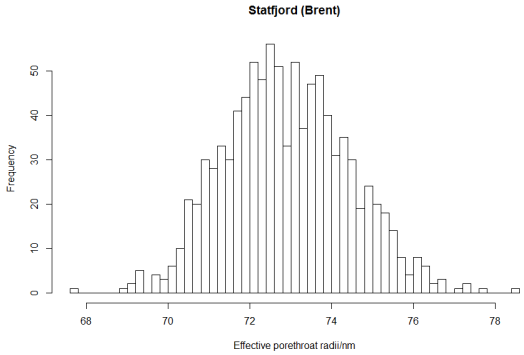
Statfjord (Brent)
Frequency
0
10
20
30
40
50
68
70
72
74
76
78
Effective porethroat radii/nm

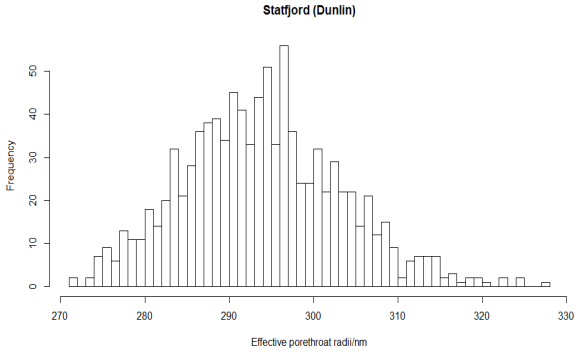
Statfjord (Dunlin)
Frequency
0
10
20
30
40
50
270
280
290
300
310
320
330
Effective porethroat radii/nm

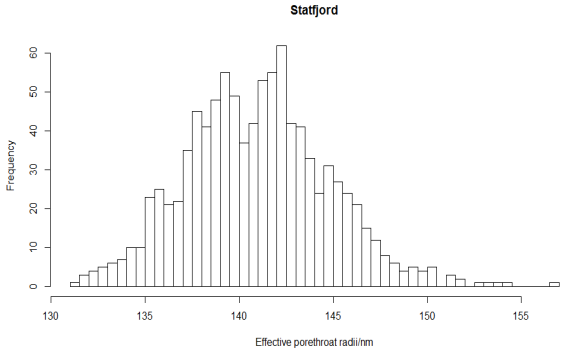
Statfjord
Frequency
0
10
20
30
40
50
60
130
135
140
145
150
155
Effective porethroat radii/nm

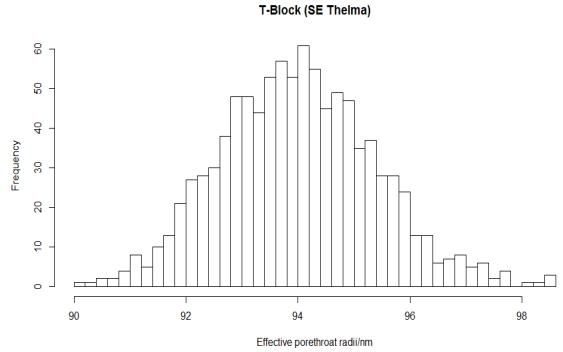
T-Block (SE Thelma)
Frequency
0
10
20
30
40
50
60
90
92
94
96
98
Effective porethroat radii/nm

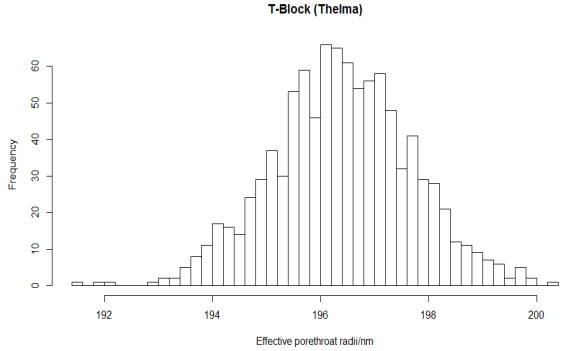
T-Block (Thelma)
Frequency
0
10
20
30
40
50
60
192
194
196
198
200
Effective porethroat radii/nm

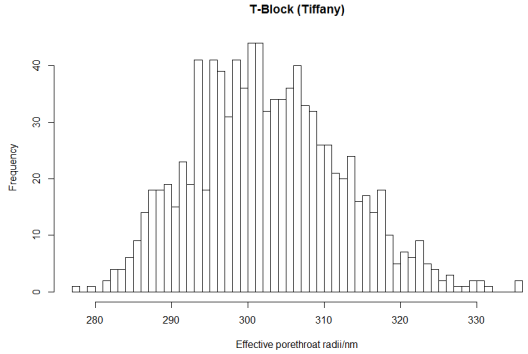
T-Block (Tiffany)
Frequency
0
10
20
30
40
280
290
300
310
320
330
Effective porethroat radii/nm

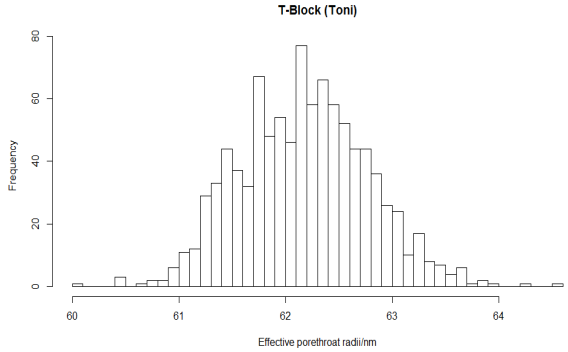
T-Block (Toni)
Frequency
0
20
40
60
80
60
61
62
63
64
Effective porethroat radii/nm

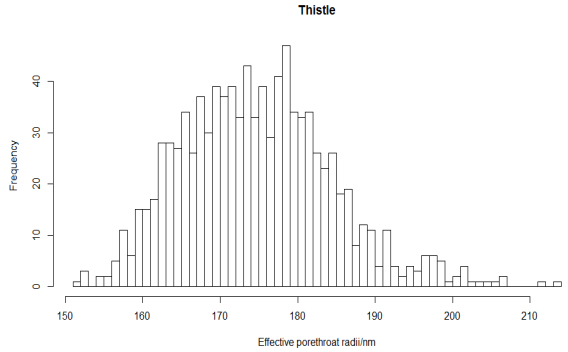
Thistle
Frequency
0
10
20
30
40
150
160
170
180
190
200
210
Effective porethroat radii/nm

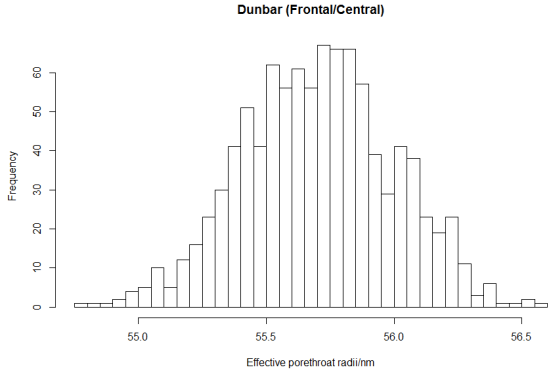
Dunbar (Frontal/Central)
Frequency
0
10
20
30
40
50
60
55.0
55.5
56.0
56.5
Effective porethroat radii/nm

Appendix 5: XRD result for T2-vein

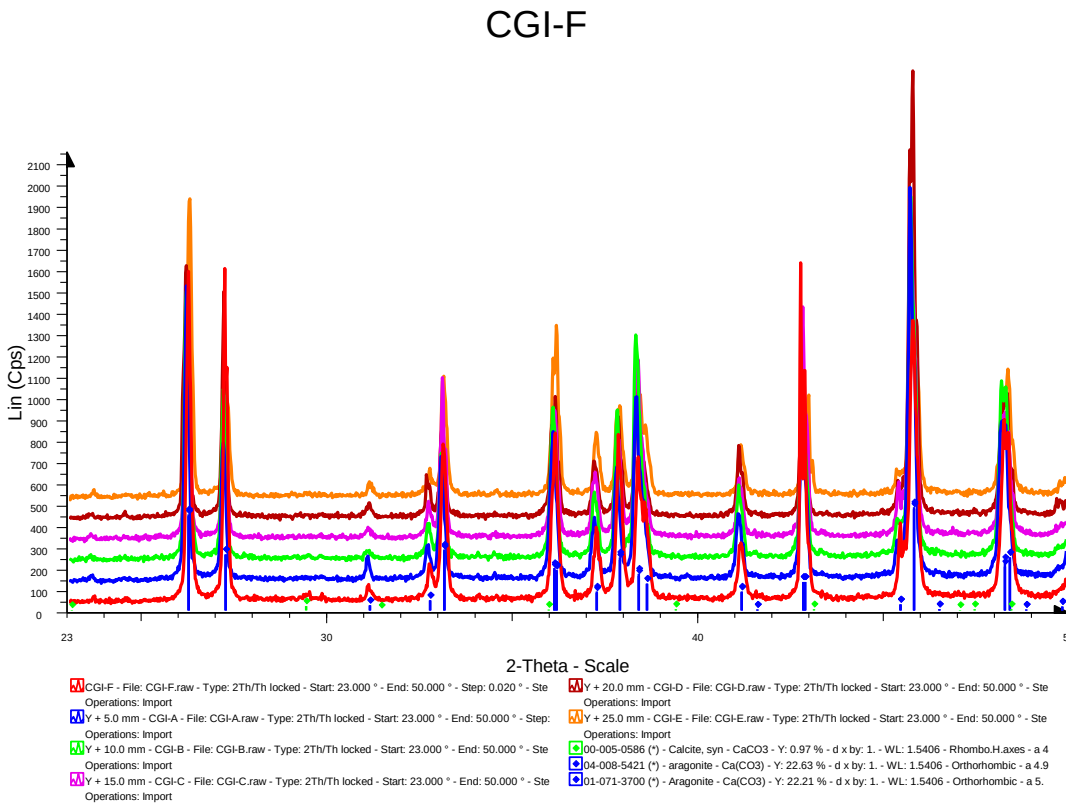

Appendix 6: Electron microprobe results

Elemental analysis by electron microprobe on sample CG1-1, CG1-2 and CG1-4.

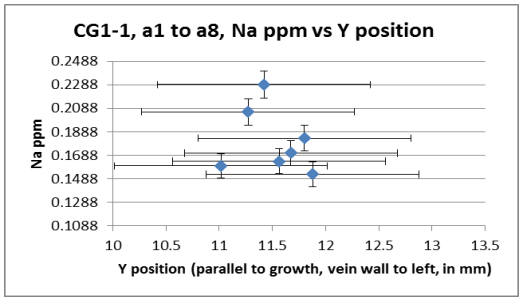

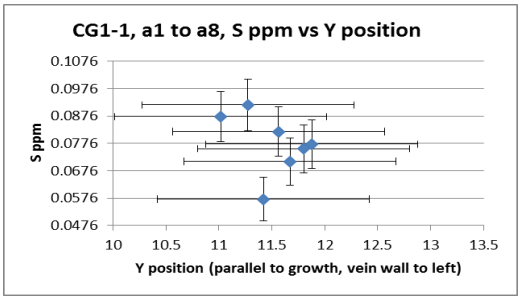

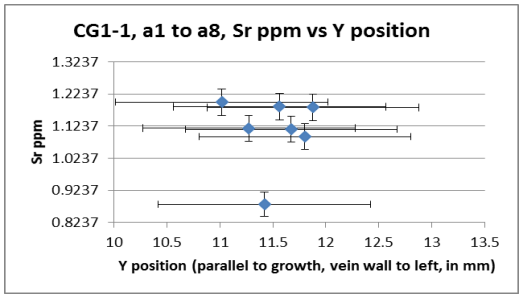

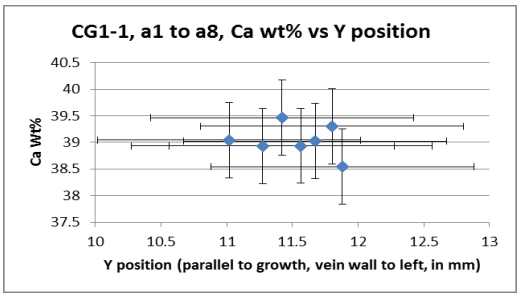

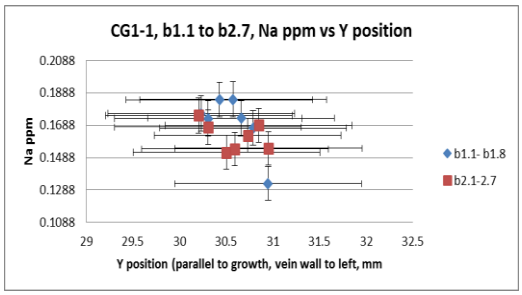

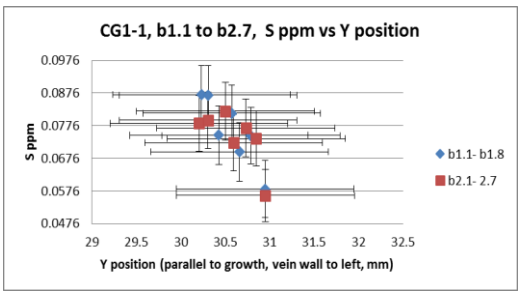

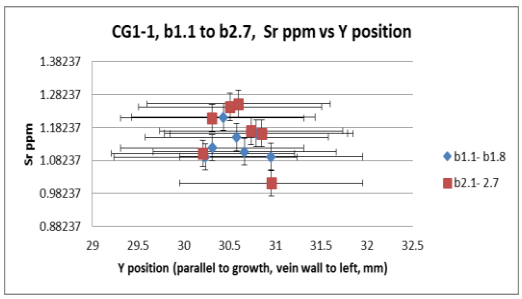

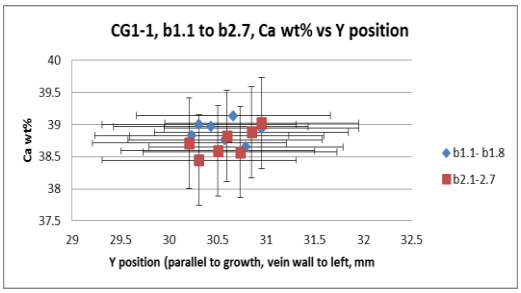

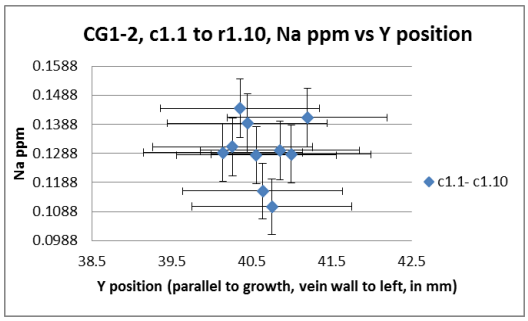
CG1-2, c1.1 to r1.10, Na ppm vs Y position
Na ppm
0.1588
0.1488
0.1388
0.1288
0.1188
0.1088
0.0988
38.5
39.5
40.5
41.5
42.5
Y position (parallel to growth, vein wall to left, in mm)
c1.1- c1.10

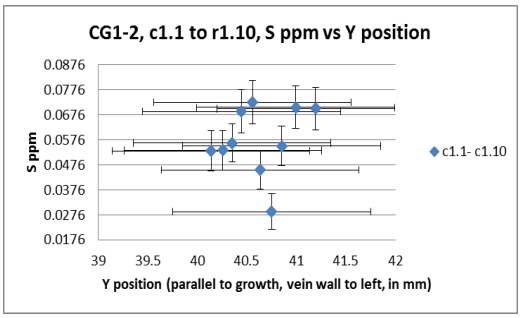
CG1-2, c1.1 to r1.10, S ppm vs Y position
S ppm
0.0876
0.0776
0.0676
0.0576
0.0476
0.0376
0.0276
0.0176
39
39.5
40
40.5
41
41.5
42
Y position (parallel to growth, vein wall to left, in mm)
c1.1- c1.10

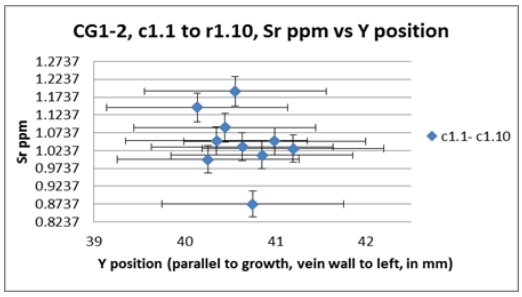
CG1-2, c1.1 to r1.10, Sr ppm vs Y position
Sr ppm
1.2737
1.2237
1.1737
1.1237
1.0737
1.0237
0.9737
0.9237
0.8737
0.8237
39
40
41
42
Y position (parallel to growth, vein wall to left, in mm)
c1.1- c1.10

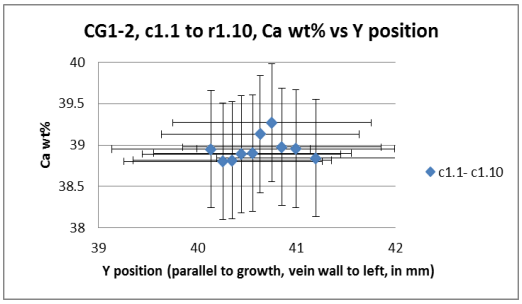
CG1-2, c1.1 to r1.10, Ca wt% vs Y position
Ca wt%
40
39.5
39
38.5
38
39
40
41
42
Y position (parallel to growth, vein wall to left, in mm)
c1.1- c1.10

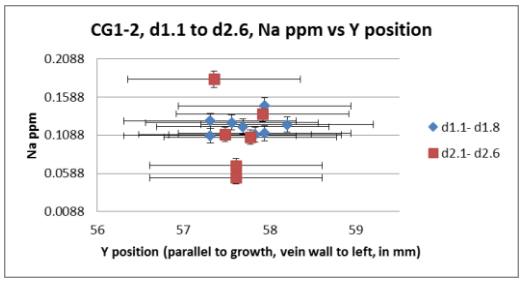
CG1-2, d1.1 to d2.6, Na ppm vs Y position
Na ppm
0.2088
0.1588
0.1088
0.0588
0.0088
56
57
58
59
Y position (parallel to growth, vein wall to left, in mm)
d1.1- d1.8
d2.1- d2.6

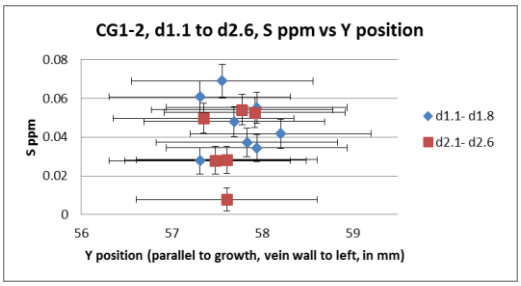
CG1-2, d1.1 to d2.6, S ppm vs Y position
S ppm
0.08
0.06
0.04
0.02
0
56
57
58
59
Y position (parallel to growth, vein wall to left, in mm)
d1.1- d1.8
d2.1- d2.6

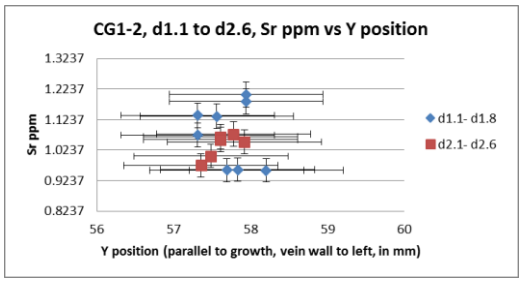
CG1-2, d1.1 to d2.6, Sr ppm vs Y position
Sr ppm
1.3237
1.2237
1.1237
1.0237
0.9237
0.8237
56
57
58
59
60
Y position (parallel to growth, vein wall to left, in mm)
d1.1- d1.8
d2.1- d2.6

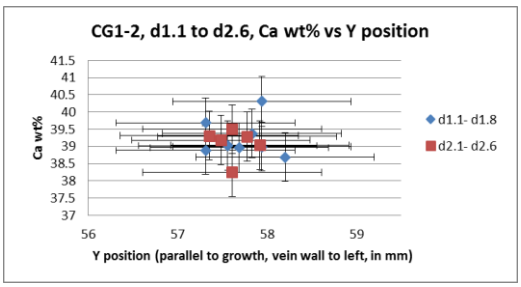
CG1-2, d1.1 to d2.6, Ca wt% vs Y position
Ca wt%
41.5
41
40.5
40
39.5
39
38.5
38
37.5
37
56
57
58
59
Y position (parallel to growth, vein wall to left, in mm)
d1.1- d1.8
d2.1- d2.6

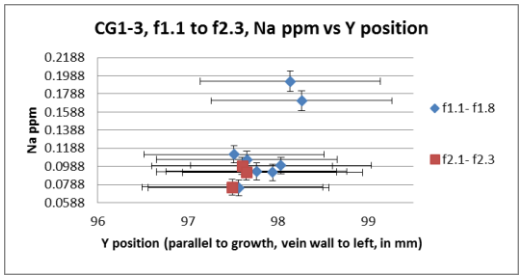
CG1-3, f1.1 to f2.3, Na ppm vs Y position
Na ppm
0.2188
0.1988
0.1788
0.1588
0.1388
0.1188
0.0988
0.0788
0.0588
96
97
98
99
Y position (parallel to growth, vein wall to left, in mm)
f1.1- f1.8
f2.1- f2.3

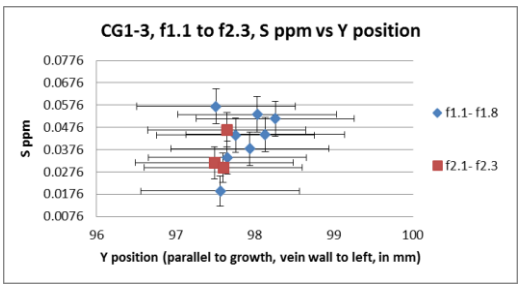
CG1-3, f1.1 to f2.3, S ppm vs Y position
S ppm
0.0776
0.0676
0.0576
0.0476
0.0376
0.0276
0.0176
0.0076
96
97
98
99
100
Y position (parallel to growth, vein wall to left, in mm)
f1.1- f1.8
f2.1- f2.3

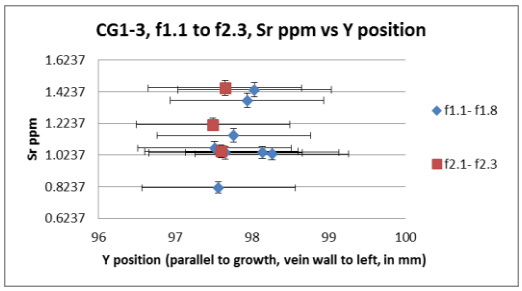
CG1-3, f1.1 to f2.3, Sr ppm vs Y position
Sr ppm
1.6237
1.4237
1.2237
1.0237
0.8237
0.6237
96
97
98
99
100
Y position (parallel to growth, vein wall to left, in mm)
f1.1- f1.8
f2.1- f2.3

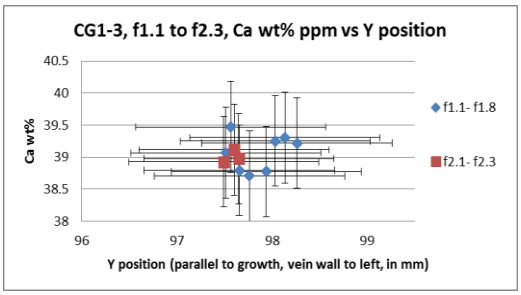
CG1-3, f1.1 to f2.3, Ca wt% ppm vs Y position
Ca wt%
40.5
40
39.5
39
38.5
38
96
97
98
99
Y position (parallel to growth, vein wall to left, in mm)
f1.1- f1.8
f2.1- f2.3

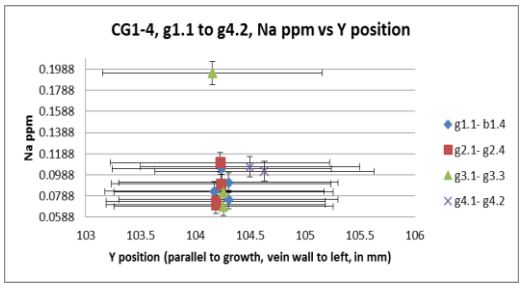
CG1-4, g1.1 to g4.2, Na ppm vs Y position
Na ppm
0.1988
0.1788
0.1588
0.1388
0.1188
0.0988
0.0788
0.0588
103
103.5
104
104.5
105
105.5
106
Y position (parallel to growth, vein wall to left, in mm)
g1.1- b1.4
g2.1- g2.4
g3.1- g3.3
g4.1- g4.2

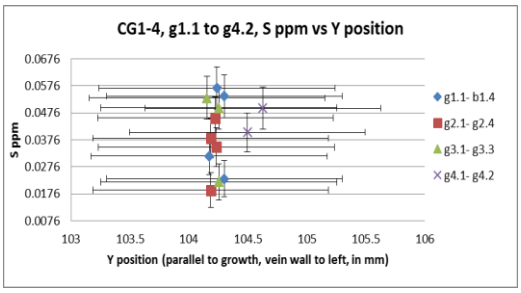
CG1-4, g1.1 to g4.2, S ppm vs Y position
S ppm
0.0676
0.0576
0.0476
0.0376
0.0276
0.0176
0.0076
103
103.5
104
104.5
105
105.5
106
Y position (parallel to growth, vein wall to left, in mm)
g1.1- b1.4
g2.1- g2.4
g3.1- g3.3
g4.1- g4.2

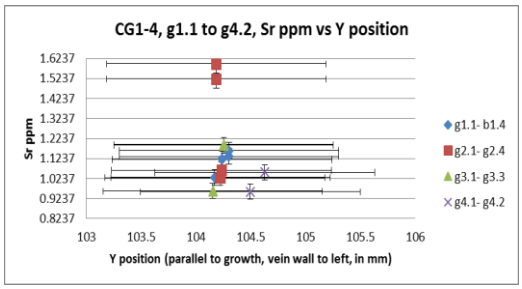
CG1-4, g1.1 to g4.2, Sr ppm vs Y position
Sr ppm
1.6237
1.5237
1.4237
1.3237
1.2237
1.1237
1.0237
0.9237
0.8237
103
103.5
104
104.5
105
105.5
106
Y position (parallel to growth, vein wall to left, in mm)
g1.1- b1.4
g2.1- g2.4
g3.1- g3.3
g4.1- g4.2

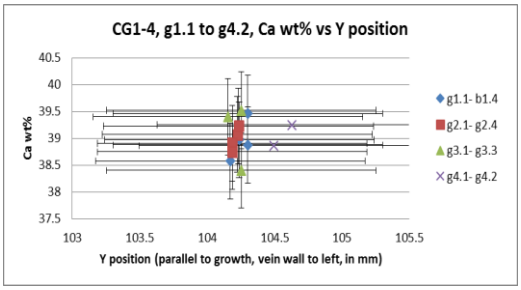
CG1-4, g1.1 to g4.2, Ca wt% vs Y position
Ca wt%
40.5
40
39.5
39
38.5
38
37.5
103
103.5
104
104.5
105
105.5
Y position (parallel to growth, vein wall to left, in mm)
g1.1- b1.4
g2.1- g2.4
g3.1- g3.3
g4.1- g4.2

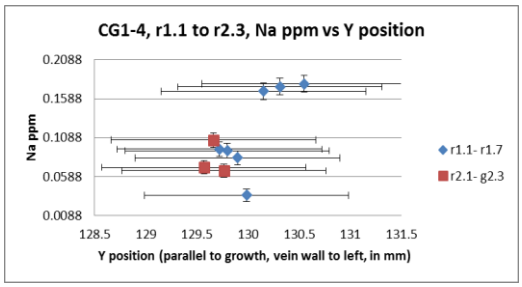
CG1-4, r1.1 to r2.3, Na ppm vs Y position
Na ppm
0.2088
0.1588
0.1088
0.0588
0.0088
128.5
129
129.5
130
130.5
131
131.5
Y position (parallel to growth, vein wall to left, in mm)
r1.1- r1.7
r2.1- g2.3

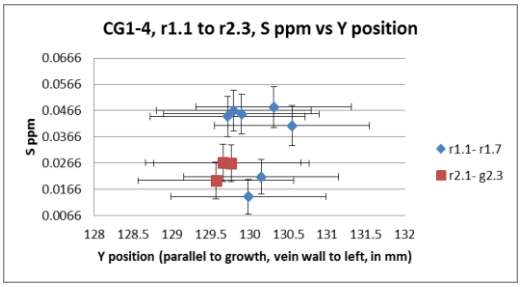
CG1-4, r1.1 to r2.3, S ppm vs Y position
S ppm
0.0666
0.0566
0.0466
0.0366
0.0266
0.0166
0.0066
128
128.5
129
129.5
130
130.5
131
131.5
132
Y position (parallel to growth, vein wall to left, in mm)
r1.1- r1.7
r2.1- g2.3

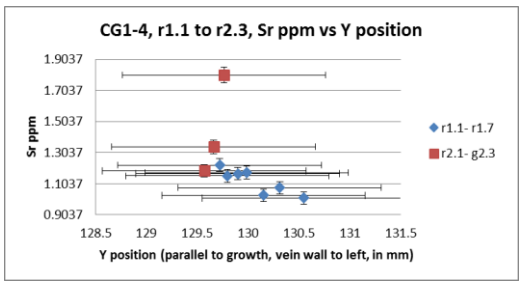
CG1-4, r1.1 to r2.3, Sr ppm vs Y position
Sr ppm
1.9037
1.7037
1.5037
1.3037
1.1037
0.9037
128.5
129
129.5
130
130.5
131
131.5
Y position (parallel to growth, vein wall to left, in mm)
r1.1- r1.7
r2.1- g2.3

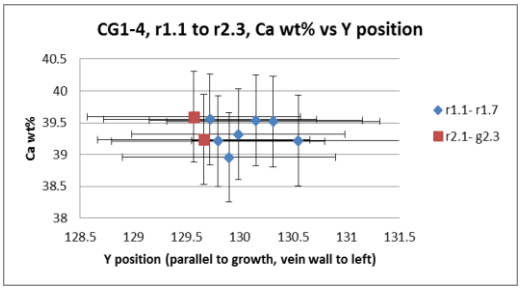
CG1-4, r1.1 to r2.3, Ca wt% vs Y position
Ca wt%
40.5
40
39.5
39
38.5
38
128.5
129
129.5
130
130.5
131
131.5
Y position (parallel to growth, vein wall to left)
r1.1- r1.7
r2.1- g2.3

Appendix 7: ICP-MS results

Sample No.	Position (mm)	Li (ppb)	B (ppb)	Na (ppb)	Mg (ppb)	Al (ppb)	P (ppb)
YTCG1a	1.10E+01	7.47E-01	4.61E+00	2.96E+03	6.51E+00	6.37E+00	4.42E+01
YTCG1b	1.90E+01	4.16E-01	-7.07E-01	2.10E+02	1.01E+01	8.43E+00	7.71E+00
YTCG1C1	2.90E+01	2.77E-01	-2.64E+00	1.91E+02	9.05E+00	8.00E+00	7.24E+00
YTCG1C2	3.80E+01	2.39E-01	-4.25E+00	1.72E+02	4.59E+00	4.18E+00	9.61E+00
YTCG1C3	4.70E+01	3.04E-01	-4.53E+00	2.71E+02	6.84E+00	6.75E+00	3.07E+01
YTCG1D1	5.90E+01	1.84E-01	-1.82E+00	4.99E+02	1.54E+01	2.02E+01	7.76E+00
YTCG1D2	6.80E+01	1.30E-01	-2.00E+00	3.08E+02	6.77E+00	1.10E+01	5.19E+01
YTCG1E1	7.50E+01	2.40E-01	-2.42E+00	7.07E+02	6.80E+00	7.31E+00	6.39E+00
YTCG1E2	8.00E+01	2.02E-01	1.40E+00	1.86E+03	5.61E+00	2.02E+00	1.33E+01
YTCG1E3	8.80E+01	2.30E-01	-6.07E+00	7.77E+02	6.36E+00	6.35E+00	5.03E+00
YTCG1F1	9.10E+01	1.78E-01	-6.47E+00	2.64E+03	1.04E+01	1.35E+01	1.04E+01
YTCG1F2	1.00E+02	2.66E-01	-5.16E+00	1.33E+03	7.41E+00	1.33E+01	1.08E+00
YTCG1F3	1.09E+02	3.07E-01	-3.82E+00	1.40E+03	6.07E+00	5.88E+00	1.55E+01
YTCG1F4	1.19E+02	2.39E-01	6.02E+01	1.59E+03	8.66E+00	4.26E+00	1.27E+00
YTCG1F5	1.29E+02	2.95E-01	-3.79E+00	1.43E+03	5.63E+00	2.50E+01	1.08E+01

LOD (µg/l) ppb	0.00E+00	1.53E-01	3.90E+00	4.88E+02	3.02E+00	3.28E+00	2.35E-02
STD		1.47E-01	1.97E+00	4.92E-01	3.58E-01	1.79E+00	1.13E+01

Sample No.	Position (mm)	K (ppb)	Ca (ppb)	Mn (ppb)	Fe (ppb)	Cu (ppb)
YTCG1a	1.10E+01	1.03E+01	4.44E+04	2.92E+00	4.34E-01	6.68E-01
YTCG1b	1.90E+01	2.01E+01	4.63E+04	3.68E+00	5.37E+00	4.17E-01
YTCG1C1	2.90E+01	1.93E+01	4.25E+04	2.86E+00	1.42E+01	5.66E-01
YTCG1C2	3.80E+01	3.30E+00	4.73E+04	2.60E+00	-7.02E+00	4.99E-01
YTCG1C3	4.70E+01	1.60E+01	5.23E+04	2.71E+00	-6.36E+00	4.28E+00
YTCG1D1	5.90E+01	8.17E+00	4.51E+04	2.29E+00	-2.35E+00	1.30E-01
YTCG1D2	6.80E+01	1.91E+01	4.57E+04	2.10E+00	-4.00E+00	5.82E-01
YTCG1E1	7.50E+01	1.49E+01	4.66E+04	2.85E+00	-2.03E+00	2.40E-01
YTCG1E2	8.00E+01	1.30E+01	4.33E+04	2.12E+00	-7.34E+00	4.63E-01
YTCG1E3	8.80E+01	1.28E+01	4.81E+04	2.28E+00	-6.90E+00	1.44E+00
YTCG1F1	9.10E+01	7.98E+00	5.25E+04	2.47E+00	-6.63E+00	4.49E-01
YTCG1F2	1.00E+02	1.48E+01	4.65E+04	2.19E+00	-5.64E+00	1.01E+00
YTCG1F3	1.09E+02	1.69E+01	4.38E+04	1.82E+00	-6.68E+00	3.22E+00
YTCG1F4	1.19E+02	1.93E+01	4.80E+04	1.97E+00	-7.69E+00	4.60E-01
YTCG1F5	1.29E+02	1.48E+01	4.59E+04	1.81E+00	3.00E-01	2.90E-01
LOD (µg/l) ppb	0.00E+00	1.60E+01	3.78E+02	1.70E-01	2.72E+01	8.61E-01
STD		3.22E+00	1.07E+02	9.07E-02	2.28E+00	1.21E-01

Sample No.	Position (mm)	Zn (ppb)	Sr (ppb)	Ba (ppb)	U (ppb)
YTCG1a	1.10E+01	1.56E+00	1.06E+03	9.66E-01	5.15E-01
YTCG1b	1.90E+01	8.37E+00	1.08E+03	7.27E-01	5.82E-01
YTCG1C1	2.90E+01	8.08E+00	1.00E+03	6.42E-01	4.76E-01

YTCG1C2	3.80E+01	9.16E-01	1.13E+03	6.26E-01	5.00E-01
YTCG1C3	4.70E+01	2.27E+00	1.20E+03	7.50E-01	5.18E-01
YTCG1D1	5.90E+01	3.36E+02	1.04E+03	9.22E-01	4.10E-01
YTCG1D2	6.80E+01	4.76E+01	1.02E+03	5.47E-01	3.75E-01
YTCG1E1	7.50E+01	1.27E+01	1.08E+03	6.39E-01	4.20E-01
YTCG1E2	8.00E+01	1.69E+00	1.00E+03	6.10E-01	3.85E-01
YTCG1E3	8.80E+01	1.69E+00	1.13E+03	6.52E-01	3.86E-01
YTCG1F1	9.10E+01	2.08E+02	1.21E+03	1.12E+00	4.03E-01
YTCG1F2	1.00E+02	6.42E+00	1.10E+03	9.47E-01	3.84E-01
YTCG1F3	1.09E+02	4.30E+01	1.03E+03	5.89E-01	3.44E-01
YTCG1F4	1.19E+02	5.80E+00	1.20E+03	8.22E-01	3.21E-01
YTCG1F5	1.29E+02	4.56E+02	1.20E+03	7.39E-01	3.75E-01
LOD (µg/l) ppb	0.00E+00	2.14E+00	5.00E-01	1.14E-01	4.08E-03
STD		1.06E+00	9.71E-02	8.74E-02	1.10E-01

Appendix 8: Element concentration of present Crystl Geyser spring

Sample ID	Ca mmol/l	Na mmol/l	Sr um/l	Mg mmol/l	Mn umol/l	Ba umol/l
CG1	26.13	163.56	147.12	9.63	28.4	0.08
CG2	26.27	164.41	148.64	9.64	28.25	0.08
CG3	26.11	166.21	148.67	9.61	27.63	0.07
CG4	26.31	169.29	149.41	9.73	27.75	0.09
CG5	25.84	169.69	147.55	9.67	27.08	0.07
CG6	26.03	168.38	148.09	9.54	26.8	0.07
CG7	25.94	168.87	147.63	9.52	26.6	0.08
CG8	25.71	170.81	146.66	9.61	26.58	0.08
CG9	26.33	170.65	150.35	9.56	26.62	0.07
CG10	26.45	162.5	148.28	9.71	29.62	0.08
CG11	26.32	160.07	148.46	9.64	29.51	0.08
CG12	26.24	158.24	148.8	9.64	29.42	0.08
CG13	26.5	158.09	150.33	9.7	29.89	0.07
CG14	26.48	156.75	150.69	9.76	29.84	0.08
CG15	26.73	148.57	154.19	9.97	30.81	0.08
CG16	26.81	133.06	158.03	10.21	32.19	0.08
CG17	26.67	127.74	158.87	10.22	32.23	0.08

Data from Kampman et al., (2014)

Appendix 9: Composition of the spring water in Green River region

The geochemistry data for Green River springs are derived from Spangler et al., (1997).

Spring of the region	Ba/Ca	Mg/Ca	Mn/Ca	Na/Ca	Sr/Ca
Green River Airport Well	7.09E-06	4.03E-01	1.15E-03	9.17E-01	5.70E-03
Crystal Geyser	4.59E-06	4.14E-01	1.15E-03	7.30E+00	6.56E-03
Small Bubbling Spring	6.58E-06	4.87E-01	1.04E-03	8.79E+00	7.56E-03
Big Bubbling Spring	4.64E-06	3.97E-01	3.35E-04	9.88E+00	7.31E-03
Side Seep Big Bubbling	5.76E-06	4.53E-01	3.95E-04	1.11E+01	6.86E-03
Pseudo-Tenmile Geyser	4.15E-06	4.20E-01	1.12E-04	1.18E+01	8.53E-03
Tenmile Geyser	6.32E-06	4.26E-01	8.33E-04	9.88E+00	1.07E-02
Torrey's Spring	5.53E-06	3.37E-01	8.12E-04	1.07E+01	6.17E-03
Tumble Weed Geyser	6.38E-06	4.73E-01	6.41E-04	1.01E+01	8.16E-03
Chaffin Ranch Geyser	3.08E-06	3.76E-01	6.68E-04	7.44E+00	6.36E-03

The geochemistry data for Green River springs are derived from Kampman et al., (2007)

Spring of the region	Ba/Ca	Mg/Ca	Mn/Ca	Na/Ca	Sr/Ca
Green River Airport Well	6.31E-06	3.96E-01	1.08E-03	9.23E-01	4.69E-03
Crystal Geyser	3.83E-06	3.68E-01	1.09E-03	6.27E+00	5.64E-03
Small Bubbling Spring	6.06E-06	4.80E-01	9.70E-04	8.32E+00	6.49E-03
Big Bubbling Spring	4.31E-06	4.01E-01	2.93E-04	9.41E+00	6.41E-03
Side Seep BBS	5.29E-06	4.47E-01	4.66E-04	1.03E+01	6.13E-03
Pseudo-Tenmile Geyser	3.86E-06	4.11E-01	9.18E-05	1.08E+01	7.28E-03
Tenmile Geyser	5.81E-06	4.19E-01	7.88E-04	9.13E+00	9.18E-03
Torreys Spring	5.12E-06	3.31E-01	7.80E-04	9.74E+00	5.22E-03
Tumble Weed Geyser	4.24E-06	3.64E-01	6.33E-04	6.81E+00	5.46E-03
Chaffin Ranch Geyser	2.90E-06	3.73E-01	6.30E-04	7.04E+00	5.33E-03

The geochemistry data for Green River springs are derived from Carruthers' doctorate thesis (2012).

Spring of the region	Ba/Ca	Mg/Ca	Mn/Ca	Na/Ca	Sr/Ca
Green River Airport Well	6.05E-06	3.98E-01	1.13E-03	1.10E+00	5.70E-03
Crystal Geyser	4.09E-06	3.70E-01	1.17E-03	6.10E+00	6.62E-03
Small Bubbling Spring	3.87E-06	3.72E-01	8.23E-04	7.13E+00	7.16E-03
Big Bubbling Spring	3.01E-06	4.10E-01	3.48E-04	1.10E+01	7.35E-03
Side Seep Big Bubbling	1.86E-05	6.84E-01	4.77E-04	1.83E+01	7.06E-03
Pseudo-Tenmile Geyser	3.25E-06	4.22E-01	1.11E-04	1.28E+01	8.40E-03
Tenmile Geyser	4.51E-06	4.32E-01	8.50E-04	1.08E+01	1.04E-02
Torreys Spring	2.97E-06	3.41E-01	8.28E-04	1.15E+01	6.28E-03
Tumble Weed Geyser	3.29E-06	4.13E-01	8.01E-04	9.76E+00	7.23E-03
Chaffin Ranch Geyser	1.71E-06	3.72E-01	6.41E-04	8.06E+00	6.18E-03

Appendix 10: Geochemistry of fluids sampled from the CO2W55 drill-hole

Formation	Depth	Ba^{2+}	Ca^{2+}	Mn^{2+}	Na^{+}	Sr^{2+}
unit	m	µmol/l	mmol/l	µmol/l	mmol/l	µmol/l
Entrada	98	0.4	27.6	42.3	47.6	186.3
Carmel	188	0.6	24.1	88.5	48.3	110.1
Navajo	206	0.2	25.3	103.8	52.6	119.7
Navajo	224	0.3	23.4	75.6	72.4	123.9
Navajo	276	0.4	23.4	68.9	92.6	128.5
Navajo	322	0.3	24.1	63.6	112.5	135.1
Navajo	203	0.4	23.2	79.4	52.5	119.9
Navajo	206	0.6	22.6	177.1	57.1	120.6
Navajo	206	0.3	22.1	67.6	59.9	111.9
Navajo	206	0.4	22.9	73.8	55.9	120
Navajo	206	0.5	20.4	70.8	52.5	114.8
Navajo	224	0.3	23.3	81.8	67.1	117.1
Navajo	224	0.3	24	74.9	76.9	128.3
Navajo	286	0.4	23.4	73	88.9	116.7
Navajo	292	0.3	21	71.2	106.6	106.2
Navajo	298	0.4	19.3	64.1	109.7	99.4
Navajo	298	0.4	24.1	82.6	103.7	121.8
Navajo	316	0.3	20.7	66.8	90.6	110.4
Navajo	322	0.3	21.2	65.5	94.9	117.3

*Data from Kampman et al., (2014)

Appendix 11: Geochemistry of fluid from Aneth and Ismay oil field

Oil field brine ID	Ba (µmol/l)	Mg (mmol/l)	Mn (µmol/l)	Na (mmol/l)	Sr (umol/l)	Ca (mmol/l)	δ18O (‰ VSMOW)
PRD3	Na	66.67	9.27	2260.87	62.79	192.50	2.19
PRD1	8.03	54.17	na	956.52	2054.79	142.50	-6.70
PRD5	2.92	41.67	1.27	869.57	1598.17	110.00	-7.58
PRD2	2.92	50.00	5.02	869.57	2283.11	125.00	-7.51
PRD4	0.73	62.50	5.84	1043.48	1826.48	145.00	-5.60

Data from Spangler et al., (1996)

Appendix 12: Element composition of paradox brine and Airport well from the Green River region.

	Paradox brine from wells (Rosenbauer, 1992)					Airport well (Kampman et al., 2014)
mg/l	4E mg/kg	8E mg/kg	12E mg/kg	Average mg/kg	mmol/l	mmol/l
Na^{+}	77000	76500	77400	76966.67	3.35E+03	2.05E+01
Mg^{2+}	1278	1477	1311	1355.333	5.65E+01	8.80E+00
Sr^{2-}	22.1	22.2	22	22.1	2.51E-01	1.04E-01
Mn^{2+}	0.47	0.49	0.11	0.356667	6.48E-03	2.40E-02
Ba^{2+}	0.064	0.043	0.043	0.05	3.65E-04	1.00E-05
Ca^{2+}	1187	1248	1142	1192.333	2.98E+01	2.22E+01
SO_4^{2-}	5100	5218	5090	5136	5.35E+01	1.92E+01
K^{+}	3630	3810	3850	3763.333	9.65E+01	2.20E+00
Cl^{-}	127100	129300	126250	127550	3.59E+03	3.70E+00
Br^{-}	71.5	73.3	74.3	73.03333	9.13E-01	2.51E-03
SiO_2	5.8	4.7	5.2	5.233333	8.72E-02	3.18E-01
Fe^{2+}	0.25	0.25	0.58	0.36	6.43E-03	1.06E-01
H_2S	77.6	68.8	35.3	60.56667	1.78E+00	na
pH	6.18					6.28

Appendix 13: XRD traces for Mancos shale

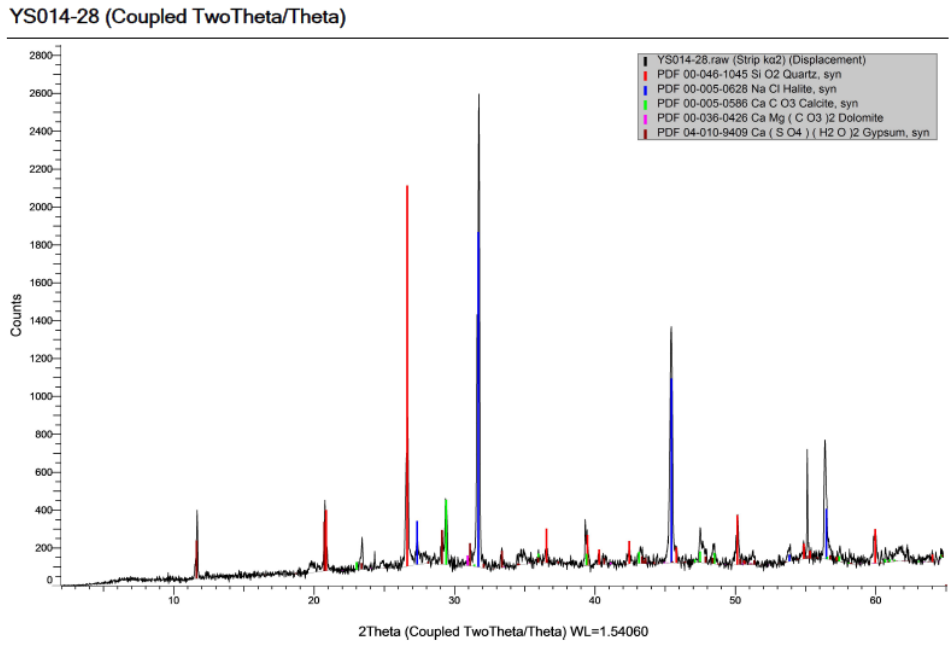

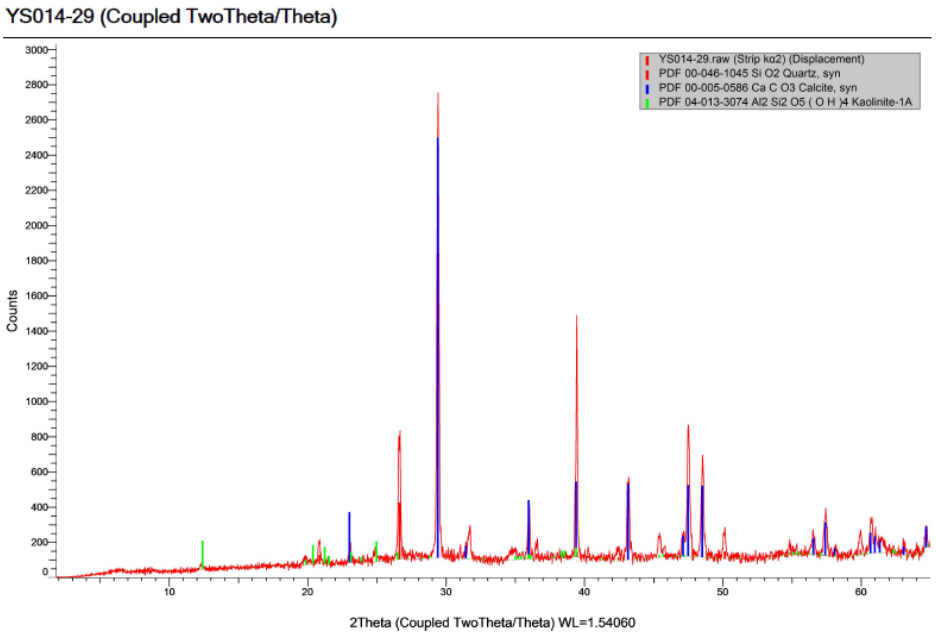

YS014-30 (Coupled TwoTheta/Theta)

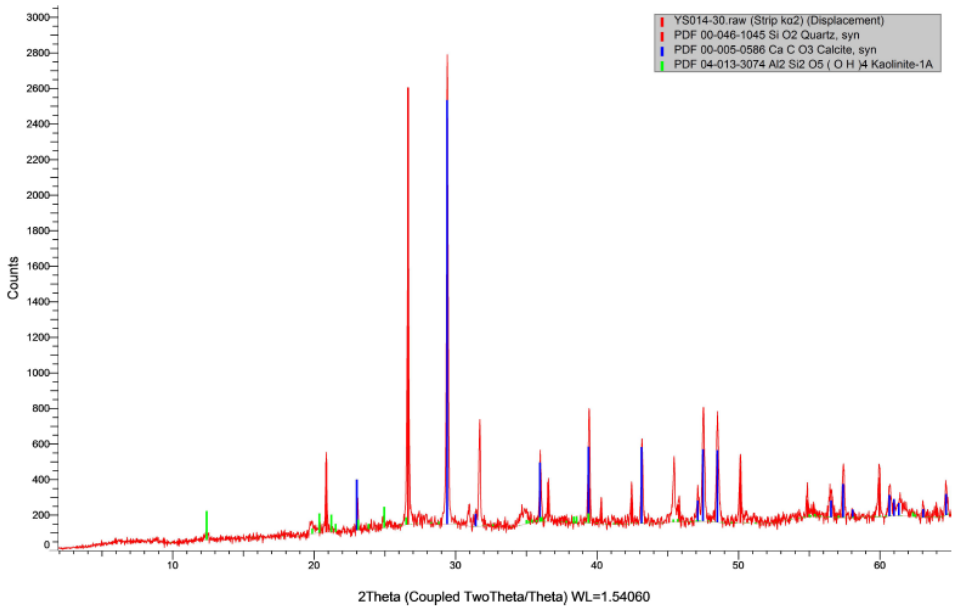

YS014-31 (Coupled TwoTheta/Theta)